CYPRUS UNIVERSITY OF TECHNOLOGY
FACULTY OF ENGINEERING AND TECHNOLOGY

PhD Dissertation

MULTI-PURPOSE ROBOTIC SYSTEM OF THERAPEUTIC ULTRASOUND GUIDED BY MAGNETIC RESONANCE IMAGING

Marinos Yiannakou

Limassol, January 2017

CYPRUS UNIVERSITY OF TECHNOLOGY

FACULTY OF ENGINEERING AND TECHNOLOGY

DEPARTMENT OF ELECTRICAL ENGINEERING, COMPUTER AND
INFORMATICS

PhD Dissertation

MULTI-PURPOSE ROBOTIC SYSTEM OF THERAPEUTIC ULTRASOUND GUIDED BY MAGNETIC RESONANCE IMAGING

Yiannakou Marinos

Supervisor

Faculty of Engineering and Technology, Christakis Damianou, Associate Professor

Limassol, January 2017

Acknowledgements

I would like to express my gratitude to my advisor Dr Christakis Damianou for the continuous support during my Ph.D study. I am grateful for the research motivation, enthusiasm and immense knowledge I have gained from him. His guidance and patience in all the time of my research and especially with the writing of this thesis were invaluable.

Also, I would like to thank Dr Christos Yiallouras for sharing his knowledge about software and all the help he provided during my research. Furthermore, I wish to thank George Menikou for all the great help with MRI imaging and wonderful collaboration.

Last, I would like to thank my parents and my sister for supporting me spiritually throughout my Ph.D. study and my life in general, as well as Maria Chatzifrangkeskou for all her help and encouragement.

Abstract

High Intensity Focus Ultrasound (HIFU) can offer completely non invasive or minimally invasive therapies for various diseases while sparing intervenient tissue. Furthermore Magnetic Resonance Imaging (MRI) can provide well defined margins between tumors and healthy tissue as well as the ability of monitoring the tissue temperature. HIFU can also be used to induce high temperatures hence, it can be utilized to ablate malignant tumors in various organs.

In this study the main objective was the development of MR safe robotic systems to maneuver HIFU transducer in five degrees of freedom (3 linear, 2 angular). The range of motion is up to 14 cm for the linear axis and 180° for the angular axis. Optical encoders enable motion accuracy of 20 μm. The positioning devices incorporate only MRI compatible materials and are small enough to fit in most commercial MRI scanners.

The robotic systems were tested successfully in phantoms and freshly excised tissue in various tasks (robot motion, MR compatibility, and MR thermometry). With minimum changes these robotic systems can be converted into devices for performing interventions with focused ultrasound in various human organs.

Due to the heating in the pre-focal field the delay between successive movements in HIFU are sometimes as long as 60 s, resulting to treatment time in the order of 2-3 h. To reduce the treatment time alternative transducer motion algorithms explored in order to reduce pre-focal heating and treatment time. The simulations suggest that it is possible to reduce the treatment time up to 93 %. Therefore, it will be possible to achieve treatment time of focused ultrasound therapies shorter than 30 min.

Keywords: HIFU, Ultrasound, MRI, Robot, Brain, Liver, Kidney, Fibroid, Prostate, Bone.

Table of Contents

List of Tables

List of Figures

List of Abbreviations

ABS: Acrylonitrile Butadiene Styrene

BBB: Blood-Brain Barrier

CAD: Computer Aided

CT: Computerized Tomography

DAQ: Data Acquisition

DOF: Degrees of Freedom

ETL: Echo train length

FGRE: Fast Gradient Recall Echo

FOV: Field of view

FSE: Fast Spin Echo

HIFU: High Intensity Focused Ultrasound

MBs: Micro-Bubbles

mFU: Modulated Focused Ultrasound

MRgFUS: MRI guided Focused Ultrasound

MRI: Magnetic Resonance Imaging

NEX: Number of Excitations

PD: Parkinson Disease

ROI: Region of Interest

UCA: Ultrasound Contrast Agent

US: Ultrasound

Chapter 1 : Introduction

1.1 Introduction to High Intensity Focus Ultrasound (HIFU)

Ultrasound is essentially sound waves, at frequencies above the human hearing range. When ultrasonic waves propagate in a medium are attenuate due to the absorption, scattering and reflection. These effects depend on the acoustic properties of the medium and the frequency of the ultrasonic beam. When ultrasound travels in a medium, it causes the temperature to increase due to the absorption. Therapeutic ultrasound is used either to induce thermal changes or mechanical effects for various applications. By concentrating the acoustic power of a focused transducer in a small area the temperature is rapidly raised in the focal region in lethal levels. To focus the ultrasound, a transducer with top concaved surface is used. The distance between the focus and the top surface is strongly depended on the radius of curvature.

This ability of the HIFU to induce thermal changes has been investigated first in 1942 [1]. A transducer was designed with a top concaved surface to concentrate the ultrasonic waves to a focal spot. The ultrasonic energy at the focus was found to be approximately 150 times higher compared to the energy near the transducer surface. This difference in temperature can result to tissue necrosis at the focus while leaving intact the intervenient tissue. Follow-up studies showed that based on the ultrasonic dose delivered to a tissue, the changes can be either temporary or permanent [2].

Focused ultrasound appeared effective for the treatment of neurological brain disorders such as Parkinson and Essential Tremor which have been investigated in the 50s [3]. Although focused ultrasound proved effective for the destruction of tumors and treatment for brain disorders, until then it could not be applied without the risk of exposing vital tissue to lethal sonication. Due to the lack of imaging there was no way to estimate the thermal dose and verify the location and the shape of the lesion. This limitation was solved with the introduction of the Magnetic Resonance Imaging (MRI). MRI has the ability to produce accurate stereotactic images with well defined margins of the organs. Therefore monitoring the changes of tissue noninvasively is feasible, and thus the delivery of focused ultrasound is safe. Also MRI can detect small thermal changes below the threshold of tissue destruction in order to locate the focus.

Cranium constitutes a physical barrier for the ultrasound due to its high attenuation coefficient, thus preventing focusing in the brain. The high attenuation of the skull bone

absorbs a major percentage of the ultrasound which results in rapid overheating of the skull. Furthermore, the uneven thickness of the skull distorts the focus of the beam. For these reasons HIFU was not exploited extensively for the treatment of brain deceases in the early stages. For very long time, it was widely accepted that a craniotomy was mandatory to deliver the ultrasound in the brain. The risks of a flap removal from the skull are high and this kind of treatment was not appealing due to possible complications of the craniotomy. The feasibility of the focused ultrasound transmission through an intact skull was demonstrated by Hynynen et al. [4]. According to this study, frequencies below 1 MHz with a single element transducer and 0.6 MHz-1.58 MHz for a phased array system proved to be optimal for transcranial penetration with focused ultrasound.

HIFU technology must be guided with an automated positioning device. The use of such devices aims to reduce the complications and the treatment time. The development of a MRI compatible positioning device, is challenging because the materials must be non-magnetic. Size is also very important since the MRI imaging coil has very limited space so a design with a small and compact structure is required. These devices are especially useful for reliably targeting and positioning an ultrasonic transducer with high accuracy during a treatment. To correlate the focus of the beam with the region of interest (ROI), a low power sonication is initially performed to locate the focus prior the delivery of the therapeutic exposure [5]. With MRI thermometry the small temperature rise indicates the location of the focus. In case that the focal spot appears away from the target, the user instructs the positioning device to move the focus towards the ROI. Such a robotic system moves the transducer less than a millimeter for precise targeting. The transducer must be maneuvered to cover large tumors with overlapping lesions. Since the diameter of a lesion varies from 1-3 mm, the transducer must be moved in a grid formation. The technology of a robotic system with MR guidance is commonly known as MRI guided focused ultrasound surgery (MRgFUS). MR-safe robotic systems have increasingly attracted the interest of many groups. Many different systems have been evolved, specialized in various organs accessible to focused ultrasound. Some of those systems have already reached the clinics with success. Systems for the treatment of gynecological deceases such as uterine fibroids [6]- [7] as well as Leiomyomata [8]–[10] are commercially available. There are MR positioning devices that are specialized for prostate treatment [11]- [12].

HIFU was also applied for breast tumors which are easily accessible to focused ultrasound, since breast has no physical obstacles to block the ultrasonic beam. Several studies have reported progress for the treatment of breast cancer [13]–[18]. Liver is also an organ that was exposed to HIFU treatment [19]- [20]. Furthermore, HIFU was proven effective for pain palliation of bone metastasis [21]–[24].

Similar technologies, emerged that utilized HIFU for tissue necrosis with ultrasound imaging using a specially designed transducer [25]- [26]. This was a dual transducer which was made for both treatment and imaging. The image was provided though the central circular portion of the transducer. During a therapeutic sonication the whole surface of the transducer is excited. In contrast with the MRgFUS this type of technology cannot provide information for the estimation of thermal dose delivered to the tissue.

1.2 Brain HIFU

The major challenge for the treatment of brain diseases with HIFU technology is to develop efficient propagation of the ultrasound through an intact skull. The skull forms a physical barrier preventing the ultrasound due to its high attenuation and reflection coefficient to penetrate through the skull bone [27]. When focused ultrasound travels through the skull bone, the high absorption properties of the bone result in rapid temperature elevation. The temperature rise causes the skin cortex of the brain to overheat. The transmitted ultrasonic waves that reach the brain are distorted and the energy at the focus is significantly reduced. The uneven thickness of the skull bone can complicate the HIFU transmission even further because it prevents sharp focusing [28]. In the early stages these limitations believed to be unsurpassed, hence it became accepted that a craniotomy was mandatory for the ultrasonic waves to access the brain. For this reason in the first clinical trials a section of the skull was surgically removed [29]–[31] to provide a window to allow the ultrasound penetration inside the brain. This was one of the main reasons that this technology was not exploited for brain therapies for many years. With the growth of the technology and the introduction of more efficient transducers, high power amplifiers and phased array systems, transcranial sonications became feasible. Sharp focus can be established through an intact skull [4]. Phased array systems became popular for transcranial ablation since their construction allows the energy to evenly spread to a wider area on the head surface, thus reducing the risk of skin burns and skull overheating. A subsequent study from Hynynen and Jolesz [4] showed that ultrasound can be transmitted through an intact skull with adequate

acoustic power to reach into the brain. The results indicated that a range of frequencies lower than 1MHz were capable to transmit sufficient acoustic power through a skull.

Latter *in vitro* trials that attained to a half human skull demonstrated further the ability of ultrasound to reach areas inside the calvaria [32]. For this experiment a phased array system was constructed with a total of 200 elements. The results revealed a strong focus after a phase correction that was sharp enough for ablation. Similar tests had been performed with a 500-element ultrasound phased array demonstrating the capability of the HIFU to induce lesions transcranially with consistency in rabbit muscle and in gel phantom [33].

A simulation study investigated ultrasonic propagation for a phased array with high number of elements which simulated transcranial sonications without aberration correction [34]. For these simulations computed tomography (CT) image data of 3 cadaver skulls was used. The assessment of the acoustic pressure disruption was simulated for several foci inside the cadaver skull. These computer simulations revealed that for applications that do not require sharp focusing, therapeutic ultrasound can be applied without specific phase correction.

Transcranial ultrasound propagation is highly dependent to the frequency due to the acoustic properties of the bone. Investigation of different frequencies is very important in order to calculate the optimal frequency that maximizes the delivery through skull. In fact for a higher frequency, the shorter the distance that ultrasonic waves can propagate in a medium, due to the attenuation. To achieve deep penetration the frequency must be low enough to allow the HIFU to penetrate the brain. For transcranial sonications the frequency must be kept close to 1 MHz.

The concept to control the acoustic energy delivery into the brain parenchyma with multiple frequencies was demonstrated by White et al. [35]. Frequencies within the range of 0.6-1.4 MHz for 17 points through a human skull were assessed. Their findings with this multiple-frequency technique showed increment of 230 % of the transmitted intensity in 88 % less time-average intensity transmission in the focal volume.

Ammi et al. [36] investigated the effect of different frequencies and assessed their ability to penetrate the skull temporal bone. Speciments of 5 different skulls were sonicated using two unfocused transducers operating at 0.12 MHz and 1.03 MHz and a focused transducer of 2 MHz. The aim was to provide further information for

transcranial sonications through the temporal bone for treatment of the ischemic stroke. The data gathered for the aberrations, the attenuation, the shape of the beam and the displacement of the focus can be used to develop a thrombosis treatment device.

The simulations are very important in order to predict and calculate the optimal path and parameters for a surgery. An approach for transcranial surgery has been proposed using information acquired from CT scans [37]. The idea is to simulate a virtual source from inside the brain to obtain the signals. Then those signals are time-reversed in order to be used experimentally to attempt propagation through the skull. With this process the acoustic power reaching the brain appeared to be near the optimal with accuracy of 0.7 mm. The use of CT images for correcting the phase aberration is a common process and has been done in several other studies [27], [34], [37]–[39]. From CT images the thickness of the skull of a patient and density are known which is very important since for each patient the anatomy differs. This information is used to calculate and correct the phase aberration of the ultrasonic beam that travels though the skull bone. Also with the application of the Zernike polynomials, transcranial focusing of the ultrasound appears to be improved [39]. Another proposed technique to improve the focusing of the US beam is to record and quantized the acoustic radiation resulted from in vitro experiments [40]. This data was later used to map the focus in a rat brain in order to assess the accuracy and estimate the intensity at the focus prior to the sonication.

Furthermore complications with formation of standing waves have been observed during transcranial treatment with FUS. The standing waves are critical and require further attention. The formation of standing waves is a result of the closed area inside the skull that might induce thermal changes in other locations apart from the focus. To deal with the effect of standing waves formation, during experiments it was found that with large-scale phased array operating at low frequencies this effect is reduced and a sharp focus is preserved in the cranium [41].

Commonly in therapies that the purpose is the destruction of tissue, the aim is to induce high temperatures lethal to the cells. In contrast to necrosis there is another mechanism known as apoptosis that disposes the compromised cells or the superfluous cells. This mechanism is also known as "programmed cell death". Apoptosis is found to occur for temperatures near the tissue destruction threshold. After a tissue is exposed to ultrasound radiation, apoptotic cells can increase up to $17 \pm 9\%$ within 48 hours [42]. A latter study was performed to examine the possibility to induce tissue damage to the

brain with short duration sonications aiming to gather information regarding the limitations of this technique [43].

Primate model can provide more representative results due to the skull shape similarities with those of humans. McDannold et al. performed trials with primate model to assess the feasibility of targeting intracranial targets using a frequency of 1.5 MHz [44]. The ability to heat deep brain tissue with focused ultrasound while sparing the surrounding tissue was demonstrated. The navigation was established with MRI imaging as well as temperature monitoring. Pre-clinical trials have been performed with rhesus monkeys to evaluate the thermal damage with a 512 element transducer [45]. The results revealed that treatment through the skull bone could be performed successfully, but circulating water was necessary to cool down the skull. Power and duration of the sonications were found to be limited by the brain temperatures. Furthermore the thickness of the skull bone is proportional to the total mass of the patient [46] and thus the US waves are blocked in different degrees.

Microbubble contrast agent has been used for opening the blood brain barrier (BBB) with the combination of focused ultrasound. By opening the BBB it is possible to deliver drug in a targeted area inside the brain for various brain deceases [47]. Furthermore it has been proved that microbubbles can also help to produce lesions with temperatures lower than the threshold of necrosis [48]. It was also found that these lesions that produced with the presence of ultrasound contrast agent and under ultrasound sonications of low level are dominated by apoptotic cells [49]. In contrast lesions which are created with higher intensity sonications consist of necrotic cells. This technique for producing lesions might suggest the possibility for transcranial sonications with reduced magnitude thus reducing the energy absorption by the skull. These microbubbles can be injected through the vasculature or generated under high acoustic pressures causing caviation. Cavitation is a mechanical effect that occurs when the microbubbles are oscillating in an ultrasonic field. It is vital to control this effect and hence the imaging of its activity is a significant step since this effect is unpredictable and its mechanism is not yet clear. In order to control cavitation an approach to map the cavitation activity with MRI [50] was proposed. This will be a useful tool for the planning and the enhancement of future HIFU brain therapies.

Apart from the ability to coagulate tumors and the disruption of BBB, ultrasound can be applicable for the treatment of neurological disorders. This possibility of the focused

ultrasound was proposed in the 1960 by Fry and Fry [2]. In this study, animal trials were performed in order to calculate the parameters which cause reversible or irreversible damage. This data was used to apply therapy to Parkinson patients with focused ultrasound. A multibeam system that includes four elements was developed. Each of the element's focusing was achieved with a lens in front of ultrasound source. X-rays imaging was used for the planning of the operation. To deliver the ultrasound into the brain a flap was removed from the skull. At that time, neurosurgery was conducted with various mechanical methods that destroy intervenient tissue during the insertion of invasive device to the brain. The removal of a section of the skull was necessary to avoid overheating of the brain during ultrasound exposure which can lead to a rapid increase of the temperature. Shear waves also contribute to the development of high temperatures at the bone since they are absorbed to a greater extend compared to the longitudinal mode [51].

HIFU induces thermal changes and hence the most efficient imaging method is MRI [52]–[55] since some of its parameters are sensitive to temperature [56]. With MRI it is possible to monitor the surgery near real time and simultaneously observe the tissue changes and adjust the treatment accordingly. McDannold et al. investigated further the ability of the MRI to monitor the temperature elevation [57]. The purpose of their study was to use MRI in order to predict the optimal power for HIFU surgery without knowing the exact properties of the tissue.

A review of the current neurological applications of HIFU are described by Foley et al. [58]. Furthermore, with focused ultrasound the ability to stimulate or suppress the nerves causing reversible or irreversible effects was demonstrated. With high intensity sonications it was shown to block the conduction of nerves and the effects may vary depending on the ultrasound properties or the exposure duration. HIFU can selectively suppress nerve functions to reduce conditions of spasticity and pain which are related with CNS disorders, stroke, traumatic injury and multiple sclerosis. Parkinson and Alzheimer disease can be treated by utilizing the ultrasound for targeted drug delivery by reversibly disrupting the BBB. Healing of injured nerves cells is also possible with a subtle ultrasound delivery. The thermal as well as mechanical properties of HIFU must be studied extensively in order to gather more information regarding the dosage in order to trigger mechanisms to safely produce the desired result. In addition nerves that are located deep into the brain was widely believed to be unreachable with ultrasound. Recently the results of a study proved that is feasible to deliver ultrasound to the

trigeminal nerve with a good treatment planning [38]. With careful planning of the surgery and the use of CT data to compensate the aberrations of the skull's, uneven thickness ultrasound was successfully reached into the region. This was possible with the use of a 1024 element phased array and managed to form a narrow focus and raised the temperature up to 18 ℃.

A tanskull treatment with ultrasound can be implemented for neurological disorders like Alzheimer decease by causing stimulation of hippocampal neurogenesis [59]. The HIFU parameters selected were similar to those used for the BBB opening in synergy with microbubbles which showed that HIFU can stimulate the brain to generate new neurons. By focusing HIFU to the dentate gyrus (DG) of the dorsal hippocampus which is the region of the brain associated with learning and memory, it was found that HIFU restarts the generation of new neurons. A similar process can be applied to cases of cerebral ischemia by increasing the permeability of the blood-brain barrier to deliver Erythropoietin (EPO) [60].

1.3 Brain Ablation

Brain ablation is the method for destruction of tumor cells in brain tissue. With focused ultrasound the common method to produce lesions is to deliver continious sonication in order to expose the tissue to high temperatures that result in tissue destruction. Such thermal tissue necrosis can be achieved with various therapeutic technologies. A technology to create lesions with hyperthermia method is the radiofrequency ablation that utilizes radiofrequency energy to induce tissue necrosis. With this technology the procedure requires a probe to be inserted into the brain to create thermal lesions [61]. With the MRI the probes can be guided to the tumor with the patient locally anesthetized. The radiofrequency generator raises the local temperature to 80 ℃ when activated for 1 minute and causes coagulation necrosis.

Exposures to HIFU with a relative long duration for 20-30 s at therapeutic levels induce permanent thermal changes to a tissue. The ultrasonic energy is so intense at the focus and as a result the temperature grows to more than 60 ℃, and therefore due to the high thermal dose the tissue is destroyed. The temperature elevation is caused due to the friction and the absorption of the acoustic waves. The parameters that can be set for brain ablation are the frequency, the transducer geometry, the total duration of a sonication and the acoustic power.

With the HIFU technology the production of thermal lesions can be performed completely noninvasive since that ultrasonic energy can be delivered extracorporeal. In clinical trials three Glioblastoma patients were treated with focused ultrasound with the use of hemispherical transducers and the therapy was guided by MRI [62]. The transducer's construction is intended to evenly spread the heat onto a much larger surface of the calvaria to avoid overheating and skin burns.

Although HIFU is known for its potential to induce thermal effects to tissue with continuous sonication, it can also be utilized in a pulsed mode creating higher pressure amplitude thus producing mechanical effects. This feature of ultrasound is extensively used for targeted drug delivery by disrupting the BBB. This was utilized to develop an alternative treatment for cancer by utilizing pulsed ultrasound to deliver a chemotherapeutic agent into the malignant tumor [63]. Chemotherapy drugs cannot reach to therapeutic levels in the brain due to the impedance of the BBB. Pulsed ultrasound can contribute to the local delivery of the agents to destroy the tumor cells. This technique increased considerably the survival time of the animal [64].

1.4 Applications of HIFU

Unlike brain HIFU interventions that are limited by the skull bone, the organs in the abdominal are easily accessible by ultrasound. Therefore, HIFU can be used for a number of diseases mainly for oncology. Uterine fibroids treatment is an example which demonstrates the effectiveness of HIFU against tumors. Fibroids are tumors formed by muscle fibers that can cause pelvic discomfort or menstrual bleeding, depending on their size and location. The common treatment for large fibroids is surgical intervention. The main downside of a surgical intervention is that it is possible to affect women who desire pregnancy. With HIFU on the other hand, the treatment can be delivered extracorporeal thus, these risks are largely reduced.

To remove fibroids with HIFU the tissue is destroyed with ultrasound selectively. As a result the tissue coagulates and reduces in size. The treatment was approved by food and drug administrator (FDA) since 2004 [65]. More than 2000 patients were treated with this technology [66]. The post treatment follow up of the patients suggest that resulted shrinkage of fibroid size is related to non-perfused tissue volume [65]. The efficacy of HIFU treatment was highlighted by various follow up studies [67]–[69]. These studies

evaluated the improvement based on the fibroid shrinkage while others, reviewed also the improvement of the patients life quality.

Breast cancer is the most frequent disease in women [70]. Treatment with HIFU, which is a completely noninvasive and local therapy would require fewer anesthesia, would reduce recovery time, and could avoid infections and scar formation. HIFU accompanied with MRI provides accurate information on the anatomy of the target and with the aid of MR thermometry the ultrasonic dose can be precisely delivered to the target.

Gianfelice et. al. reported treatement of 12 patients with invasive breast cancer using MRI-guided FUS prior to surgery[71]. Histopatholy of resected tumour in 9 patients showed that a mean of 88 % cancer tissue was necrosed. Residual tumour was in all cases observed at the periphery of the tumour mass, indicating the need for safety margins greater than 5 mm.

In agreement with these findings, Zippel et. al. [72] conducted a phase 1 human trial using HIFU ablation for breast cancer, with use of Insightec's ExAblate 2000 system. Ten patients were treated one week prior to lumpectomy. They reported complete necrosis in only two patients (20%), and concluded that there were still several issues that needed to be resolved before MRgFUS can become a gold standard treatment for breast cancer.

Recently, Furusawa et. al. 2006 [14] conducted human trials with MRI-guided HIFU in 30 patients with breast cancer. All patients followed radical mastectomy after HIFU treatment. On pathologic examination the mean percentage of tumour necrosis was 97 % of tumour volume. In another study Kovatcheva et. al. 2015 [73] conducted clinical trials on 42 women with 51 fibroadenomas in one or both breasts using ultrasound-guided HIFU. Ultrasound-guided HIFU treatment was proven as an effective noninvasive method and was well tolerated by the patients.

The treatment with HIFU for prostate cancer which is the most common malignancy for men, has been investigated since 1990s [74]. Prostate is easily accessible to HIFU since there are no obstacles to block the ultrasonic beam. Various devices were produced to guide prostate HIFU treatment and are commercially available [75]. This procedure is performed either endorectaly or via the urethra. The majority of these devices are guided using ultrasonic imaging which is less expensive than MRI [76]. Despite that,

the ultrasound imaging is less expensive it does not provide information regarding the thermal dose or the temperature of the tissue.

The main advantage of a HIFU treatment for prostate is that, it does not require surgical incision thus, the hospitalization duration and risks for infections are reduced. This type of treatment can also be performed to patients that have local recurrent of previous tumor, or for people that cannot undergo surgical treatment [77]. After a HIFU treatment, the majority of patients did not showed evidence of the disease for up to 92.4% [78].

Clinical trials were also conducted for patients suffering from kidney cancer [79], [80]. These studies showed partial or complete tumor ablation of the tumor. As a result symptoms associated with the malignancy such as hematuria disappeared in 7 of 8 patients. Furthermore 9 out of 10 patients have reported that flank pain was ceased [80]. HIFU treatment was delivered to kidney with two deferent methods. One method used a laparoscopic probe to ablate tumors in 8 patients with a mean 22 mm tumor size [81]. The other technique used an extracorporeal device to deliver treatment to 30 patients [82]. Illing et al. suggest that this is a safe and feasible technique for future HIFU treatments based on their findings.

Liver was exposed to HIFU treatment, as with many organs in the abdominal that are easily reached by ultrasound. The trials were performed to patients with 5-10 cm size of tumors. In this study 69.6% of the lesions were necrosed in the first session and a complete ablation of the tumors was established in the second session [83]. In another study which included 154 patients with hepatocellular carcinoma (HCC) improved the symptoms and also relieved pain for 84.8% of the patients [84]. Additionally, complications were reported in this study such as increase of the body temperature, abnormal cardiac rhythm and various degrees of skin burns. Despite this complications the survival quality of the patients suffering from HCC can be improved when treated with HIFU [84].

Bone metastasis is a frequent complication observed in patients suffering from advanced stages of cancer. This can be attributed to the blood flow in the red cells, the presence of adhesive molecules on tumor cells that bind them to stromal cells in the bone marrow and the production of angiogenic and bone-resorbing factors that enhance tumor growth in the bone [85], [86]. More than 60% of advanced breast and prostate cancers, which are the most common malignancies in adults, metastasize to skeletal

sites during their disease [87]. Metastases in bones from other types of primary solid tumors, such as lung, kidneys, thyroid, bladder and melanoma, also occur but at a lower prevalence. Usually metastatic bone lesions appear predominantly osteolytic [88]. Pain is the most common and distressing symptom associated with bone metastasis [89]. About 83% of patients with bone metastases complain of pain with wide variation and severity [90], [91].

The emerging application of HIFU as standard practice in the curative and palliative medicine of bone tumors is receiving a lot of research interest. Combined with MRI these image-guided systems offer a completely non-invasive, safe treatment option, free of long-term adverse effects, with excellent monitoring of the procedure. The major goal of HIFU applications in palliating pain from bone metastases is the denervation of the periosteum, which contains pain-reporting nerve fibers though thermal coagulation necrosis [92]. Catane et. al. [93] was the first to attempt to assess the safety and initial efficacy of MRgFUS for pain palliation of pain caused by bone metastasis. In a similar study by Gianfelice et al. [94] 11 patients with lesions residing in non-weight-bearing bones were treated with HIFU. Napoli et al. [95] conducted a similar single arm research study of 18 patients with painful metastasis and local tumor control treated with HIFU; an improvement in pain severity score dropping from an average of 7.1 to 1.1 at the 3 month follow up was reported.

The number of applications for HIFU in oncology along with the promising results from clinical trials highlighted the effectiveness of HIFU. With this technology it is possible to access many organs non-invasively to deliver a treatment. In addition this may improve the quality of life of a patient. Furthermore, risks of a surgical incision are avoided since in most of the treatments HIFU is delivered extracorporeal, thus sparing the surrounding tissue which reduces hospitalization for patients. Also with the technology advances nowadays, it is possible to access organs such as brain which was thought to be impossible in the past. The advances of MRI enable excellent visualization of any anatomies and enable temperature monitoring completely non-invasive. With the advantages of HIFU over the surgical interventions, it is possible that HIFU will replace the current treatments for many severe conditions in the future.

1.5 MR Compatible HIFU Robots

The positioning device must be composed of non-magnetic materials for MR compatibility. The size is also limited by the available space in the MRI scanner. MR-safe positioning device refers to the device that is not hazardous in any way, does not generate interference with the MRI scanner and does not affected from the strong electromagnetic field of the MRI scanner [75], [96], [97].

The first positioning device that was developed uses hydraulic principles for the actuation, but proved unreliable since the motors interfered with the MRI scanner [98], [99]. Placing the motors away from the MRI to reduce interference resulted in complicated systems, and thus the concept of a hydraulic positioning device was abandoned. Robotic systems nowadays use piezoelectric motors or pneumatic principles for the actuation which are accurate.

A very successful system is Insightec's ExAblate 2000 [100]. This device is driven with piezoelectric motors and is embedded in the patient's table. It has been primarily designed to be used for the treatment of uterine fibroids [6]- [7] and Leiomyomata [8]- [9], but later was also used for the treatment of prostate cancer [11]- [12], breast cancer [13]- [14], [17], liver cancer [19]- [20], pain palliation and bone metastasis [21]–[24]. Some artifacts were observed caused by the piezoelectric motors [101], but later these were reduced significantly by placing the motors away from the imaging coil. Following the success of the ExAblate 2000, Insightec introduced the ExAblate 4000. This is a very promising system to execute a non-invasive transcranial focused ultrasound delivery into the brain. It is composed of hundreds of elements to spread the acoustic waves in a larger surface across the skull, thus reducing significantly the risk to overheat the skull bone. The potential of this device to focus in the brain though an intact skull can be applicable for the treatment of stroke, brain tumors and functional disorders. The main disadvantage of the phased array is the dimensions prevent the use of the head coil, thus the imaging is acquired through the body coil.

Most of the robotic devices are designed for a specific use. Positioning devices have been manufactured initially for small animal trials. Subsequent positioning devices were made for treatment of human organs accessible by HIFU. A good example of these positioning devices is a computer controlled three axis robot that has been developed by Chopra et al. 2000 which is intended to be used on small animal models [102]. This particular system is designed using aluminum, beryllium copper and ceramic balls

which are non-magnetic. The motion was enabled with the use of piezoelectric motors. The motion precession was established with optical encoders.

Another robotic system that can be used for the treatment of various organs accessible to ultrasound has been developed by Damianou et al. [103]. It has the ability to navigate the transducer in three dimensions. Also it includes a flexible coupling design that enables the targeting to various anatomies. This robot is mainly composed from acrynolitrine butadiene styrene (ABS), and brass rods. The motion is enabled with a belt and pulley system and is energized by three piezoelectric motors. The motion is monitored by optical encoders in real time for adequate accuracy and reliability. An advantage of this device is that it does not require to be integrated in an MRI table and thus it can be used in any MRI scanner. Mylonas et al. 2014 [104] introduced an MR conditional robotic system for the treatment of brain deceases. It was designed based on a similar concept an earlier system of the group [103], but with a less complicated design. The motion was produced by three piezoelectric motors, and the conversion of the rotational to linear motion was achieved with a rack and pinion.

A recent positioning device was introduced by Yiallouras et al. 2014 [76] specialized for the treatment of prostate cancer. This device is very small and compact with a length of 24.5 cm, width of 19.5 cm and a weight of less than 2 kg. It is made out of ABS plastic and its motion is produced by two piezoelectric motors. The device has two degrees of freedom (DOF), (linear and angular). The use of optical encoders ensures an accuracy of 20 μm. The surgery with this device is performed endorectally in order to deliver the ultrasound to the prostate. It can be placed in any available MRI scanner.

1.6 Thesis goals

Thesis goal was to develop 3 MRI compatible positioning devices. The robots were designed using a computer aided (CAD) software and fabricated from ABS plastic. The positioning devices were able to move in three dimensions (X, Y and Z) and in two different angular stages to enable targeting through multiple trajectories The robots were tested in an MRI (Signa, General Electric, Fairfield, CT, USA).

A smaller and more compact positioning device with 2 DOF was developed to perform trials in small animals for preclinical studies (Chapter 7). The mechanical components of this device are immersed in water. The device has the ability to maneuver the transducer in X and Y-axis only. Using 2 linear stages, the transducer can easily access any target of small size without the need of a vertical axis. The advantage of using the

proposed system over a phased array system is that the focus is steered mechanically, instead of electronically thus, the system is less complex and affordable. Although this device was designed for small animals, yet the motion range is wide. Hence, it can easily be adjust for clinical trials if combined with a phased array transducer.

All the robots were tested for MR compatibility, accuracy and functionality in gel phantoms and freshly excised tissues. These robots can be considered as cost effective positioning devices for MRgFUS. These devices operate without any modifications to the MRI scanner. They placed on the MRI bed and maneuver a single element transducer in five dimensions. Single element transducer was activated with a HIFU signal generator that makes the system package compact. Furthermore, the test showed that are safe, accurate and reliable in MR environment.

The devices are simple to use and include a user friendly software interface. User can choose any protocol for thermal ultrasound or pulsed ultrasound. Automated motion control is also available. The software enables user to adjust automated motion control by choosing the size and number of the steps for each dimension. It also has option for manual motion of each stage, thus enabling precise targeting. All the ultrasound parameters are adjustable for optimal sonications. This allows inducing any thermal or mechanical effects required for the different applications. Delay between sonications is also adjustable to avoid pre-focal heating effect.

Due to the heating in the pre-focal heat the delay between successive movements in high intensity focused ultrasound (HIFU) are sometimes as long as 60 s, resulting to treatment time in the order of 2–3 h. Because there is generally a requirement to reduce treatment time, we were motivated to explore alternative transducer motion algorithms in order to reduce pre-focal heating and treatment time.

To reduce the duration for the ablation of large targets, various algorithms were assessed with simulations. Six algorithms (sequential, Euler, triangular, square, random and spiral) were proposed and evaluated. A simulation study was performed evaluating two main indicators: pre-focal heating and treatment time. The simulation model was then evaluated in an in vitro experimental model using a gel phantom. The algorithms used a non linear motion to cover the target in order to avoid pre-focal heating. The results showed reduction of the time duration up to 93 % for a 100 X 100 steps grid. These algorithms combined with the proposed positioning devices can drastically improve the efficacy of HIFU procedures and reduce the duration.

Chapter 2 : MRI guided HIFU Robot (Version 1)

The positioning device was developed to maneuver an ultrasonic transducer on three dimensions (x, y and z axis) in MR environment. The robot Version 1 was designed using CAD (Autocad, Autodesk, California, USA) software. It was manufactured using a 3D printing machine (FDM400, Stratasys, 7665 Commerce Way, Eden Prairie, Minnesota, 55344, USA). The parts were made of ABS plastic which are non-magnetic and hard material, hence are ideal for use in MRI.

The drawings were exported to Stereo lithography (STL) format and loaded to a computer aided manufacturing software (Insight V. 6.4.1, Stratasys Inc.). The Insight software was used to prepare the necessary files for the 3D printing machine (FDM400, Stratasys, 7665 Commerce Way, Eden Prairie, Minnesota, 55344, USA) to manufacture.

The majority of the robot components were manufactured with the 3D printer, with exception of the water container which was made of transparent acrylic plastic. To attach the motors, encoders and other small parts such as pinions, tooth rack and brackets, brass screws were used.

The motion was established with the development of a three-stage concept design; each stage is responsible to move the transducer in one direction. Ultrasonic motors (USR60-S3N, Shinsei Kogyo Corp., Tokyo, Japan) were installed on each stage to induce motion. Optical encoders EM1-0-500-I (US Digital Corporation, Vancouver, WA 98684, USA) were used to detect the motion. The motors move the robot through a pinion and rack system as shown in figure 2.1.
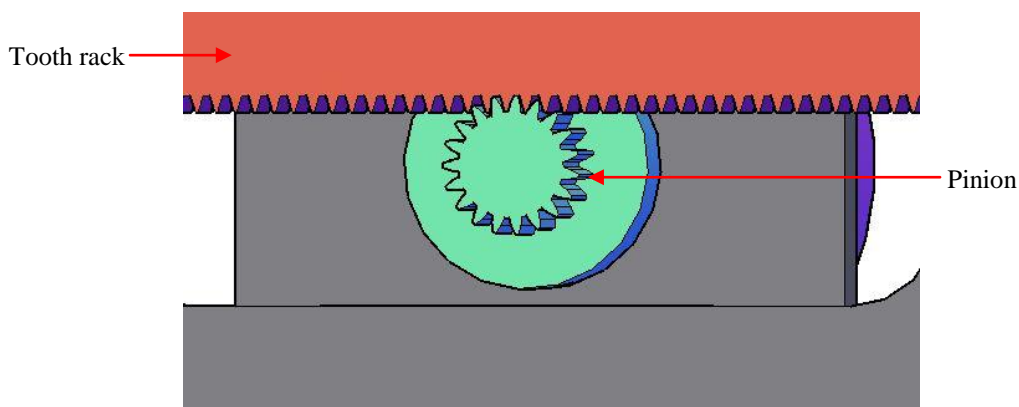
Figure 2.1: The rack and pinion pair.

This type of mechanism (figure 2.1) converts the motors angular motion to linear. The rack and pinion pair was implemented for the motion of X and Y stages. These stages were assembled in trapezoidal guides to ensure linear operation. The Z-stage uses a jack screw mechanism to move the transducer vertically. The jack screw was designed with thick trapezoidal shaped thread. For each complete rotation of the motor, the Z-plate moves 6 mm. A clockwise rotation of the jack screw causes the Z-stage to move upwards, whereas an anticlockwise rotation caused the Z-stage to move downwards.

The structure of the Z-stage shown in figure 2.2 was placed on the X-Y-stage. The compact dimensions are beneficial because of the space limitations in the MRI scanner. The total height of this robot with the Z-mechanism (retracted at the lowest setting) is 25 cm. It has a motion range of approximately 6 cm. The motion range of the positioning device for the X-Y is 14 cm x 12 cm. Due to the relatively large motion range in comparison to an average target volume, this robot can access targets using a bottom to top approach.
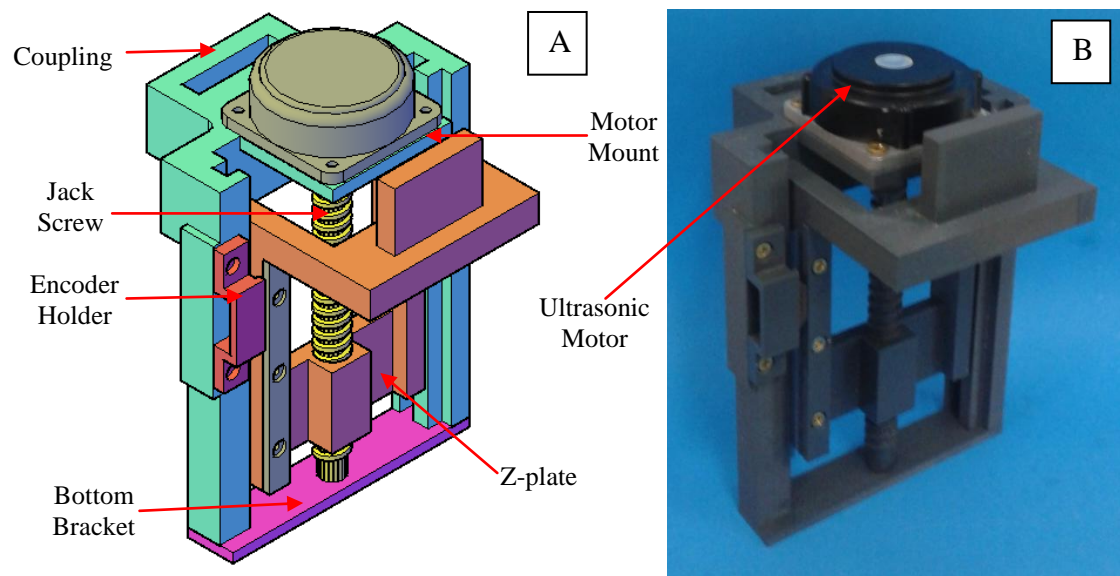
Figure 2.2: A) The AUTOCAD drawing of the Z-stage, B) photo of the Z-stage.

2.1 Version 1 Robot Parts

The majority of the robot parts were made of ABS plastic. The ABS plastic properties provided rigidity to the structure and therefore, good accuracy during positioning. The parts for the motion mechanisms (pinion, rack, jack screw) were also manufactured using the 3D printing machine; which enabled to achieve the optimal motion ratio.

The base shown in figure 2.3 supports the positioning device. The bottom section of the base is 3 cm thick. At the front of the base a coupling is included to secure the water

container holder as shown in figure 2.4. The water container holder hosts the water container. This ensured the water container holder and the positioning device maintain their alignment during operation. The X-stage motor holder is embedded in the middle of the base. The vertical sections on the sides include trapezoidal guides to secure the X-plate as shown in figure 2.5. The openings below the guides provided access for the screws which holds the motor. A reinforcement rod was added on the rear side of the vertical side sections to prevent flexing thus improving the rigidity of the base.

Figure 2.5 shows the X-plate which has a similar structure with the base. It includes trapezoidal guides on the vertical side sections for the Y-plate (figure 2.6). On the X-plate, male guides couples to the guides of the base. The motor holder for the Y-stage motor and the encoder strip holder were placed in the center of the X-plate.
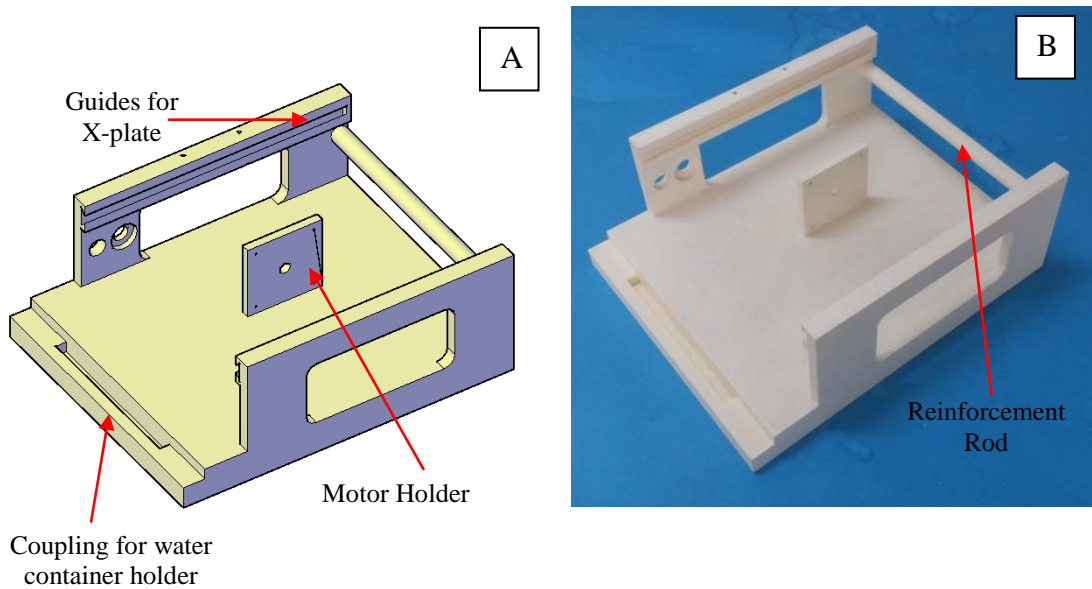
Figure 2.3: A) The AUTOCAD drawing of the Base, B) photo of the Base.
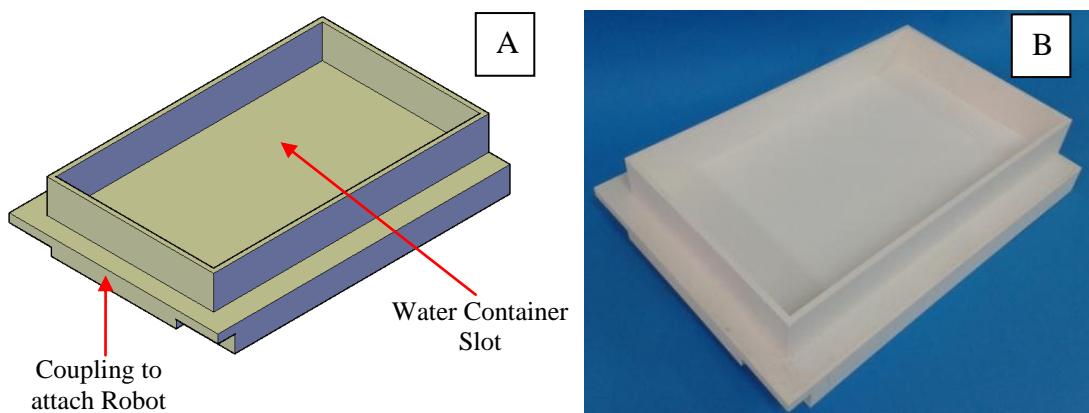
Figure 2.4: A) AUTOCAD drawing of the Water Tank Holder, B) Photo of the water container holder.

18

Furthermore, openings on the vertical side sections of the X-plate and a reinforcement rod were also included.
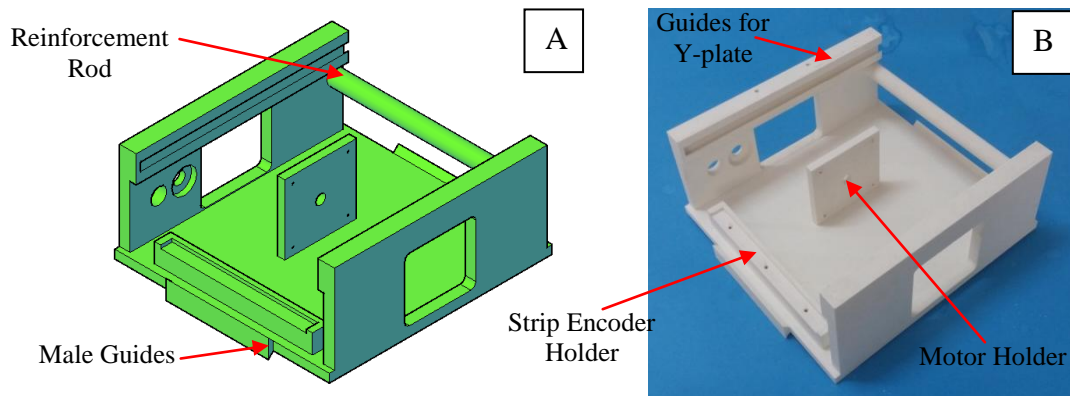
Figure 2.5: A) The AUTOCAD drawing of X-plate, B) Photo of the manufactured X-plate.

On the Y-stage shown in figure 2.6 male guides, slide in the corresponding guides of the X-plate; these also hold the Y-plate onto the robot. A coupling for the attachment of the Z-stage (figure 2.2) was added on the Y-plate. The encoder strip holder was included in the back of the Y-plate.
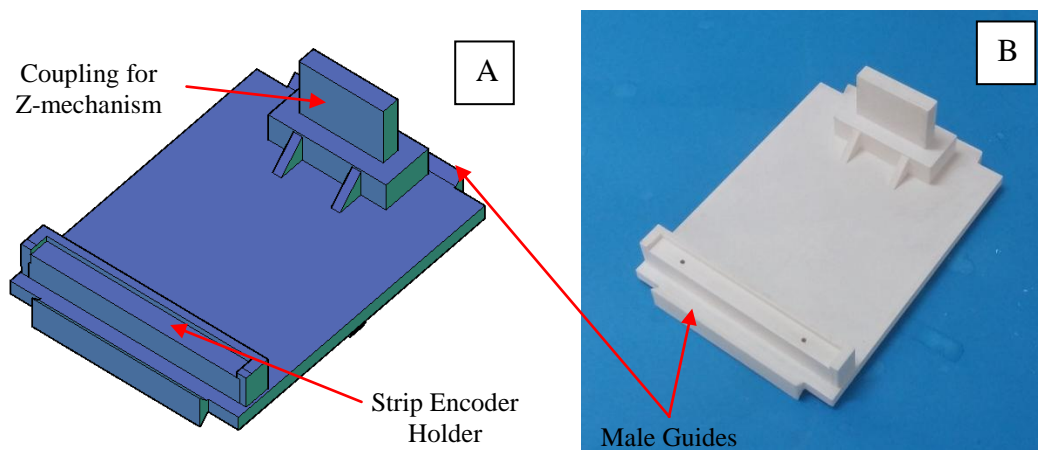
Figure 2.6: A) AUTOCAD drawing of the Y-pate, B) photo of the Y-plate.

To transfer the motion of each motor to the X and Y-stages a pinion shown in (figure 2.7) is attached on the shaft of the motor. Initially an 80 teeth bronze pinion gear was used. The large diameter of the pinion gear (80 teeth) required that the motors operate at the lowest speed. To operate in a more efficient speed a custom-made pinion was designed. The pinion has 19 teeth which are small enough to move the stages smoothly. Generally gears with large teeth require loose coupling to prevent instability between the rack and the pinion. The coupling of the pinion for the shaft of the motor was large enough to enable the brass screw to be tighten enough to prevent the gear slipping.
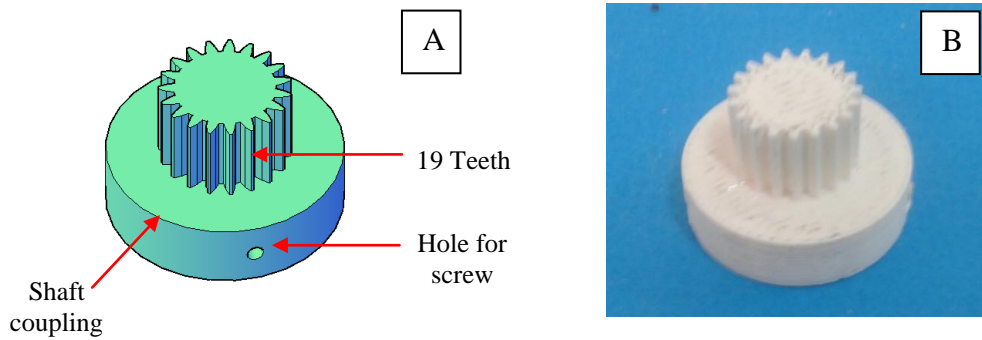
Figure 2.7: A) AUTOCAD drawing of the pinion gear, B) photo of the pinion gear.

To couple with the pinion gear (figure 2.7) a tooth rack was designed. The rack and pinion pair is used to convert the angular motion to linear. The tooth rack shown in figure 2.8 has a base to attach to the X-plate and Y-plate.

The Z-stage design is more complex compared to the X-Y-stage. The Z-frame shown in figure 2.9 has a thin and rigid structure. The frame includes two rectangular guides on the inner sides. It includes a motor holder to mount the Z-motor. To attach the Z-stage onto the positioning device a coupling was designed on the back of the frame. On the left side there is space for the installation of the optical encoder module.
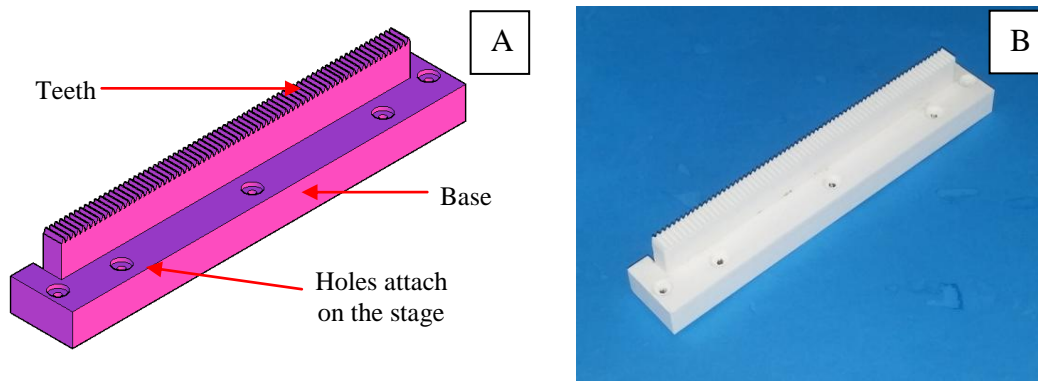
Figure 2.8: A) AUTOCAD drawing of the tooth rack, B) photo of the tooth rack.
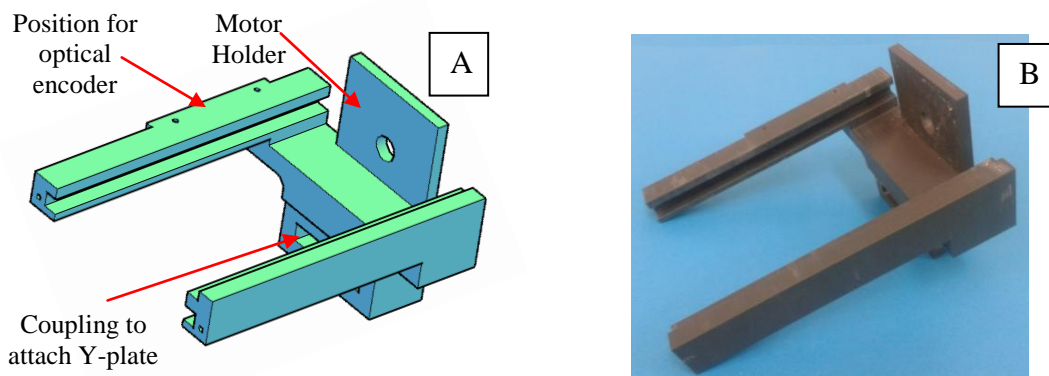
Figure 2.9: A) AUTOCAD drawing of the Z-frame, B) photo of the Z-frame.

Figure 2.10 shows the Z-plate which includes rectangular guides into the frame to establish the linear motion. A female thread is integrated at the lower section that couples with the jack screw as shown in figure 2.11. On the top section of the Z-plate a "Π" shaped coupling attached to the Z-arm shown in figure 2.12. The shape of the coupling creates an opening to avoid hitting the motor holder. The Z-stage is moved by the jack screw that is attached to the motor and centered using the bottom bracket shown in figure 2.13. The bottom bracket also increases the rigidity of the frame and prevents the Z-plate from moving out of the frame.
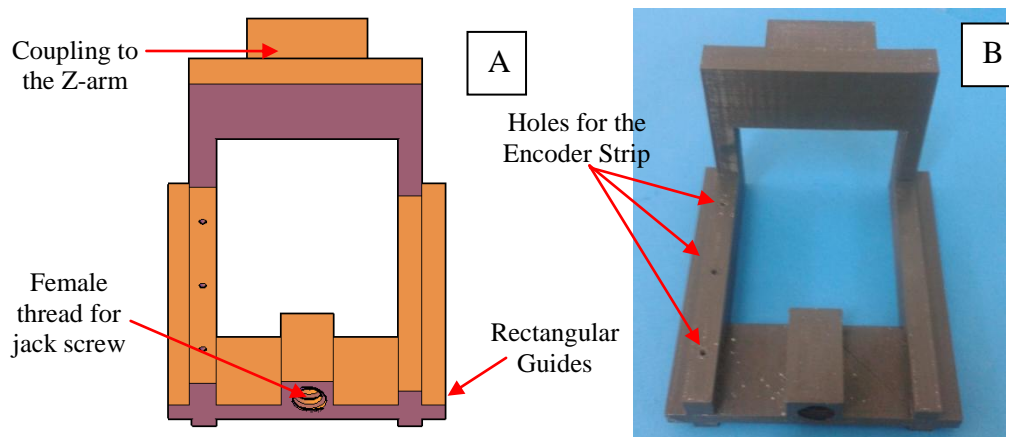
Figure 2.10: A) AUTOCAD drawing of the Z-plate, B) photo of the Z-plate.

The jack screw is attached on the motor with the same coupling as the pinion gear (figure 2.7). To ensure the true rotation of the jack screw, the lower end of the screw has a cylindrical section that couples to the bottom bracket hole. The step size of the thread has a length of 6 mm which effectively reduced the motion ratio compared to the rack-pinion pair. A lower motion ratio requires more revolutions to move the stage a certain amount compared to a higher motion ratio. The reduced motion ratio increased the torque of the system and thus, reduced the stress to the motor, improved accuracy and smoothened the positioning. In addition, the jack screw is a self-locking mechanism which can only be moved when the motor is activated.
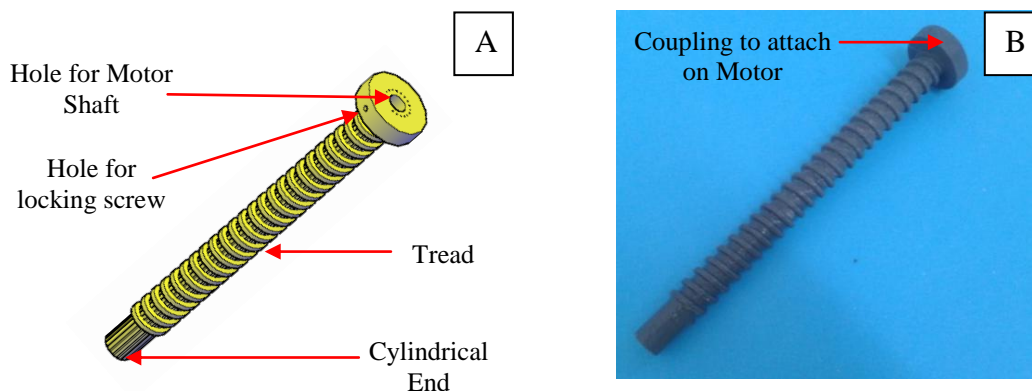
Figure 2.11: A) AUTOCAD drawing of the Jack Screw, B) A photo of the Jack Screw.

The Z-arm is used to attach the transducer to the positioning device. The upper coupling is attached on the Z-stage and the lower coupling is attached to the transducer. The design of the Z-arm enables the transducer to submerge in the water container. The transducer is attached on the Z-arm through the transducer holder shown in figure 2.14. The transducer holder has a hole to secure the transducer and at the back there is coupling for attaching the Z-arm. The use of couplings to secure the transducer onto the Z-arm and Z-stage made the assembly detachable without requiring any tools.

The encoder modules for all three stages were attached using the encoder holders shown in figure 2.15. The optical encoder module is placed under the holder and secured by the two pins. The encoder holder is fixed onto its position by the tabs on the sides. In addition, mounting the encoder modules under the encoder holder also provided protection.
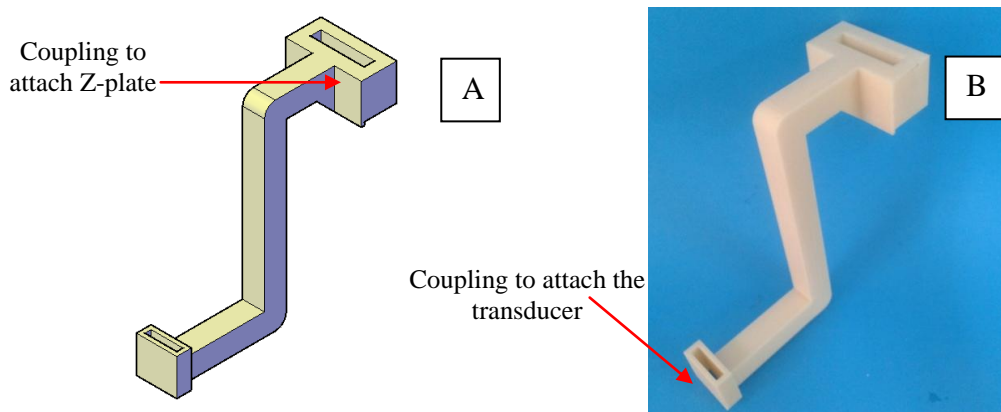
Figure 2.12: A) The AUTOCAD drawing of the Z-arm, B) A photo of the manufactured Z-arm.
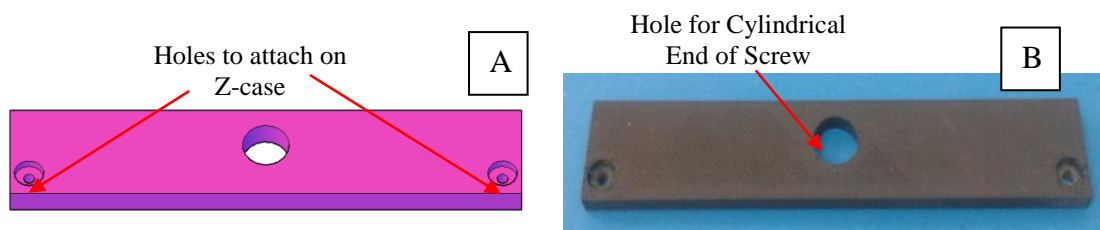
Figure 2.13: A) AUTOCAD drawing of the bottom bracket, B) photo of the bottom bracket.
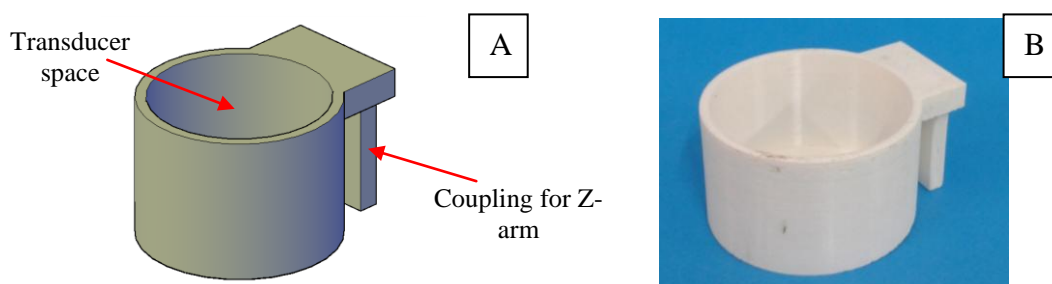
Figure 2.14: AUTOCAD drawing of transducer holder, B) photo of transducer holder.

To enable the ultrasound transmission the water container is filled with degassed water. The transparency of the acrylic tank allows visual inspection of the transducer. The water container is secured with the water container holder (figure 2.4). On the top of the water container a cover with a circular opening (figure 2.17) is placed to support the target. The opening allowed the ultrasound to reach the target. The surface of the table was 2 cm lower in order to submerge the target into the water, thus enabling ultrasound transmission. Under the cover, two slots on each side are coupled to the water container; the slots enable the cover to be slide back and forth to optimize positioning.
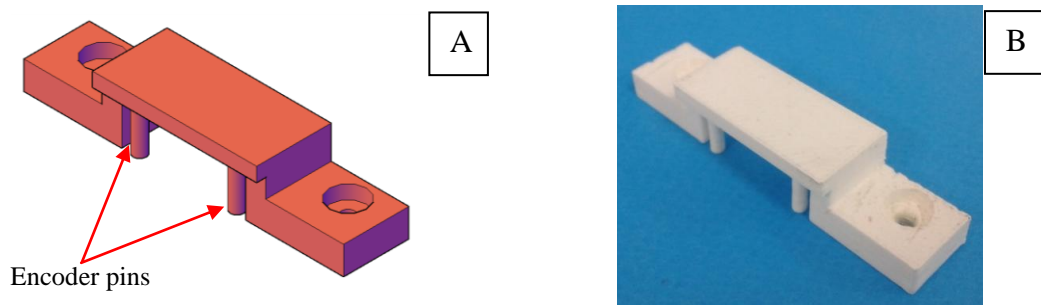
Figure 2.15: A) AUTOCAD drawing of the Encoder holder, B) photo of the encoder holder.
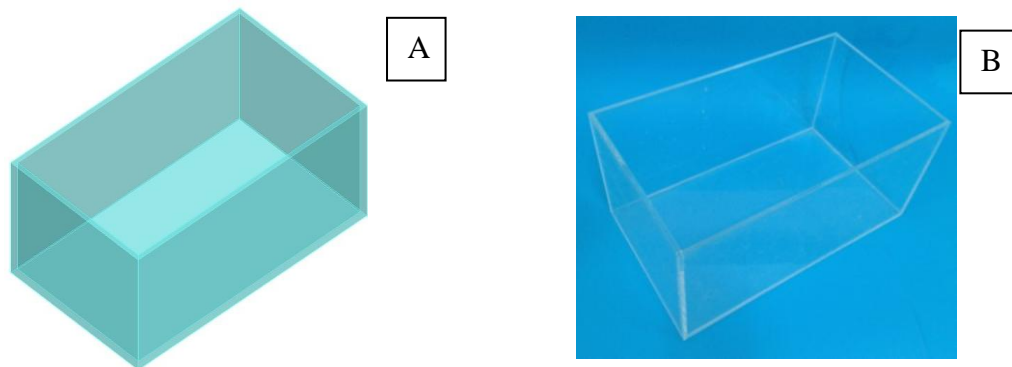
Figure 2.16: A) The AUTOCAD drawing of the water tank, B) Photo of the actual water tank container.
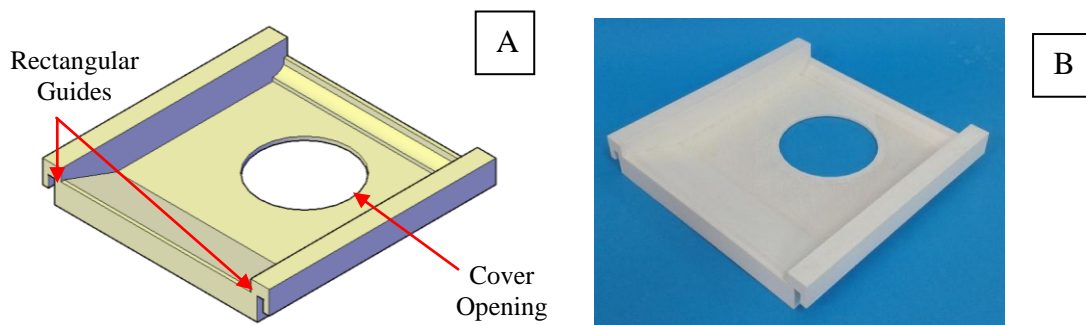
Figure 2.17: A) AUTOCAD drawing of the cover, B) photo of the cover.

The positioning device shown in figure 2.18 has an overall length of 64 cm, width of 25 cm, and height of 25 cm when the Z-stage is retracted at the lowest setting. When Z-plate is fully extended it can reach up to a height of 31 cm. Since the distance from the MRI table to the top of the coil is approximately 32 cm, this device operates with no restrictions in the MRI.
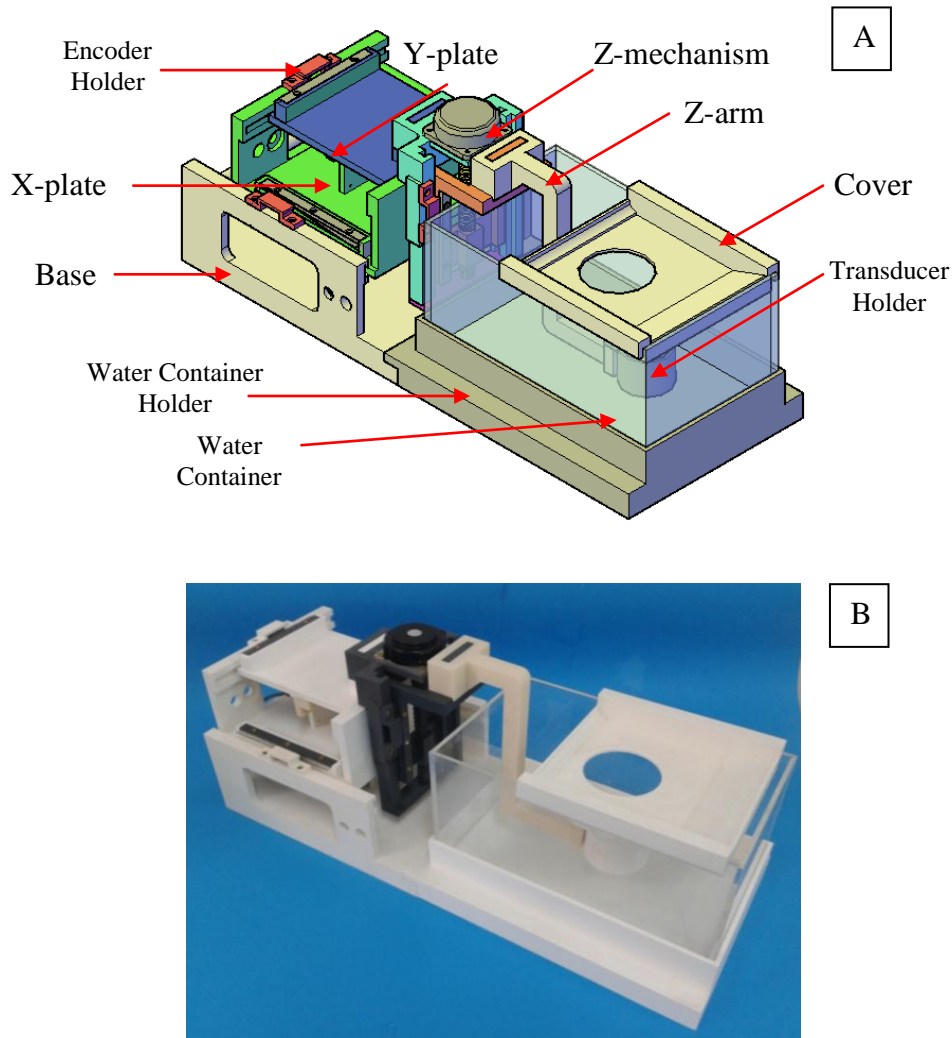
Figure 2.18: A) AUTOCAD drawing of the Positioning Device, B) Photo of the fully assembled Positioning Device.

2.2 Assembling of the positioning device (Version 1)

The motor of the X-stage was fixed with brass screws to the motor holder on the base. The pinion was attached on the motor shaft and was secured as shown in figure 2.19. Additionally, the Y-stage motor and the pinion gear were installed on the X-plate. The encoder strip of the X-stage was installed on the left side of the X-plate as shown in figure 2.20. Under the X-plate, the tooth rack was attached to transfer the motion of the motor from the Base (that is mounted), to the X-plate.
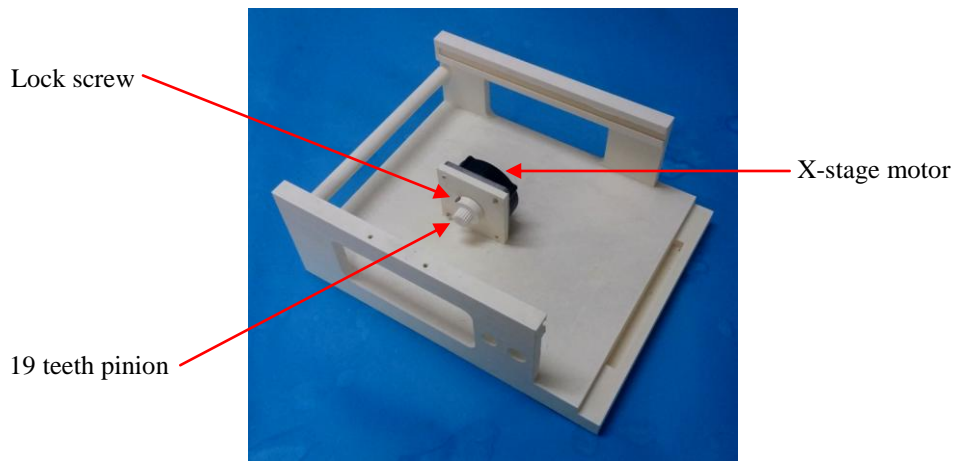
Figure 2.19: Photo of the Base assembly with the motor and pinion.

The X-plate assembly was placed in the guides of the base and coupled to the rack and pinion gear. On the left side of the encoder strip, the optical encoder module was installed on the base using the encoder holder. To measure the motion, the optical encoder module (mounted on a fixed position on the base) detects the motion of encoder strip that is moved with the X-plate. The completed X-stage is shown in figure 2.21.
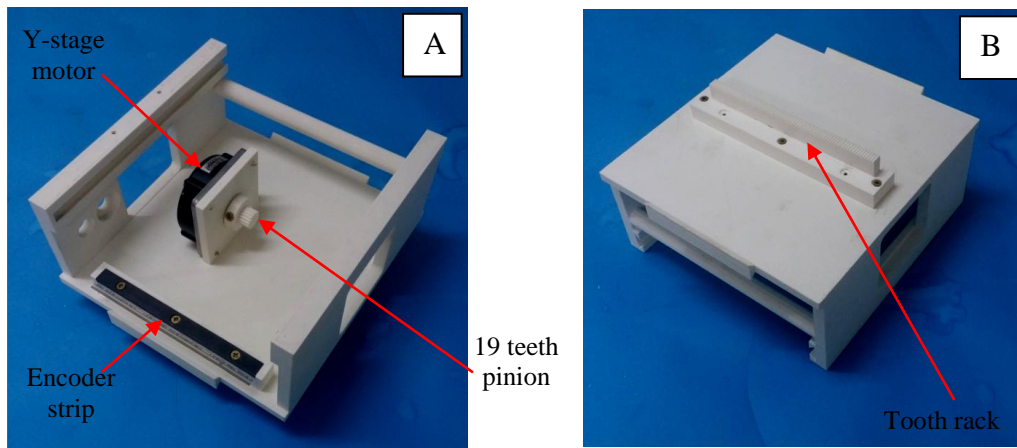
Figure 2.20: A) Photo of the X-plate assembly, B) Photo of X-plate assembly underside.
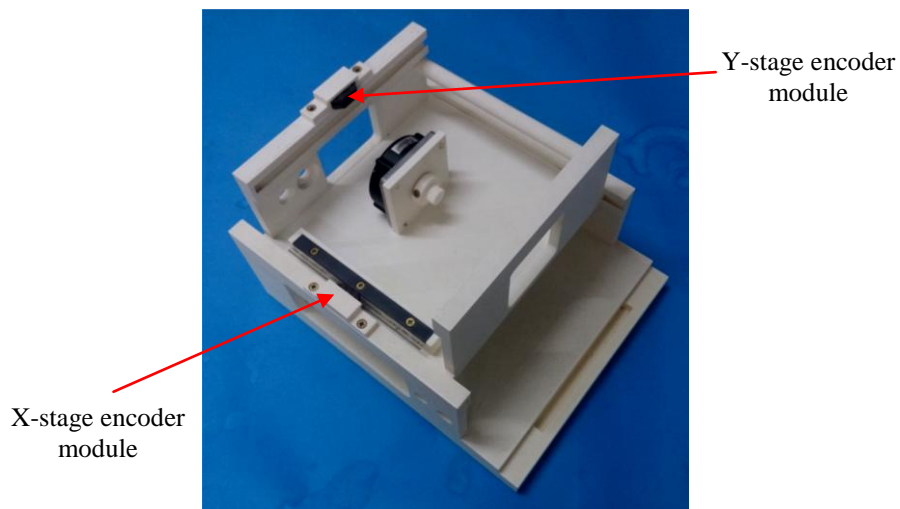
Figure 2.21: Base and X-plate assemblies completed.

The encoder strip was attached on the rear side of the Y-plate as shown in figure 2.22A. The tooth rack of the Y-plate was fixed under the Y-plate (figure 2.22B). The Y-plate was placed in the guides of the X-plate. The X-Y-stage was completed with the installation of the optical encoder module for the Y-stage as shown in figure 2.23.
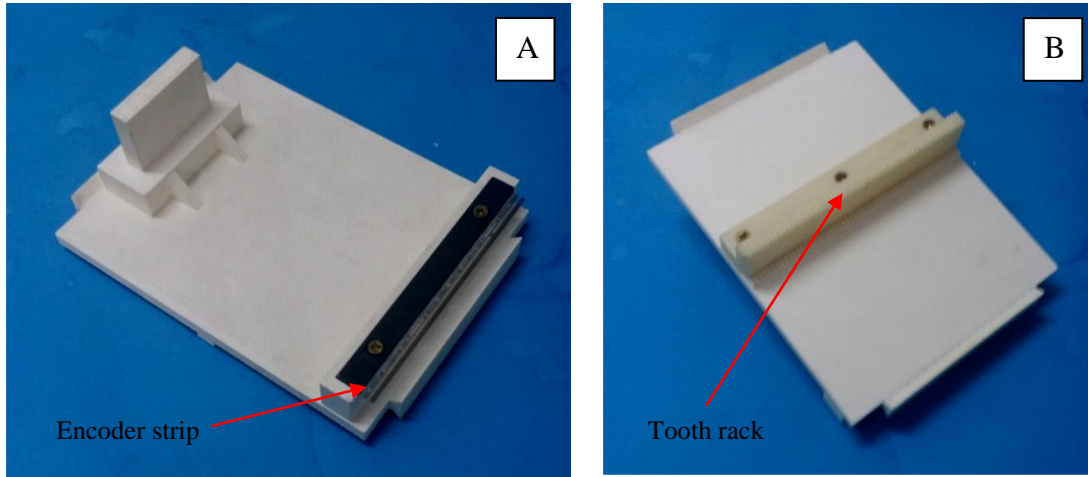
Figure 2.22: A) Y-plate assembly, B) Y-plate assembly underside.
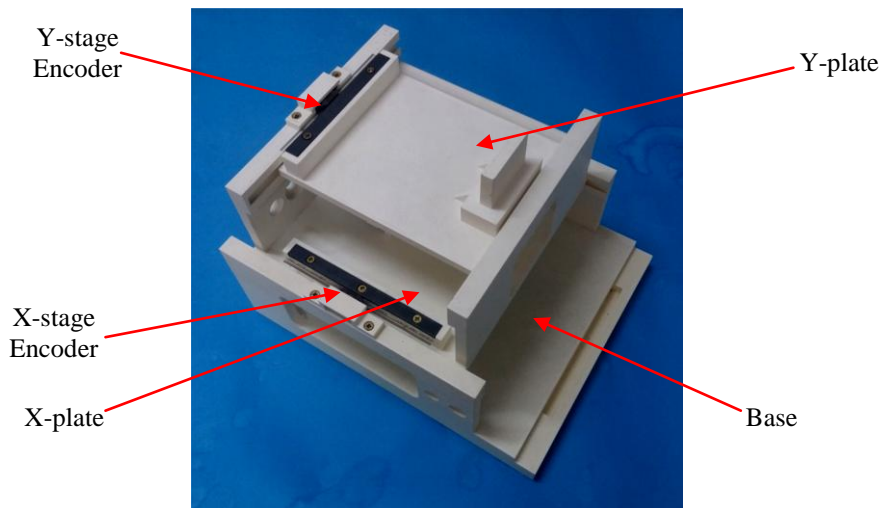
Figure 2.23: X-Y stages assembly including the encoders.

To assemble the Z-stage, the motor was attached on the top of the frame. Under the motor holder, the jack screw was fixed as shown in figure 2.24A. The X-plate was placed in the guides and coupled to the jack screw. Figure 2.24B shows the Z-plate as installed to the frame. Since the jack screw mechanism is self-locking, the motor needed to be activated in order to install the Z-plate. After the Z-plate was installed to the frame, the bottom bracket was attached. Figure 2.25 shows the completed Z-stage including the encoder strip, encoder module and bottom bracket.

After the installation of the Z-stage on the X-Y-stage, the assembly of the positioning device shown in figure 2.26 was completed. The other parts (water container, holder,

cover, Z-arm, transducer) were installed to complete the positioning device using couplings. This design is useful for setting up the device or during trials since it enables easy detachment of these components.
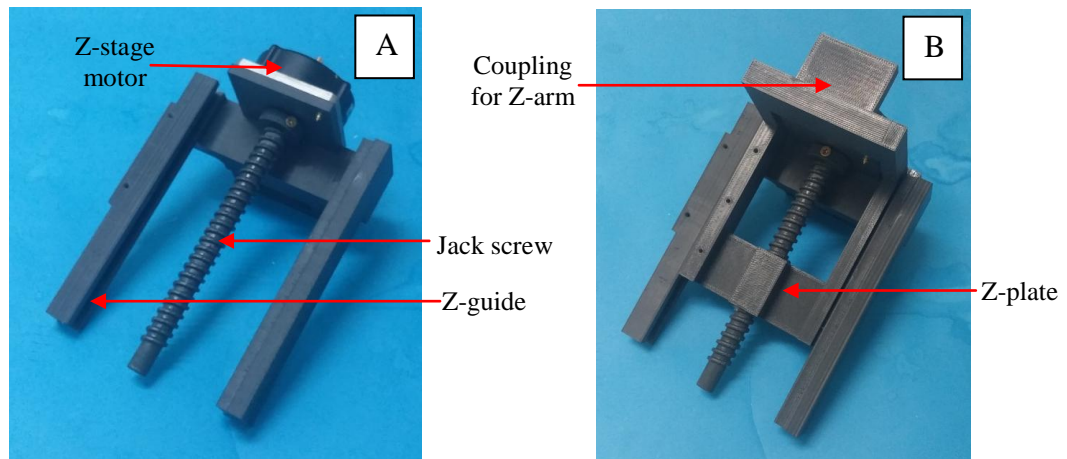
Figure 2.24: A) Frame with motor and jack screw, B) Z-plate as installed to the frame.
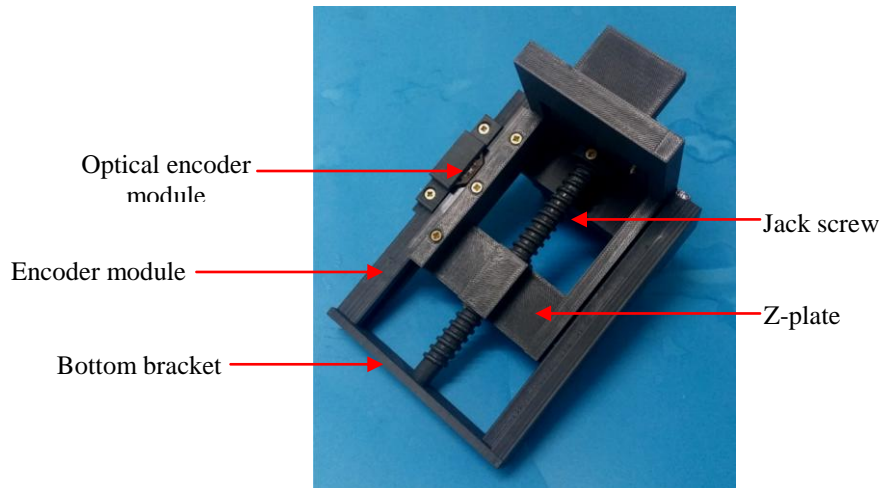
Figure 2.25: Assemble Z-stage including bottom bracket and encoder.
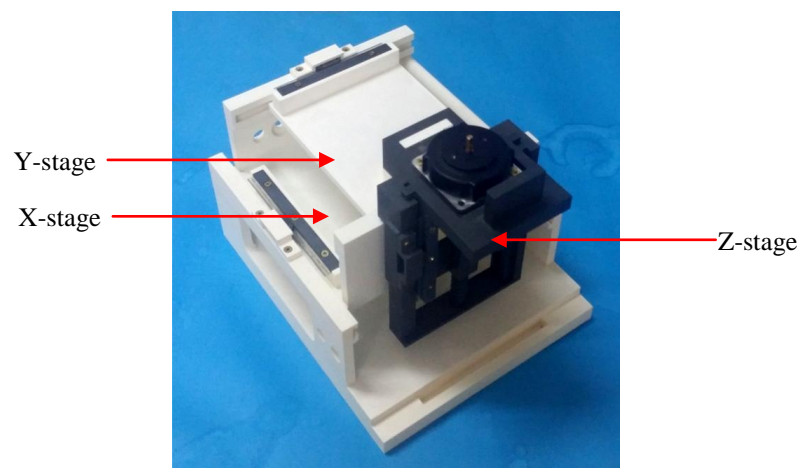
Figure 2.26: Z-stage attached to X-Y-stages.

Figure 2.27 shows the positioning device which includes the water container holder, the Z-arm and transducer holder. The absence of the water container and the cover enables the visualization of the Z-arm with the transducer holder. This demonstrates how the system is aiming the target.
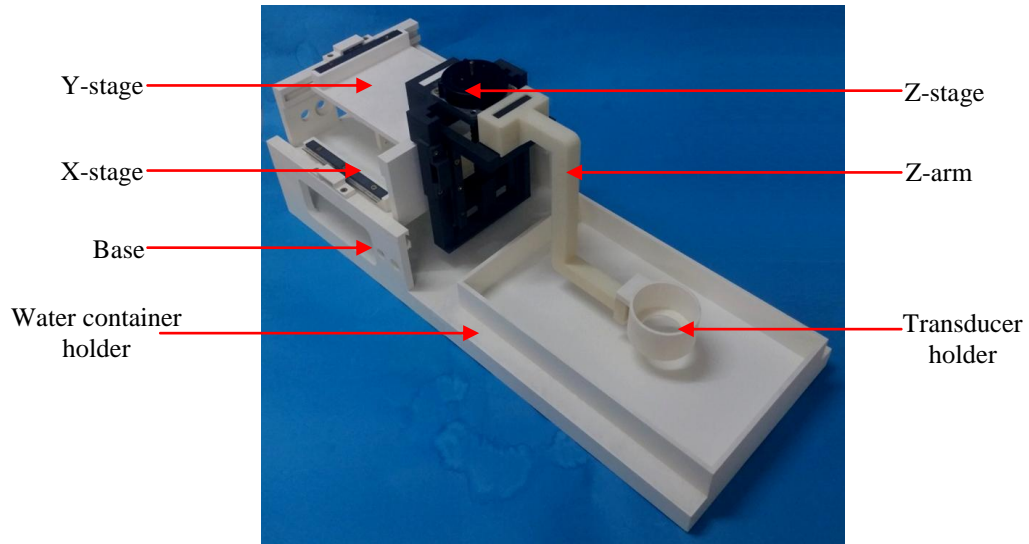
Figure 2.27: Completed positioning device without the water container and cover.

Chapter 3 : MRI guided HIFU Robot (Version 2)

3.1 Version 2 improvements

The second version of the positioning device was manufactured in order to improve the design of the first one (version 1) and to offer a more compact solution. The principle of operation remains the same, but most of the parts have been redesigned decreasing the total height of the positioning device by 4 cm.

By reducing the thickness at the bottom of the water container holder shown in figure 3.1, resulted to a height reduction of 2 cm. Moreover the water container shown in figure 3.2 was increased in width by 5 cm in order to place bigger targets. The height of the water container was reduced by 3 cm since a transducer with smaller focal length, is intended to be used with this version.
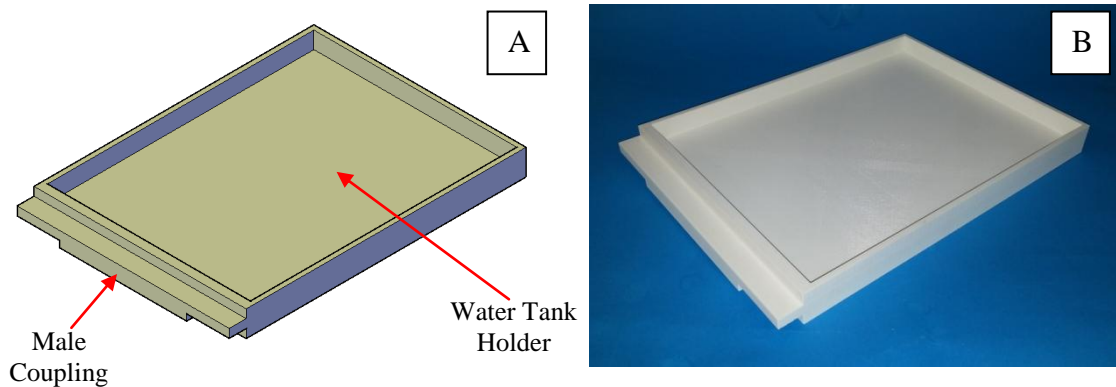
Figure 3.1: A) Water Container Holder (CAD Drawing), B) Water Container Holder (Photo)
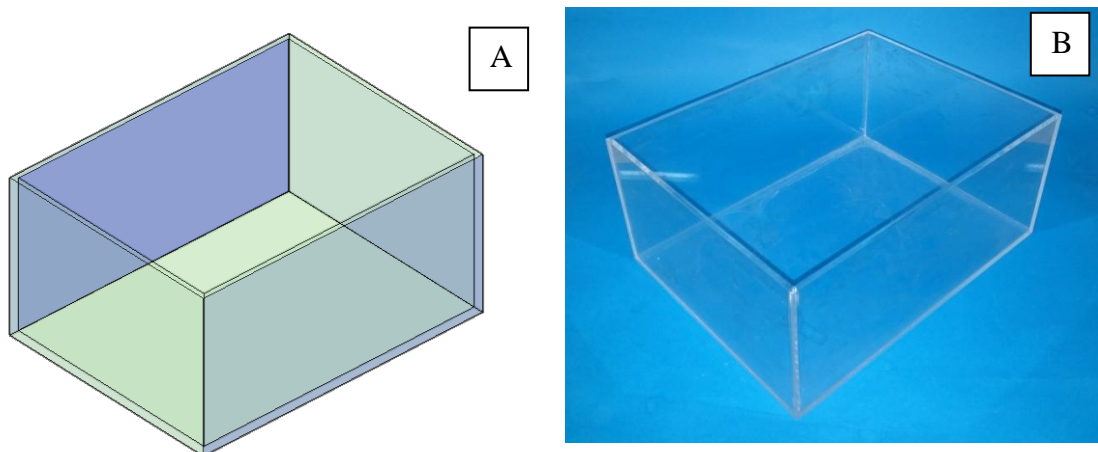
Figure 3.2: A) Water Container (CAD Drawing), B) Water Container (Photo)

The base shown in the figure 3.3 was also revised as a result of the thinner water container holder. The two parts are coupled together hence, it was necessary to reduce the bottom part of the base by 2 cm. The motor mount was updated so that the motor is placed lower by 18 mm. The lower motor position resulted to lower guides, thus

reducing the height (of the positioning device) further; this improvement increased the stiffness of the base and therefore the bar between the guides was removed. In order to further increase the rigidity of the structure, triangle wedges were added on the rear end of the base. Those wedges were not included at the front of the base because of motion limitations.
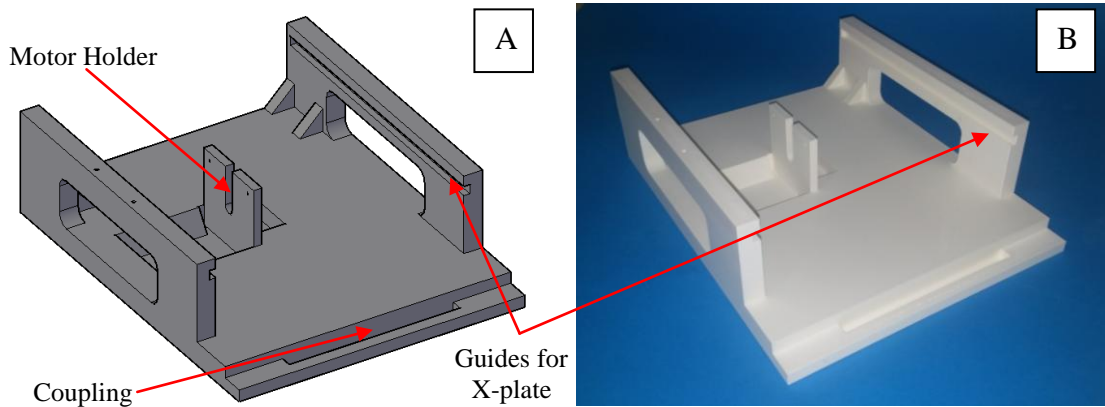
Figure 3.3: A) Base (CAD Drawing), B) Base (Photo)

The motor of the X-stage as well as the X-plate (figure 3.4) were placed lowered by 18 mm. The X-plate received significant updates that reduced its height and eliminated complex designs. The guides of the X-plate were lowered and the rear stiffener rod was replaced with the triangular wedges similar to what was used in the base.
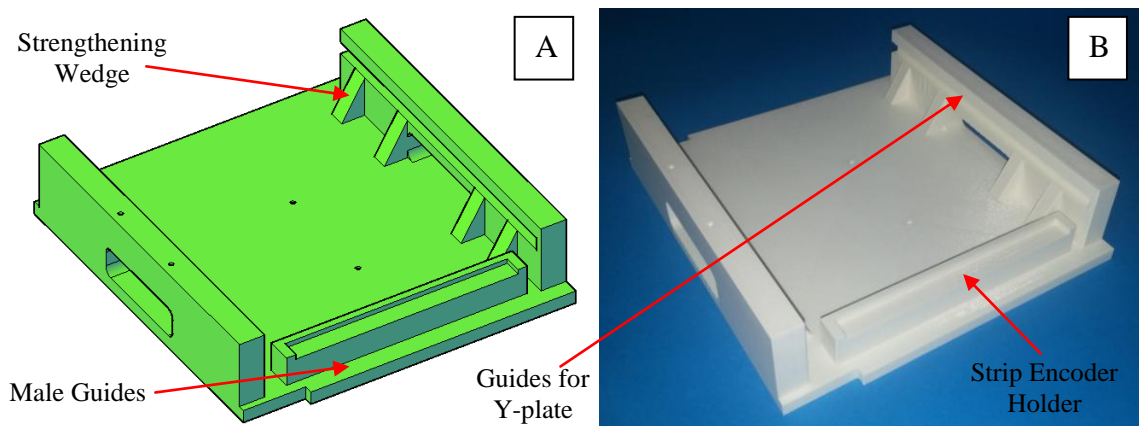
Figure 3.4: A) X-plate (CAD Drawing), B) X-plate (Photo)

The X-plate was designed differently, although the principle of rack and pinion pair remained the same. The most noticeable difference was that the rack of the Y-stage instead of being installed under the Y-plate was installed on the X-plate. By placing the rack on top of the X-plate, the Y-stage motor was placed on the Y-plate as shown in figure 3.5, (facing down). Despite of all these changes, the encoder strip holder remained at the same position.
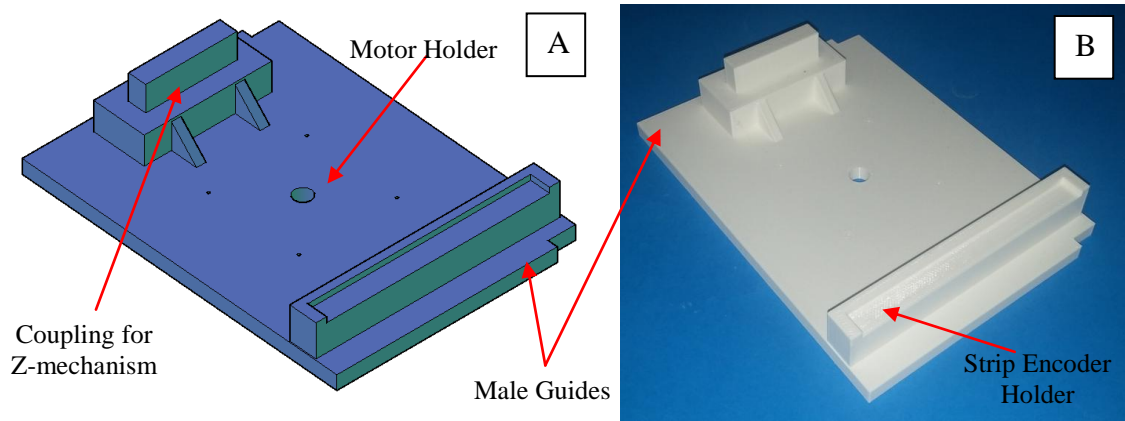
Figure 3.5: A) Y-plate (CAD Drawing), B) Y-plate (Photo)

The Y-plate did not require major modifications other than the holes in the middle that hosted the motor. The trapezoidal shape guides were replaced with rectangular shaped guides for all three stages. The guides on the left side did not cover the entire width of the plate since the corresponding guides on the X-plate are close to the end. This technique increased the range of motion. The height of the Z-stage coupling was decreased by 50 % for easier installation. The Z-mechanism shown in figure 3.6 was improved slightly to fit this robot version. To couple to the Y-plate the female coupling of the Z-stage was decreased by 1 cm due to the changes of the X-Y stage. The principle of operation was the same as the first version. In other words, the motor rotates the jack screw to move the Y-plate and the optical encoder monitored the motion for good accuracy.
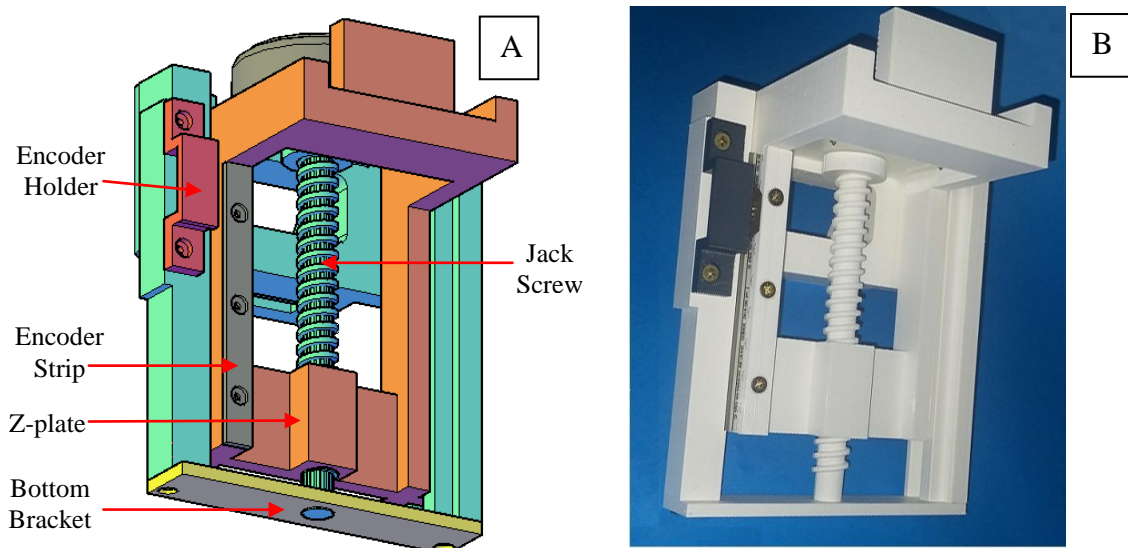
Figure 3.6: A) Z-mechanism (CAD Drawing), B) Z-mechanism (Photo)

The Z-mechanism coupling was lowered to compensate for the X-Y stage height reduction. Also the overall height of the Z-mechanism was reduced by 1 cm. The motor holder was also lowered by 1 cm. Therefore the motor was placed between the guides of

31

the Z-plate. As a result the space between the bracket and the motor holder was reduced by 2 cm (shorter jack screw was required). Figure 3.7 shows the Z-frame with the motor holder placed between the two guides and the different shape of the coupling.
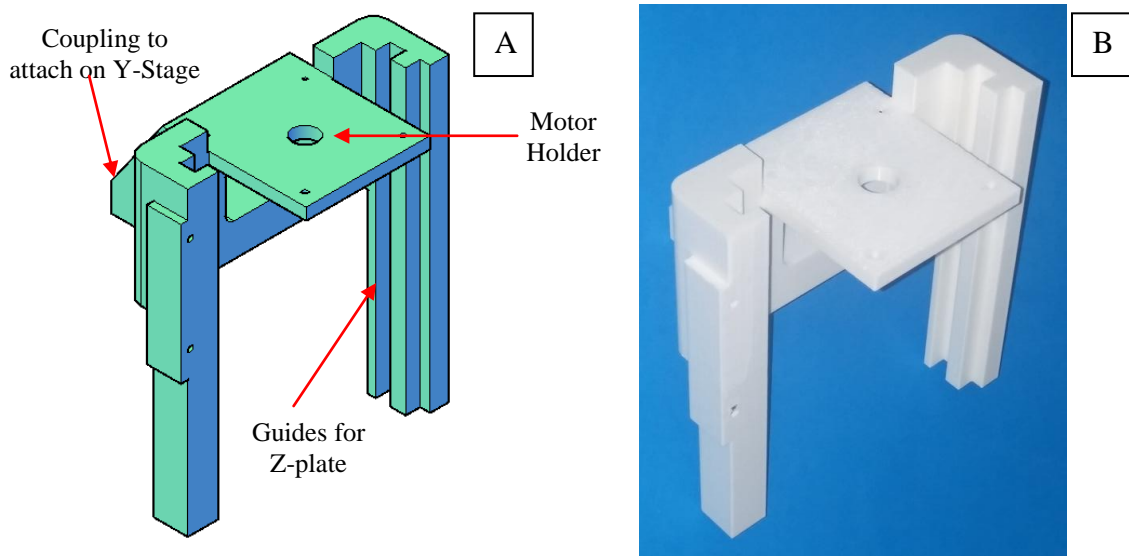
Figure 3.7: A) Z-frame (CAD Drawing), B) Z-frame (Photo)

The Z-plate shown in figure 3.8 was also shortened in order to work with the shorter Z-frame. The bottom section which included the female thread was reduced by 1 cm to provide more clearance from the coupling of the jack screw. These changes of the Z-stage preserved the range of motion despite using a more compact design.
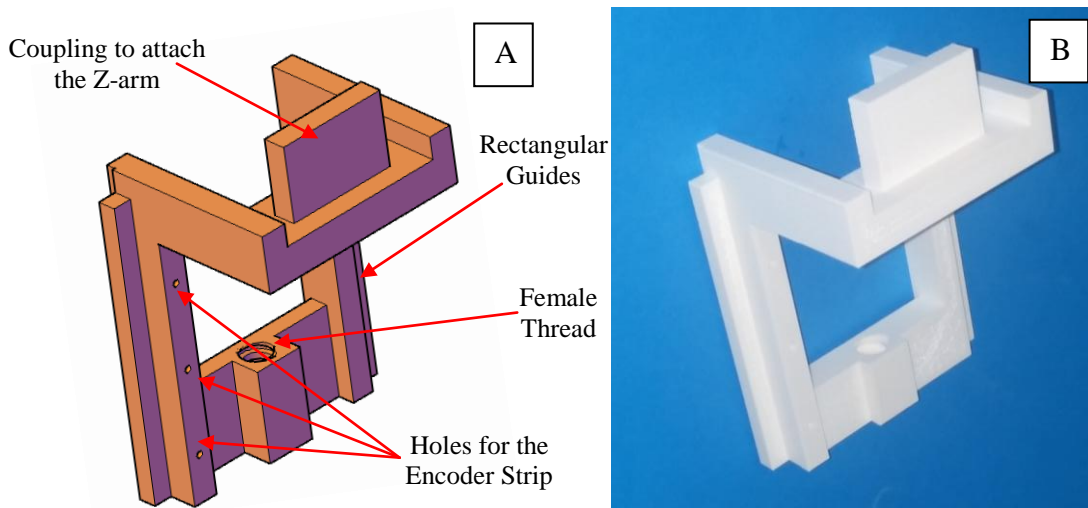
Figure 3.8: A) Z-plate (CAD Drawing), B) Z-plate (Photo)

The Z-arm shown in figure 3.9 was also shortened since this positioning device was redesigned to reduce its size. The coupling of the Z-arm and the transducer holder shown in figure 3.10, were revised since the transducer was smaller in size. It was modified so that the top surface of the transducer was on the same level with the top of

the arm. This was feasible because this transducer was thinner compared to the Z-arm. The coupling on the lower side was reduced to 11 mm as a result of the thinner transducer holder.
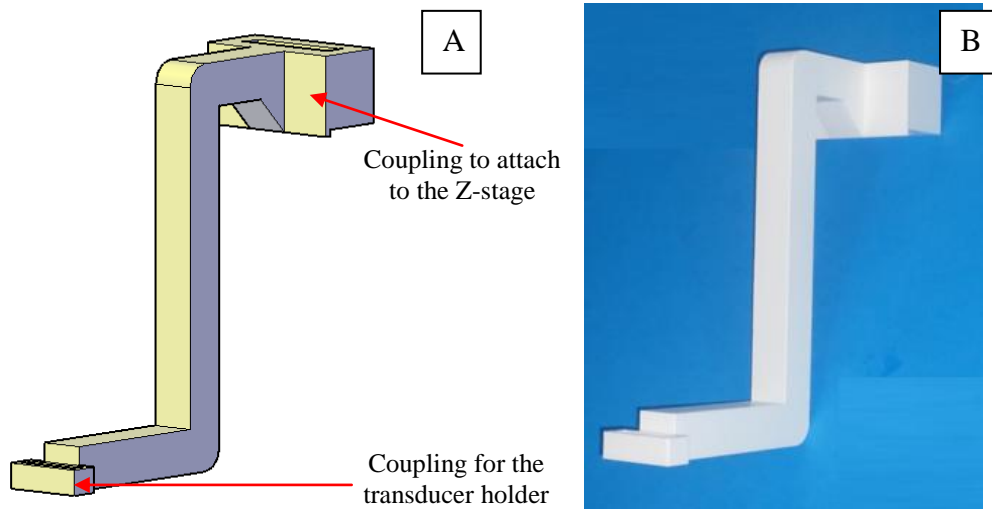
Figure 3.9: A) Z-arm (CAD Drawing), B) Z-arm (Photo)

The transducer holder in figure 3.10 was designed based on the transducer dimensions. Due to the small thickness of the transducer, a smaller design was possible, thus the transducer was lowered by 30 mm. The transducer cable exited from the side, so the transducer could be submerged to the bottom of the water container. For this reason the left side of the transducer holder included a slot for the transducer cable. The transducer was pushed under the holder, in order to be removed safely.
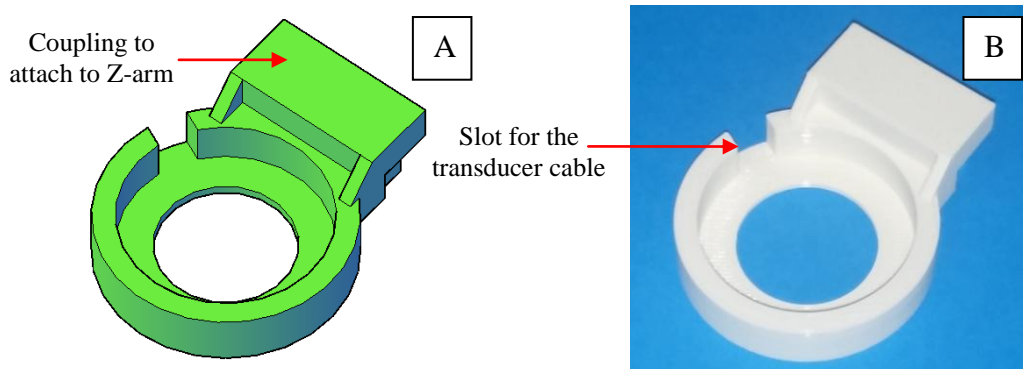
Figure 3.10:A) Transducer Holder (CAD Drawing), B) Transducer Holder (Photo)

The cover of the water container was redesigned to include two openings. The rear piece of the cover is shown in figure 3.11; the opening in the middle provided access to the Z-arm to be submerged in the water container.

The front piece of the cover, shown in figure 3.12 supported the tissue on the water surface. The window in the middle allowed ultrasound propagation to the target. This window was larger than version 1 in order to host larger targets.

Rectangular Slot
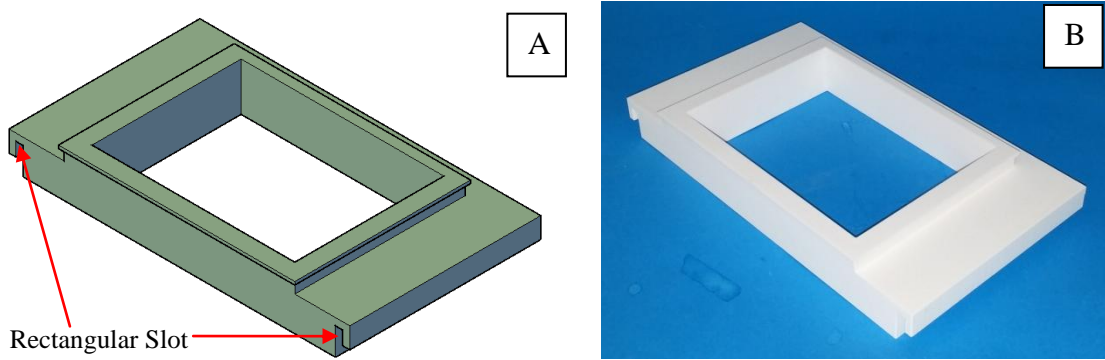
Figure 3.11: A) Cover rear piece (CAD Drawing), B) Cover rear piece (Photo)

Rectangular Slot

Opening for ultrasound
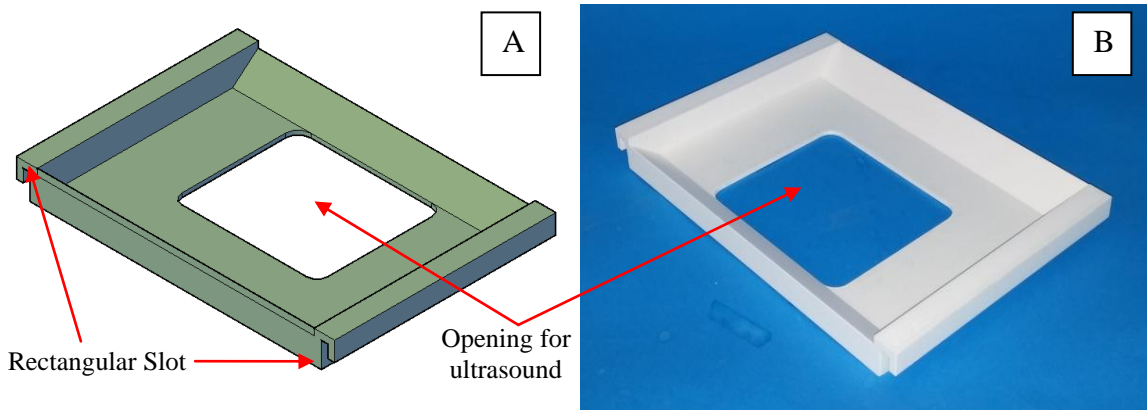
Figure 3.12: Cover front piece (CAD Drawing), B) Cover front piece (Photo)

3.2 Assembling of the positioning device (Version 2)

To assemble the positioning device, the motor of the X-stage was attached first on the base as shown in figure 3.13A. The lower taps of the motor were secured to the base by the channels. After the installation of the motor, the pinion gear was attached to the motor. The base assembly was completed with the installation of the optical encoder as shown in figure 3.13B.

Motor

Pinion Gear
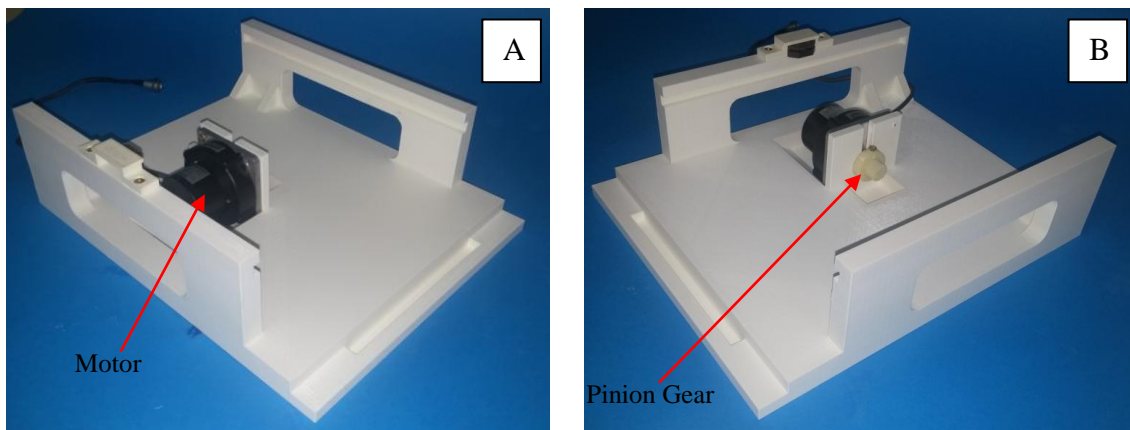
Figure 3.13: A) Motor view, B) Pinion view.

34

The Y-rack shown in figure 3.14A included two holes for mounting in the middle of the X-plate. The encoder strip for the X-stage was fixed by the encoder strip cover. On the top left side of the X-plate the optical encoder module for the Y-stage was held by the encoder cover. The upper section of the X-plate assembly is shown in figure 3.14B.
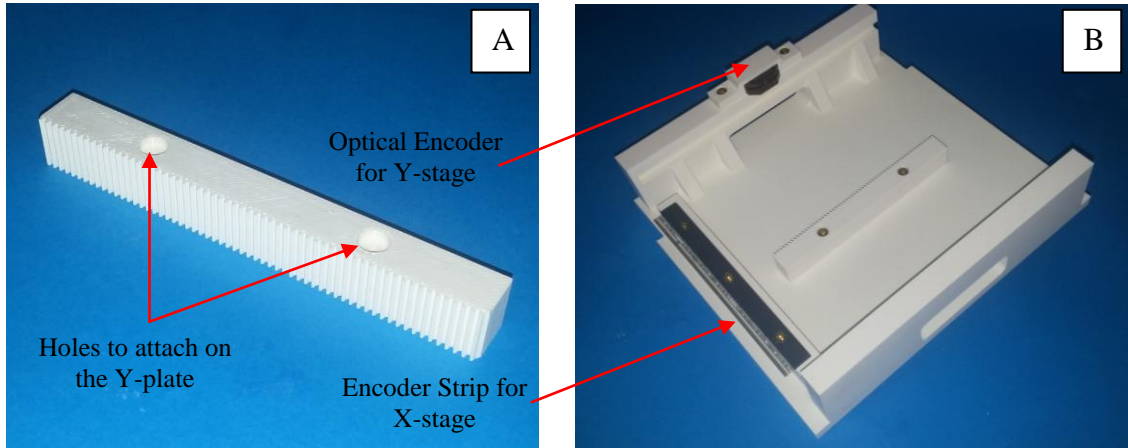
Figure 3.14: A) Photo of the rack, B) Photo of the rack attached to the X-stage.

The rack of the X-stage (figure 3.15A) was attached as shown in figure 3.15B. It was mounted under the lower surface of the X-plate and was fixed at specific holes that were included in the design to ensure accurate alignment of the rack with the plate. The accurate placement of the part was critical for proper coupling and smooth operation between the rack and pinion.
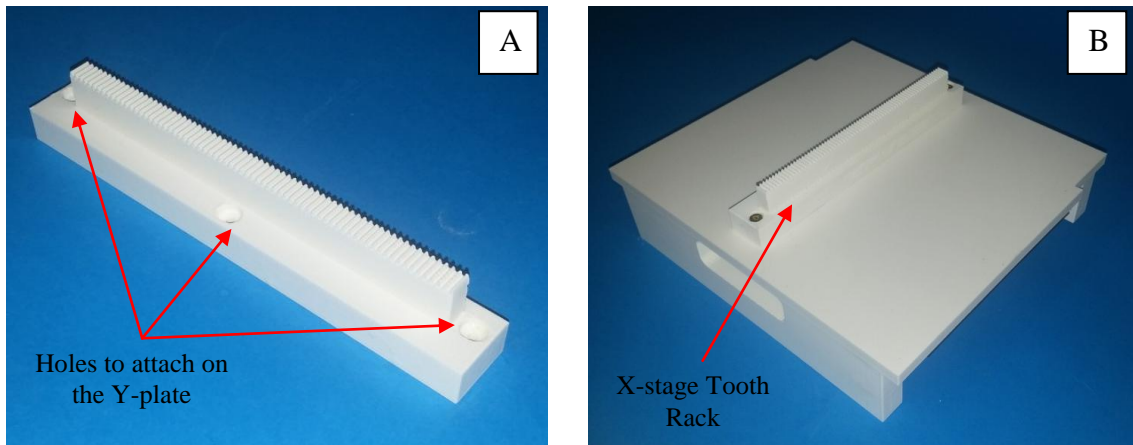
Figure 3.15: A) Photo of the X-stage rack, B) Photo of the X-stage tack installed under the X-plate.

The Y-plate slide in the guides of the X-plate so that the pinion was coupled with the rack. Similarly the X- Y plate slides along the guides embedded on the base to complete the X-Y stage for the forward/reverse and the left/right motion respectively. The positioning device with the X-Y-stage is shown in figure 3.16. The motor, encoder, and the jack screw were mounted on the Z-stage as shown in figure 3.17A.
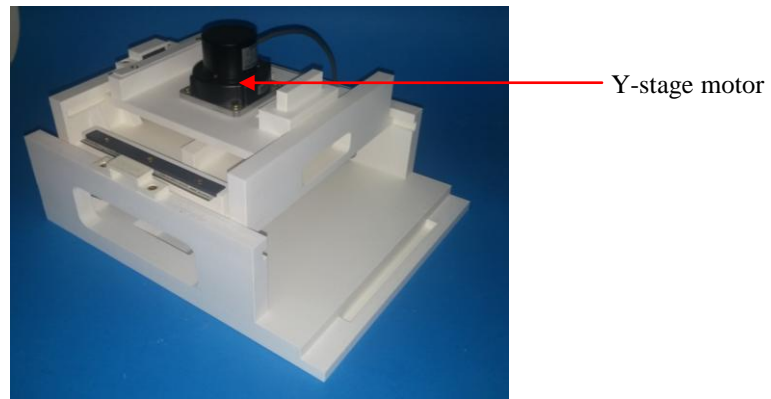
Figure 3.16: Photo of the base, X-plate and Y-plate assembled.
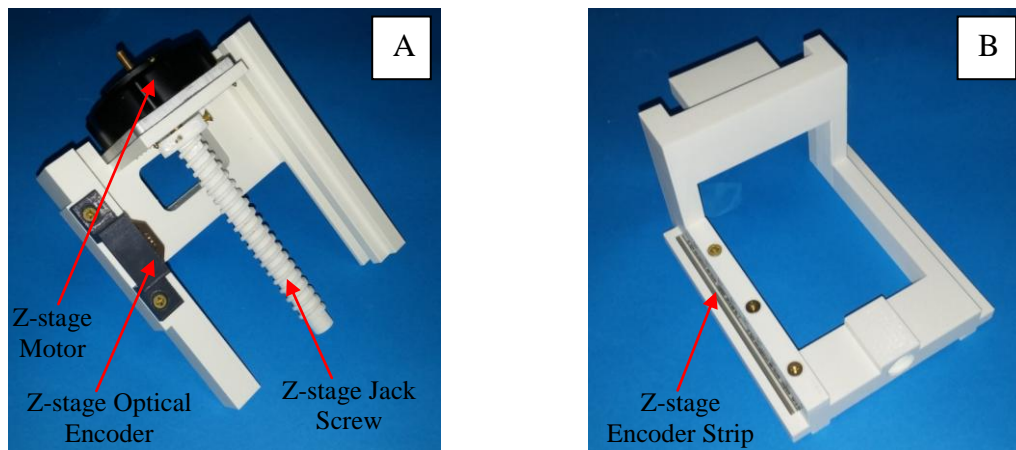
Figure 3.17: A) Photo of the Z-frame with motor, jack screw and optical encoder, B) Photo of the Z-plate with encoder strip.

The encoder strip of the Z-stage was mounted on the Z-plate as illustrated in figure 3.17B. To asemble the Z-stage the Z-plate was placed in the Z-frame guides, and the bottom bracket was fixed with two screws to add regidity to the mechanism stucture and center the screw's lower end. The photo of figure 3.18 shows the assembly sequence of the Z-stage.
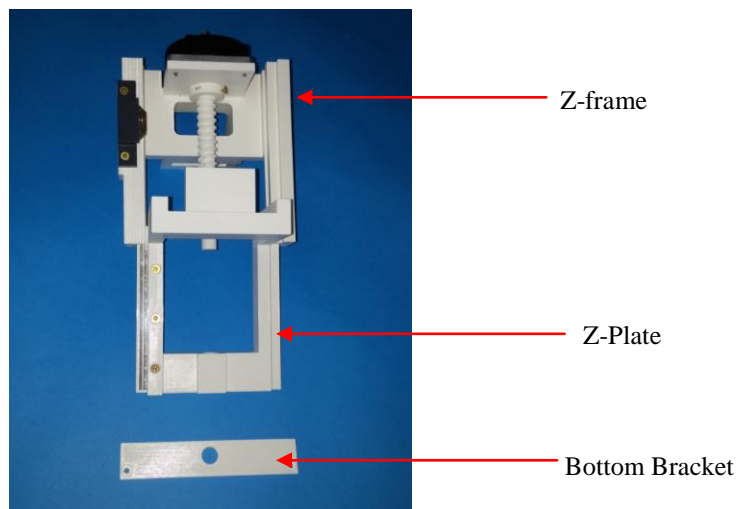
Figure 3.18: Photo of the Z-plate inserted into the guides of the Z-frame and locked with the bottom bracket.

36

The completed deivce is shown in figure 3.19 which includes the Z-stage, water container and the covers of the water container.
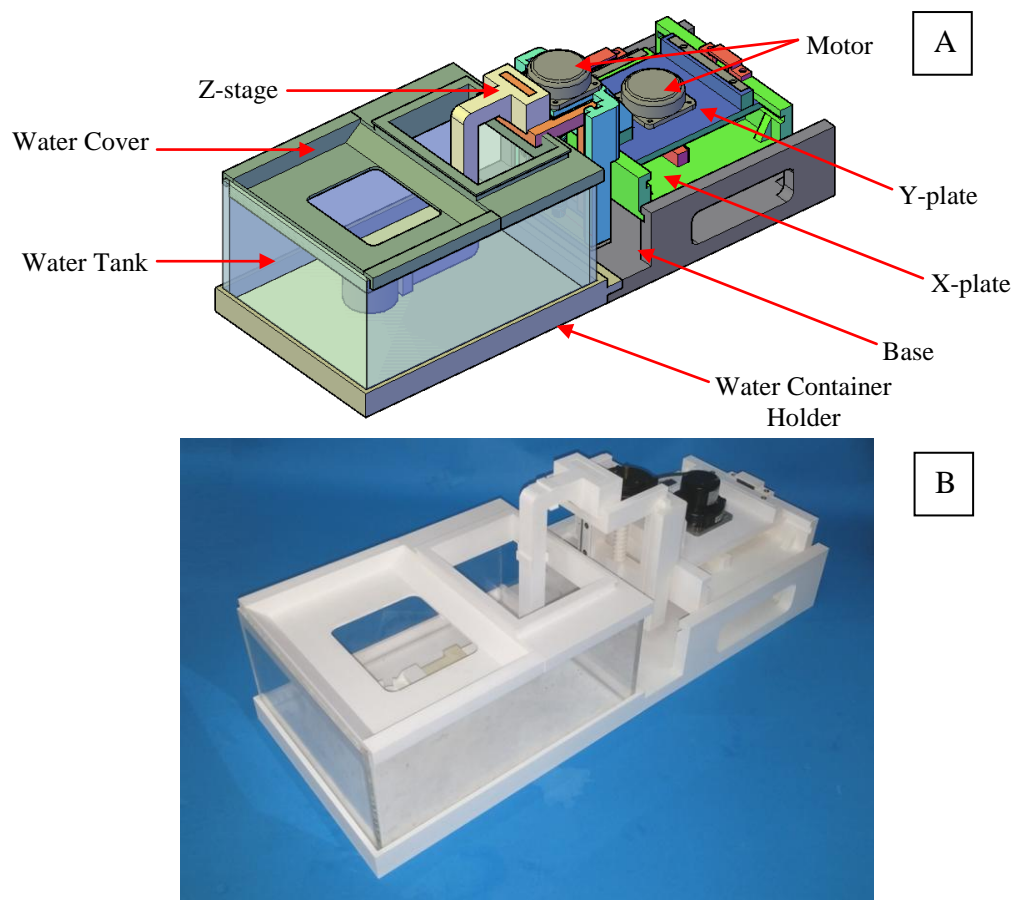
Figure 3.19: (A) Positioning device (CAD drawing), (B) Positioning device (Photo)

Chapter 4 : MRI guided HIFU Robot (Version 3)

4.1 Version 3 Improvements

The main improvement of this version of the positioning device is that it utilizes the principle of jack screw for all three motion axes. The advantage of the jack screw mechanism is that the ratio between the linear motion and the revolutions of the motor is larger than the rack and pinion pair. This means that this system requires more revolutions for the motor in order to establish the same amount of motion compared to the rack and pinion pair. As a result, the speed of each stage was reduced significantly thus, the accuracy was improved. Since the speed was reduced, the use of an extra encoder cable for each of the stages was no longer needed, making the device cost effective and simple. This cable was needed for the connection of the motor encoder with the driver for a consistent operation at the lowest motor speed. The electronic drivers need this information from the motor encoder to operate at a stable speed. The design of this positioning device was more demanding and complicated, but it proved more reliable compared to the previous versions. Furthermore the accuracy was improved because of the slower motion which allowed sufficient time for the encoder reading.

The base of this positioning device shown in figure 4.1 was similar to the second version apart from the motor holder orientation and the slot for the bracket. The motor holder was positioned at the back of the base due to the jack screw concept. In order to provide enough space for a longer jack screw, the motor was positioned at the edge of the rear end. This was necessary because longer jack screw provided a wider motion range. The slot at the middle of the base was designed to attach a bracket that supported the other end of the jack screw. The length of the screw achieved good motion range for the X-stage and allowed enough space for the Z-stage, so that the system can fully benefit the jack screw mechanism.
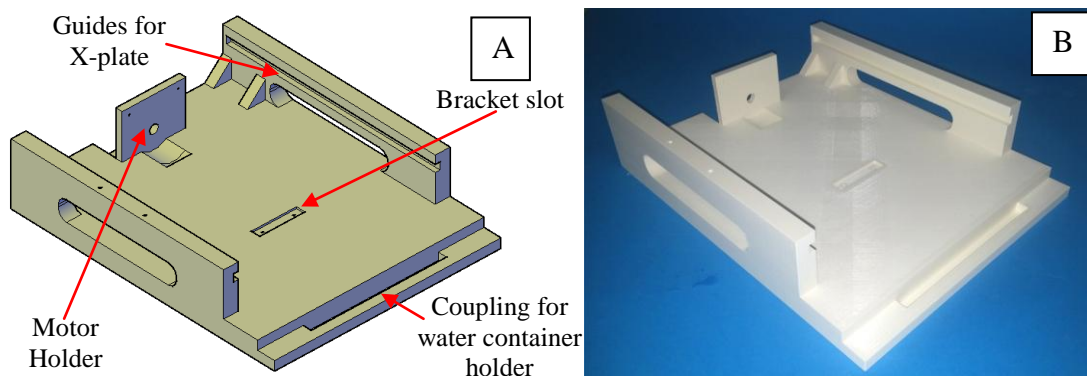
Figure 4.1: A) Base (CAD drawing), B) Base (Photo)

The bracket which fits in the slot at the middle of the base is shown in figure 4.2. This ensured that the jack screw was centered during rotation for smooth positioning of the X-plate.
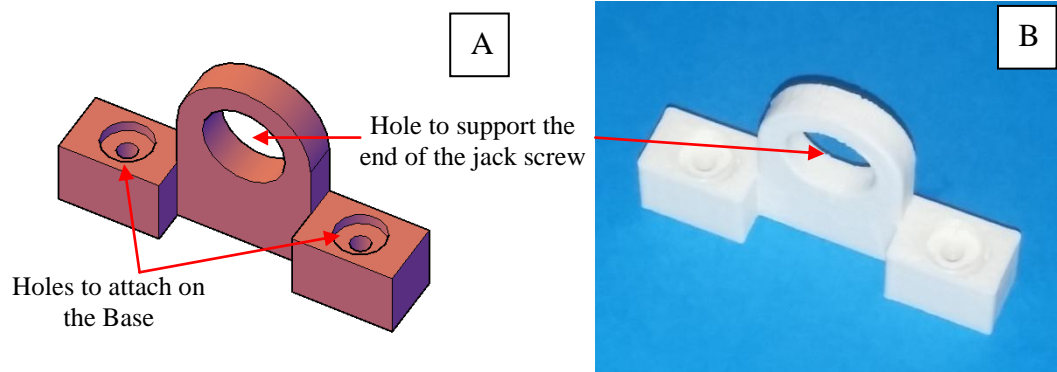
Figure 4.2: A) Bracket for X-stage (CAD drawing), B) Bracket for X-stage (Photo)

The X-plate in figure 4.3 features a motor holder which is bigger than the one at the base. This placed the motor higher, thus avoiding contact of the motor holder with the X-plate. Another difference of the X-plate compared to the previous version is the large opening at the rear end. The opening prevented the motor of the base to hit the X-plate. This remedy reduced the height of the robot by 2 cm.
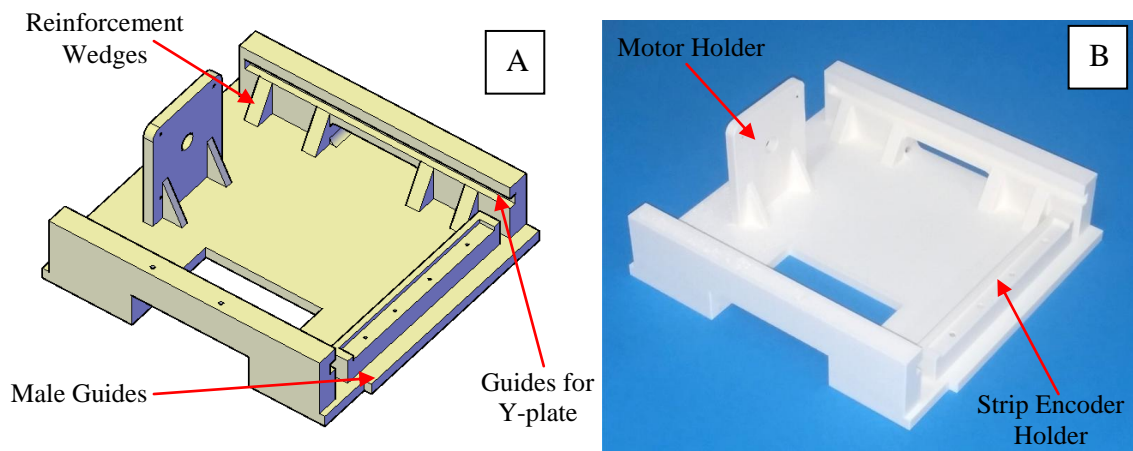
Figure 4.3: A) X-plate (CAD drawing), B) X-plate (Photo)

The encoder strip holder of the X-stage shown in figure 4.4 has been redesigned to support the end of the Y-stage's jack screw. With this modification, the encoder holder was used for two purposes and therefore the number of parts was reduced.

Figure 4.5 illustrates the Y-plate of the positioning device. The most obvious difference where the two bridges added for extra rigidity of the Y-plate (the middle part was reduced). On both sides of the Y-plate, openings were added to provide enough room between the parts, thus increasing the motion range. The coupling to attach the Z-mechanism which is shown in figure 4.6 remained the same. The encoder strip mount

remained at the same position. The two holes in the middle of the plate marked the position to accurately align the threaded bracket with the jack screw. The correct placement of the bracket was very critical for the smooth operation of the positioning device.
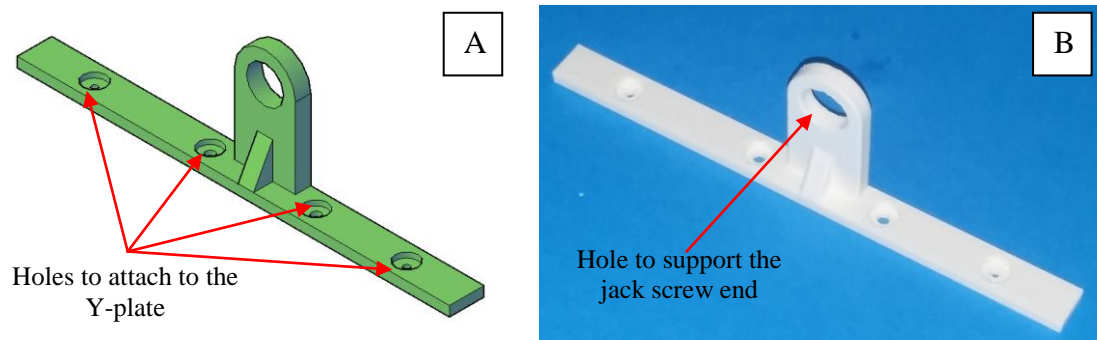
Figure 4.4: A) Encoder strip holder for Y-stage (CAD drawing), B) Encoder strip holder for Y-stage (Photo)
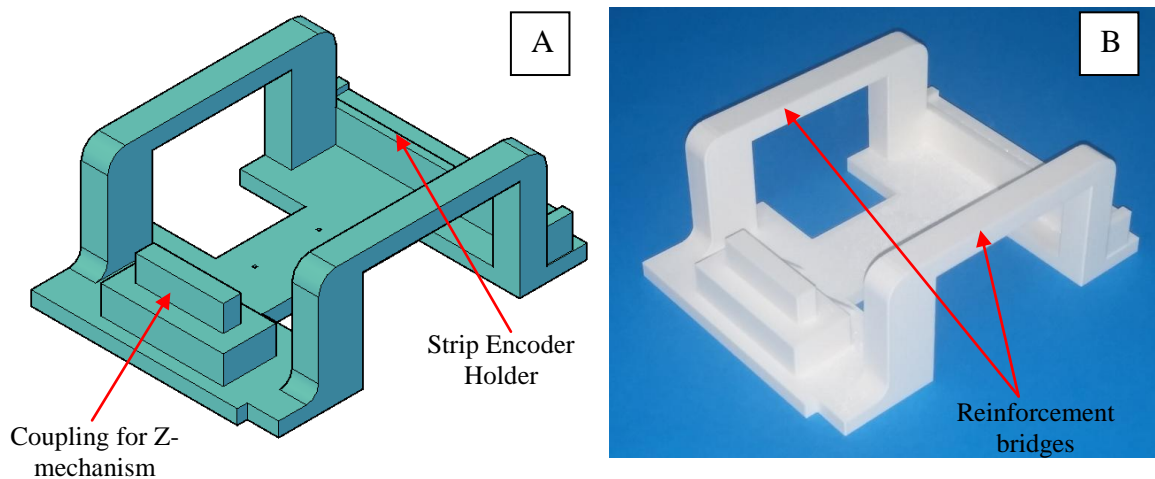
Figure 4.5: A) Y-plate (CAD drawing), B) Y-plate (Photo)

The Z-mechanism required some minor modifications in order to fit on this positioning device since the height of the X-Y stage was reduced by 2 cm. The total height of the Z-mechanism was necessary to reduced by 1 cm. Due to the lower X-Y stage, the coupling behind the Z-stage was also lowered. The updates preserved the range of motion even though the Z-mechanism was reduced in height.

The Z-plate shown in figure 4.7 was reduced in height by 1 cm in order to be adjusted to the height of the Z-mechanism. Additionally 1 cm was removed from the top of its middle section that includes the thread. The narrower middle section has a smaller number of female threads; hence the drag generated due to the friction between the plate and the jack screw was reduced.
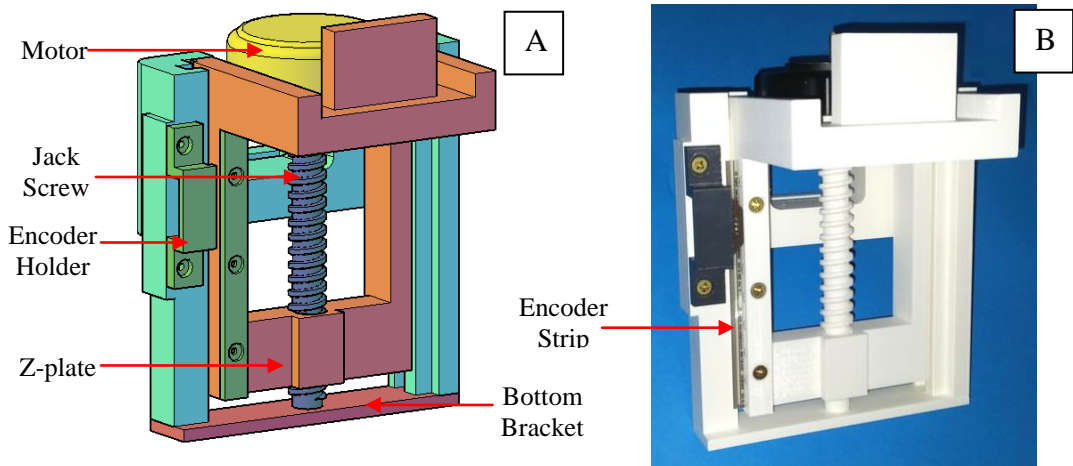
Figure 4.6: A) Z-mechanism (CAD drawing), B) Z-mechanism (Photo)
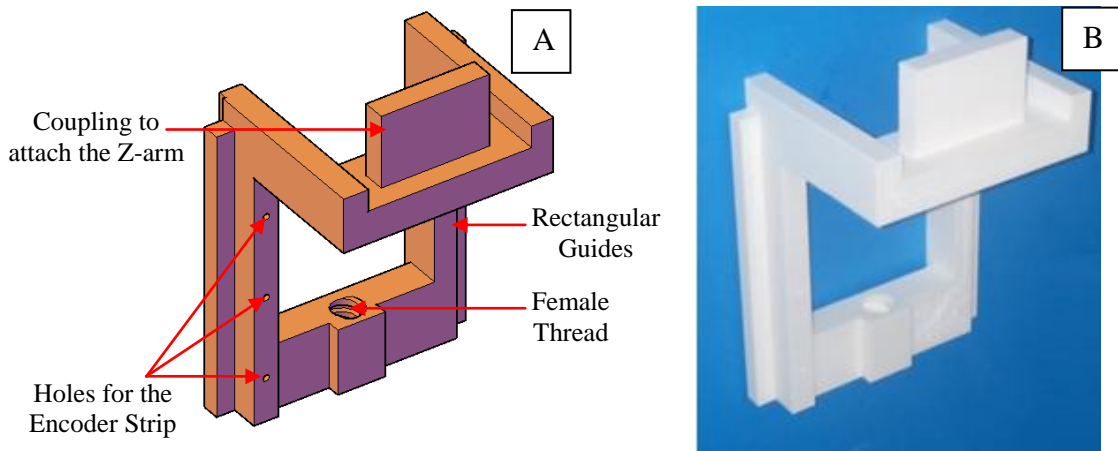
Figure 4.7: A) Z-plate (CAD drawing), B) Z-plate (Photo)

The Z-frame shown in the figure 4.8 was also modified to fit in the positioning device. Although the differences are not very obvious, the height was reduced by 1 cm. In addition, the motor holder was lowered.
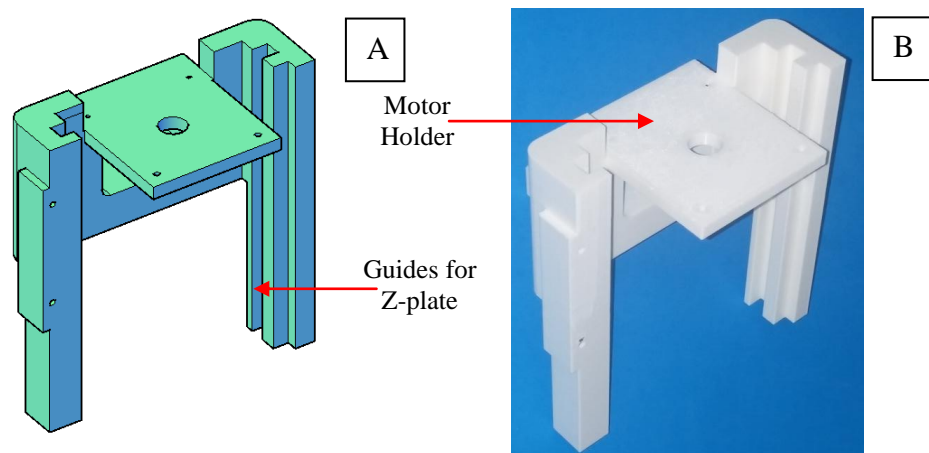
Figure 4.8: A) Z-frame (CAD drawing), B) Z-frame (Photo)

For the X-plate and the Y-plate, the brackets (detachable) included a female thread to couple with the jack screw. The bracket shown in figure 4.9 was attached under the X-plate. This stage carries most of the weight and therefore it was designed wider to ensure a solid contact with the X-plate.
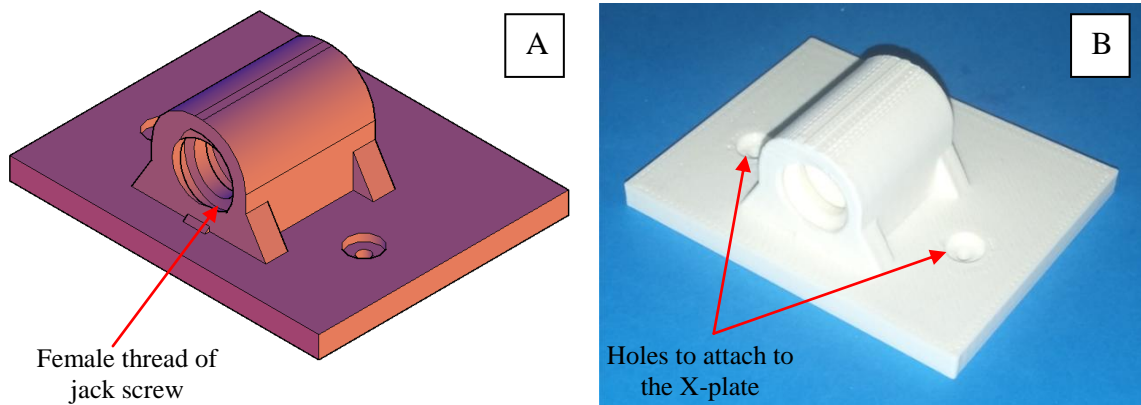
Figure 4.9: A) X-stage bracket (CAD drawing), B) X-stage bracket (Photo)

The same idea was applied to the bracket of the Y-stage which is shown in figure 4.10. This bracket was mounted on the top of the Y-plate. The Y-plate was smaller and therefore the bracket of the Y-stage was made with a narrower base (larger range of motion).

This version of the robot was more complex design compared to the previous two devices in order to be more efficient, reliable and compact.
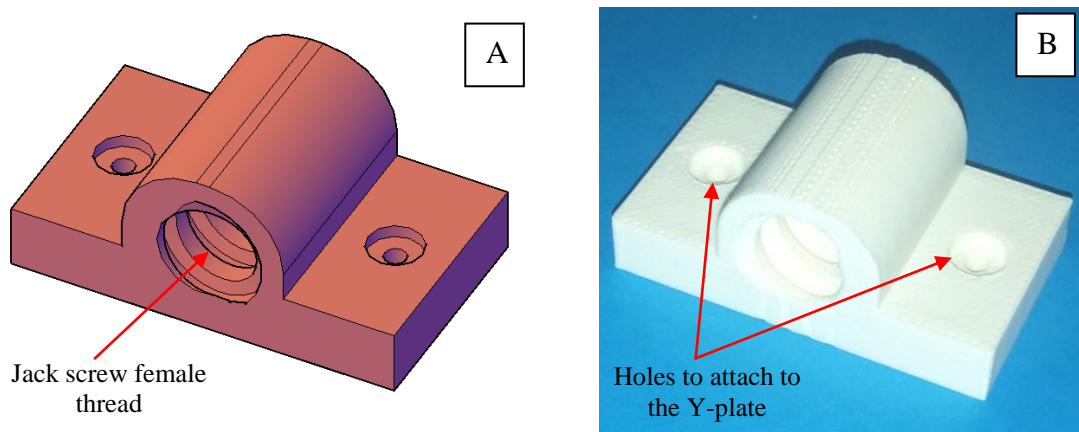
Figure 4.10: A) Y-stage bracket (CAD drawing), B) Y-stage bracket (Photo)

4.2 Assembling of the positioning device (Version 3)

The first step to assemble the base was to install the motor on the rear end of the base. After the motor was secured, the jack screw was fixed on the shaft of the motor and

locked by two brass screws on the shaft. Figure 4.11 shows the motor and the jack screw as installed on the base.

Motor

Jack Screw for
X-stage
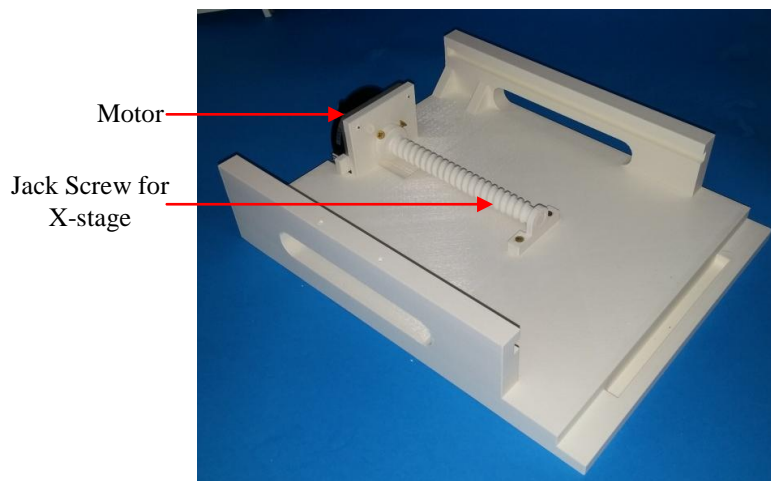
Figure 4.11: Photo of the assembly of the Base.

The encoder strip was placed on the Y-plate and secured under the encoder strip holder as shown in figure 4.12. After the encoder strip was installed and aligned parallel to the direction of the motion, the threaded bracket of the Y-stage was properly fixed (guided by the two holes on top of the Y-plate).

Threaded Bracket
for Y- Jack Screw

Encoder Strip for
Y-stage
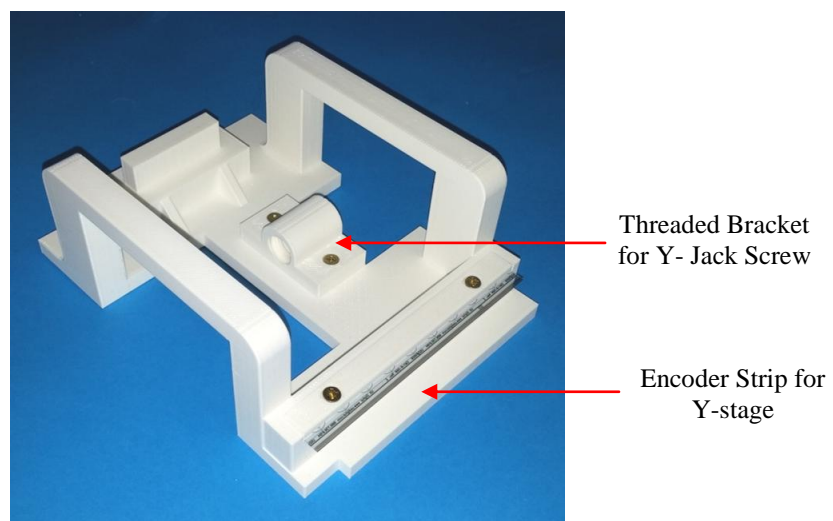
Figure 4.12: Photo of the assembly of the Y-plate.

The motor of the Y-stage was fixed on the X-plate and the jack screw was attached to the shaft of the motor. Then the Y-plate was inserted in the guides of the X-plate. After the X-plate and Y-plate were assembled, the encoder cover was fixed. The X-Y stage was assembled as shown in figure 4.13. Figure 4.13A shows the encoder strip of X-stage as installed on the rear of the X-Y stage assembly. The X-Y-stage assembly was then completed with the installation of the female threaded bracket under the X-plate, as shown in the figure 4.14.
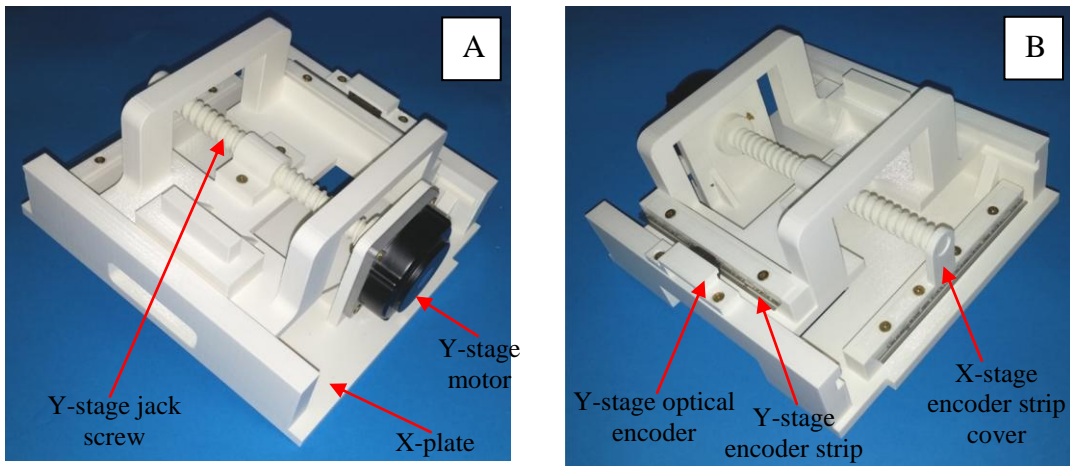
Figure 4.13: Photos of the X-Y-stage.
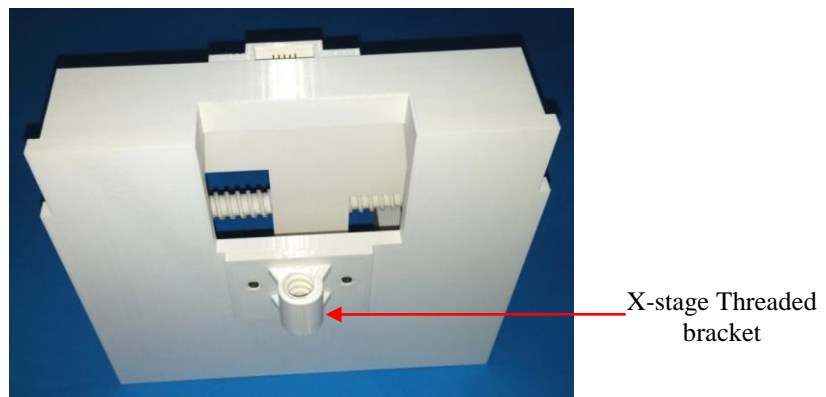
Figure 4.14: Photo of the X-Y plate assembly.

The installation of the X-Y-stage to the base followed the same procedure as the Y-plate. It was inserted to the base and coupled with the jack screw of the X-stage. The completed X-Y-stage of the positioning device is shown in figure 4.15. Figure 4.15B shows the rear view of the positioning device demonstrating the placement of the motors. The 3D positioning device was completed by attaching the Z-stage on the coupling of the X-Y stage as shown in figure 4.16. This positioning device is as compact as the second version.
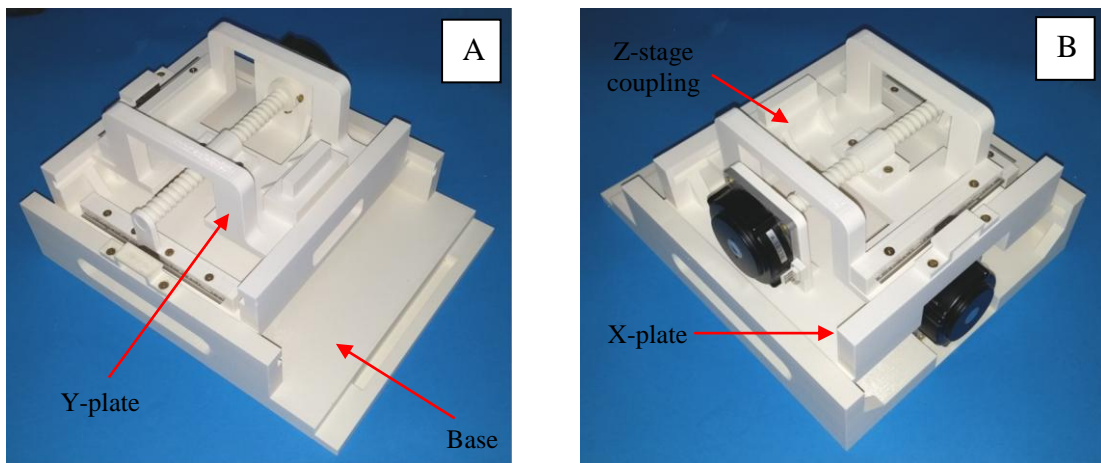
Figure 4.15: Photos of the X-Y-stage and base assembly.
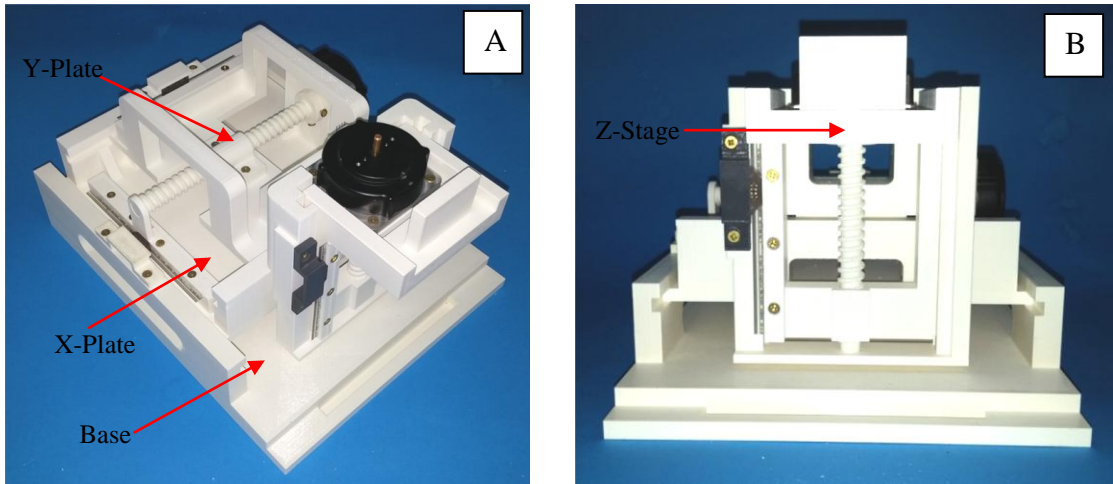
Figure 4.16: Photos of the three axis positioning device.

The front view of the positioning device is shown in the Figure 4.16B. In this photo the jack screw for the Z-stage and the encoder on the right side are visible. The top of the Z-mechanism includes the coupling for the Z arm. Figure 4.17 shows the completed positioning device. The water container was made out of acrylic material so that the transducer movement was visible.
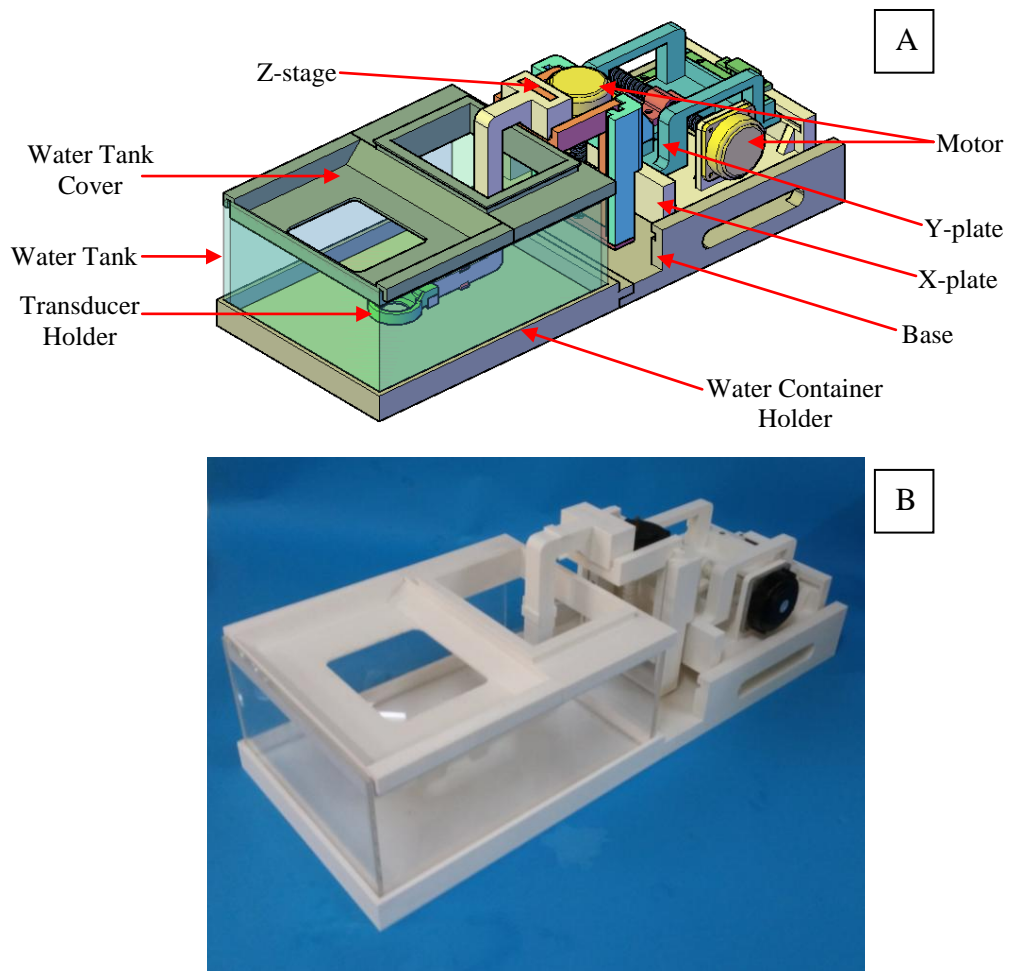
Figure 4.17: A) Completed version of the positioning device (CAD drawing), B) Completed version of the positioning device (Photo).

45

Chapter 5 : Theta stage

For some HIFU applications, sonication at an angle is needed in order to allow lateral ultrasound transmission into the tissue. By targeting through different angles the ultrasound can be delivered to anatomies where targeting through a vertical path is not feasible. It is rather helpful in situations where ultrasound is blocked (bone for example). Additionally, reflection of ultrasound through an interface may disturb the beam, thus overheating unwanted regions may occur. Therefore the angular stage can provide more options for targeting from optimum angle. The theta stage shown in figure 5.1 allows ultrasound to be guided in order to avoid obstacles (bones, interfaces, air spaces) that blocks the ultrasonic beam.
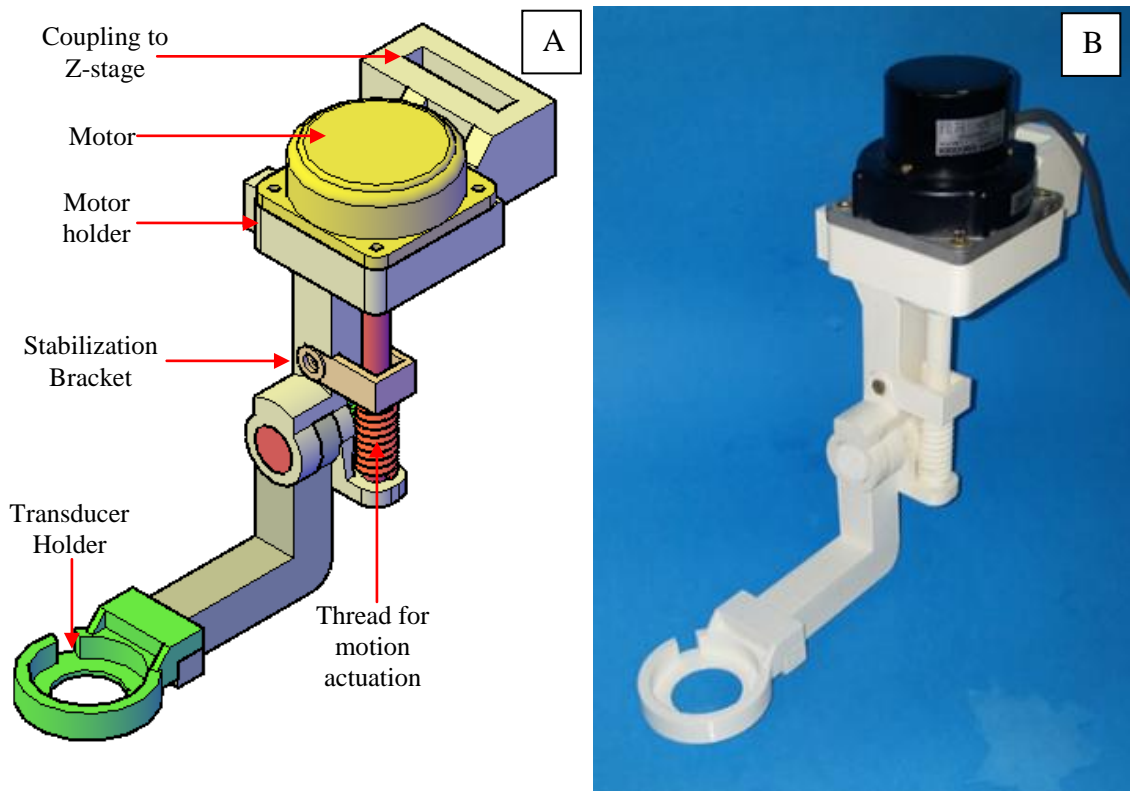
Figure 5.1: A) Theta Arm (CAD drawing), B) Theta Arm (photo)

The motion of the theta stage was energized by a piezoelectric motor placed on the top of the structure. Coupling was included behind the motor that attached to the Z-stage of the positioning device. The transducer can be rotated between -90° and + 90° resulting in a range of motion of 180°. The placement of the transducer remained the same with respect to the Z-arm.

5.1 Parts of the Theta (Θ) stage

The encoder holder shown in figure 5.2 was attached to the motor and secured the encoder strip. The motion of the motor was transferred from the encoder holder to the theta shaft which is shown in figure 5.3. The encoder strip was secured between the theta shaft and the encoder holder. The use of the optical encoder ensures high accuracy of the theta stage due to the feedback provided.
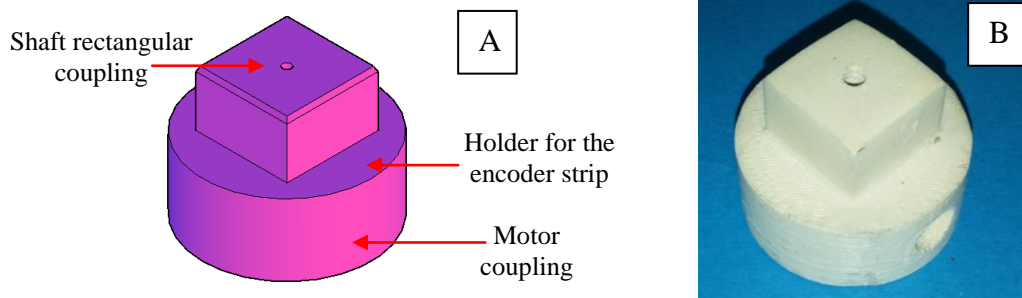
Figure 5.2: A) Encoder Holder (CAD drawing), B) Encoder Holder (photo)

The theta shaft shown in the figure 5.3 included a thread which transferred the motion to the gear. The thread was embedded to the lower section of the shaft and was coupled with the gear. As a result the thread rotates the gear at low speed as shown in figure 5.4. For every full rotation of the screw the gear moved by one tooth. Since the gear has 31 teeth, it results to a motion ratio of 32:1. In addition this setup enabled the motion to be transmitted at a 90° angle. Because of this configuration the motor was placed vertically, thus decreasing the height of the structure and improving the rigidity.

On the middle of the theta shaft (between the coupling and the thread) there was a collar embedded. The purpose of this design is to guide the theta shaft in the stabilization bracket shown in figure 5.5. The stabilization bracket supported the middle section of the theta shaft to ensure that the thread was coupled to the gear. Under the thread there was a shaft extension that is used for centering the lower section of the theta shaft.
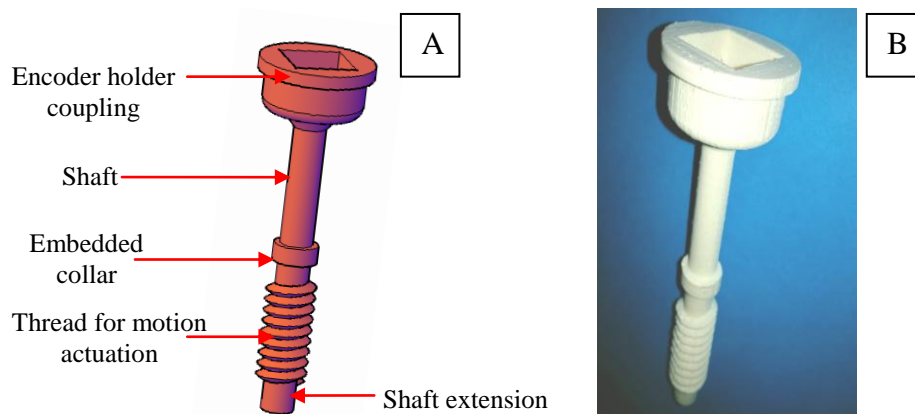
Figure 5.3: A) Theta shaft (CAD drawing), B) Theta shaft (photo)
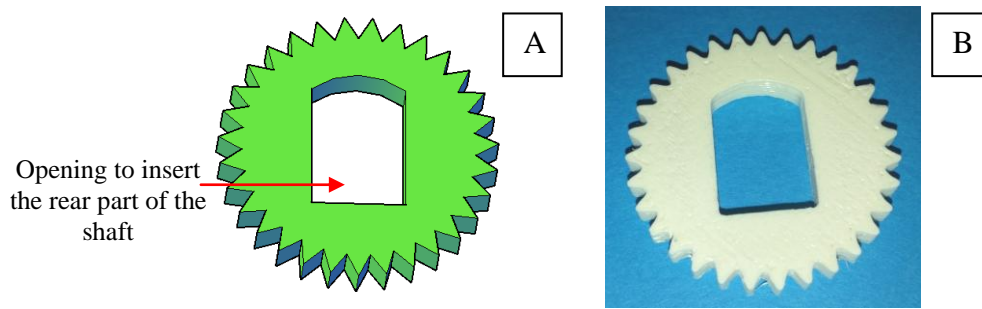
Figure 5.4: A) Gear (CAD drawing), B) Gear (photo)

The angular optical encoder module was secured under the optical encoder cover as shown in figure 5.6. The optical encoder module was coupled with the two cylindrical rods to the encoder cover. The encoder cover has two guides designed to slide in the slots of the motor holder and was secured by the motor itself. With this technique the optical encoder was mounted on the device without the need of screws making the design much simpler. The motor holder shown in figure 5.7 was integrated to the upper arm section thus reducing the complexity of the mechanism. The motor holder/upper arm of the theta stage included also the coupling for the Z-stage. With this method the design of the theta stage was composed with fewer parts, thus keeping the design lightweight and smaller in size.
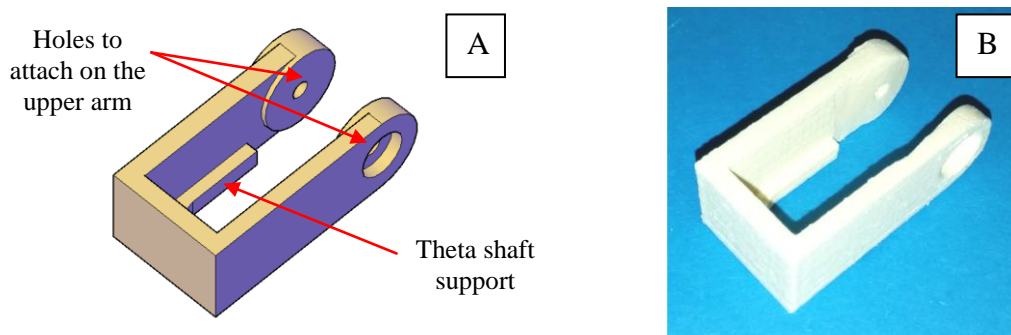
Figure 5.5: A) Stabilizer Bracket (CAD drawing), B) Stabilizer Bracket (photo)
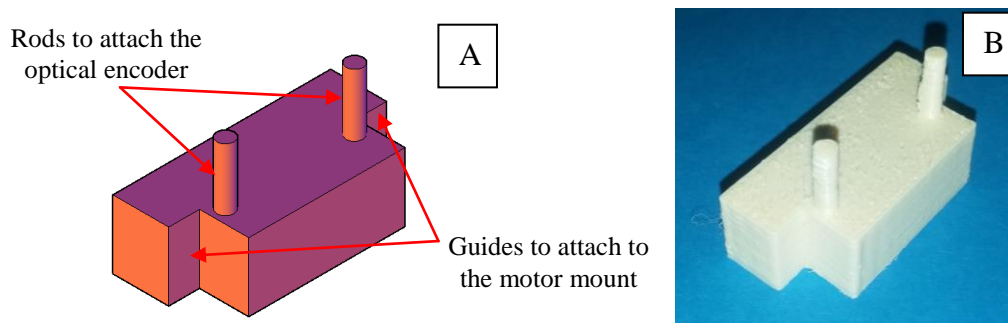
Figure 5.6: A) Optical encoder cover (CAD drawing), B) Optical encoder cover (photo)

48

The joint between the upper and lower parts of the arm was at the lower section of the motor holder/upper arm as shown in the figure 5.7. The middle ring holds the joint which was the pivotal point for the rotation of the lower arm section. The tab integrated at the lower section of the joint included a hole for the lower end of the theta shaft. This ensured that the theta shaft rotated around the center and thus the relation between the screw and the gear shown in figure 5.4 was precise. The support hole for the shaft was necessary due to the forces applied to the gear by the weight of the lower arm and transducer. The torque which was generated by the gravity force of the lower arm increased as the angle between the upper and lower sections of the arm moved closer to 90°. The force that the torque applies to the screw was larger since the leverage was smaller at the transition side due to the smaller diameter of the gear. The torque is described by the distance between the joint and the point where the force is acting, multiplied with the amount of the force applied. Due to the proposed design the force applied by the thread to the gear can be doubled compared to the force generated by the weight of the arm with the transducer. Due to this effect and the long size of the shaft it was prone to flex with the risk, to skip the gear teeth thus affecting the motion precision. To eliminate this risk the stabilization bracket was attached in the two slots on the upper arm section forcing the shaft towards the gear. With the stabilization bracket and the lower tab, the thread was pushed against the gear by two points, for smooth and reliable operation. A diagram of the forces applied to the assembly is shown in figure 5.9.
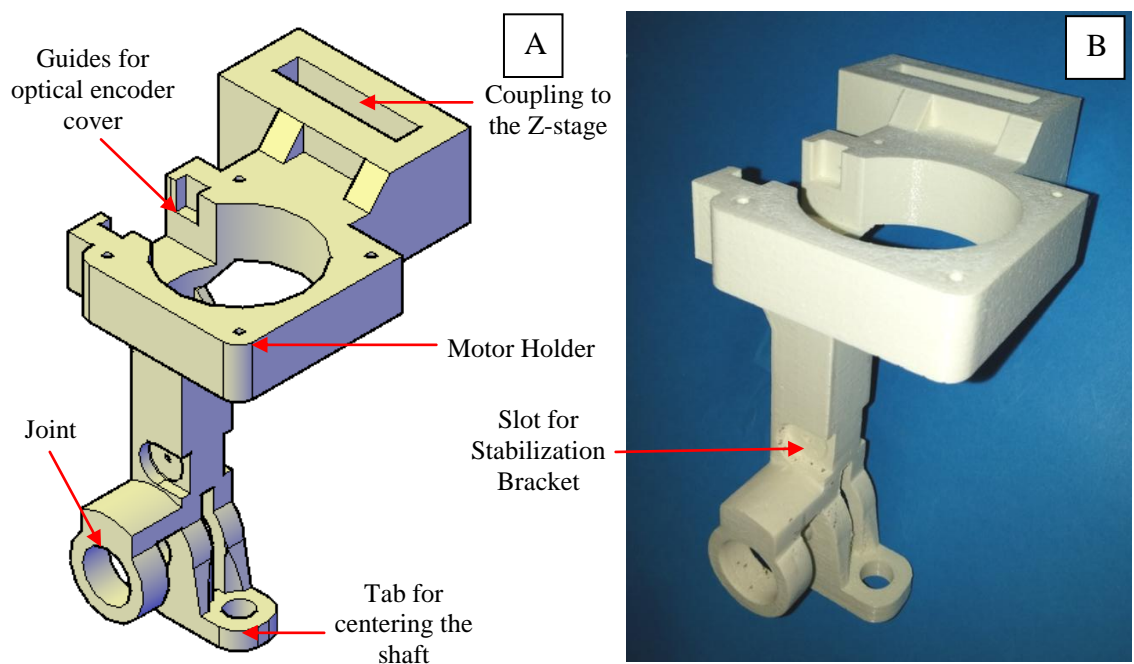
Figure 5.7: (A) Motor mount/upper arm (CAD drawing), B) Motor mount/upper arm (photo)

The lower arm section as shown in figure 5.8 included a cylindrical section for the joint. In the joint there was a rectangular hole to couple with the joint shaft. The joint shaft which is shown in figure 5.10 was inserted in the hole to transfer the motion of the gear to the arm. At the lower end of the arm there was coupling for the transducer holder.

Hole to insert the shaft

Transducer Holder Coupling
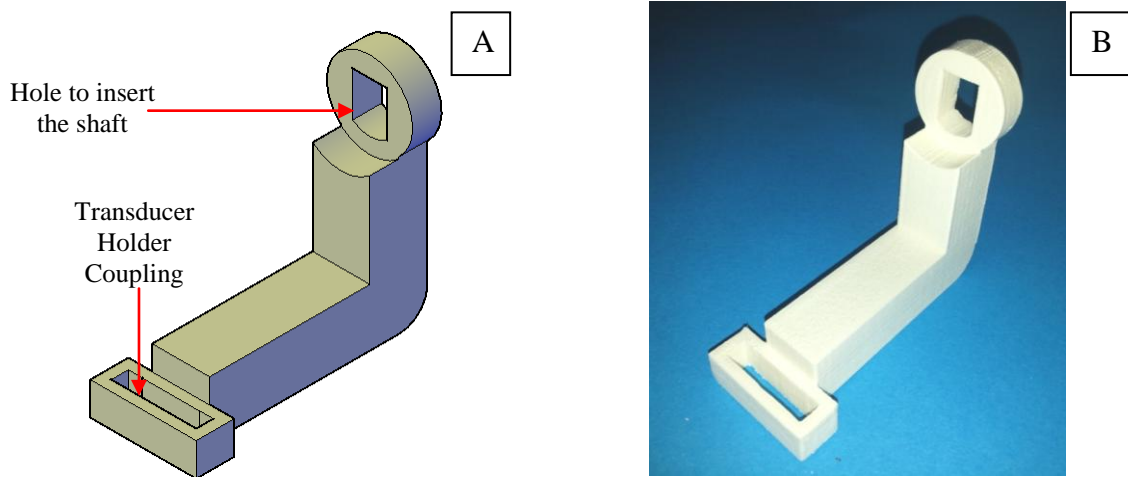
Figure 5.8: A) Lower arm (CAD drawing), B) Lower arm (photo)

Joint- Pivot point

Distance from joint to the center of mass of the lower arm and transducer

Component of the gravity force that create the torque

Gravity force applied to the center of mass

Component of the force applied by the screw to the gear torque

Distance from joint to the screw

Center of Mass for lower arm with transducer
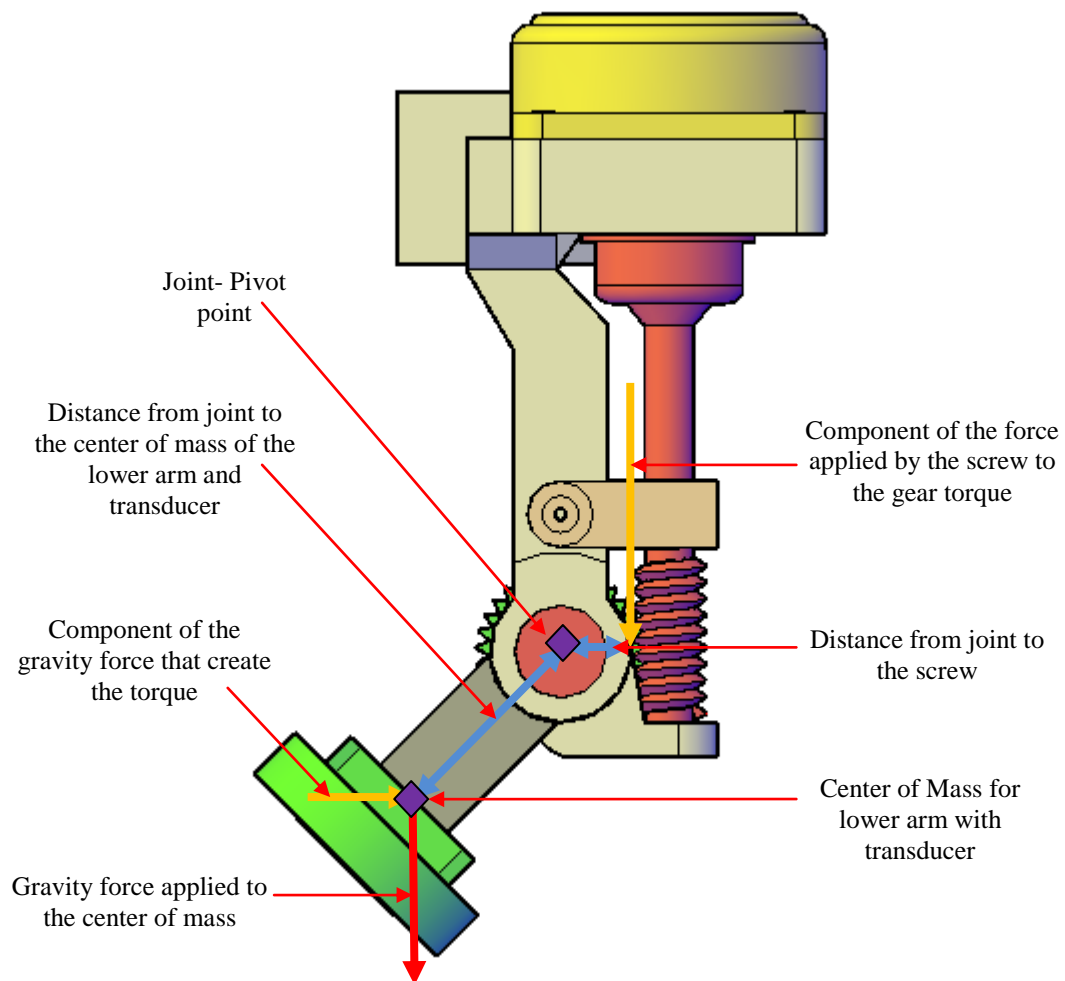
Figure 5.9: Diagram of the forces applied to the mechanism.

50

The gear in figure 5.4 has a corresponding rectangular shaped opening (same with the one on the cylindrical part of the lower arm). This design enabled the shaft to be attached to the gear and the lower portion of the arm locking them together. Since the lower part of the arm was locked to the gear, the arm was forced to rotate with it.

The joint shaft was composed by two sections that were attached together through a coupling and were fixed with a single screw. The advantage of this design was that the two pieces of the shaft were coupled together inside the joint, thus allowing larger motion range. The shaft itself was the pivot where the arm rotates thus establishing the angular motion. Figure 5.11 shows the longitudinal section of the joint assembly. The middle hole of the upper arm joint was reduced so that the shaft mechanism created a stable joint.
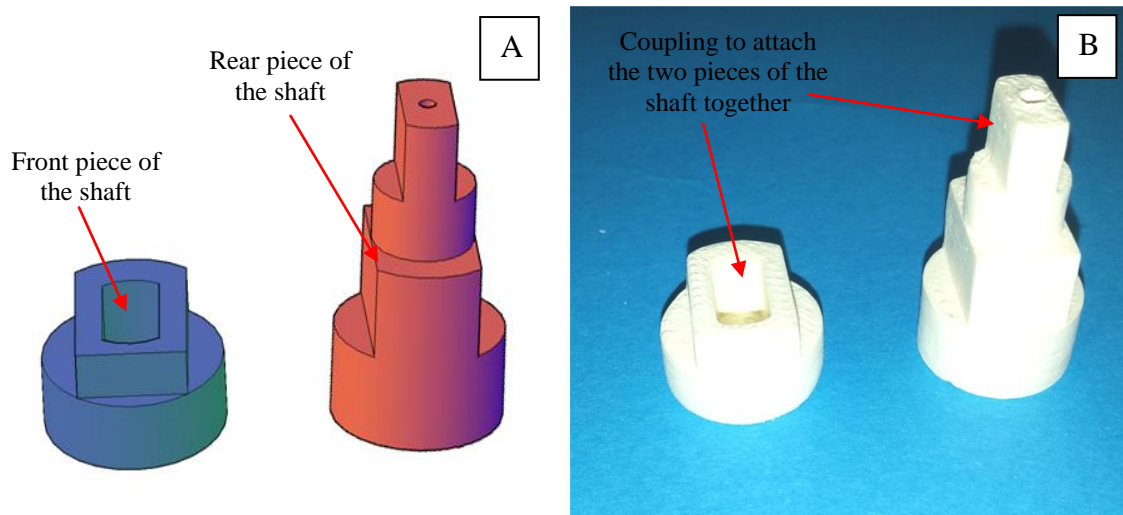
Figure 5.10: A) Joint Shaft (CAD drawing), B) Joint Shaft (photo)
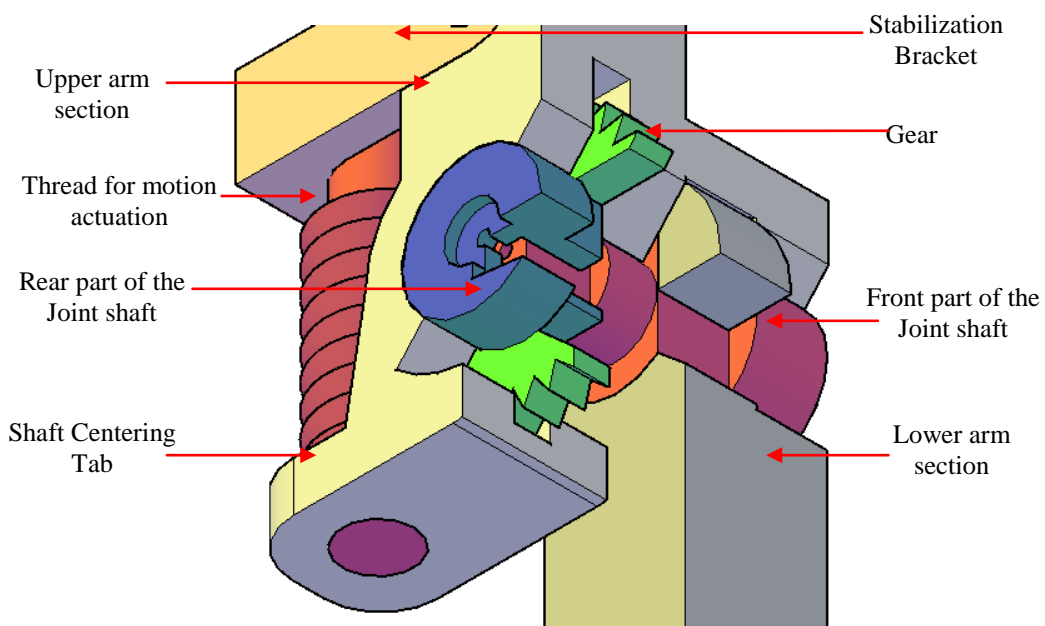
Figure 5.11: Longitudinal section of the joint assembly.

Figure 5.12 shows the complete positioning device with the theta stage installed to the coupling of the Z-stage. Although the theta stage was a complex structure that included several parts, the design did not increase the size of the positioning device significantly. It actually reduced 1 cm from the total height of the Z-axis. The 1 cm was spared due to the fact that the motor holder was designed at a lower level. Since the dimensions of the Theta arm were made similar to the Z-arm, the range of the motion was not affected. Also the smaller arm length was essential in order to take advantage of all the space in the water container. Therefore when the arm was positioned at 90°, the transducer was placed to a position beyond the Y-stage range of motion.
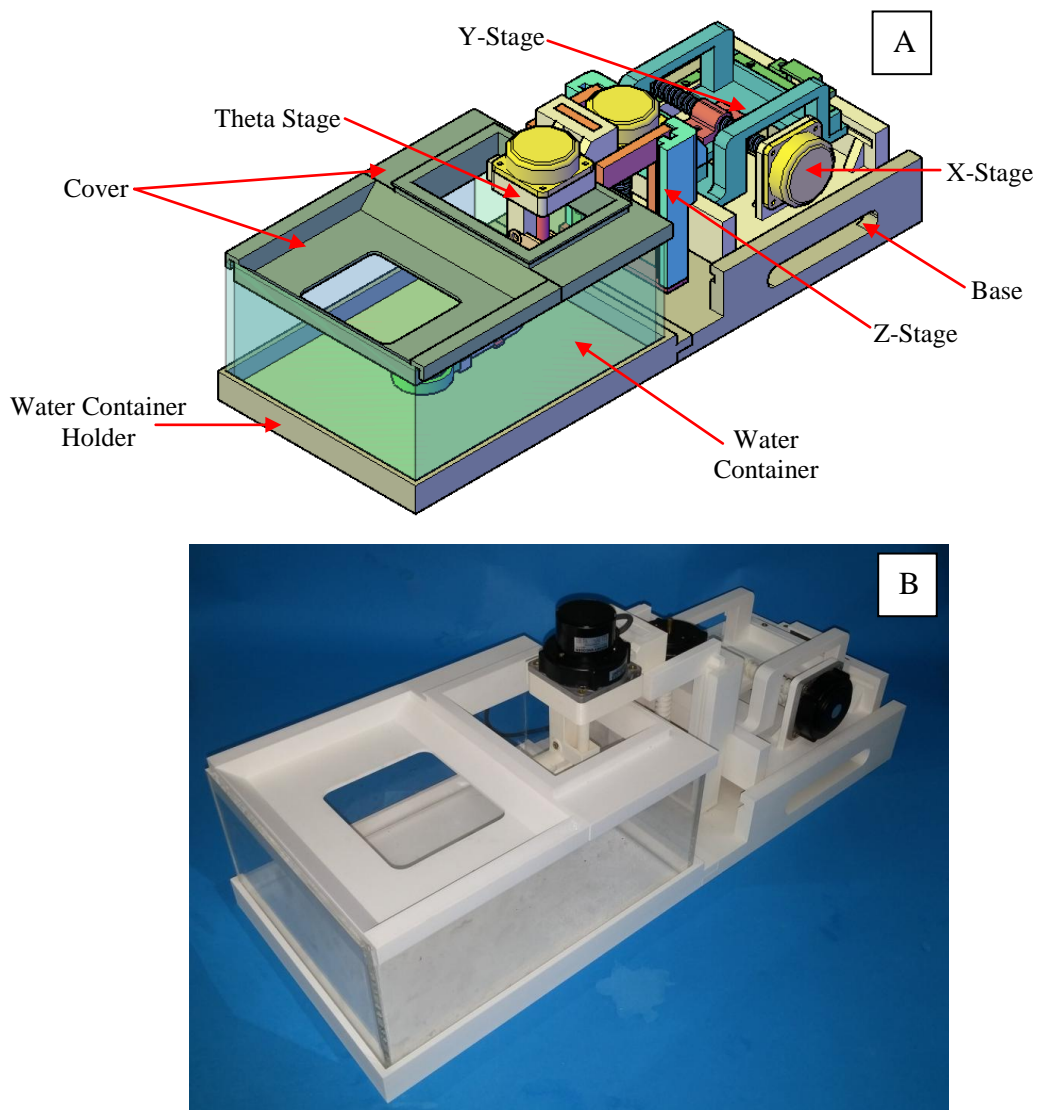
Figure 5.12: A) Positioning device with theta stage (CAD Drawing), B) Positioning device with theta stage (photo).

5.2 Assembly of the Theta stage

The assembly of the theta stage had to be performed in a specific order. As shown in figure 5.13A the encoder strip was placed on the encoder holder. The encoder strip was secured with the installation of the shaft which on its upper section included a hub for attaching the encoder holder. The hub pressed the encoder strip uniformly against the encoder holder keeping it flat, so that the optical encoder could measure the motion accurately. The encoder holder/shaft assembly (figure 5.13A) was attached to the motor and was fixed with a screw to the motor shaft as shown in figure 5.13B.
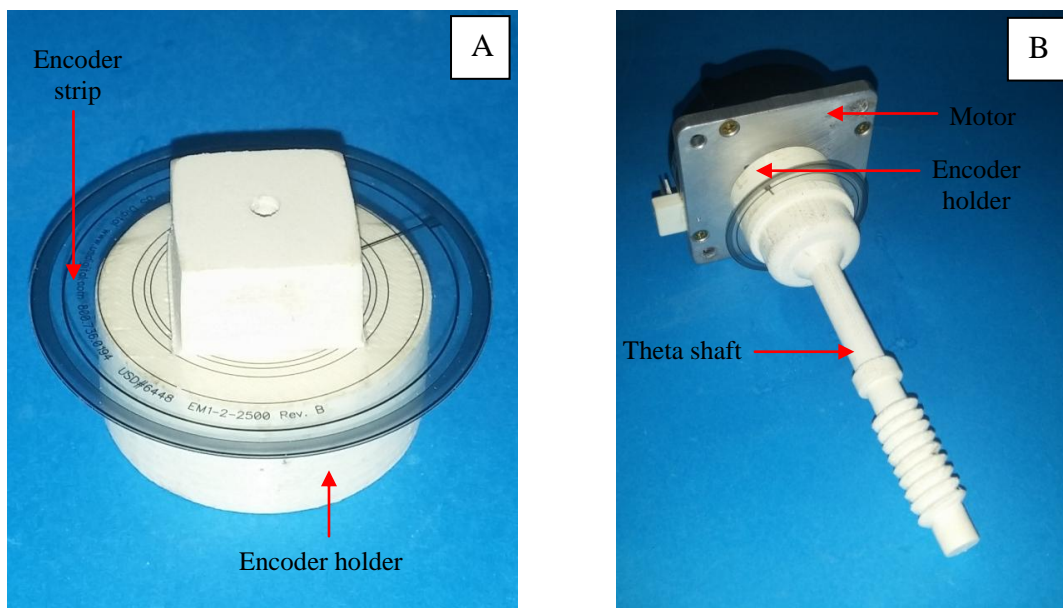
Figure 5.13: A) Encoder strip on the encoder holder, B) Encoder holder/shaft assembly attached to the motor.

Figure 5.14A shows an exploded view of the components of the theta arm assembly. To assemble these parts, the lower part of the arm and the gear were placed in the slots of the joint. To secure the parts together the joint shaft was installed. The front part of the joint shaft (long) was placed first. The rear part of the shaft (short) was attached in the rear, thus the joint of the theta stage was completed. All the parts were secured using a single screw one the back of the shaft. The rear side of the assembled arm joint is shown in figure 5.14B.

Figure 5.15A shows the optical encoder module attached to the encoder holder. These two parts were placed in the slots of the motor holder (figure 5.15B). The motor assembly (figure 5.13) was fixed to the motor holder securing the encoder in between as shown in figure 5.15C. Figure 5.15C shows the encoder strip in the center of the motor mount assembly.
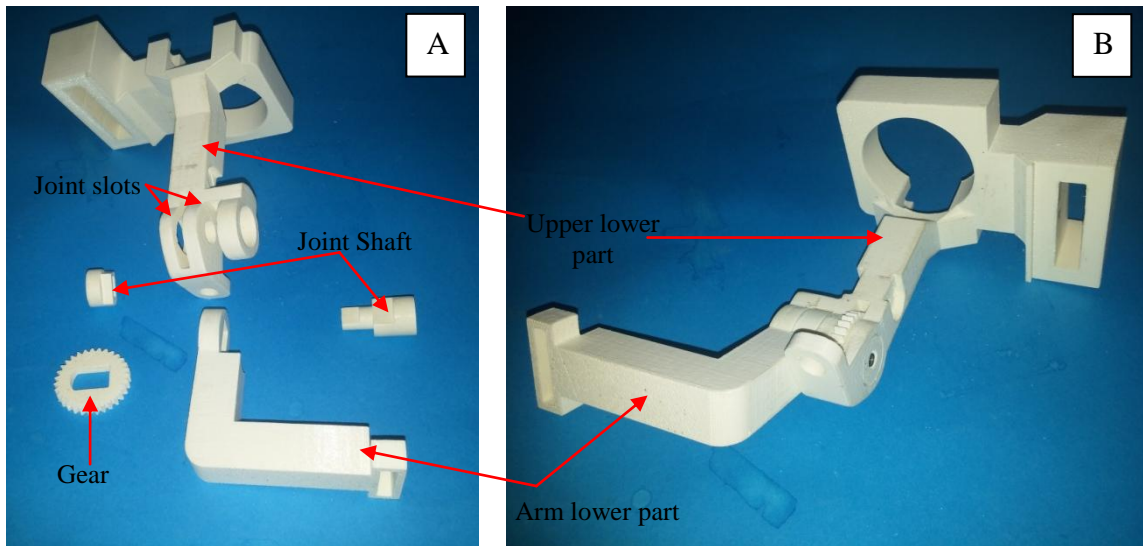
Figure 5.14: A) Exploded view of the parts for the joint, B) The assembled joint.
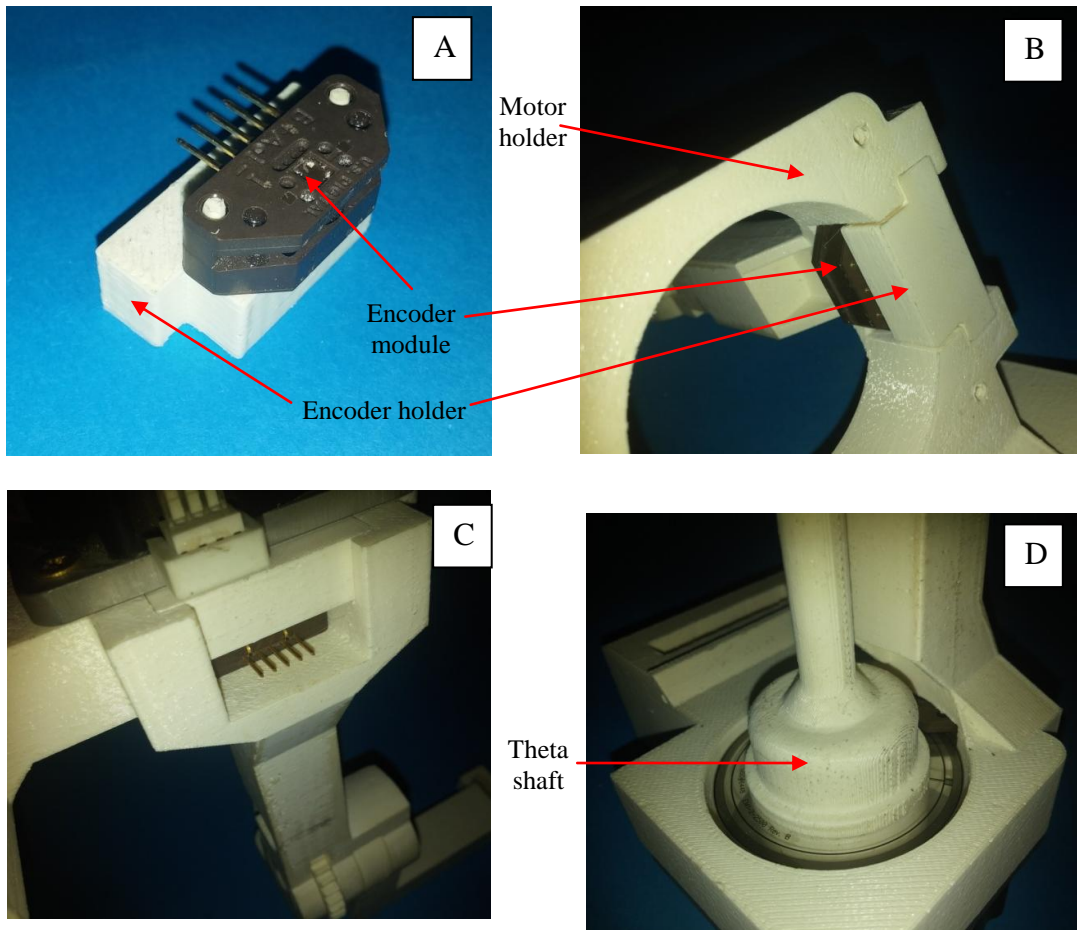
Figure 5.15: A) Encoder module attached to the encoder holder, B) Optical encoder module installed, C) Motor fixed to the motor holder, C) Encoder strip placed in the center of the motor holder.

The completed theta-stage after the installation of the stabilizer bracket and the transducer holder is shown in figure 5.16A. Figure 5.16B shows a detailed view of the assembled theta stage where the encoder strip and encoder module are visible.
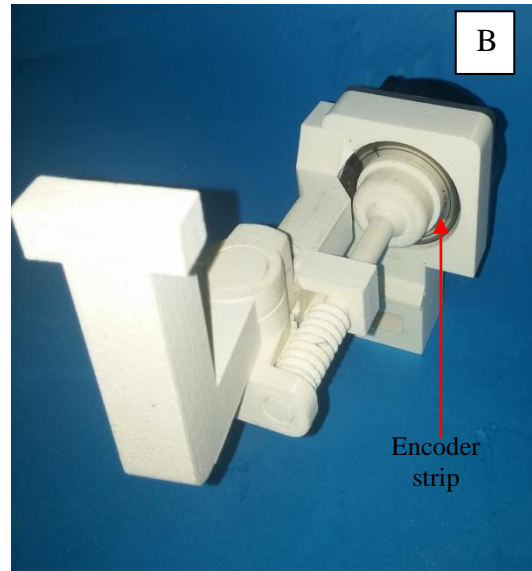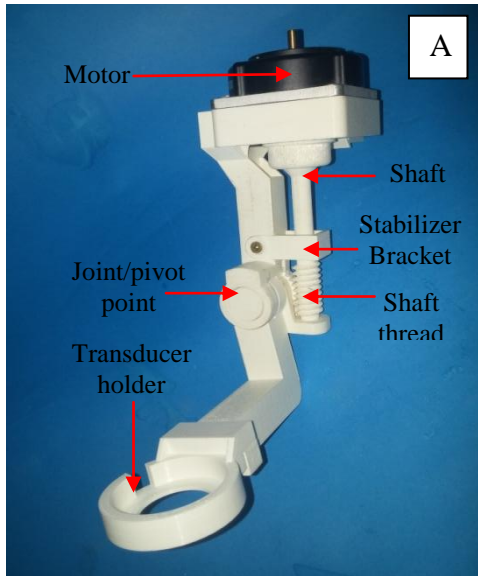
Figure 5.16: A) Theta stage, B) View of the Theta stage showing the encoder.

Chapter 6 : Phi (Φ) arm with planetary high reduction gearbox

The Phi arm enables the positioning device to rotate around the X-Y plane. This extra DOF can improve targeting by position the transducer at a different plane. The phi stage is useful for applications where angulation at a different plane is needed. This mechanism could potentially be used for targeting HIFU for different organs.. The ability to deliver HIFU through different paths can increase significantly the efficiency of the system by choosing the optimal path.

The phi mechanism includes a high reduction gearbox for smother operation and improved reliability. With this reduction unit the positioning speed was reduced enough to eliminate the extra cable of the motor encoder. The motor revolutions per minute (RPM) have been reduced by 64 times with this mechanism thus improving motion accuracy. For the linear stages this mechanism was not needed since the jack screw offered a low ratio between the actual motion and the motor speed. Furthermore, the jack screw concept converts rotational motion into linear and hence was not applicable for the theta stage, where the rotational motion must be preserved.

The planetary gearbox which was used for the phi stage is composed of two stages. The first stage has a reduction ratio 4:1 and the second stage 16:1. This gives a final ratio of 64:1 which is high reduction ratio in relation to the size of the mechanism. This high reduction unit significantly increased accuracy because it allowed more time for the system to respond. The main advantage of a planetary reduction unit was the high reduction ratio with only two stages.

Inside the first stage of the planetary gear box a 10-teeth pinion gear was used also known as "sun gear". The motion was transferred though the two ten-teeth carrier gears to the outer 30 teeth "ring gear". The 10-teeth carrier gear was also called "planetary gear". Figure 6.1 shows the first stage of the planetary gear reduction unit. The pinion gear in the middle of the assembly transfers the motion from the motor to the planetary gears. The planetary gears were coupled with the ring gear. The ratio of the first stage was defined by the pinion and the ring gear. The planetary gear did not affect transmission ratio and their teeth number was calculated by the distance between the pinion, the ring gear and the module of the gears. The module of a gear is the relation between the number of teeth and its circumference. The module is important for engaging the gears properly.
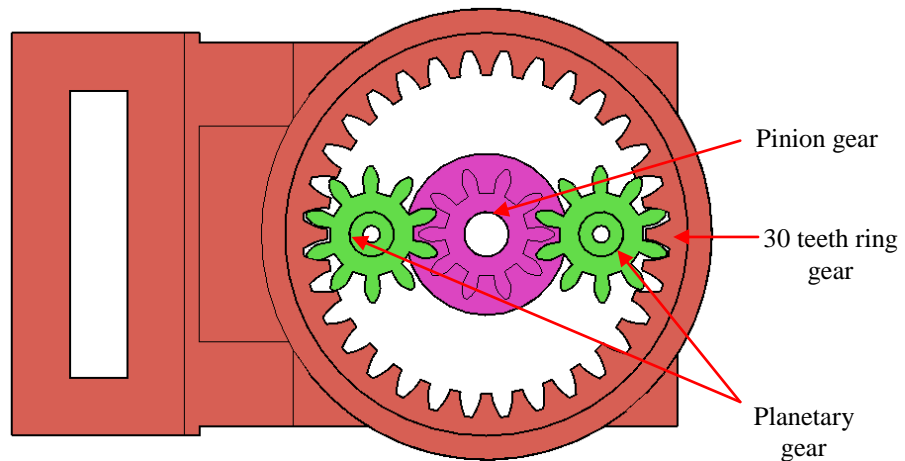
Figure 6.1: First (4:1) stage gear.

The second stage of the planetary gearbox was completed with the installation of a second ring gear. This ring gear included 32 teeth and was coupled with the planetary gears of the first stage as shown in figure 6.2. The planetary gears were made thicker in order to couple simultaneously with the two ring gears. The second stage delivered a 16:1 reduction ratio which means that for every full rotation of the 32-teeth ring gear the planetary assembly must complete 16 full rotations.
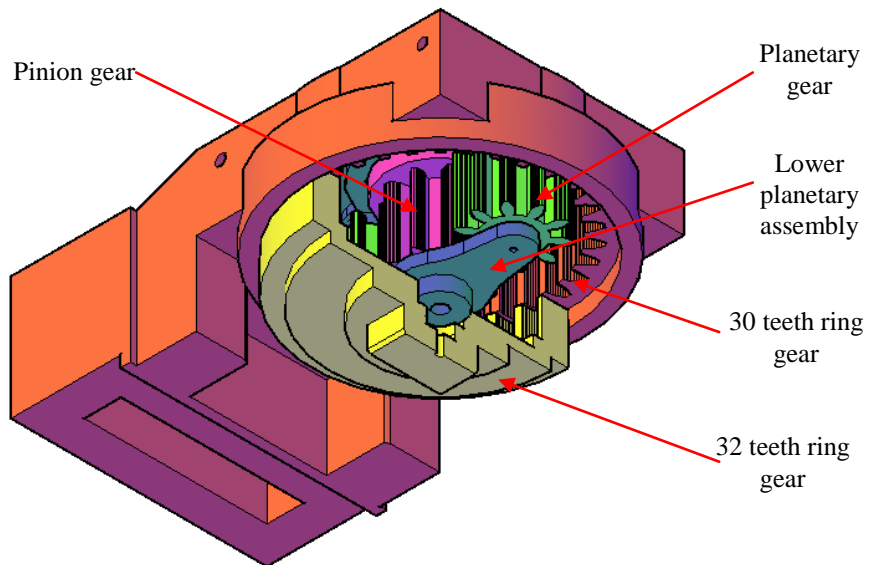
Figure 6.2: Planetary gearbox cross section view.

The planetary assembly shown in figure 6.3 is driven by the pinion gear. The rotation of the pinion gear resulted to a rotation to an opposite direction of the planetary assembly which was four times slower. In addition the planetary assembly was forced to rotate because the 30-teeth gear was incorporated with the gearbox cover, and therefore it could not be move. The rotation of the planetary assembly forced the second stage to move. The second stage was assembled with the addition of the 32 teeth ring gear.

Therefore this system offered this high reduction ratio with less moving parts compared to other mechanisms that were designed to reduce the speed.
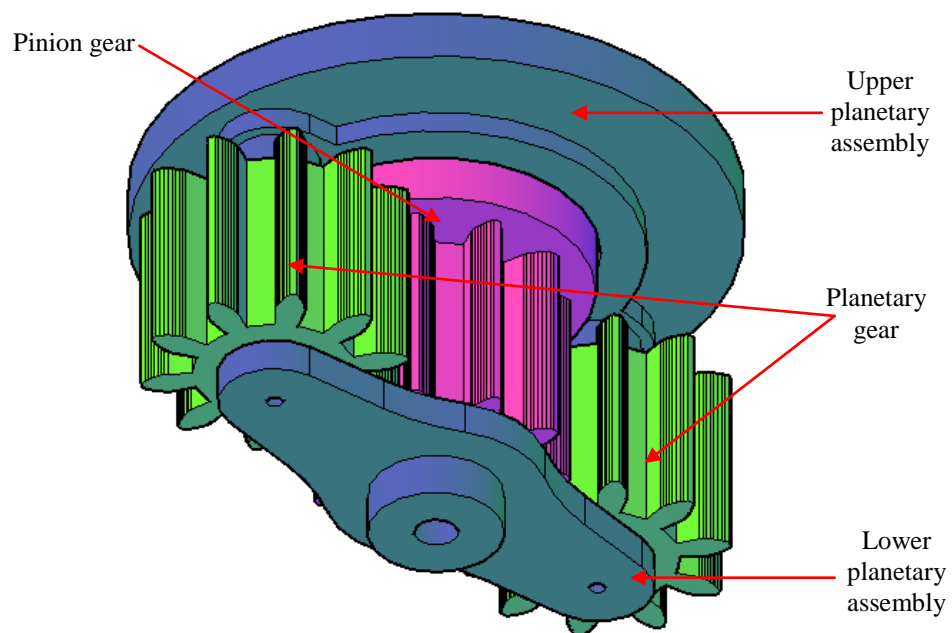
Figure 6.3: Planetary assembly.

To transfer the motion to the second stage, the planetary gears were made longer in order to be able to couple with the 32 teeth ring gear. The 32 teeth ring gear could only aligned with the 30 teeth ring gear of the first stage at the two opposite sides, as shown in figure 6.4. Since the gear alignment was feasible only in the two opposite sides the planetary gears were coupled there. During the rotation of the planetary assembly, the planetary gears are moved inside the ring gears. The next teeth of the 30 teeth "ring gear" was not perfectly aligned with the 32 teeth "ring gear", hence the two planetary gears rotated the 32 teeth ring gear. This process resulted to a motion of the second stage to an opposite direction with the rotation of the planetary assembly.

Since the output ring gear had two extra teeth, the output shaft would have lead by two teeth after a complete rotation of the planetary assembly. In order for the 32 teeth ring gear to rotate $360°$ it would require 16 revolutions of the planetary assembly. The 16:1 reduction ratio of the second stage multiplied with the 4:1 of the first stage gives a motion ratio of 64:1. This means for 64 revolutions of the input shaft the output will move 1.

The high reduction ratio increased the accuracy by increasing the resolution of the motion. More specific, if the motor was directly coupled to the arm and the application

required a small rotation of $2°$, then the motor should rotate only by $2°$. In contrast with the use of the planetary reduction unit for a $2°$ turn of the output shaft the motor must rotate by $128°$. The optical encoder of the system was installed to the output shaft so as to instruct the motor to stop when the desired numbers of pulses are achieved.
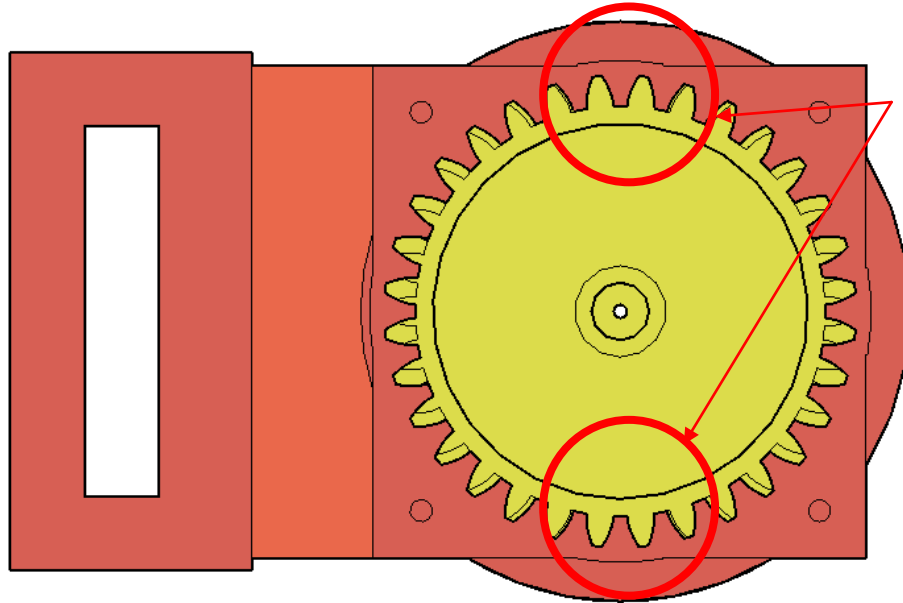
Figure 6.4: Ring gears alignment.

The dimensions of the gearbox were considered small compared with a setup which directly coupled the arm with the motor. In previous designs the motor holder thickness was 8 mm, and since there was no reduction unit, the extra encoder of the manufacturer was mandatory to establish good accuracy. The encoder of the motor had a height of 30 mm and hence increased the overall dimensions of the device. Therefore although the planetary gearbox seems to be bigger in fact is not. The overall thickness of the reduction unit was 39 mm. This system was proved efficient and offered many advantages although it was more complex.

Figure 6.5 shows the top view case of the planetary gearbox. This part was attached to the motor. The 30 teeth ring gear was embedded in the middle and also included the coupling for the Z-stage. Additionally above the ring gear a cylindrical extension (similar to a collar) was designed. This extension holds the output ring gear centered and also acted as a bearing.
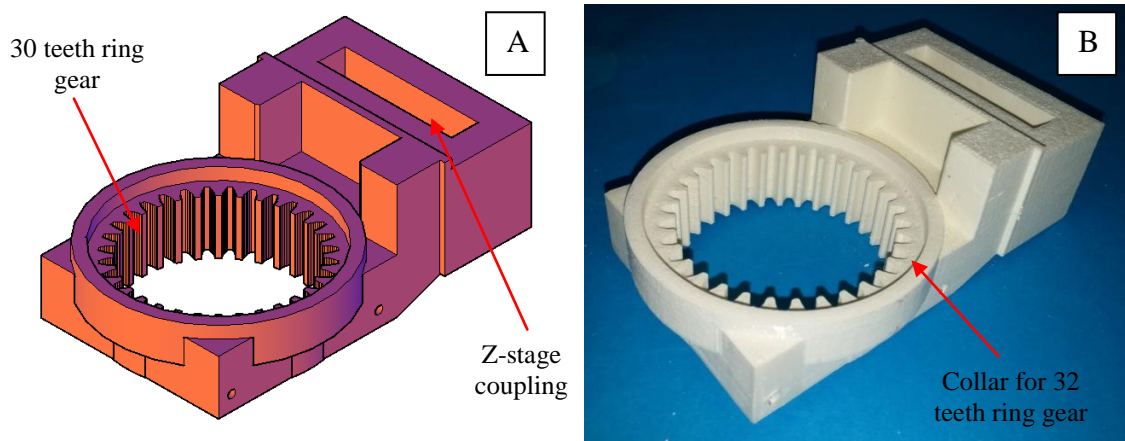
Figure 6.5: A) Planetary gearbox upper part of the case (CAD Drawing), B) Planetary gearbox upper part of the case (Photo).

The pinion gear shown in figure 6.6 was used to transfer the motion from the motor to the planetary assembly. The hole in the middle accepts the pinion gear shaft of the lower planetary assembly as shown in figure 6.7. This kept the planetary assembly centered during motion. At the lower part of the pinion a coupling was included to couple with the shaft of the motor.

The lower section of the planetary assembly (figure 6.7) supports the two planetary gears. The two outer extrusions acted as an axle for the two planetary gears. The shaft on the center extended under the lower planetary section to ensure gear alignment between them. This was important in order to ensure smooth operation of the gears.
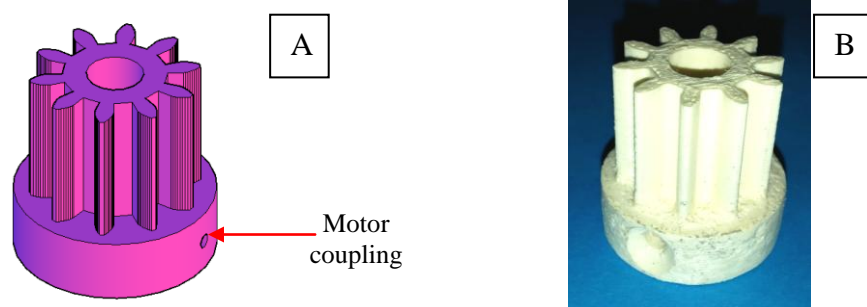
Figure 6.6: A) 10-teeth Pinion gear (CAD Drawing), B) 10-teeth Pinion gear (Photo)
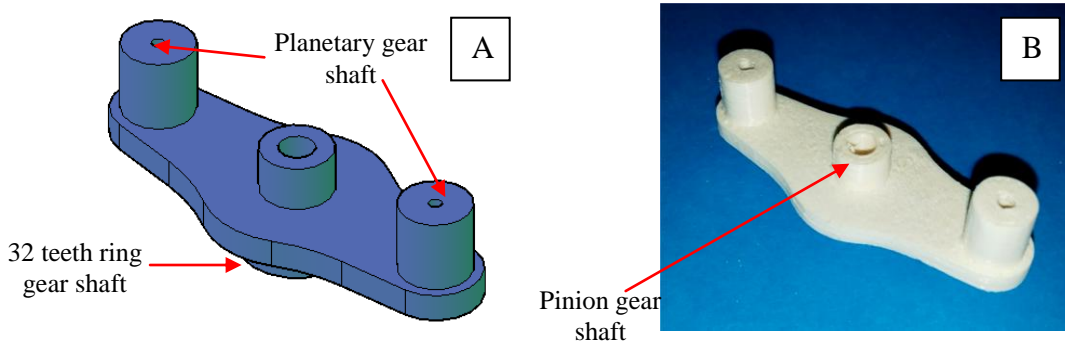
Figure 6.7: A) Lower planetary assembly (CAD Drawing), B) Lower planetary assembly (Photo)

60

The upper planetary section shown in figure 6.8 was assembled with the lower section. The two axles on top supported the top of the planetary gears. Both of the planetary sections placed the planetary gears in between them. The large hole in the middle of the upper planetary section was there in order to spin through the pinion gear.
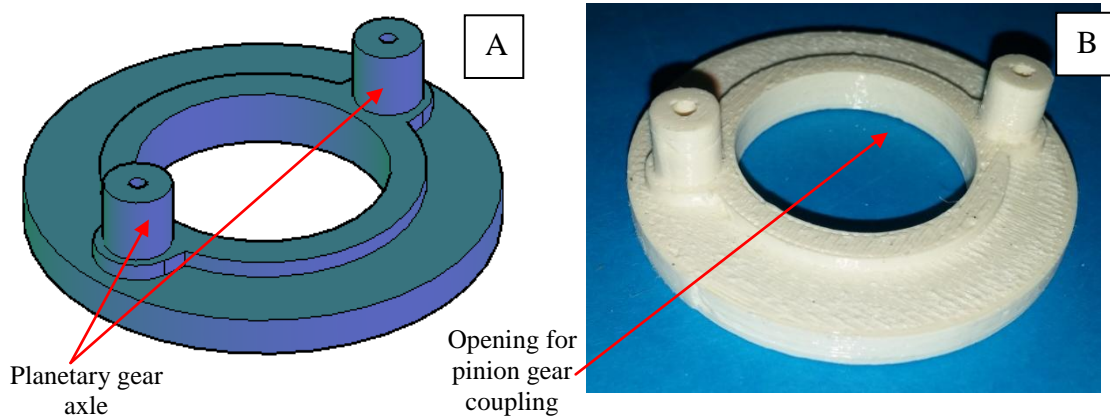
Figure 6.8: A) Upper planetary assembly (CAD Drawing), B) Upper planetary assembly (Photo)

The planetary gear shown in figure 6.9 included 10 teeth. A hole in the middle achieved coupling with the upper and lower planetary sections. The middle section of the hole had a smaller diameter so the upper and lower planetary sections were inserted in the planetary gears to a specific depth. This technique ensured smooth rotation of the planetary gears. In addition by tightening the screws of the planetary gears it was possible to adjust the tightness of the gears thus, eliminating the backlash of the assembly. The coupling between the parts was very important in mechanisms with multiple gears for noise reduction, smoother operation and reliability.
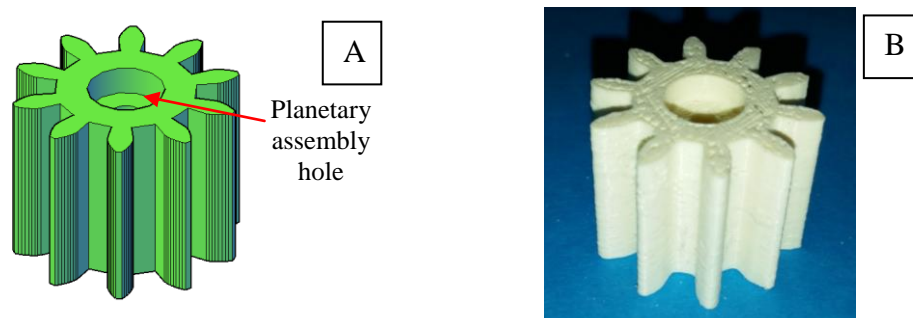
Figure 6.9: A) 10-teeth planetary gear (CAD Drawing), B) 10-teeth planetary gear (Photo)

Another part of the planetary reduction unit was the 32 teeth ring gear shown in figure 6.10. The bottom of the gear allowed the lower planetary section to spin around the center of the case. The hole in the center was made to fasten the phi shaft under the planetary assembly.
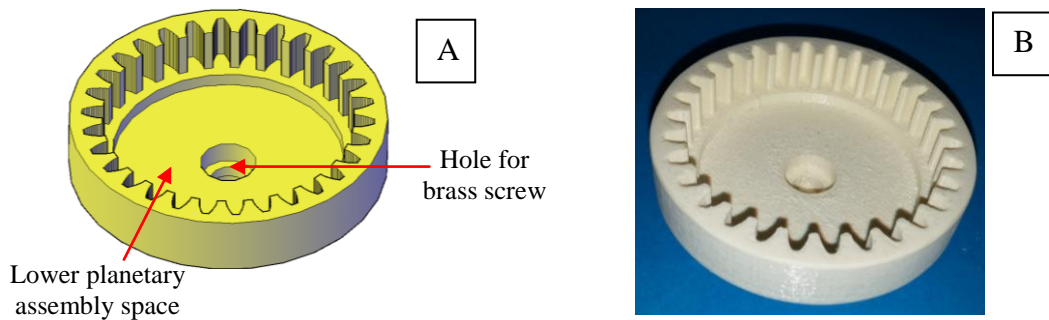
Figure 6.10: A) 32-teeth ring gear (CAD Drawing), B) 32-teeth ring gear (Photo)

The phi shaft shown in figure 6.11 transferred the motion from the output of the planetary unit to the arm mounted at the opposite end. On the top of the shaft a coupling was attached to the rectangular extrusion of the 32 teeth ring gear. This coupling was large in diameter compared to the shaft. This provided large surface for the placement of the encoder strip.
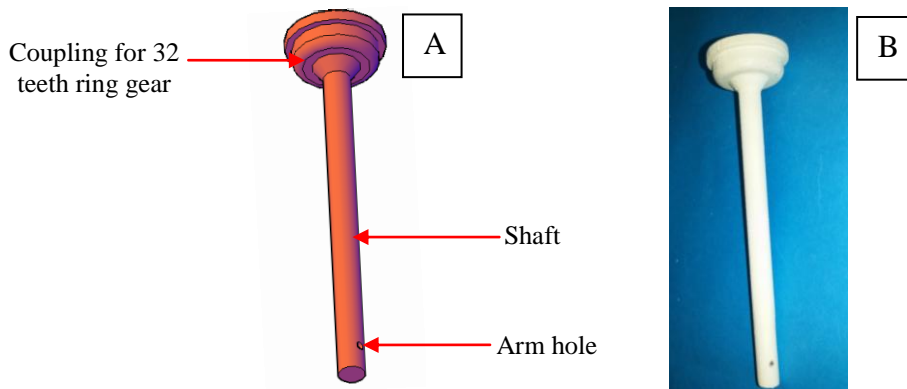
Figure 6.11: A) Phi shaft (CAD Drawing), B) Phi shaft (Photo)

The lower planetary cover shown in figure 6.12 holds together the gears of the reduction unit. The tabs on all four corners of the part were designed to fasten to the upper case of the planetary gearbox. The bottom edge supported the 32 teeth ring gear in place. In the lower case there were four holes that are attached to the encoder holder shown in figure 6.13.

The encoder cover hosts the shaft thus providing rigidity and also acted as a guide to ensure smooth rotation. At the end of the cover there was a cylindrical section which was coupled with the arm. This section was overlapped by the upper portion of the arm as shown in figure 6.14. The upper hole of the arm rotated around the tip of the encoder cover which was the pivotal point of the phi mechanism. The hole at the bottom of the arm was smaller so as to attach to the phi shaft. The arm and the phi shaft were fixed together with a brass screw through the back of the arm. On the other end of the arm a coupling was included for the transducer holder. The transducer holder that was fitted to the arm was similar to the one used with the theta stage.

32 teeth gear support

Tabs to attach to upper gear case
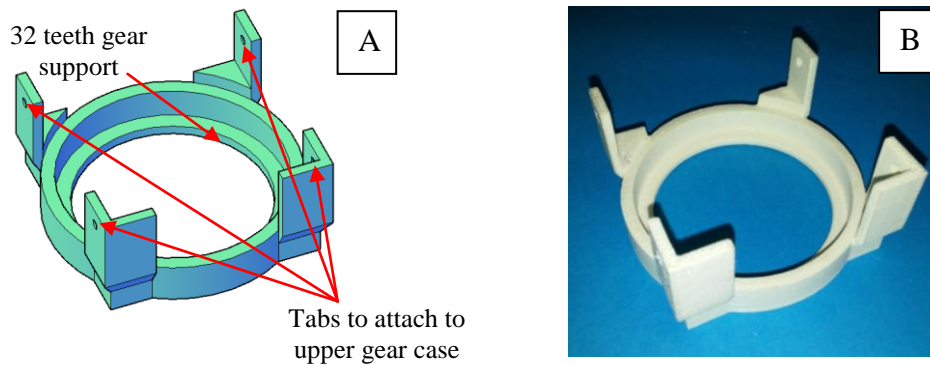
Figure 6.12: A) Lower gearbox case (CAD Drawing), B) Lower gearbox case (Photo)

Holes to attach to the gearbox

Arm is cylindrical extension

Shaft cover

Shaft hole
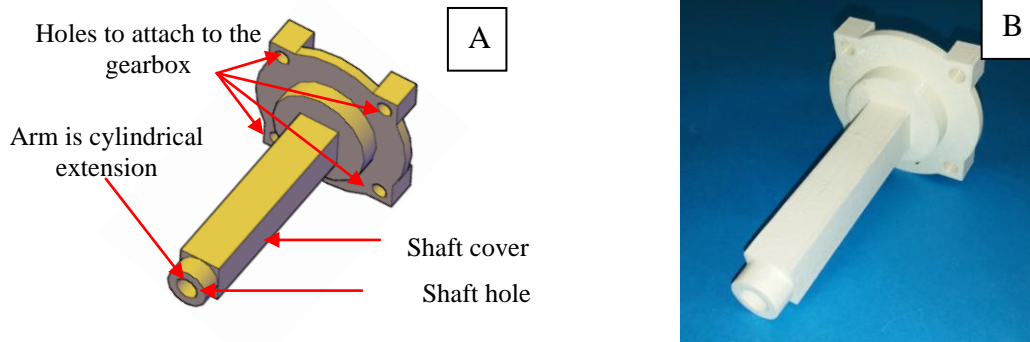
Figure 6.13: A) Encoder Holder (CAD Drawing), B) Encoder Holder (Photo)

Hole for encoder cover (cylindrical extension)

Transducer coupling
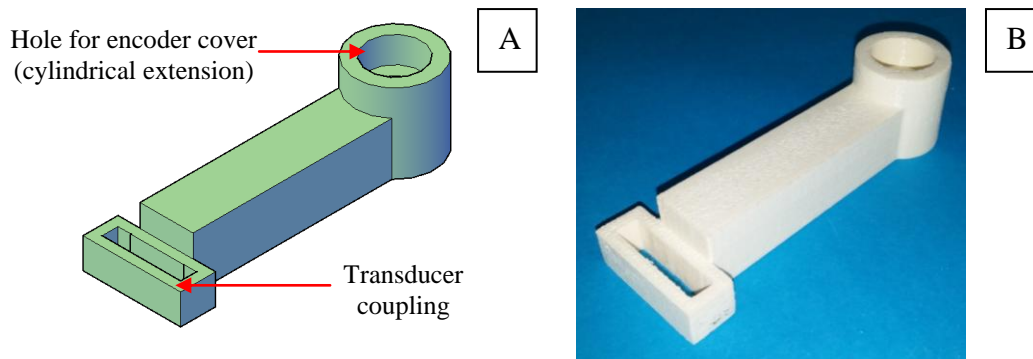
Figure 6.14: A) Transducer arm (CAD Drawing), B) Transducer arm (Photo)

6.1 Assembly of the phi stage

The pinion gear was installed on the shaft of the motor and was fixed with a brass screw as shown in figure 6.15.

Pinion gear

Motor

Brass screw
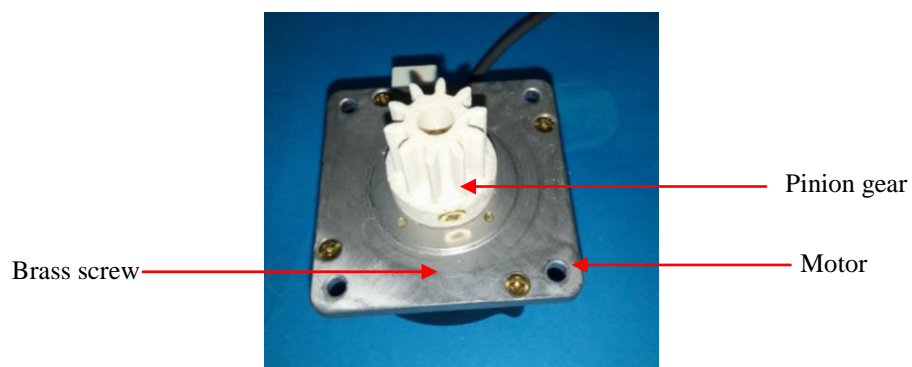
Figure 6.15: Pinion gear installation to the motor.

63

The planetary gears were placed on the corresponding shafts of the lower planetary assembly as shown in figure 6.16. To secure the planetary gears to the planetary assembly, the upper planetary assembly was placed on the top and was fastened with brass screws as shown in figure 6.17.
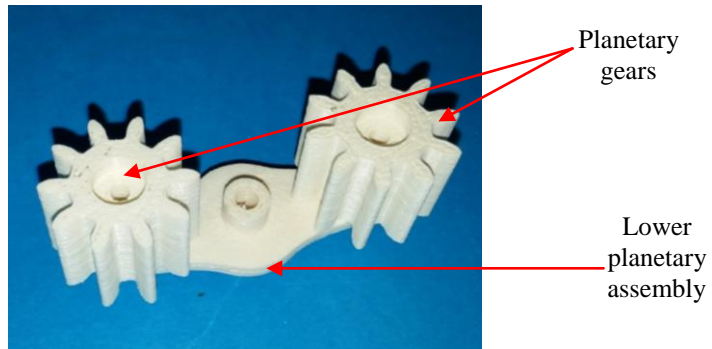
Figure 6.16: Photo of the planetary gears installed to the lower planetary assembly.
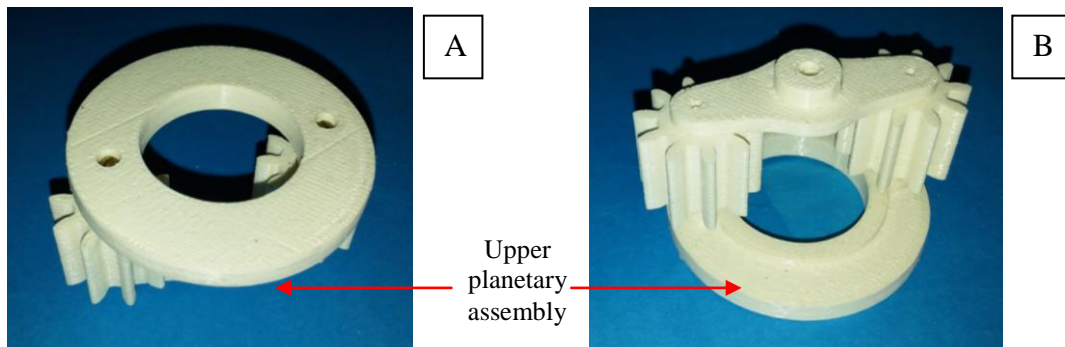
Figure 6.17: Photo of the completed planetary assembly.

Figure 6.18 shows the motor installed on the upper part of the gearbox of the planetary unit. The pinion gear was installed to the motor, in the center of the 30 teeth ring gear.
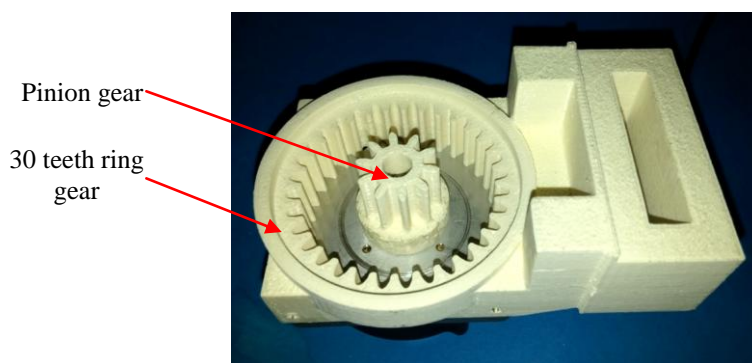
Figure 6.18: Photo of the motor-pinion gear assembly mounted on the upper gearbox case.

In order to transfer the motion from the pinion gear to the ring gear the planetary assembly was installed as shown in figure 6.19. With this step the first stage of the planetary gearbox was completed which offered a reduction ratio of 4:1.
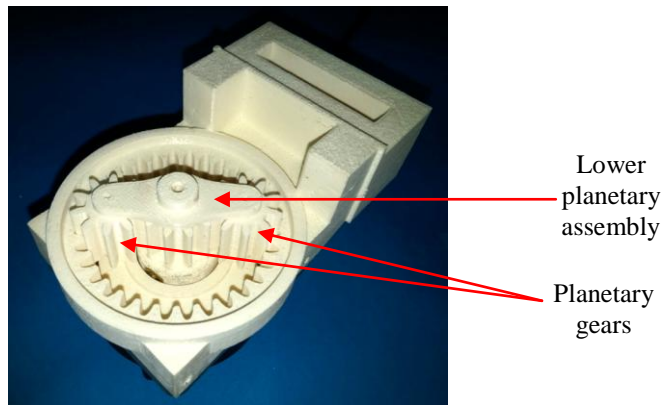
Figure 6.19: Photo of the planetary assembly installed in the gearbox.

To complete the second stage of the planetary reduction unit, the 32 teeth ring gear was installed above the first stage. The teeth of the planetary gears that extended beyond the 30 teeth ring gear was coupled to the 32 teeth ring gear. The lower planetary cover was attached to the upper planetary cover as shown in figure 6.20.
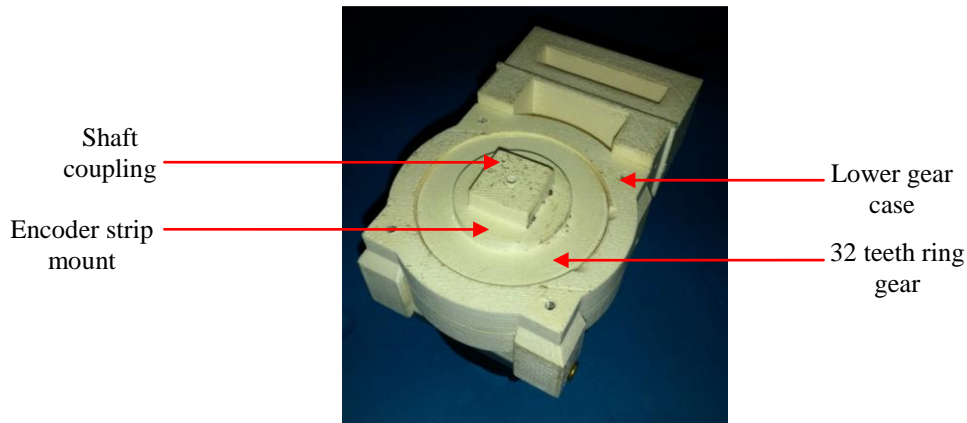
Figure 6.20: Photo of the planetary reduction unit completed with lower gearbox case installed.

Due to the multiple gears included in the gearbox enclosure, grease was used to reduce the friction (reducing the noise). The circular encoder strip was installed on the phi shaft coupling (figure 6.21) of the gearbox. The phi shaft secured the encoder strip on the planetary unit as shown in figure 6.22. With the installation of the shaft, the encoder strip was secured without any other additional hardware. Another advantage of this technique was the fact that the encoder strip was evenly pressed together, and therefore it did not affect its shape. The encoder strip was made of thin and flexible material and any deformation would have significant impacted the accuracy of the motion.

The optical encoder module was installed on the encoder holder with two brass screws as shown in figure 6.23. After the optical encoder module was installed to the holder, it was mounted on the top of the planetary unit.
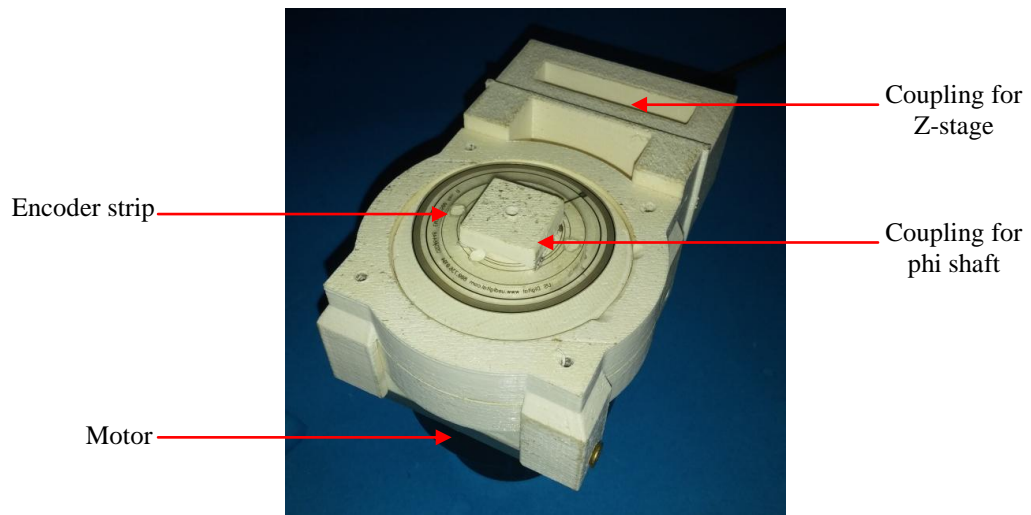
Figure 6.21: Photo of the encoder strip placed on the encoder holder.
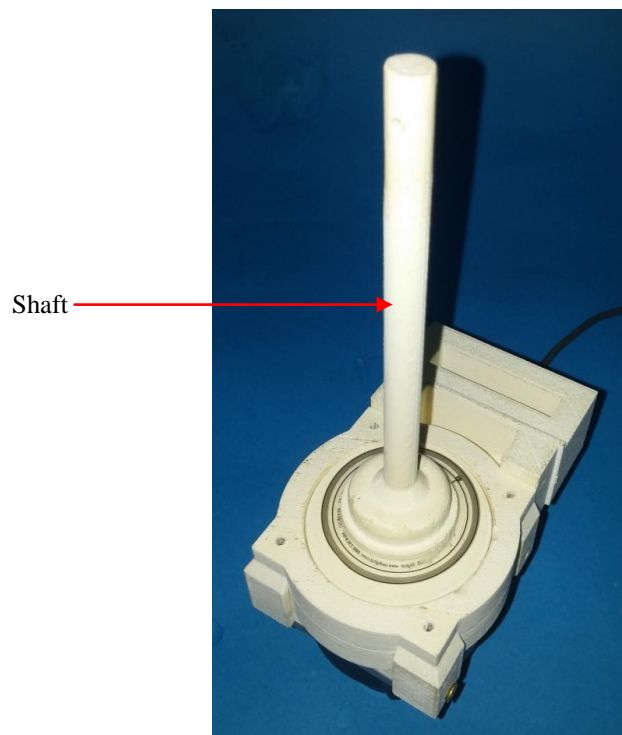
Figure 6.22: Photo of the shaft installed and secured to the encoder strip.
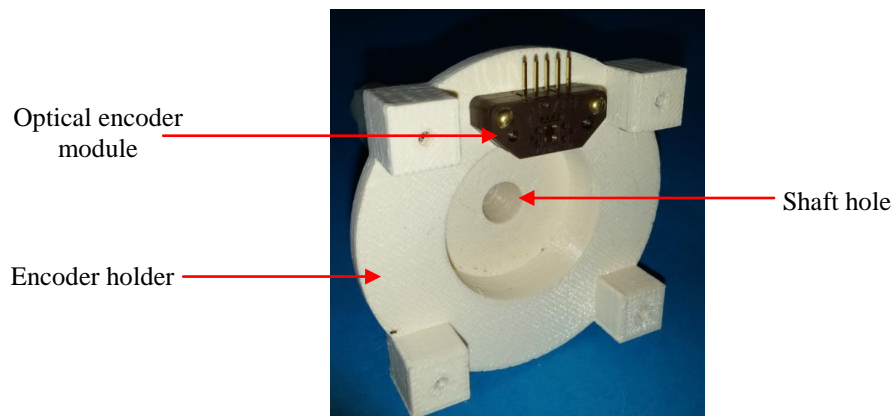
Figure 6.23: Photo of the installation of the optical encoder module.

Shaft
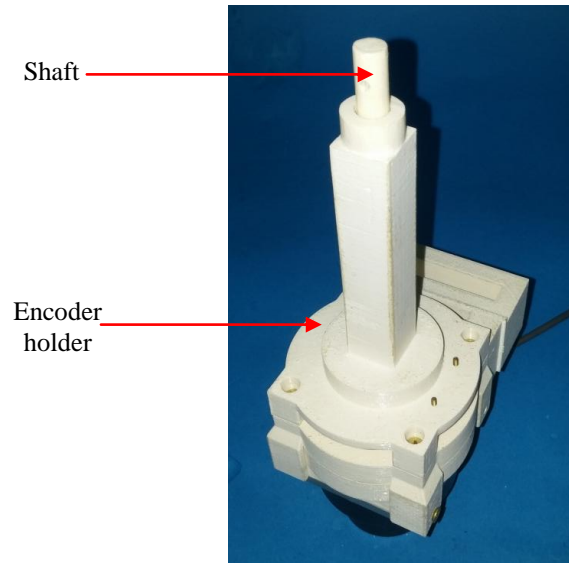
Encoder
holder

Figure 6.24: Photo of the installation of the encoder holder.

The final step of the phi axis was the installation of the arm as shown in figure 6.25. The arm was installed by attaching the arm on the phi shaft until the tip of the encoder holder was covered by the arm. When the arm was fitted to the shaft, a brass screw was used to fasten the arm to the shaft.

Arm

Brass screw
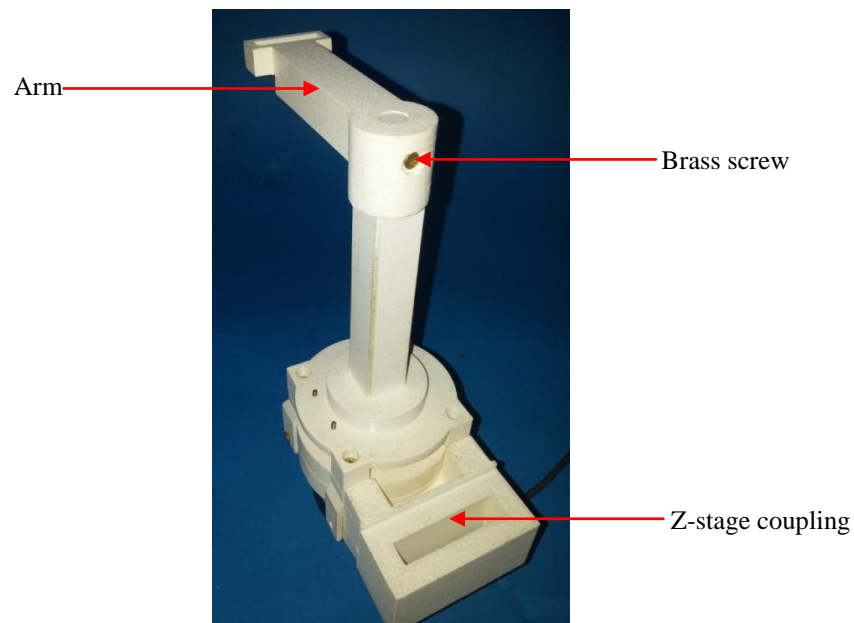
Z-stage coupling

Figure 6.25: Photo of the completed phi axis.

The phi axis with the transducer holder is shown in figure 6.26. The completed phi arm was installed to the Z-stage through the coupling. This completed the four axis positioning device as shown in figure 6.27.
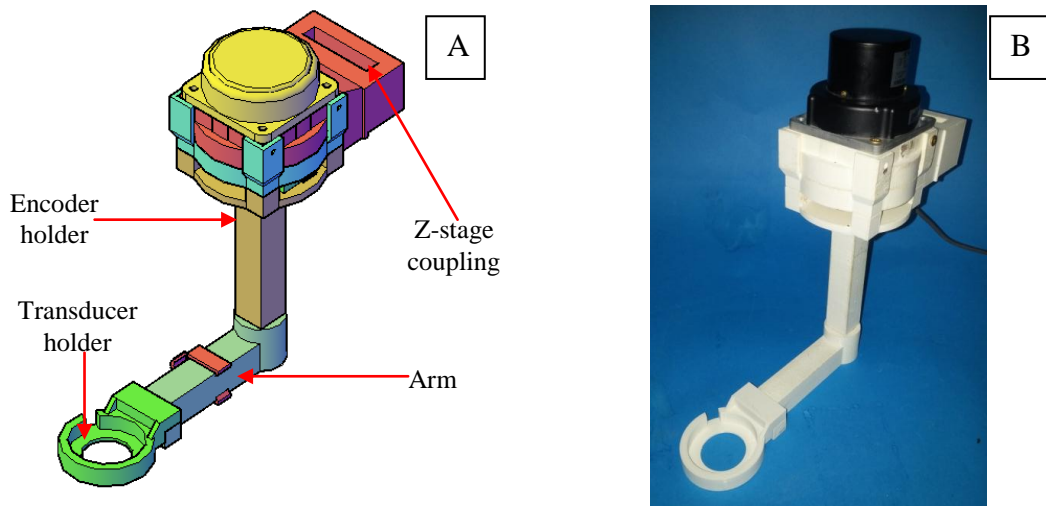
Figure 6.26: A) Phi axis mechanism (CAD Drawing), B) Phi axis mechanism (Photo)
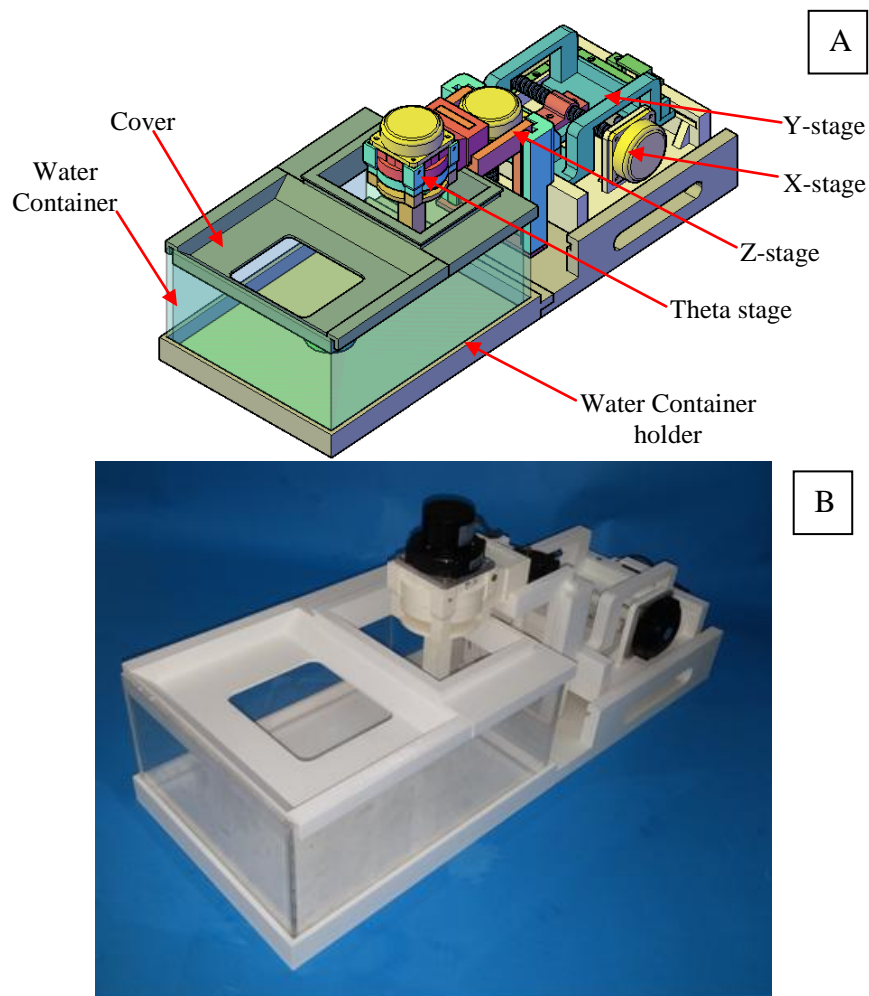
Figure 6.27:4 A) 4 DOF positioning device with phi axis (CAD Drawing), B) 4 DOF positioning device with phi axis (Photo).

Chapter 7 Animal robot (submerged type)

A two axis positioning device was developed to navigate a HIFU transducer inside the MRI. The difference compared to version 1 robot is that all its mechanical parts are submerged in a water container.

In order to establish motion in two axes, two different mechanisms were implemented. For the X-stage a Jack screw design was followed. For the Y-stage rack and pinion pair design was followed. The two mechanisms were necessary since the motors are not water proof and should be mounted out of the water container. The jack screw principle for X-stage and the rack and pinion pair on the Y-stage provided a wide range of motion.

To improve accuracy of the Y-stage a planetary gear reduction unit was added. The planetary reduction unit reduced the motion speed of the rack and pinion pair. The angular encoder calculates the angular motion and converted it to linear motion.

7.1 Animal robot design

The robot was built on the base which is shown in figure 7.1. The base was designed as thin as possible in order to reduce the total height of the device. It has a thickness of 30 mm. The bottom of the base (15 mm) provided sufficient support to the motor holders. The sidewalls are 15 mm tall to support the water container as shown in figure 7.2.
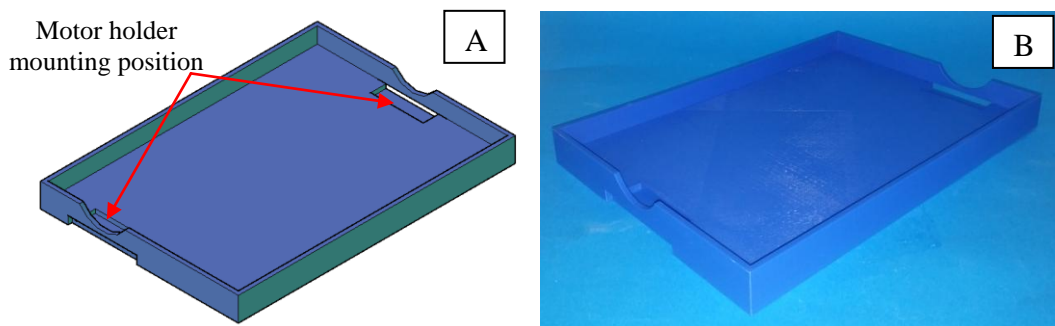
Figure 7.1 A) Base (CAD drawing), B) Base (Photo)

The water container is subjected to stress by the torque of the motors and the weight of the water. For this reason the front and the rear sides were made thicker by 5 mm. The main motion mechanisms were installed in the water container, therefore the design was such to avoid water leakage. Two holes were drilled on the front and rear sides of the tank in order to install the shaft seal mechanisms. Since the motors and the encoders were not water proof they were placed outside of the water container and with the use of

the sealing mechanism the water was kept inside the tank. The water container was made 152 mm in height.
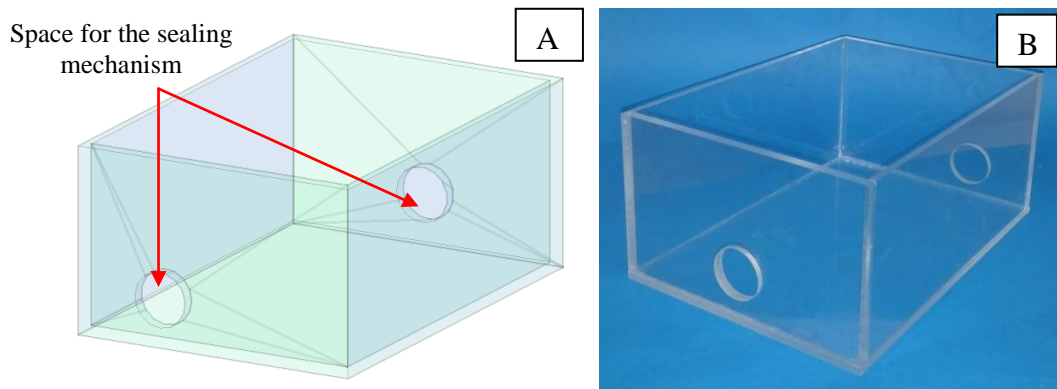
Figure 7.2: A) Water tank (CAD drawing), B) Water tank (Photo)

The sealing mechanism components are shown in figure 7.3. The inner and outer cover supported the bearing and the rubber seal on to the water container. In order to reduce the stress from the rubber seal, a bearing was used to hold the weight of shaft thus increasing the efficiency of the mechanism. The rubber gasket was installed inside the tank which sealed the surfaces between the inner teflon cover and the water container.
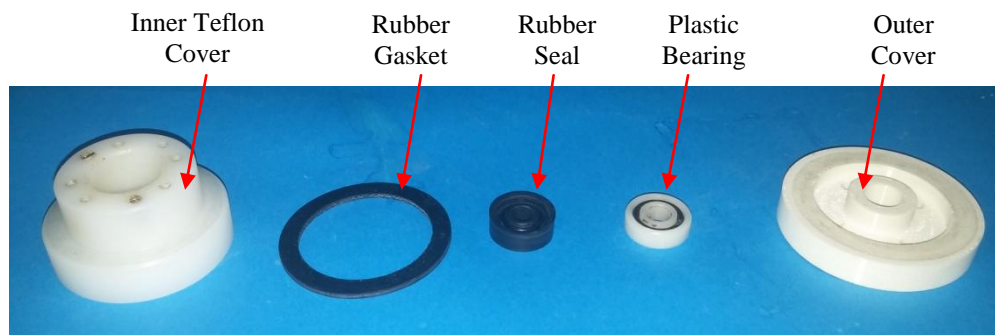
Figure 7.3: Photo of the water sealing mechanism.

In order to transfer the motion of the motor to the mechanisms inside the water container, brass shafts were used. This makes the seal durable due to the smoother surface of the bronze shaft which coupled better with the rubber seal, thus prevented any water leakage.

The bronze shaft shown in figure 7.4 was coupled to the X-stage's motor with a jack screw. It included a slot on the edge to provide a proper shape in order to rotate the coupling mechanism. The Y-stage's shaft shown in figure 7.5 was made shorter compared to the X-stage shaft, since the reduction planetary unit required more space. The shortest shaft enabled equal spacing between the coupling and the water container for both stages.

70
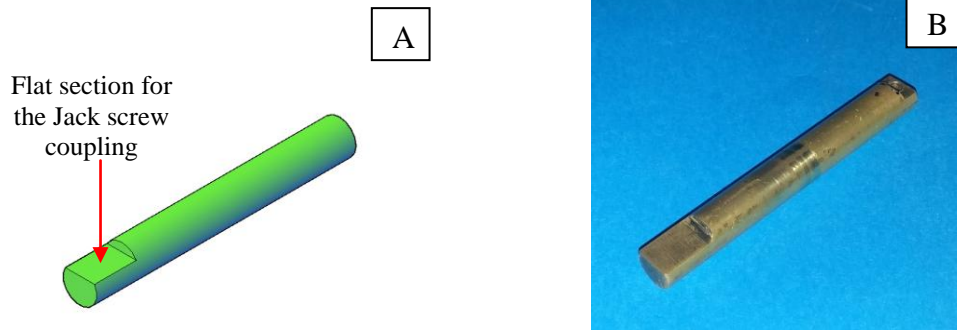
Figure 7.4: A) X-stage bronze shaft (CAD drawing), B) X-stage bronze shaft (Photo)
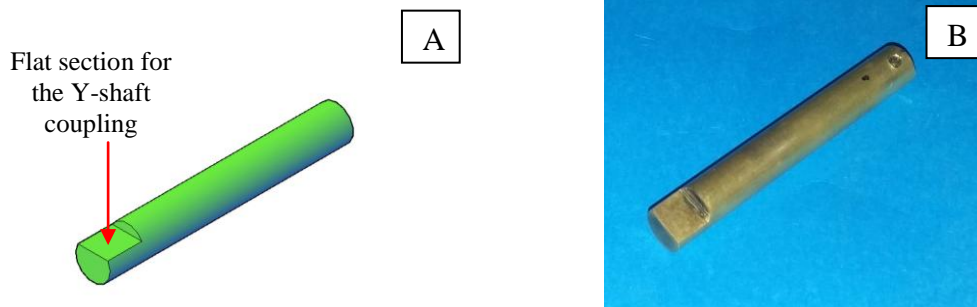
Figure 7.5: A) Y-stage bronze shaft (CAD drawing), B) Y-stage bronze shaft (Photo)

The X-motor holder shown figure 7.6 included an extension that was attached to the corresponding slot on the base. At both sides of the coupling two tabs were included to fasten the motor holder with brass screws. The vertical section of the motor holder included space for attaching the encoder holder (shown in figure 7.7).
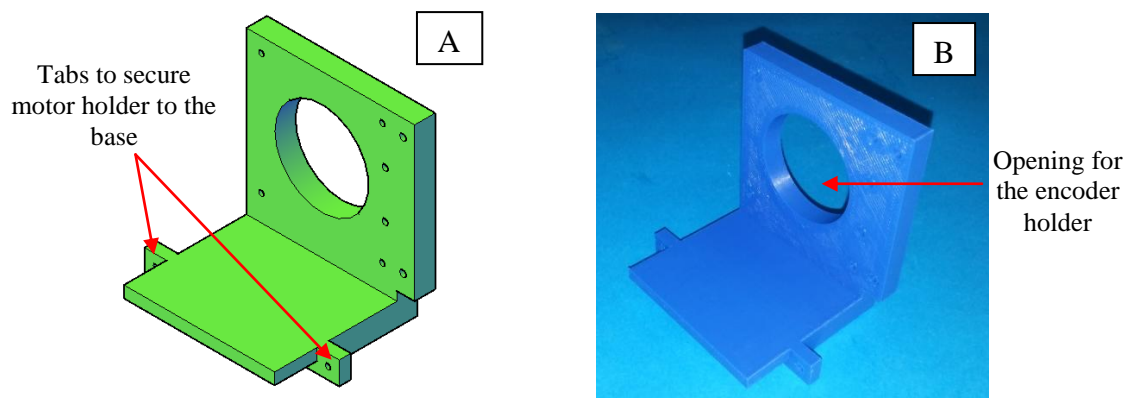
Figure 7.6: A) X-motor holder (CAD drawing), B) X-motor holder (Photo)

The opening in the center of the encoder holder joined the shaft of the motor and the bronze shaft of the X-stage. The lower section of the encoder holder has a surface to support the encoder strip. The top section was a rectangular coupling that secured the encoder cover. The encoder holder cover and the encoder holder were assembled

Encoder strip
Cover

Surface to support the
encoder strip

Rectangular
coupling

Encoder strip
holder
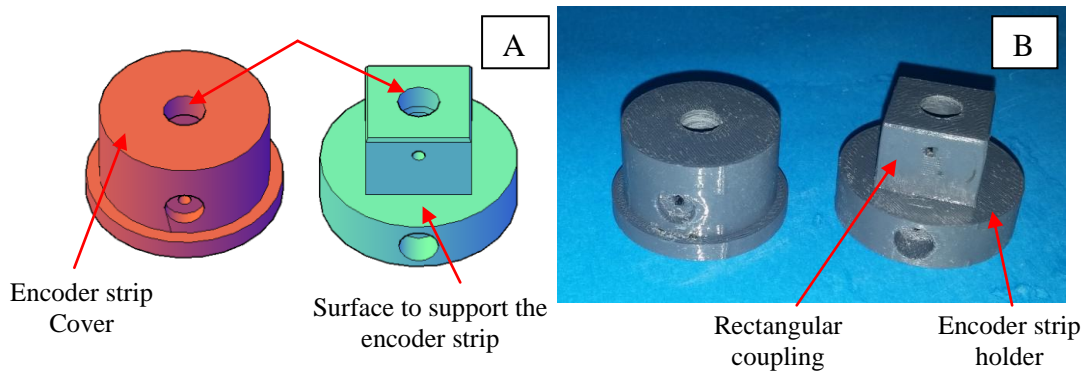
Figure 7.7: A) Encoder holder (CAD drawing), B) Encoder holder (Photo)

together to secure the encoder strip using a single screw that was long enough to secure the bonze shaft as well.

To transfer the motion to the Y-stage, a planetary unit was added which was similar with the phi stage. This part was redesigned as shown in figure 7.8. The case coupling was modified to replicate the coupling of the X-motor holder. Also the width of the gear teeth was reduced by 2.5 mm to improve the appearance of the unit. The motor of the Y-stage was fixed at the back of the planetary case.

32 teeth ring
gear

Tabs to secure
motor holder to
the base
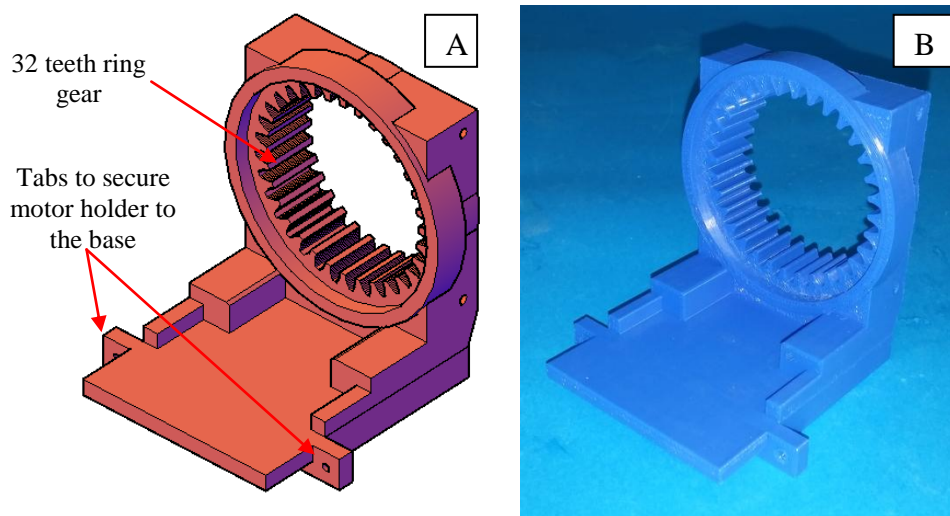
Figure 7.8: A) Planetary case (CAD drawing), B) Planetary case (Photo)

The planetary assembly was the same as the one used in the phi axis but with the planetary gears reduced by 5 mm. This improvement resulted to a smaller contact patch between the gears that reduced the friction. The reduced friction made the planetary smoother and more silent.

The planetary pinion gear shown in figure 7.10 reduced the teeth height to fit inside the smaller planetary reduction unit. Apart from the teeth height no other modification was done to the pinion gear for this robot.
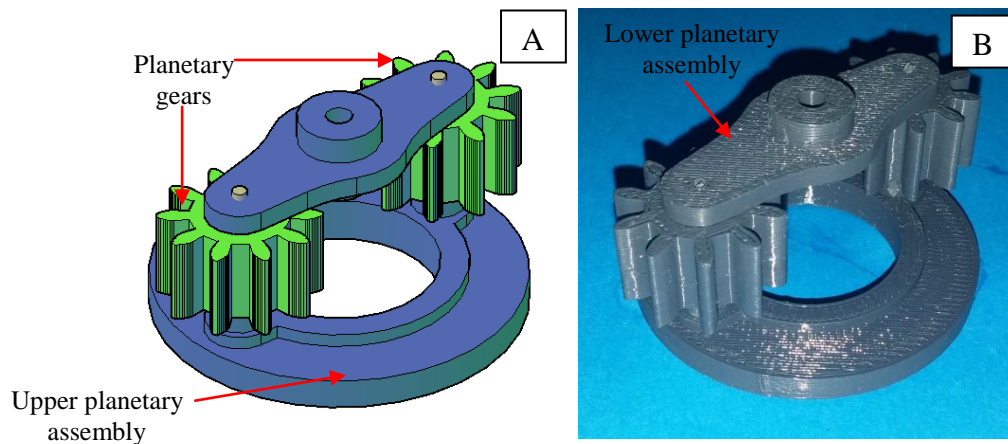
Figure 7.9: A) Planetary gear assembly (CAD drawing), B) Planetary gear assembly (Photo)
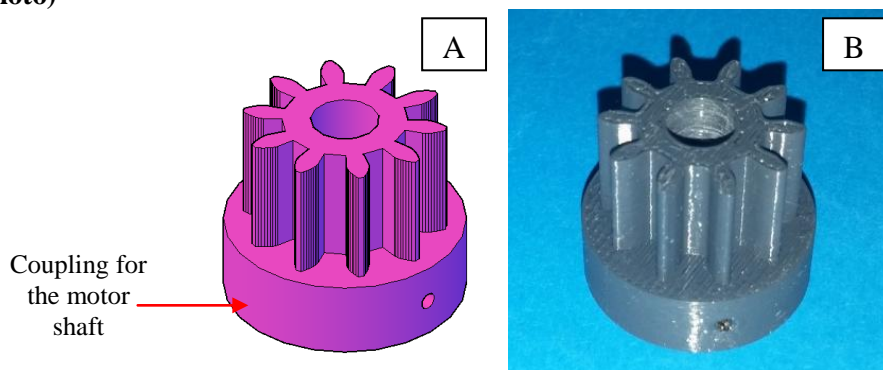
Figure 7.10: A) Planetary pinion gear (CAD drawing), B) Planetary pinion gear (Photo)

The teeth of the ring gear shown in figure 7.11 were also reduced by 2.5 mm. A rectangular coupling and a flat surface were added to support the encoder strip. The rectangular coupling was attached to the bronze shaft for the Y-stage and the encoder cover as shown in figure 7.12. Modifications were also made to the planetary cover as shown in figure 7.13 to ensure a good attachment to the reduction unit (reduce the backlash). The planetary cover dimensions were crucial for the smooth rotation of the gears.
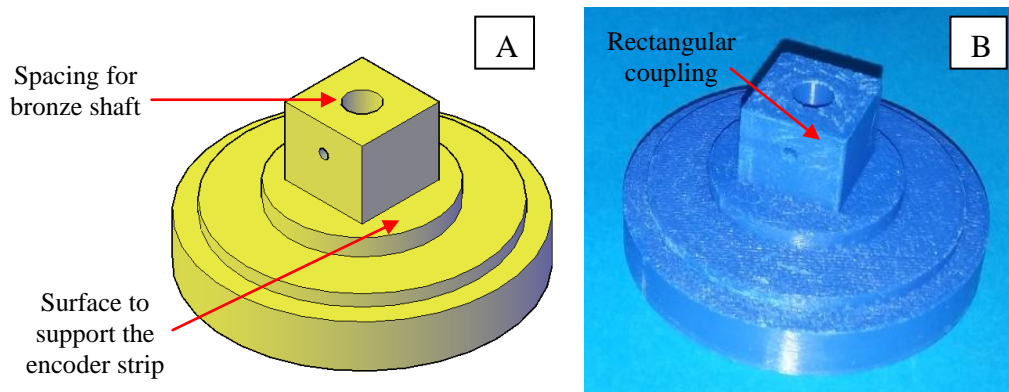
Figure 7.11: A) 30 teeth ring gear (CAD drawing), B) 30 teeth ring gear (Photo)
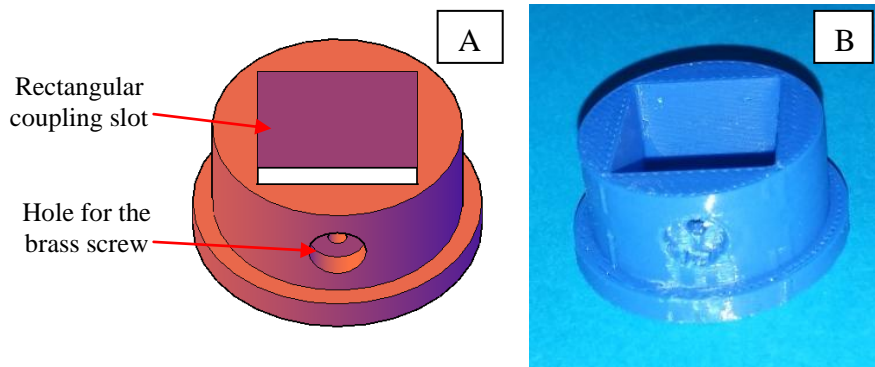
Figure 7.12: A) Encoder cover (CAD drawing), B) Encoder cover (Photo)
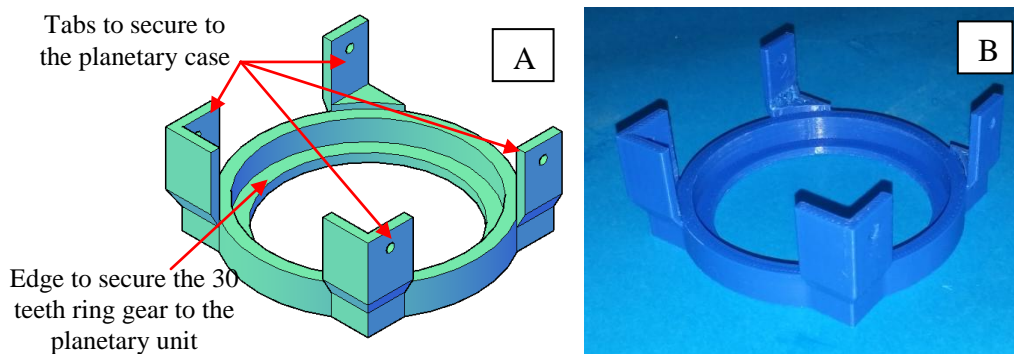
Figure 7.13: A) Planetary cover (CAD drawing), B) Planetary cover (Photo)

The last part of the assembly was the encoder module holder shown in figure 7.14. This part included two pins to mount the optical encoder module and a large hole in the middle for the encoder cover. It also has four tabs on each corner to be fastened on the planetary cover.
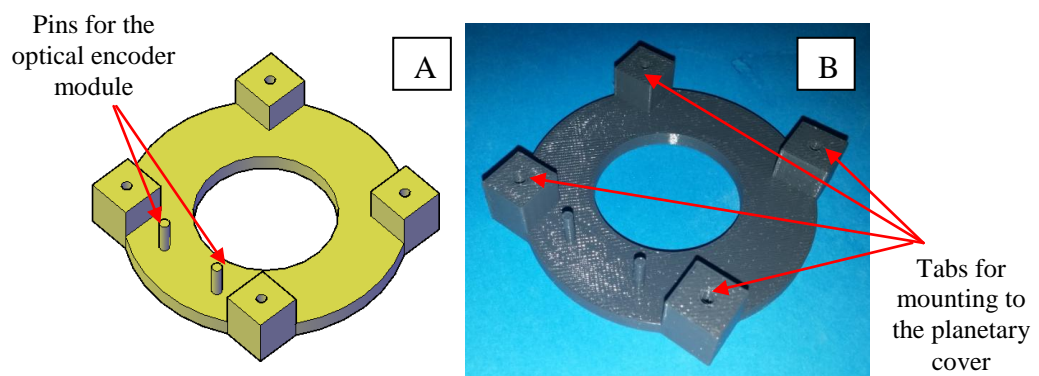
Figure 7.14: A) Encoder module holder (CAD drawing), B) Encoder module holder (Photo)

The design of the immersed motion mechanisms of the robot required detailed planning so the parts can be assembled together. The assembly sequence was critical due to the more complicate design and the limited space in the water container.

The frame for the X-stage shown in figure 7.15 was placed in the water container. Guides for the X-stage were included in the design. Two shaft holders in the middle

were added to support the ends of the jack screw and the rectangular shaped shaft. Space was also allowed for the sealing mechanism which was mounted to the water container sides. The sealing mechanisms were utilized to secure the frame on the bottom of the water container. The frame included two supports and after the installation of the sealing mechanism, the frame was secured in place. This design secured the frame in the water container.
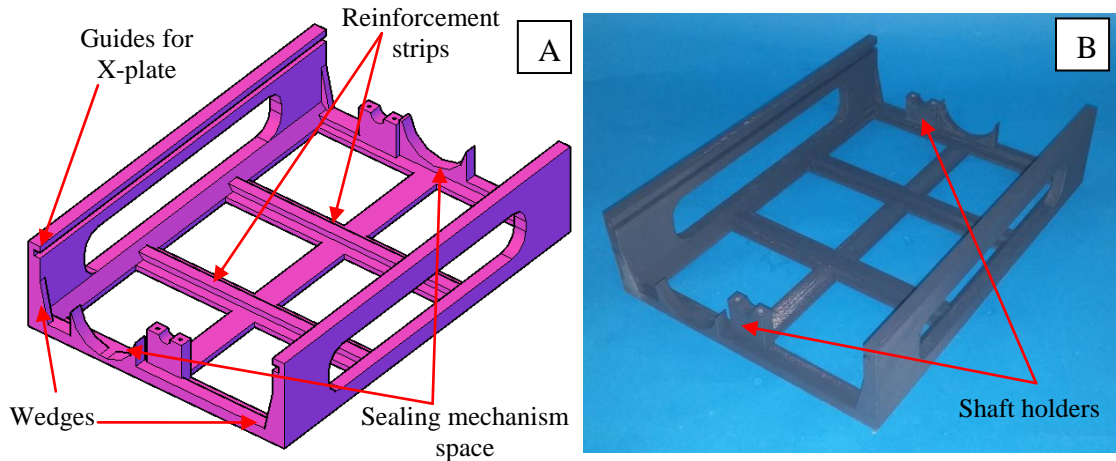
Figure 7.15: A) Frame (CAD drawing), B) Frame (Photo)

Four wedges were embedded to all the corners of the frame to reinforce its structure for increased rigidity. This enabled the frame to handle the stress of the X-stage mechanism, thus reducing the risk for leakage. The large openings on the bottom of the frame were needed to limit the amount of material. Despite using less material, the strength of this part was not compromised because of the structure's design.

The Y-plate shown in figure 7.16 included male guides on both sides. Also on the top there were female guides for the Y-plate which are shown in figure 7.17. The slot in the middle was needed for the Y-rack coupling to access the Y-plate (figure 7.18). The two holes on the top of the Y-plate were fixed in the Y-rack with brass screws. This concept allowed the rack and pinion pair to be assembled under the Y-plate which enabled exploitation of the available space in the water container, thus increasing significantly the range of motion of the X- stage. Furthermore, a coupling for the transducer holder was placed on the top of the Y-plate.

The pinion coupled with the Y-rack use the same teeth pattern with the one used for robot version 1. Its coupling was redesigned to suit the requirements of this version. The hole in the center of the pinion was made with rectangular shape to efficiently couple to the Y-shaft shown in figure 7.20. The coupling at the bottom was wider and included a

slot for the Y-plate mount which was incorporated underneath. Therefore, the pinion gear moved with the Y-plate along the X-direction. Additionally, the top section had a cylindrical extension to enable a smoother rotation of the pinion in the holder of the Y-stage.

The rectangular shape of the Y-shaft (figure 7.20) was chosen since it can withstand the load during positioning. Therefore, this shaft reliably transmitted the motion from the planetary reduction unit to the pinion. The rotation of the pinion gear forced the Y-plate
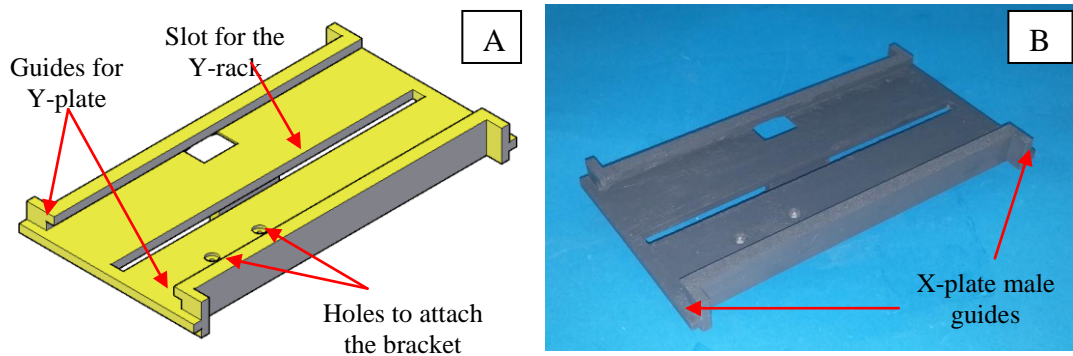
Figure 7.16: A) X-plate (CAD drawing), A) X-plate (Photo)
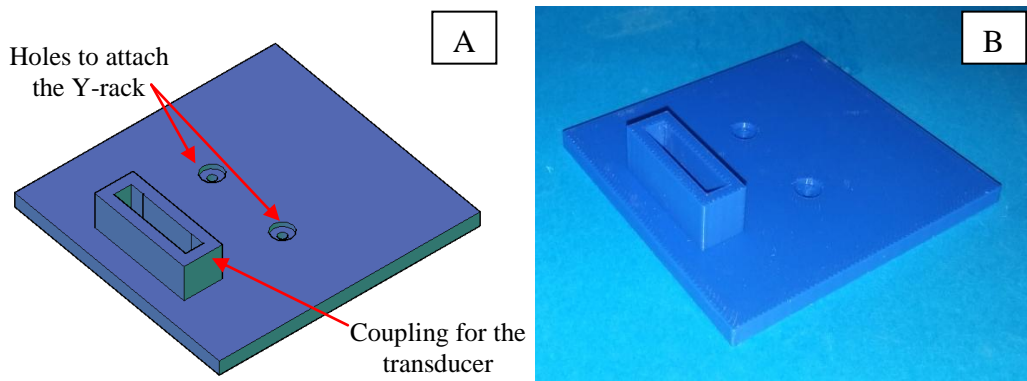
Figure 7.17: A) Y-plate (CAD drawing), A) Y-plate (Photo)
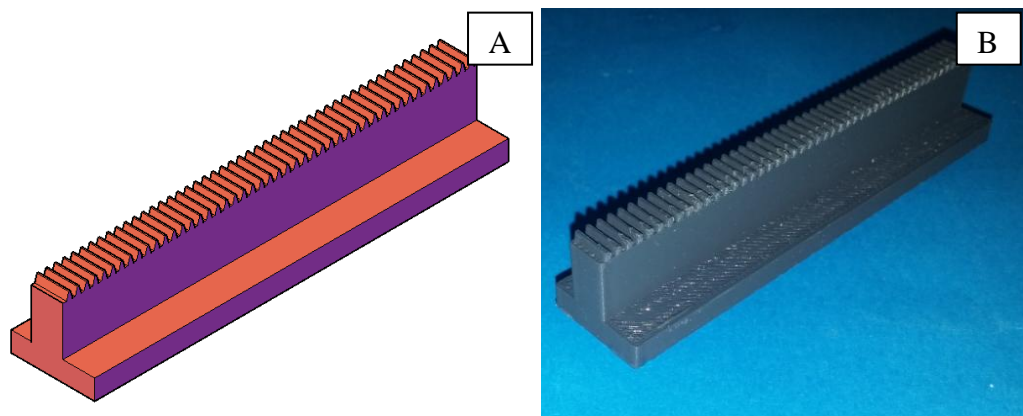
Figure 7.18: A) Y-rack (CAD drawing), B) Y-rack (Photo)

to move and with this mechanism the pinion was allowed to follow the movement of the Y-plate. At the end of the Y-shaft, a cylindrical section was incorporated for support. The other end of the shaft was coupled with the Y-stage's bronze shaft through a two-piece coupling.
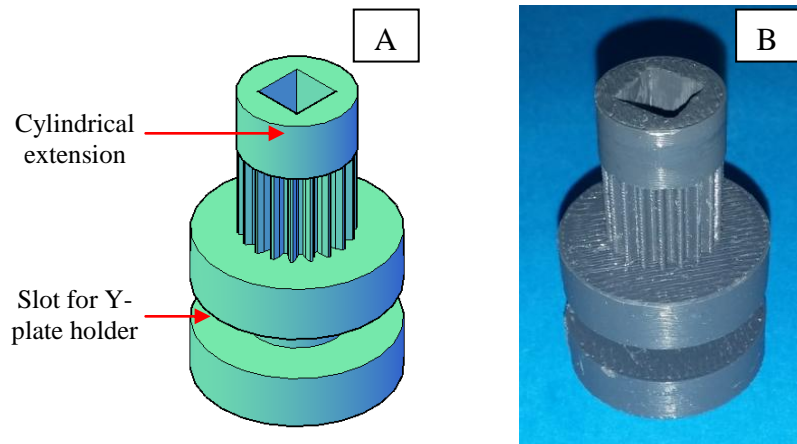
Figure 7.19: A) Pinion gear (CAD drawing), B) Pinion gear (Photo)

In order to secure the pinion on the Y-plate holder, the pinion bracket was designed as shown in figure 7.21. This bracket forced the pinion gear against the mount of the Y-plate. The holes which held the pinion on the Y-plate allowed it to spin freely, ensuring a precise coupling with the Y-rack.
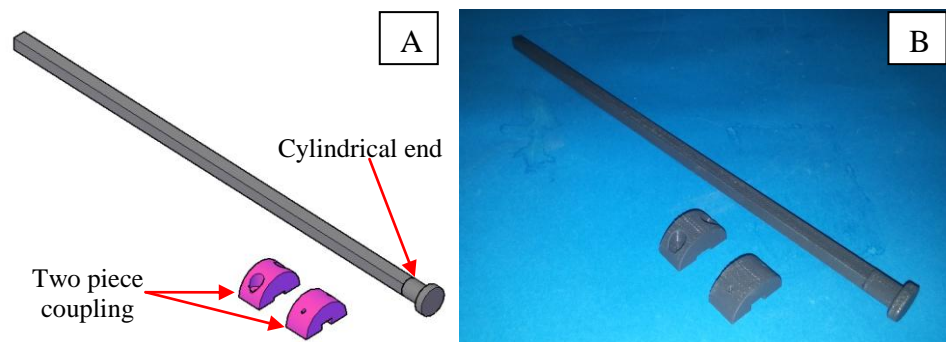
Figure 7.20: A) Y-shaft (CAD drawing), B) Y-shaft (Photo)
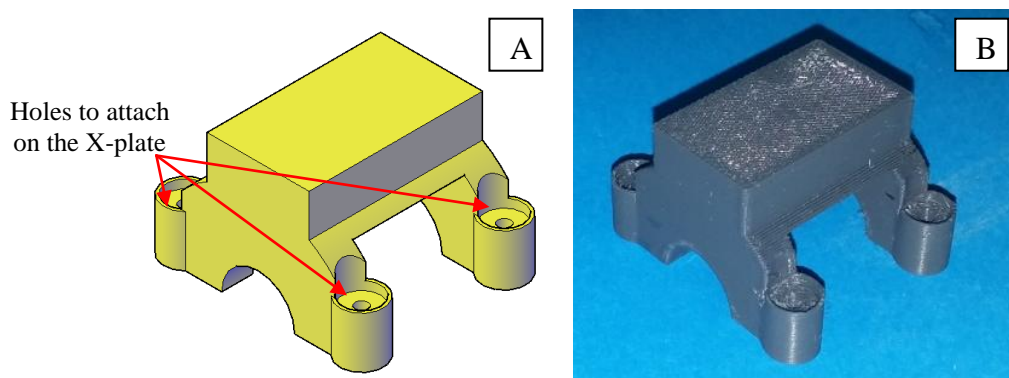
Figure 7.21: A) Pinion bracket (CAD drawing), B) Pinion bracket (Photo)

To transmit the motion to the X-stage a long jack screw was produced as shown in figure 7.22. It covered all the length of the water container offering a large range. It was placed parallel with the Y-shaft but with some offset to the side, since it was important to center the Y-shaft. On the other hand the jack screw placement did not affect the functionality of the robot in any way. By placing the two motion mechanisms side by side, the total height of the robot reduced significantly.

The bracket was mounted under the Y-plate as shown in figure 7.23. This bracket includes the female thread which was coupled to the jack screw for the motion of the X-stage. The bracket attached to the X-plate using brass screws. The shaft couplings were produced in two pieces to allow installation within the water container.
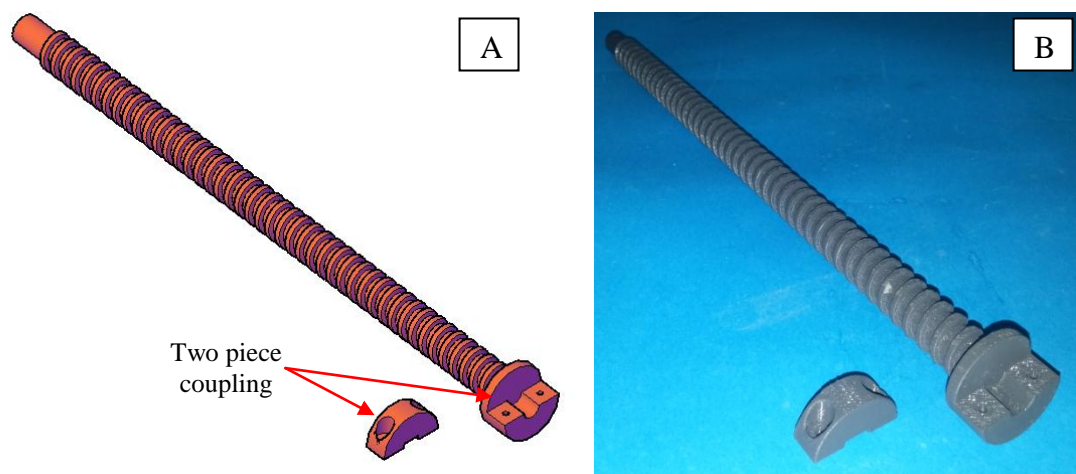
Figure 7.22: A) Jack screw (CAD drawing), B) Jack screw (Photo)
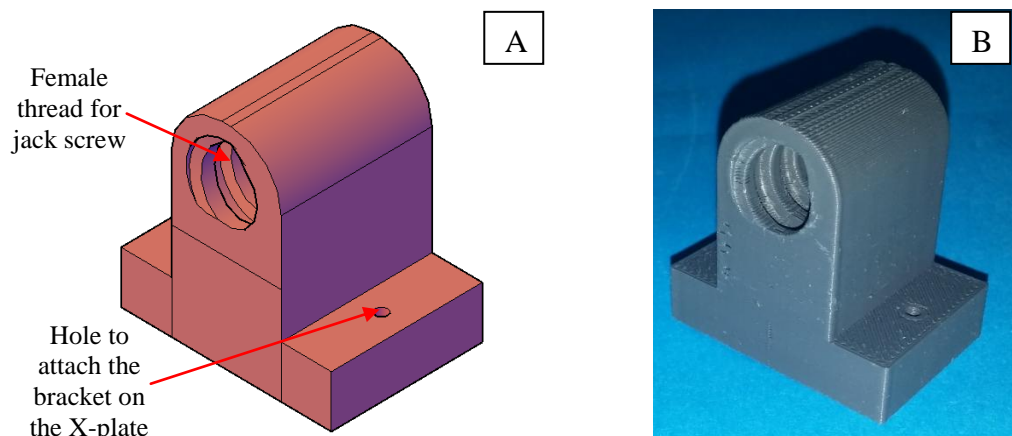
Figure 7.23: A) Female threaded bracket (CAD drawing), B) Female threaded bracket (Photo)

To cosmetically improve the positioning device three covers were designed to hide the mechanisms mounted outside of the water container. The rear and front cover are shown in figure 7.24 and figure 7.25. Both covers included a slot for attaching connectors. The covers included tabs on both sides which were used to attach the covers to the base. To mount the connectors to the base, specific connector holders were made as shown in

figure 7.26. These connector holders included a two-piece design which allowed easier installation to the positioning device. On the top of the water container a cover was manufactured as shown in figure 7.27. The top cover enabled the placement of tissue during ultrasound sonications with optimal distance from the transducer surface.

Tab to attach the cover at the base

Slot for the encoder holder
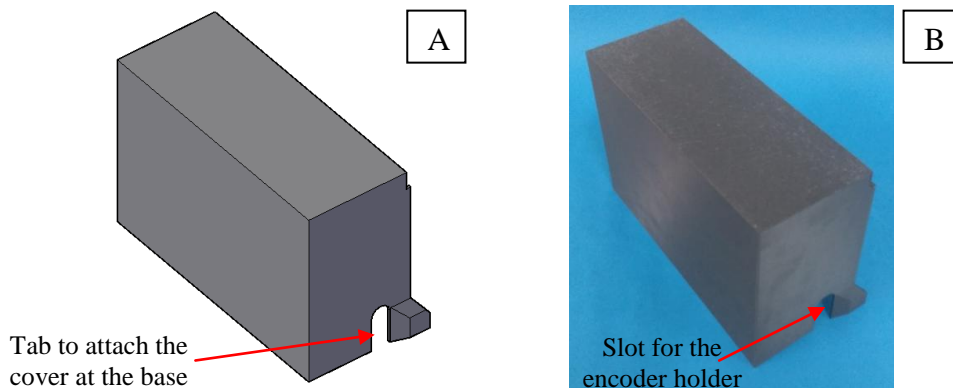
Figure 7.24: A) Front cover (CAD drawing), B) Front cover (Photo)

Tab to attach the cover at the base

Slot for the encoder holder
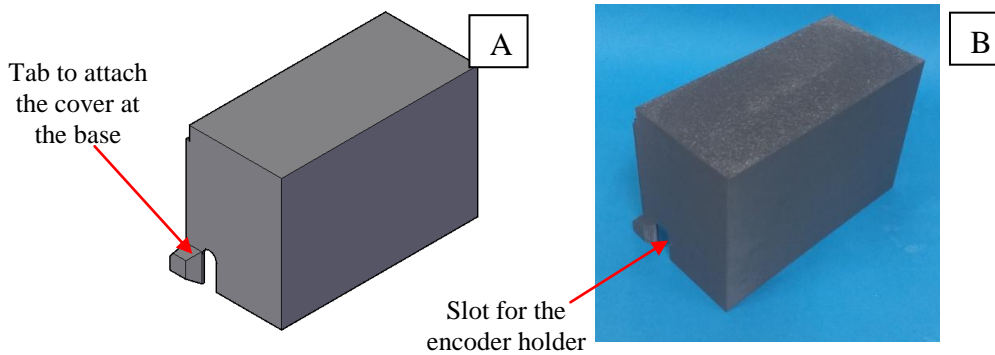
Figure 7.25: A) Rear cover (CAD drawing), B) Rear cover (Photo)
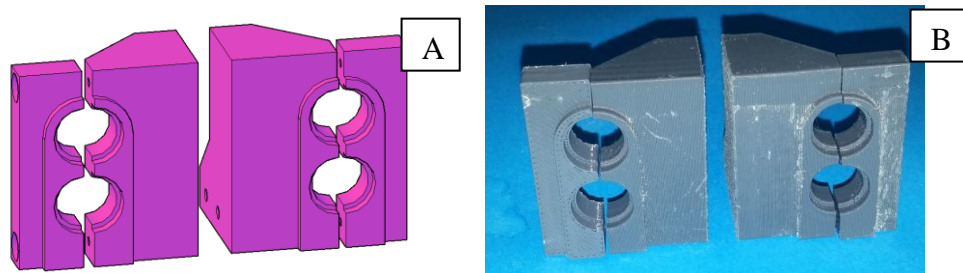
Figure 7.26: A) Connector holders (CAD drawing), B) Connector holders (Photo)

Hole for the transducer cable
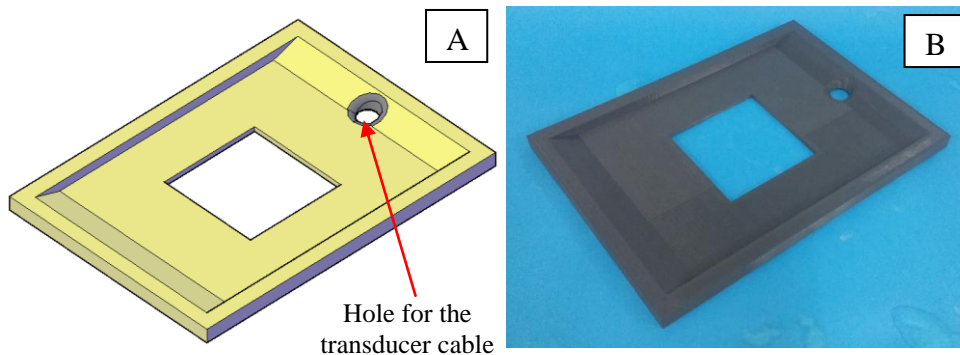
Figure 7.27: A) Top cover (CAD drawing), B) Top cover (Photo)

7.2 Assembly of the Animal Robot Version 2 (submerged type)

The encoder strip holder of X-stage was installed to the motor as illustrated in figure 7.28. This assembly was then fixed to the motor holder with brass screws as shown in figure 7.29. The angular encoder strip was placed on the encoder holder and secured by an encoder cover. The optical encoder module was attached by a holder as shown in figure 7.30. The motor/encoder was assembled with the X-stage bronze shaft attached to the encoder strip holder.
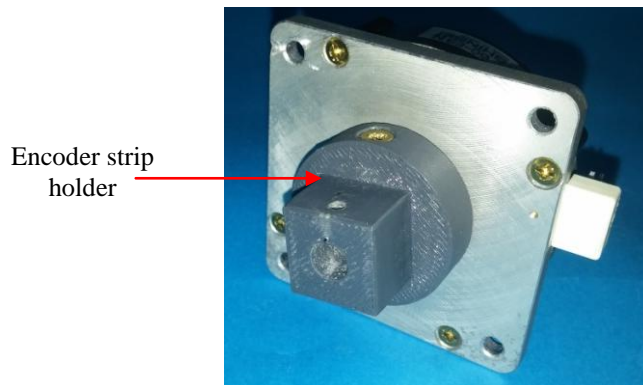
Figure 7.28: X-stage's motor with the encoder strip holder.
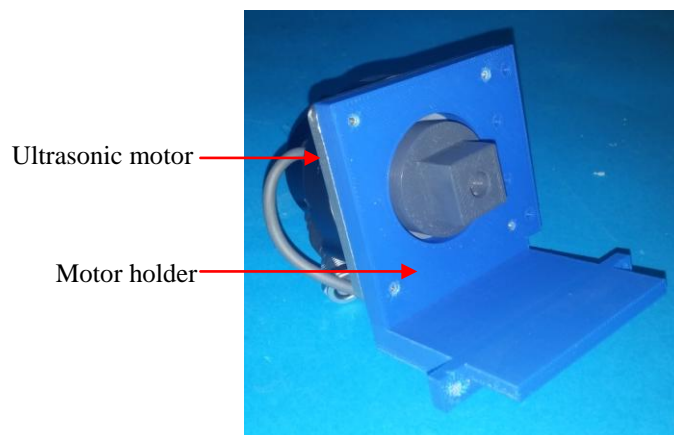
Figure 7.29: Motor attached to the motor holder.
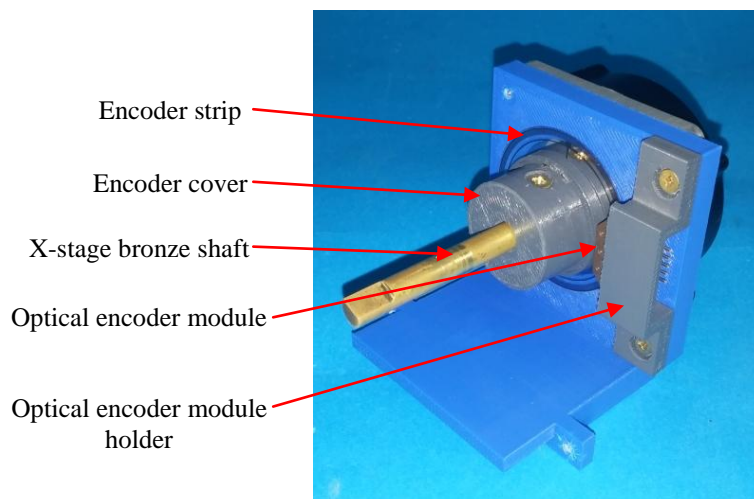
Figure 7.30: X-Motor/Encoder attachment.

80

The Y-stage mechanism was complicated due to the rack and pinion. In order to establish good accuracy a planetary, reduction unit was used, similar with the phi axis system. This unit reduced the speed of the motor to compensate with the faster ratio of the rack and pinion pair, thus enabling the encoders to properly read the signals.

To build the reduction unit mechanism, the motor with the pinion gear was initially mounted to the planetary case as shown in figure 7.31. With the installation of the planetary assembly the first stage of the reduction unit was completed as shown in figure 7.32.

The second stage of the reduction unit was completed after the installation of the 30 teeth planetary ring gear which was secured in the planetary case by the planetary cover as shown in figure 7.33. The encoder strip was attached to the 30 teeth ring gear.
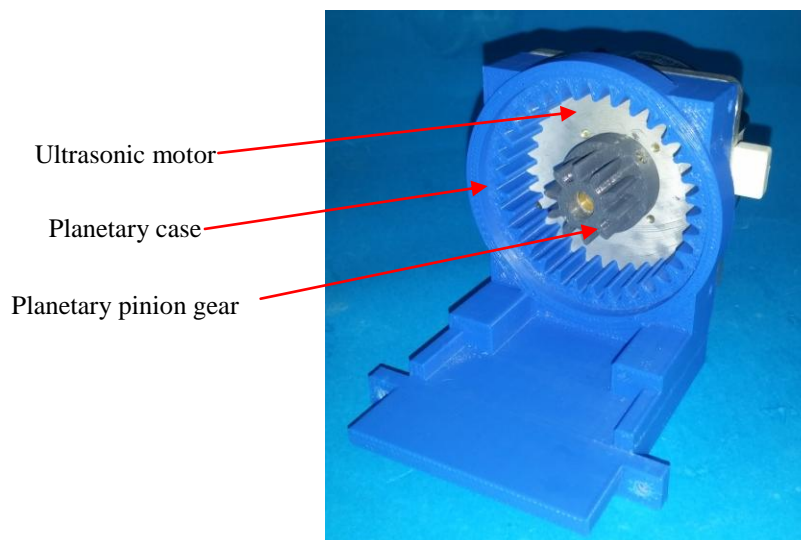
Figure 7.31: Motor with the pinion gear installed to the planetary case.
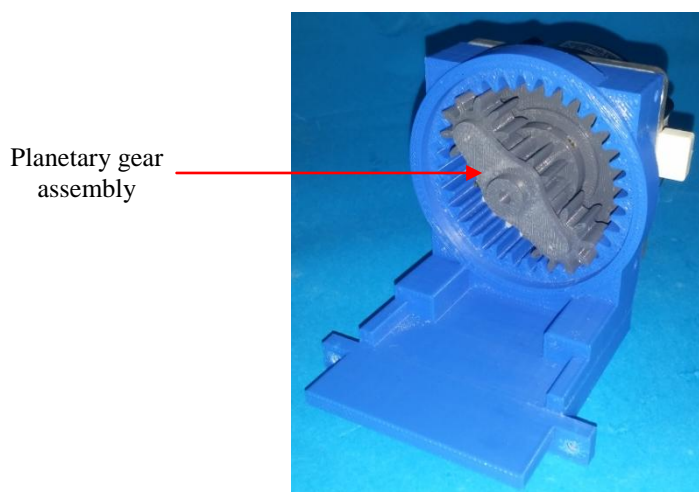
Figure 7.32: Planetary assembly as installed in the planetary case.
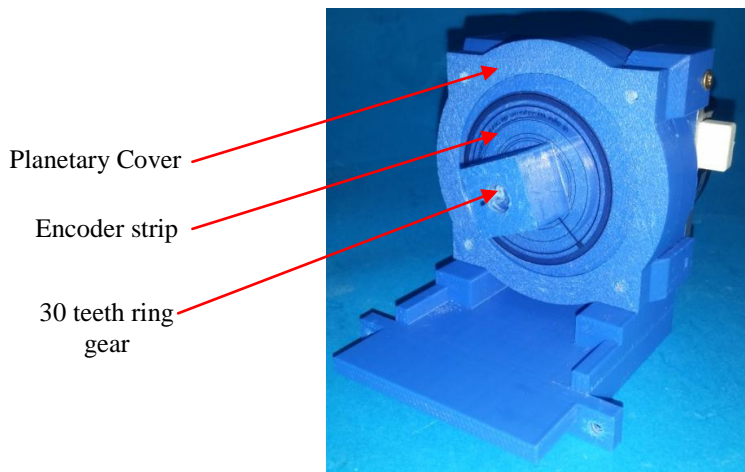
Figure 7.33: Planetary ring gear secured in the gear case by the planetary cover.

The optical encoder module was secured with the encoder module holder using the two pins as shown in figure 7.34. The planetary module holder was installed to the planetary cover and the encoder holder secured the angular encoder strip to the coupling. The Y-stage bronze shaft was installed and coupled to the Y-shaft, similar to the X-stage, as illustrated in figure 7.35.
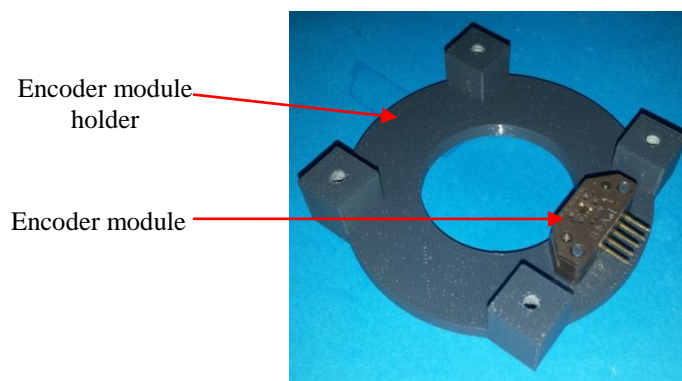
Figure 7.34: Optical encoder module as attached to the pins of the encoder module holder.
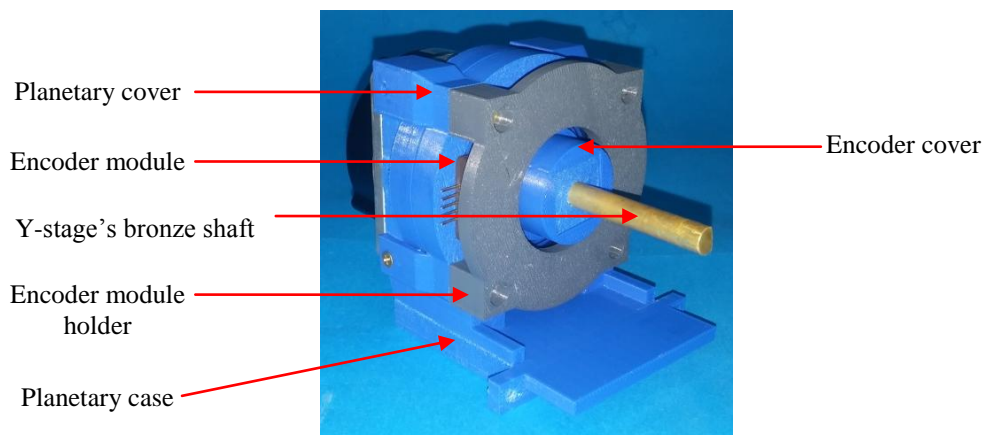
Figure 7.35: Planetary reduction unit attachment.

The Y-plate was allowed to slide in the guides of the X-plate as illustrated in figure 7.36. The X-plate included a guide for the Y-rack and, holds the pinion gear. The Y-rack was placed in the guides and was fixed under the Y-plate. Then the pinion was placed on the holders of the Y-plate as shown in figure 7.37.
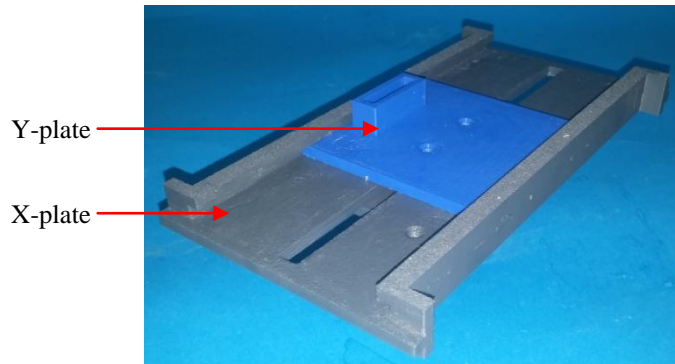
Figure 7.36: Y-plate as inserted in the guides of the X-plate.
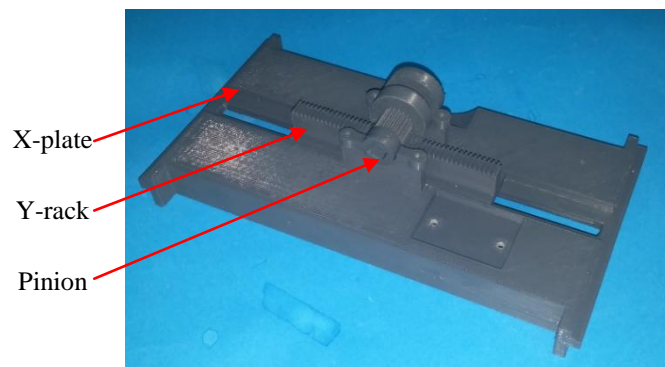
Figure 7.37: Y-rack and pinion as placed in the corresponding guides.

To secure the pinion gear a bracket was installed around it. This ensured the rack and the pinion were coupled together to avoid skipping teeth under heavy loading. A detailed view of this mechanism including the pinion bracket is shown in figure 7.38. Finally the X-plate assembly was placed in the guides of the frame as shown in figure 7.39.
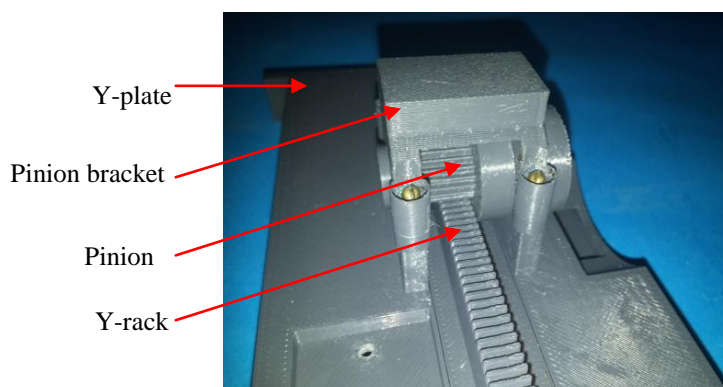
Figure 7.38: Detailed view of the rack and pinion pair secured with the pinion bracket.
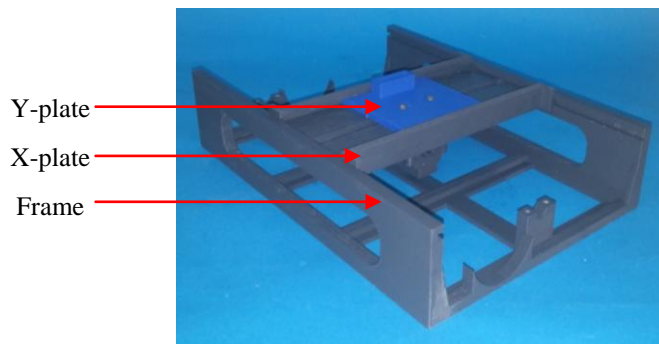
Figure 7.39: X-plate inserted in the X-guides.

To assemble the immersed parts a specific order must be followed because of the limited space of the water container. If the specified assembly sequence was not followed, it was impossible built the robot. The most important step was to correctly orient the parts on to the frame before placing them in the water container. The jack screw was bolted to the bracket in the middle as shown in figure 7.40.
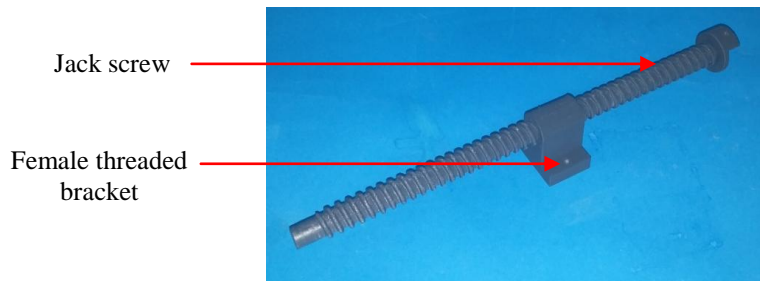
Figure 7.40: Jack screw as bolted to the bracket.

Then the jack screw was placed loose under the X-plate at an angle to provide room for the inner teflon cover of the sealing mechanism of the X-stage. The inner teflon cover of the Y-stage was inserted to the Y-shaft as illustrated in figure 7.41. This step allowed the installation of the inner parts of the sealing mechanism. There was no alternative way to install the inner cover of the sealing mechanism, since the gap was very narrow. At this point the mechanisms were placed in the water container and the sealing mechanisms were placed on the water container sides as shown in figure 7.42.
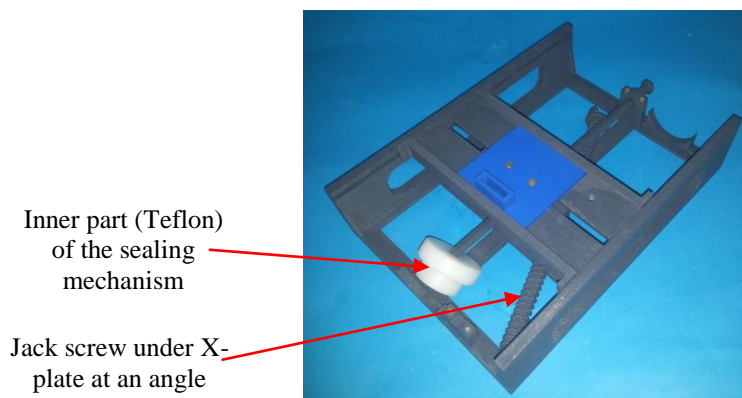
Figure 7.41: Orientation of parts prior the installation to the water container.

84
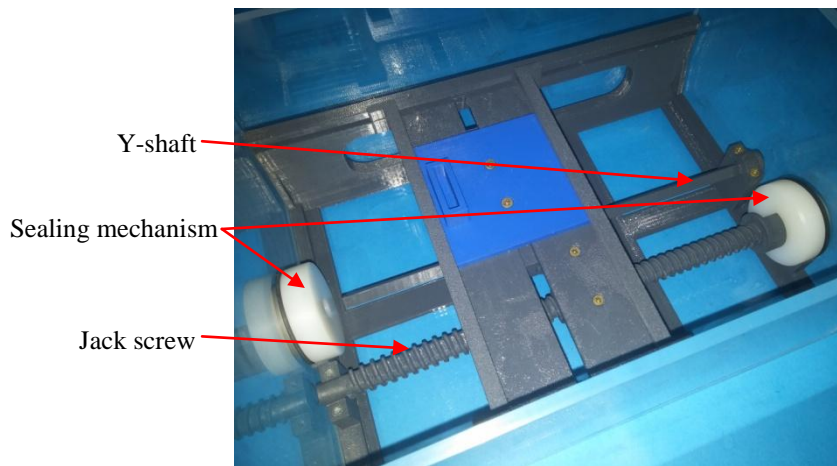
Figure 7.42: Inner side of the water tank with the sealing mechanisms.

The water container was then placed on the base and the encoder/motor assembly for both stages was attached to the base. Additionally the connector holder was attached to the connectors and cables. The connector holders as attached to the base are shown in figure 7.43. At this stage the robot was completed and was fully functional. Figure 7.44 shows the positioning device mechanical parts through the water container. The completed positioning device including the covers is shown in figure 7.45. The top cover can be easily detached to allow access for the transducer.
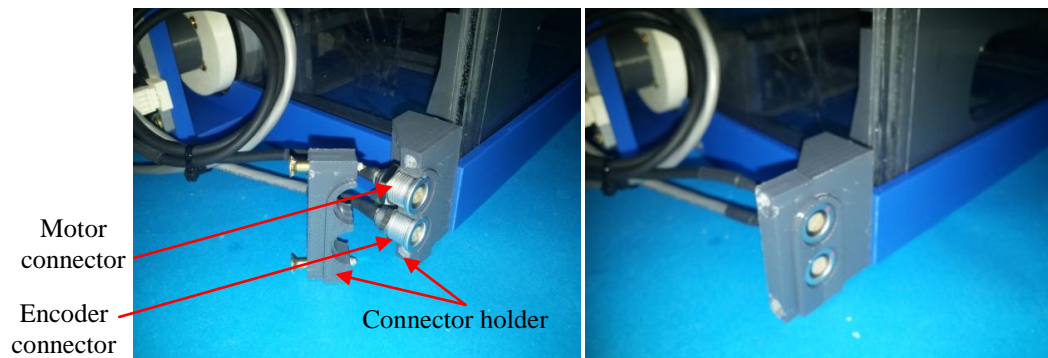
Figure 7.43: Installation of the connector for the motors and encoders.
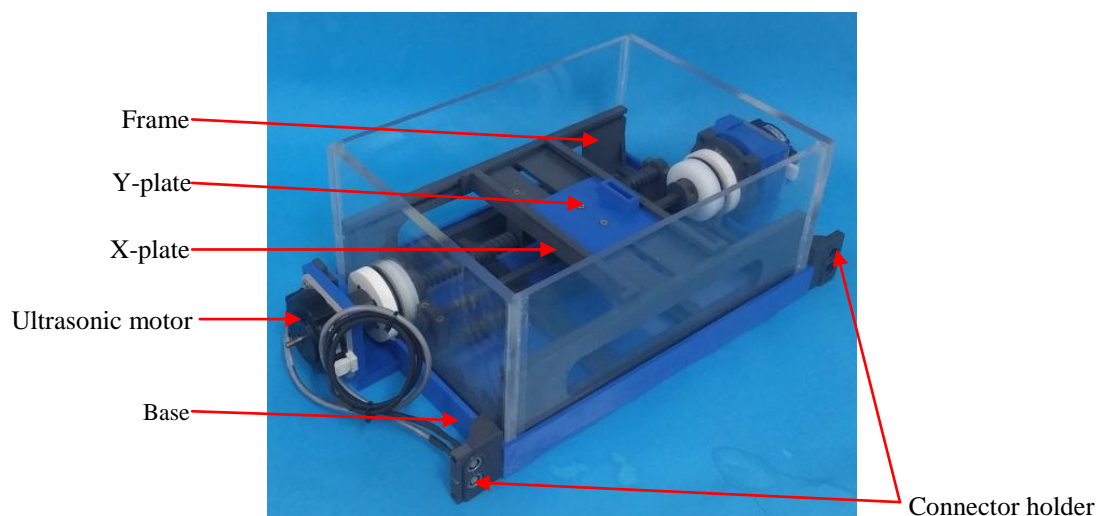
Figure 7.44: The positioning device mechanisms fully assembled.

85

Y-plate

X-plate

Frame

Rear cover

Front cover

Top cover

Base
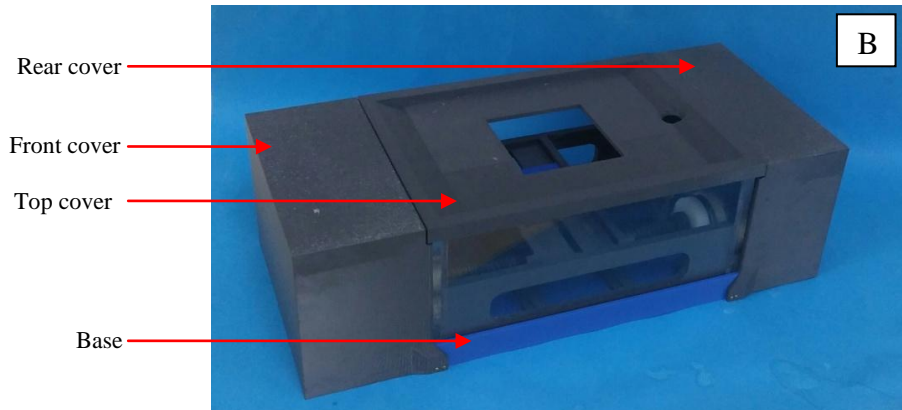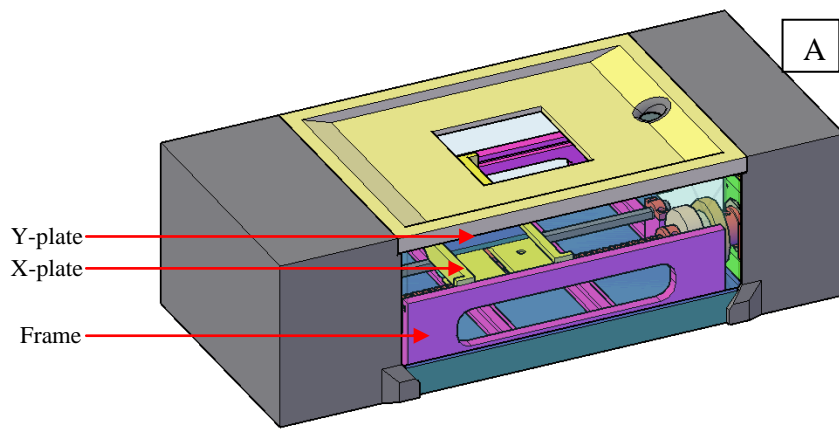
Figure 7.45: A) Submerged robot (Drawing), B) Submerged robot (Photo)

Chapter 8 : Control and Feedback System

8.1 Motion control electronics and motors

To accurate control the motion of the various robots a feedback system was implemented. The motor of each stage was activated through the motor drivers using a Data Acquisition board (DAQ) (USB 6221, NI, Austin, USA). The accuracy of the motion was achieved using optical encoders (US Digital Corporation, Vancouver, WA 98684, USA) that monitor the motion. The encoder readings were sent to a PC through the DAQ board and processed by the software to ensure accurate motion. Manual motion was also available using ON-OFF-ON switches placed on the front panel.

8.1.1 Electronic system (Version 1)

The motion control operation is shown in figure 8.1. The software utilizes the DAQ to control the motion of the device and to receive data from the encoder. The user controls the motion using the software to enter the commands for manual or automated control. The software calculates the number of pulses that are required for the specified distance. Each DAQ (NI) can control up to two stages (only two counters are available). Each counter can detect the pulses for one encoder. To control the third (Z) stage of the positioning device a second DAQ board was used. The interface USB cards can activate and deactivate the motors, and to receive and sent the information from the encoders to the PC.
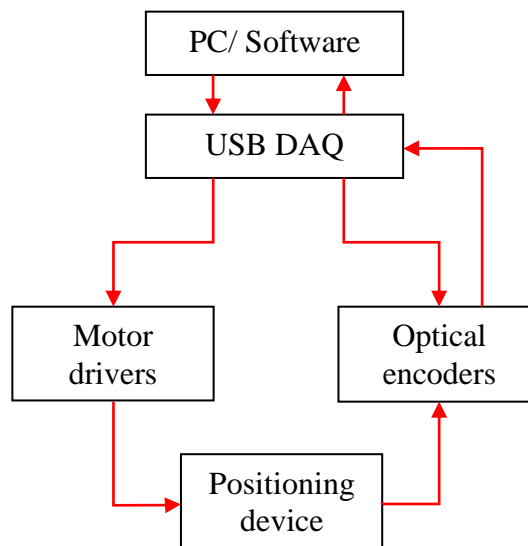
Figure 8.1: Diagram of the positioning device feedback system.

For each robotic system linear optical encoders EM1 (US Digital Corporation) were installed. The EM1 optical encoders work in conjunction with a polymer plastic strip, and it uses LED source and a monolithic detector. The EM1-0-500-I (US Digital Corporation) encoder used can detect 500 lines per inch. Each encoder output was connected to one of the counters of a DAQ USB 6221 (NI). When a stage was in motion the software counted the pulses form the optical encoder to control the motion. When the required number of pulses was counted the motor would stop. The motor driver box and interface DAQ cards are shown in figure 8.2.
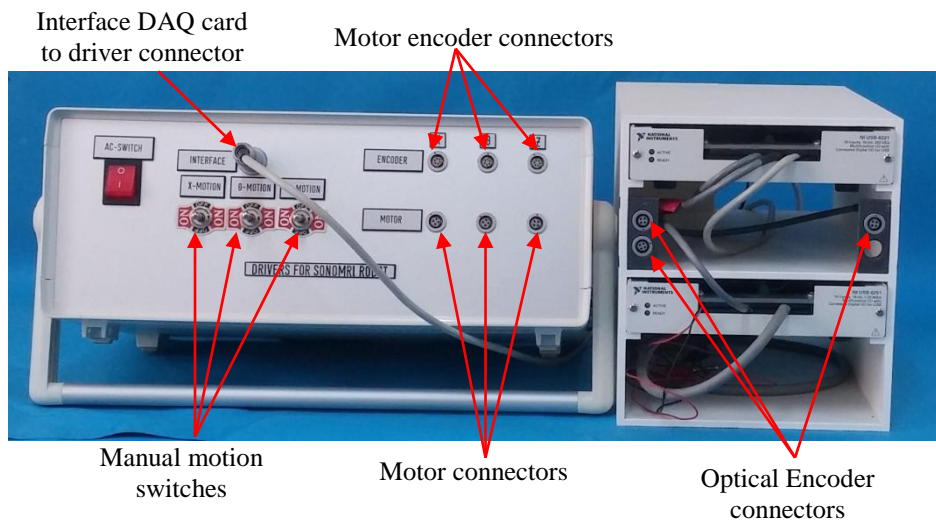
Figure 8.2: The motor drivers box and USB interface acquisition board (version 1).

Connectors were used to connect each driver (D6060, Shinsei Kogyo Corp., Tokyo, Japan) with the corresponding motor. The ultrasonic motors include an internal encoder as shown in figure 8.3 to connect with the motor driver. The motor encoders operated at low speed.
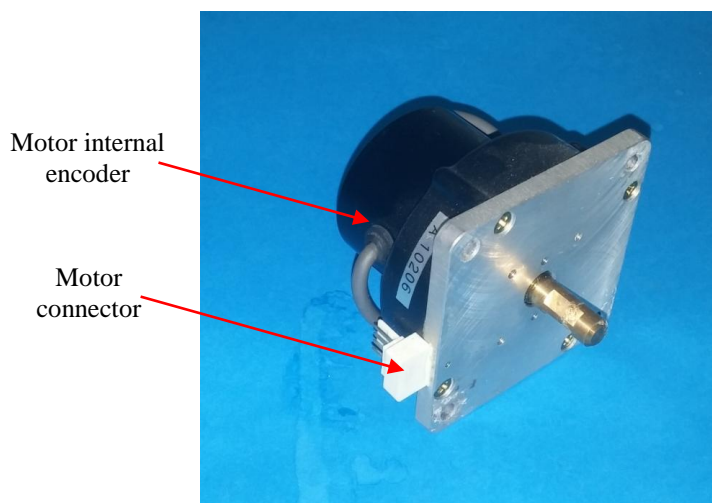
Figure 8.3: Ultrasonic motor (USR60-S3N, Shinsei Kogyo Corp., Tokyo, Japan).

The main parts of the ultrasonic motors are shown in figure 8.4. The base and the stator which produce the motion are fixed together with four brass screws. The stator is made by piezoelectric ceramics and the top of it, is covered with frictional material. The frictional material provide grip between the stator and the rotor to generate torque. The shaft of the motor is integrated to the rotor and it transfers the motion to the robot. The stator and rotor were assembled together using a cover which presses the rotor against the stator. A ball bearing made from non magnetic material is attached in the rear of the cover to reduce the rolling resistance of the rotor for smoother operation.
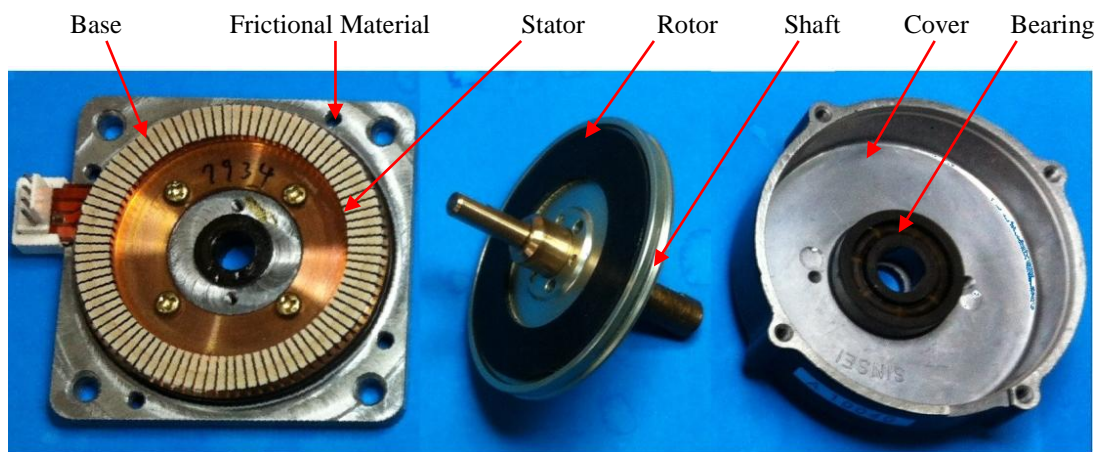
Figure 8.4: Main parts of the ultrasonic motor.

Connectors were used for the connection of the optical encoders with the DAQ board. For each stage a separate cable was used to connect each encoder to a counter on the acquisition board. When a stage was in motion, the optical encoder sent pulses through the acquisition board to the software. The number of pulses that corresponded to a length unit (1 mm) was calculated to establish the positioning accuracy of each stage. When the user enters the step size the distance was converted to pulses. As soon as the software detected the predetermined number of pulses the motor was instructed to stop.

8.1.2 Electronic system (Version 2)

With the evolution of the positioning devices, a theta stage was needed and therefore, a more advanced electronic setup was developed. The electronic system (version 1) setup was able to operate only three stages. In addition the jack screws eliminated the need for the motor internal encoder. Since an extra cable for each axis was no longer needed the electronic system was simplified as shown in figure 8.5. The most important improvement of this version was the inclusion of the USB interface card together with the drivers. This improved the appearance of the electronic system.
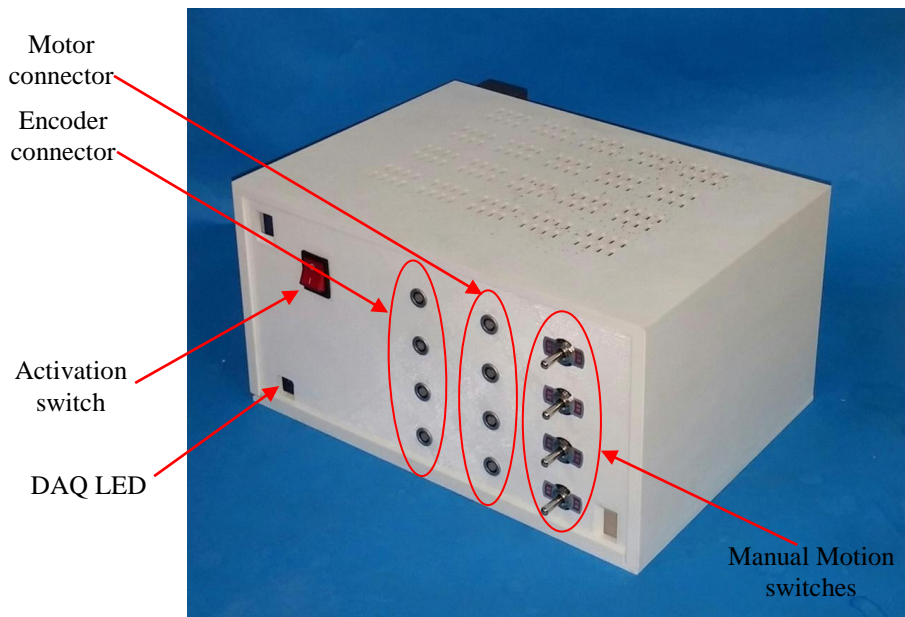
Figure 8.5: Electronic System (Version 2).

The enclosure of the electronic unit was designed using a CAD software and manufactured using a 3D manufacturing machine (FDM-400). The enclosure included the base which is shown in figure 8.6. The enclosure has the capacity for two DAQ boards, four motor drivers and a power supply (AC230V/DC24V). The power supply and the interface card were mounted vertically using specifically designed holders. To reduce the complexity of the system the two data acquisition board USB 6221 (NI, Austin, USA) were replaced with one data acquisition board USB 6351 (NI, Austin, USA) which has four counters instead of two. Since the 6351 DAQ board has four counters it can operate four encoders thus controlling up to four stages.
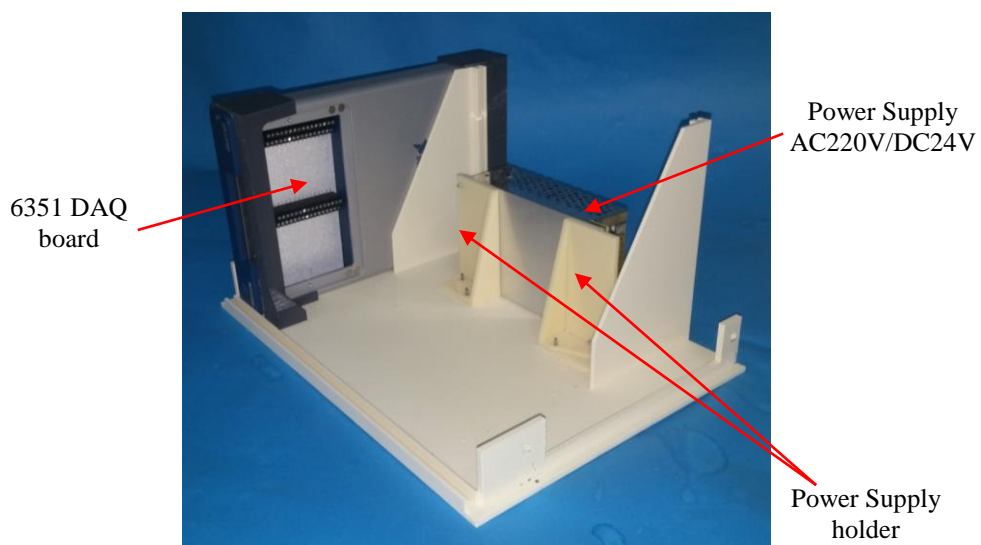
Figure 8.6: Interface card and power supply on the base of the electronic unit.

Figure 8.7 shows the motor drivers installed on the holder prior to their installation to the base. Attaching all the components onto the base using detachable holders made the wiring easier. The connector wires were connected to the terminals of the data acquisition board before installing the motors drivers as shown in figure 8.8. The AC plug was mounted at the back of the enclosure on the rear panel and connected to the power supply. The connections inside the electronic unit were completed with the installation of the motors drivers and activation switches. The interior of the electronic unit is shown in figure 8.9.
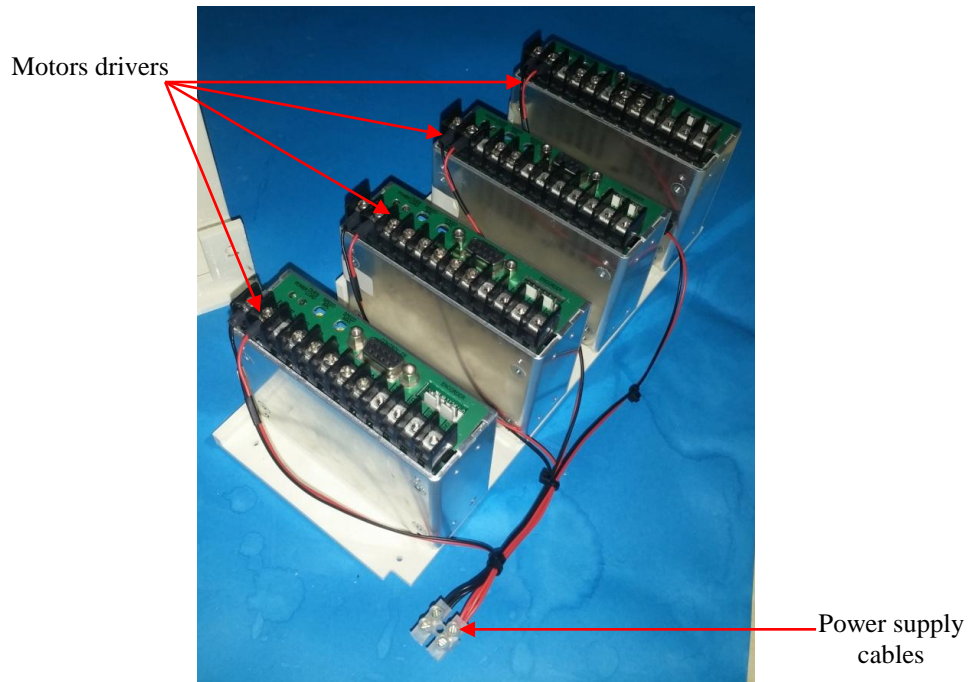
Figure 8.7: Motor drivers installation and wiring for the 24 VDC power supply.
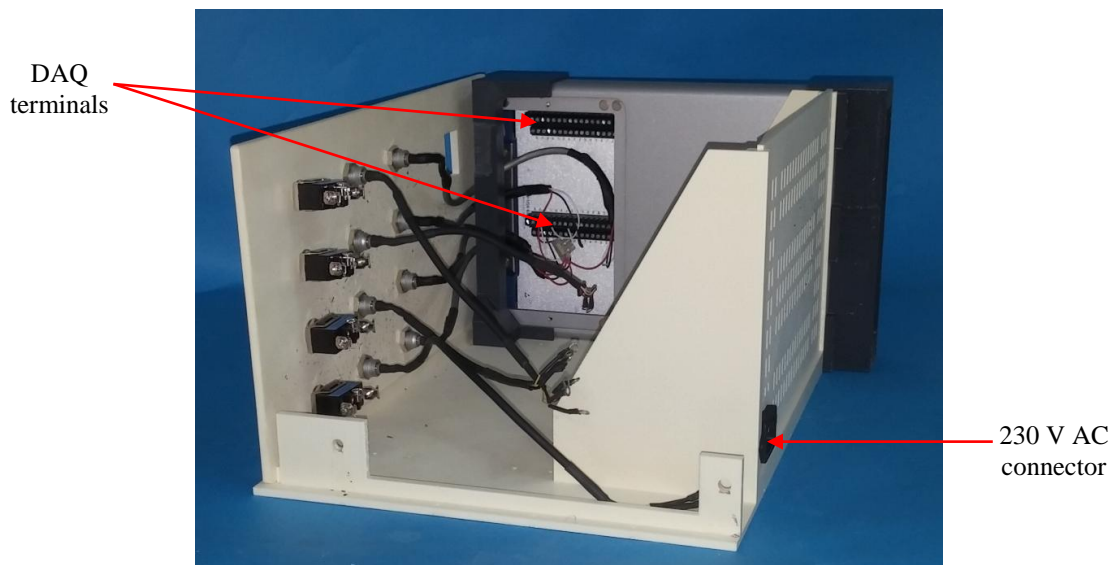
Figure 8.8: The switches, motor connectors and encoder connectors as installed. Encoder connectors were connected on the data acquisition board.
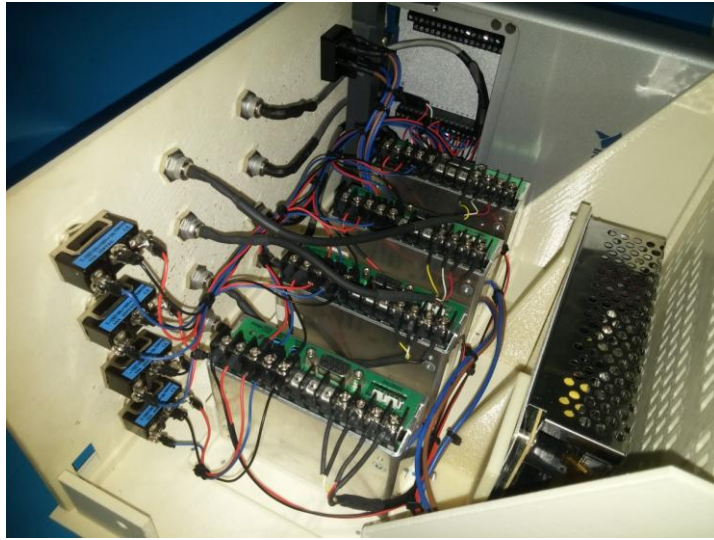
Figure 8.9: Wiring system inside the electronic system enclosure.

Figure 8.10 shows the rear view of the electronic enclosure. The top and the rear cover of the enclosure enabled air ventilation for the drivers and the power supply. The temperature is transferred through the air away from the inside of the enclosure, keeping the electronic components to their optimal operating temperatures, thus extending lifetime and ensuring the reliability of the system. The gray part on the rear right side of the enclosure is the rear DAQ board holder which was secured on the enclosure. Through the holder opening, the activation switch was accessible. On the top the power supply port and the USB port are visible. On the left side of the rear panel, the AC230V plug was attached. The gap on the rear left side is an additional holder to mount a second DAQ board.
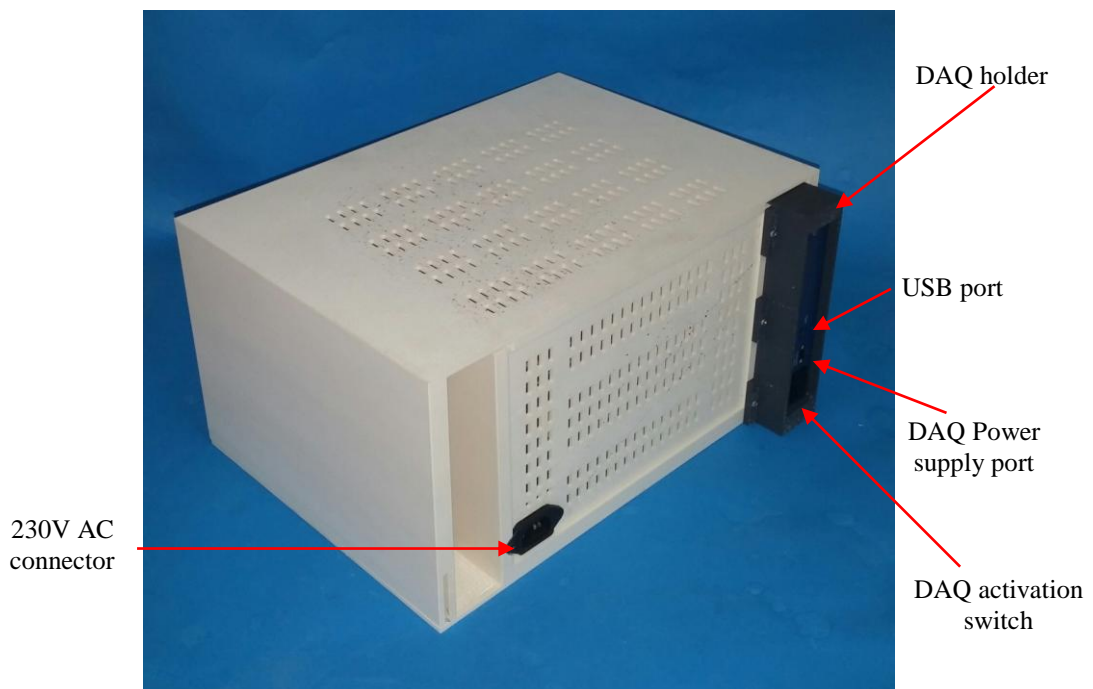
Figure 8.10: Rear View of the Electronic System (Version 2).
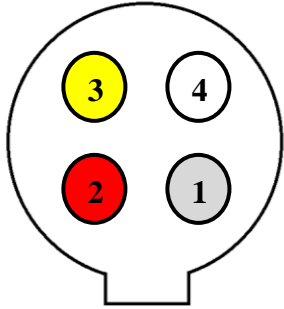
8.2 Electronic driver/interface unit wiring

8.2.1 Color coding for connectors

Table 8.1 shows the labeling for the connectors (IP50/IP68, Fischer, Saint-Prex, Switzerland) of the motor wires that connects to the drivers. A diagram of the connector terminals is shown in table 8.1. The number inside the circle corresponds to a terminal number of the connector. The color of the circle corresponds to the wire insulation color.

Table 8.1: Connector terminals for motor.

Color coding for the motor cable		
No.	**Color**	
1	Unshielded-(Black)	
2	Red	
3	Yellow	
4	White	

The connections of the encoder are listed in table 8.2. Each terminal number was connected to a wire of a specific color. The encoder wire (gray) was used to connect each of the optical encoder modules with the terminal on the DAQ board. On the left column the connector terminal number is listed. On the right the color that corresponds to the wire color is listed. Also in the table there is a diagram of the terminals represented by circles with numbers and filled with the color of the wire.

Table 8.2: Connector terminals for encoder.

Color coding the encoder cable		
No.	**Color**	
1	Red	
2	Black	
3	White	
4	Brown	
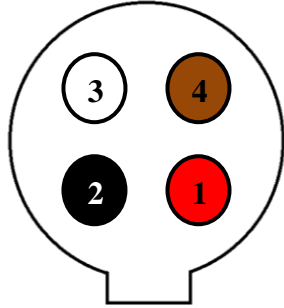
Table 8.3 shows the connections of the motor and encoder cabling to the digital input of the DAQ board. The column on the right of the terminal corresponds to the type of connection used. The cell is filled with the color of the wire that connected each port with a motor terminal or an optical encoder channel.

Table 8.3: NI card pin terminals.

DIGITAL INPUT	
TERMINAL	**CONNECTION**
65	X - MOTOR CW
66	X - MOTOR CCW
67	Y - MOTOR CW
68	Y - MOTOR CCW
69	Z - MOTOR CW
70	Z - MOTOR CCW
71	Θ - MOTOR CW
72	Θ - MOTOR CCW
73	Z - STAGE ENC. CH.A
76	Y - STAGE ENC. CH.A
78	Θ - STAGE ENC. CH.A
81	X - STAGE ENC. CH.A
82	D-GND
84	D-GND
86	D-GND
88	D-GND
90	D-GND
92	D-GND
94	D-GND
96	+5V

Figure 8.11 shows a detailed diagram of the motor, drivers, DAQ board and switches. The green tables represent the motor drivers and at the middle column the name of the terminal port is listed. The color of the lines from the drivers for each component is matched with the color of the wire used. The number indicating the DAQ board terminals in the cells below have the same color with the wire used. All the connections of the electronic unit (Version 2) are listed in detail in table 8.1 to table 8.3 and in figure 8.11.
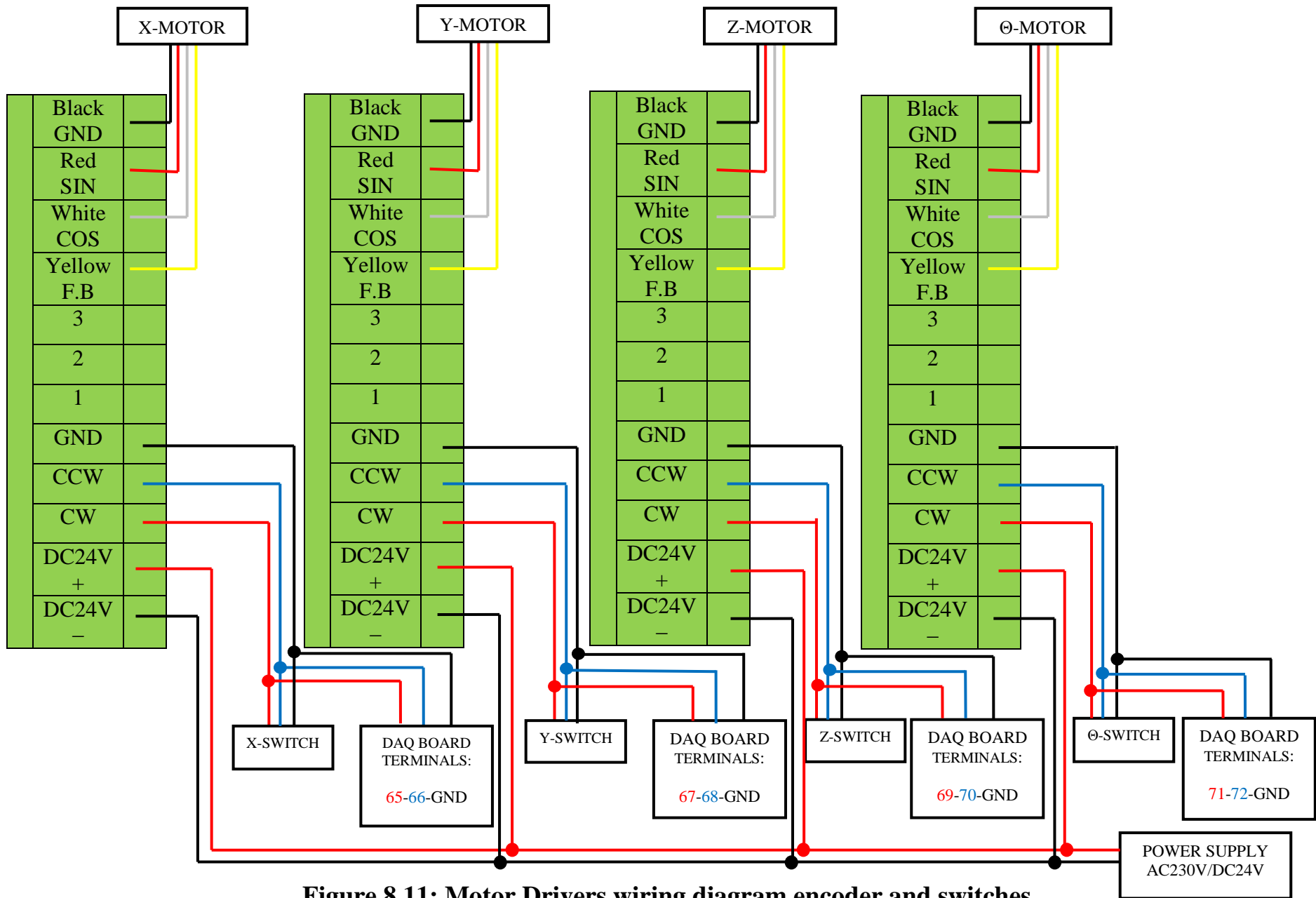
Figure 8.11: Motor Drivers wiring diagram encoder and switches.

8.3 Software

A user-friendly program written in C # (Visual Studio 2010 Express, Microsoft Corporation, USA) was developed in order to control the robotic system. The software has the following functionalities: a) Communication with MRI. b) motion control of the stages, c) history (functions activated), d) patient information, e) transducer coordinates, f) images of an MR compatible camera (MRC Systems GmbH, Heidelberg, Germany), g) Control of signal generator (voltage, time ON, frequency), and h) MR thermometry.

The software controls the positioning device through a DAQ (data acquisition) board. DAQ board enables communication between the positioning device and the software. The software controls two DAQ card models, the USB 6221 (NI, Austin, Texas, USA) which was used for the first electronic system (Version 1), and also the USB 6351 (NI, Austin, Texas, USA) which was used for the electronic system version 2.

To control the positioning device, a two way communication was required between the DAQ/PC and the robot. When the user commands the robot to move, the software sends the information to the motor drivers through the DAQ. To establish the desired motion accurately, the encoder readings are sent to the computer through the DAQ. To calculate the distance of the motion, the software converts it to encoder pulses. The user inserts the desired step size in mm.

The number of pulses which corresponds to a distance was calculated based on the resolution of the encoder. For linear stages, the resolution is 500 lines per inch and for the angular stage is 2500 lines per one rotation (360 ̊). These figures are different for the theta stage of the robot (V3) and for the linear stage of the immersed robot. For the angular stage transmitting the motion to a 90 ̊ angle to the worm gear and pinion pair reduced the motion ratio of the arm in relation to the motor, hence the motor had to rotate more. For the case of the linear stage of the immersed robot the calculation of the linear motion was done by estimating the motor angular motion. The angle was converted to distance using the jack screw lead size (360 ̊ of the motor for 6 mm).

The user friendly interface enabled the user to control the positioning device. figure 8.12 shows the menu for the motion control of the robot and ultrasound. At the left column, buttons were used for precise motion control step of each stage. The distance units are in mm, for the linear stage. For the angular stage the smallest angle possible

is 1 degree. The user can specify the distance by inserting the step size in the corresponding text box, or by right clicking on the arrows below the text box to increase or decrease the value by 1 unit at a time as shown in figure 8.13. Each stage includes two functions for each direction i.e. forward and reverse for X, up or down for Z and left or right for Y.
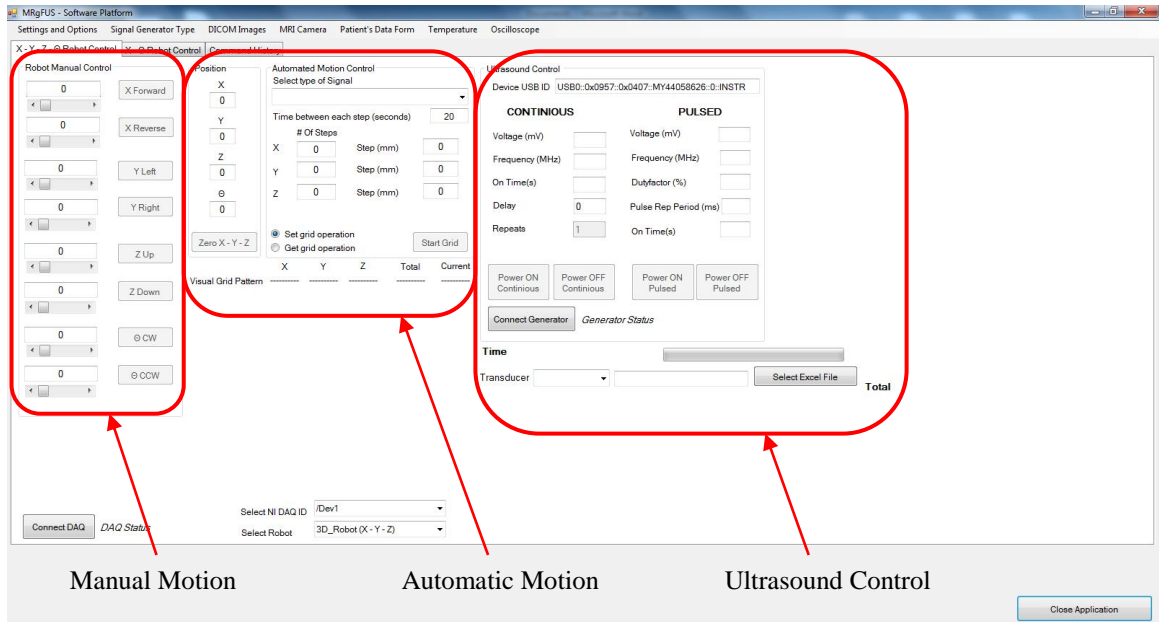
Figure 8.12: Motion and ultrasound control software interface.
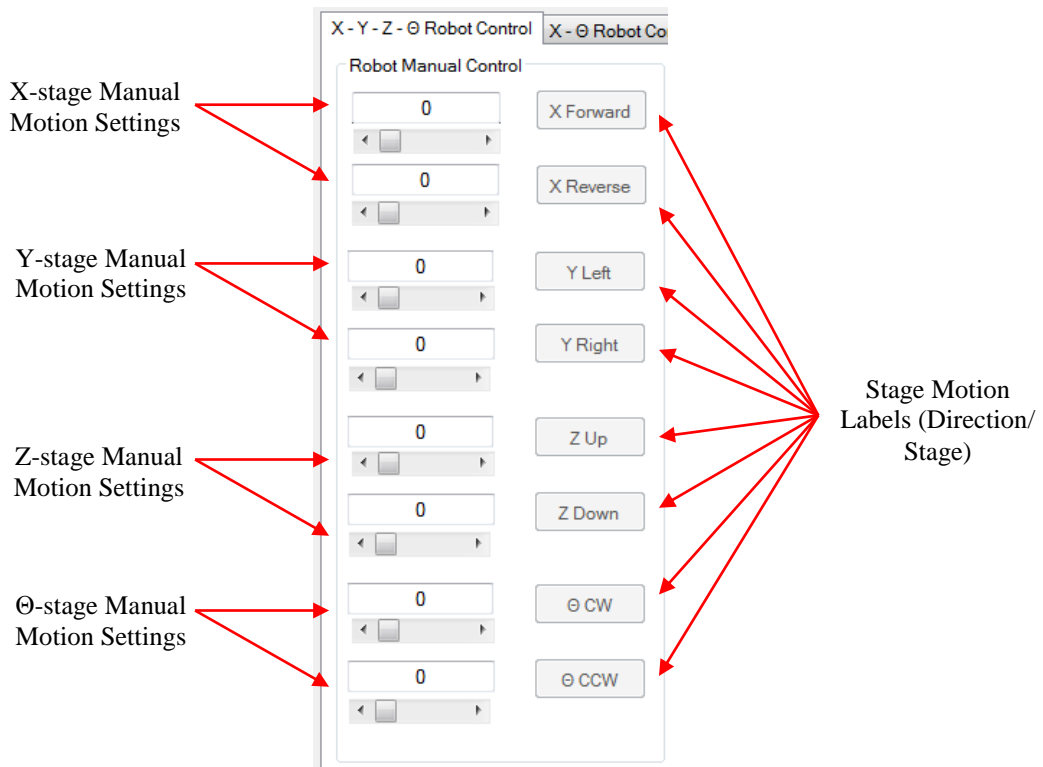
Figure 8.13: Manual motion submenu for the 4-axis of the robot (V3).

97

There is an option for choosing the robot type since there are differences in the number of stages and motion calculation. When the robot is chosen the motion submenu will enable the corresponding control buttons (i.e. 4-axis for robot V3 or 2-axis for immersed robot). To select the options for a specific robot there is an option below the motion submenu as shown in figure 8.14. There is also selection to choose the DAQ board which is connected with the desired robotic system.
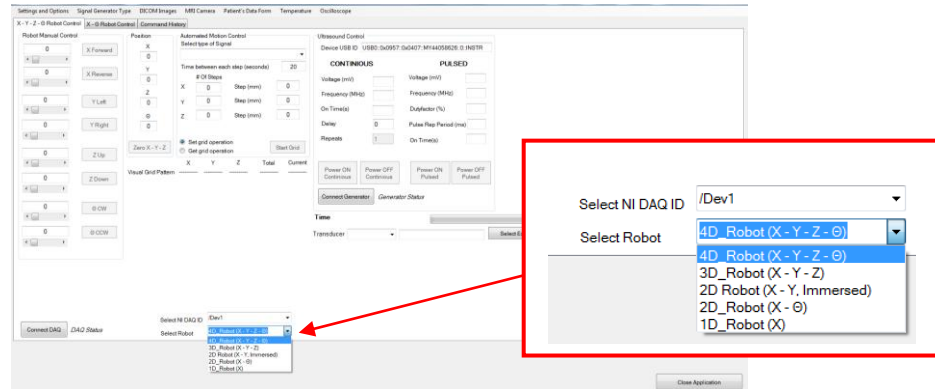
Figure 8.14: Robotic system USB DAQ board selection.

It is possible to create multiple lesions using the automatic 3 dimensional grid motion. To setup this function the size and number of steps for each dimension must be selected, and then the ultrasound parameters are selected. This submenu is shown in figure 8.15. The function "Automated Motion Control" requires to insert all the parameters to activate. By clicking the "Zero X-Y-Z" button in the "Position" submenu the current position is initialized to zero. After the coordinates are initialized, each time the motor moves, the coordinates are updated. Furthermore, to set the "Automated Motion Control" function the type of signal must be chosen. The device can deliver continuous (thermal) or pulsed (mechanical) ultrasound. To cover a large region the number of steps for X, Y and Z axis must be selected. In addition the size of the step is selected. Also to avoid the near field heating "Time between each sonication" must be selected.
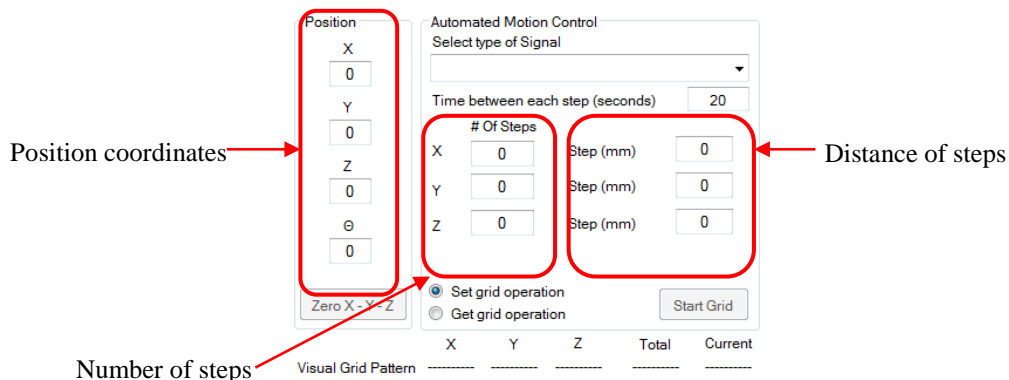
Figure 8.15: Automated Motion Control Submenu.

98

When the grid function is activated a table displays the progression of the grid. The table has blank cells colored in blue during the process to indicate that no sonication occurred. The cell of an unaffected region will remain blue even when the ultrasound is activated. After the sonication ends, the cell changes to red color to indicate the ablation of the location was completed. The size of table depends on the user inputs of the X and Y total distance. The software creates a table with dimensions of X-steps x Y-steps. The user defines also the steps in the Z-axis. Figure 8.16 shows the function of the automated motion during activation. The progression table and step information is shown in the automated motion control submenu. The number of cells covered for each axis, the total number of steps and the current steps are displayed. For safety and better control of the procedure, there is a small window on the top left corner which pops up when the grid is activated. This allows the user to cancel or to pause the process. A simulation of the grid can be performed by using the "No Power" selection from the "Select type of Signal" field. With these settings the positioning device will move without activating ultrasound to display the grid motion for visual confirmation.

To select the ultrasound parameters there are two columns in "Ultrasound Control" field. On the left column fields the parameters for continuous (thermal) ultrasound can be entered. On the right column fields is the control for pulsed (mechanical) ultrasound. The "Ultrasound Control" fields are different depending on the amplifier. The RF generator for continues or pulsed ultrasound can be chosen at the "Select Generator Type" on the menu bar as shown in figure 8.17.
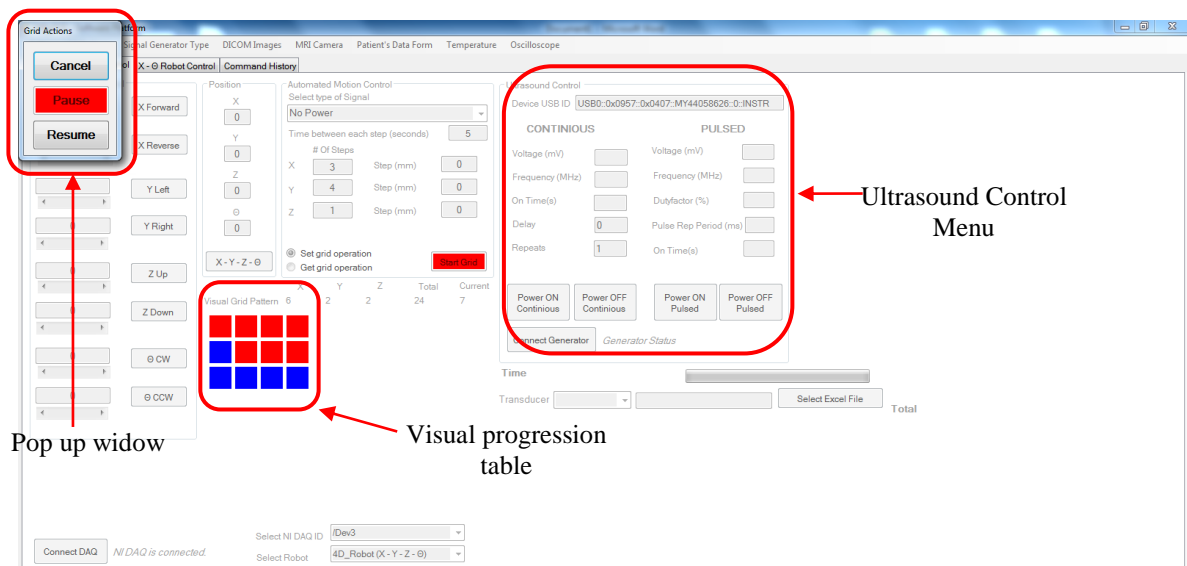
Figure 8.16: Automated grid motion activated.
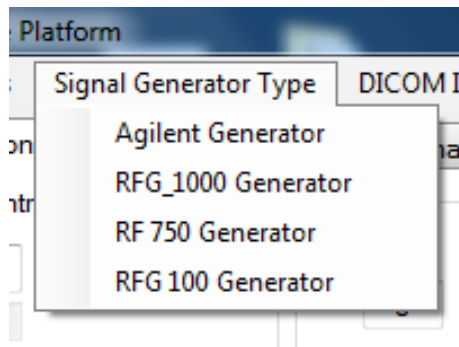
Figure 8.17: RF and signal generator options.

If "RFG_1000/750/100 Generator" option is chosen the corresponding menu for the RF generator (JJ&A Instruments, Seattle, WA, USA) will appear as show in figure 8.18A. With an RF generator in use the ultrasound power can be set by typing the power in W at the "Power" field. If the signal generator (HP 33120A, Agilent technologies, Englewood, CO, USA) is used the menu will appear as shown in figure 8.18B. The ultrasound exposure is adjusted by indicating the voltage in mV.
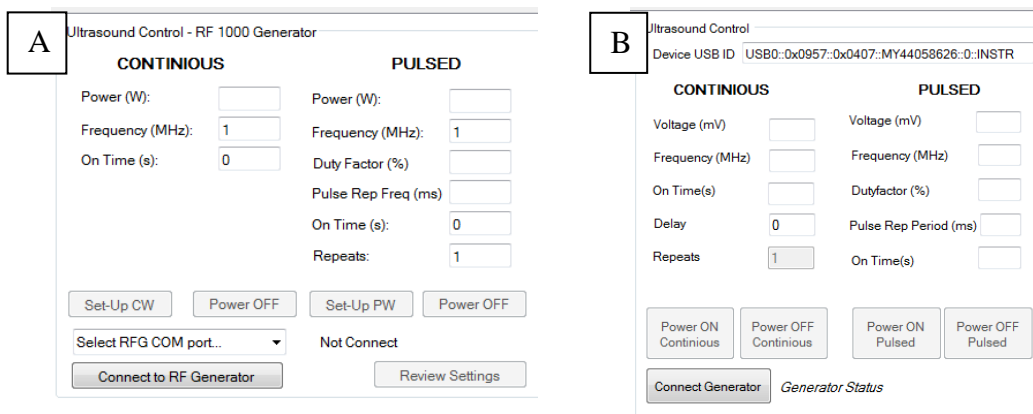
Figure 8.18: Ultrasound Control submenu for JJA RF generator (A) and Agilent generator (B).

With the options available for the ultrasound parameters the system offers precise control of the ultrasound either for continuous or pulsed. For pulsed ultrasound any protocol can be implemented by selecting "Duty factor", "Pulse Repetition Period" and "On time".

Duty factor (DF) is the percentage of the pulse duration in which the ultrasound is activated. To calculate this value the time duration of the pulse when is activated is divided by the total length of the pulse.

Pulse repetition period (PRP) is the overall time duration of the ultrasonic pulse measured in milliseconds (ms). The multiplication result of the DF with the PRP gives the activation duration within a period. With the appropriate selection of the DF and

PRP values, the precise control of the ultrasound properties is possible. By adjusting the pulsed ultrasound variables, it is possible to use mechanical effects.

In the "On time" field the time duration is entered (in s) in which the pulsed ultrasound will be activated. During the activation of pulsed ultrasound, the pulse is repeated for the entire duration as selected by the user.

Chapter 9 Evaluation of robotic system

To evaluate the positioning devices, a series of experiments were conducted. The experiments were performed in order to test the motion capabilities, positioning accuracy and functionality of the robot. The robotic systems were tested in MR environment to ensure the safety and reliability of the device.

9.1 MR compatibility

To test the MR compatibility of the positioning device, robot (Version 1) was placed in a 1.5 T MRI scanner (General Electric, USA). A polyaclylamide gel (ONDA Corporation, Sunnyvale CA, USA) was used to evaluate the FUS protocols. The setup of this experiment is shown in figure 9.1. The positioning device was placed on the MRI table. The ONDA gel was placed on the positioning device and the transducer was adjusted to target the center of the gel.
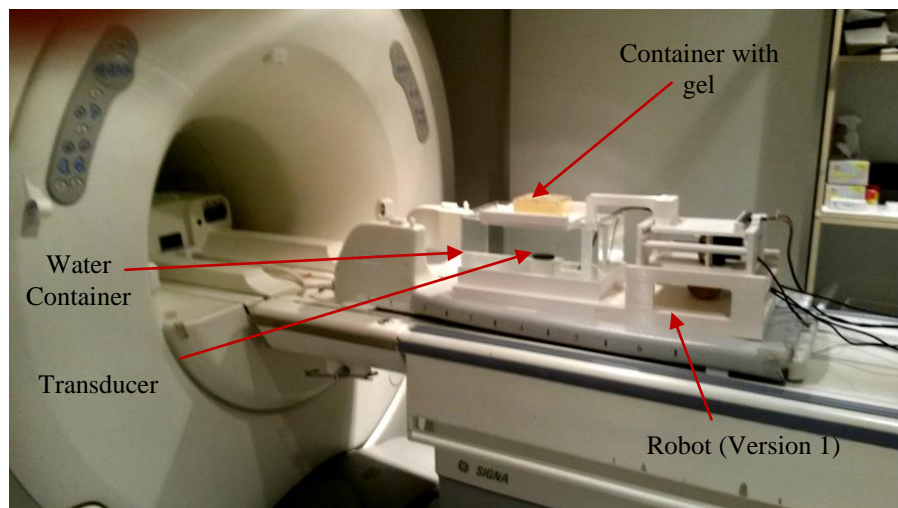
Figure 9.1: Photo of the robot (version 1) placed on the MRI table.

The MR image which was acquired using the lumbar coil (USA instruments, Cleveland, OH, USA) is shown in figure 9.2. The image acquired using T2-wheighted fast spin echo pulse sequence (FSE). The parameters for imaging was: repetition time (TR)=2500 ms, echo time (TE)=60 ms, field of view (FOV)=16 cm, matrix=256x256, number of excitations (NEX)=3, echo train length (ETL). The MRI image was affected by the HIFU transducer as a result of a small quantity of magnetic material that was used as dumping. For this reason the area near the surface of the transducer appeared dark. Despite this, the image at the gel was not significantly affected since it was quite far from the transducer.
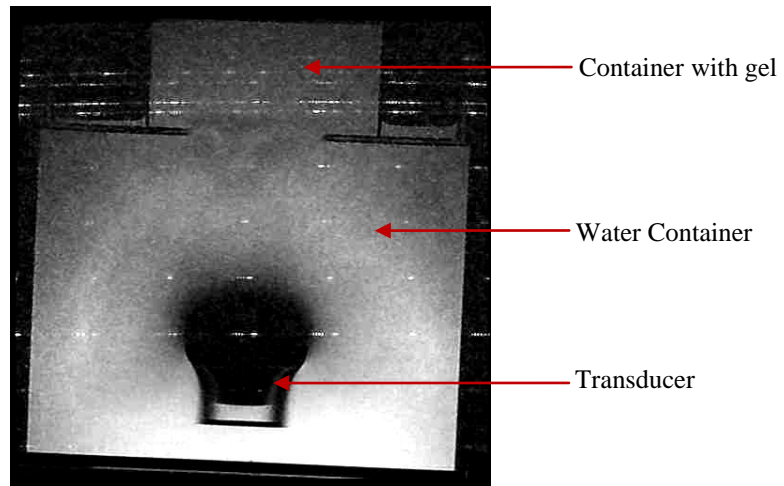
Figure 9.2: MR image of the water container and transducer (T2-W FSE: TR=2500 ms, TE=60 ms, Slice thickness=3 mm, Matrix=256 x 256, FOV=16 cm, NEX=3, ETL= 8).

9.1.1MR compatibility test

The robotic HIFU system was tested in a 1.5 T MR system (Signa, General Electric, Fairfield, CT, USA) using a GPFLEX coil (USA instruments, Cleveland, OH, USA). In order to test the MRI compatibility of the positioning device an agar/silica/milk phantom was used. The signal to noise ratio (SNR) was measured under various conditions (electronic system presence or activation, and transducer presence or activation) using T1-weighted spoiled gradient (SPGR) with the following parameters: TR=38.5 ms, TE=20 ms, FOV=21 cm, matrix=128x128, flip angle=20°, NEX=1. The same pulse sequence was used for MR thermometry. The conditions in which the SNR was measured are illustrated in table 9.1.
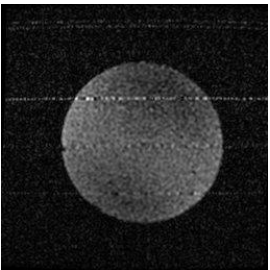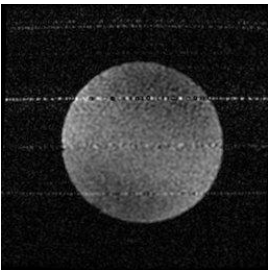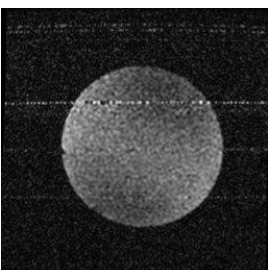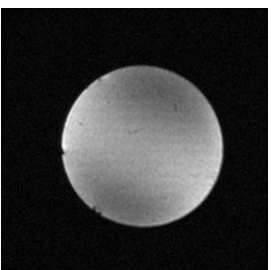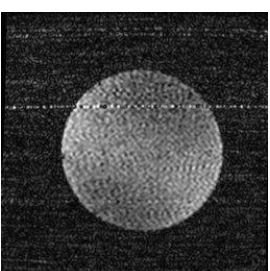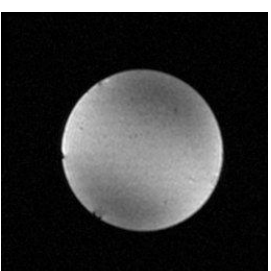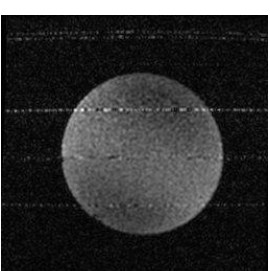
This test demonstrated how the MR images are affected by each component of the device. The results of this test indicated that the motors reduced significantly the SNR when they were activated. For this reason the robot is categorized as an MR conditional device. Although the motors affected the image when activated this does not compromise the process. The sonications were executed when the motor was idle.

9.2 Creation of lesions in a gel phantom

To test the motion accuracy of the robot, lesions were produced in the ONDA gel. When sufficient thermal dose capable to produce lesions was delivered in the gel, the exposed region became white. In addition the transparency of the gel allows visual contact of the target. Therefore, it was possible to locate the focus of the transducer and observe the progression of the lesion. Additionally useful information regarding the shape and size of the lesion were obtained.

Table 9.1. MR compatibility test for different conditions.

Conditions	MR Image	SNR	Conditions	MR Image	SNR
DC encoder (ON) amplifier (ON) transducer (OFF)		10,50	DC encoder (OFF) amplifier (OFF) transducer (OFF)		16,9
DC encoder (ON) amplifier (ON) transducer (ON)		10,51	DC encoder (OFF) amplifier (OFF) transducer removed from MRI		55,9
DC encoder (ON) amplifier (ON) transducer (OFF) motor (ON)		2,11	Robot and transducer removed		54,3
DC encoder (OFF) amplifier (ON) transducer (OFF)		17,7			

The purpose of this experiment was to calculate the optimal parameters in order to induce consistent lesions in the gel. A sonication with a transducer operating at 2 MHz for 8 s induced lesions. The size of the lesion was 2 mm in diameter. Hence to ablate larger regions it was necessary to maneuver the transducer with the positioning device, using 1 mm steps. The water container was filled with degassed water and the ONDA gel was placed above the water as shown in figure 9.3.
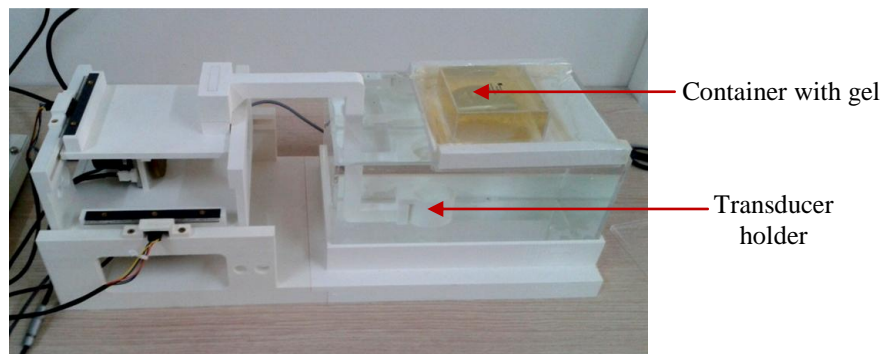
Figure 9.3: Photo of the robot V1 with the ONDA gel placed on the cover above the water tank. The transducer delivers the ultrasound using a bottom to top approach.

A 51 W (acoustical power) was produced using a signal generator (Agilent 33220A) and an amplifier. The intensity of ultrasound was sufficient to generate thermal lesions. By instructing the robot to create a grid of 3 x 5 steps (step size of 1 mm), it was possible to create a lesion of approximately 5 mm x 10 mm. After each step a 30 second delay was applied to avoid the near field heating effect. Near field heating effect could cause higher temperatures than expected, due to the accumulation of heat from the previous location. This may result to higher temperature at the sonicated area which could induce larger lesions. For this test the 30 s delay was proved sufficient to create consistent lesions as shown in figure 9.4.
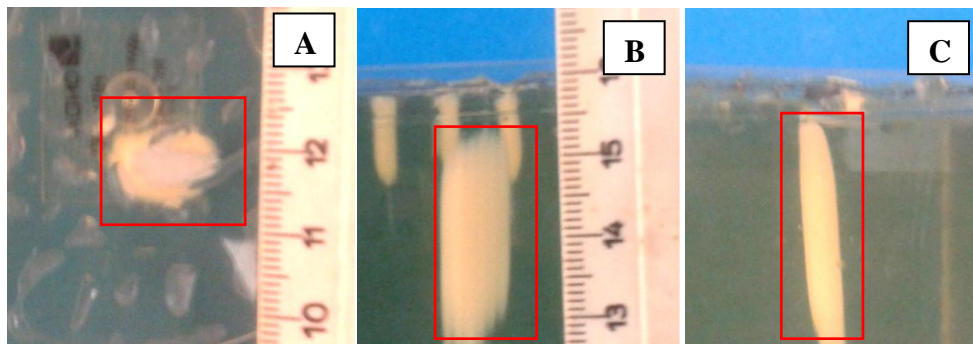
Figure 9.4: A) top view of the lesions, B) front view, C) side view of the lesions (f=2 MHz, d=5 cm, R=10 cm, Acoustic Power=51 W, duration=8 s, focal depth=2 cm).

In order to examine the repeatability and consistency of the positioning device a similar experiment was followed. The robot was instructed to create a grid of 8 x 8 lesions using the same HIFU parameters. With this protocol an area of approximately 17 mm x 15 mm was ablated. The length of the lesion was approximately 25 mm. The results demonstrated the ability of the robot to treat accurately and consistently large volumes with overlapping lesions. Figure 9.5A shows the width of the lesion on the X-

axis and figure 9.5B show the width of the lesion on Y-axis. Figure 9.6A shows the front view of the lesion and figure 9.6B shows the side view of the lesion.
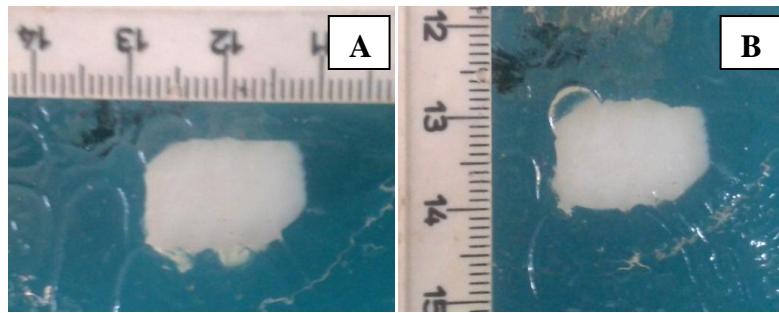
Figure 9.5: A) Width of the lesion on X-axis, B) Width of the lesion on Y-axis (f=2 MHz, d=5 cm, R=10 cm, Acoustical Power=51 W, duration=8 s, focal depth=2 cm).
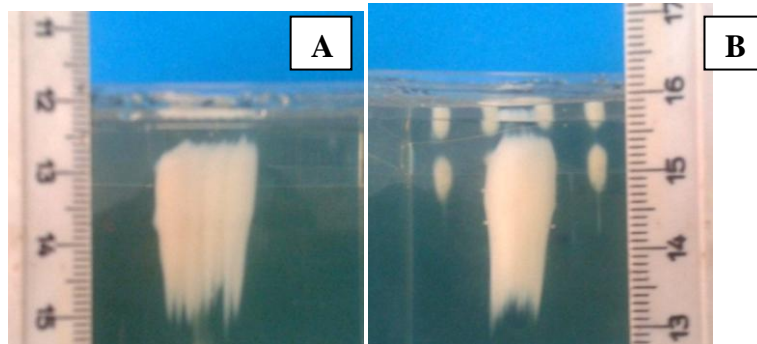
Figure 9.6: A) Front view of the lesion, B) Side view of the lesion (f= 2 MHz, d= 5 cm, R=10 cm, Acoustical power= 51 W, duration= 8 s, focal depth= 2 cm).

9.3 Evaluation of creating lesions in excised tissue

In order to evaluate the protocol with a more realistic model, excised rabbit muscle was used. A large region was ablated with overlapping lesions of approximately 2 mm in diameter. Each lesion was created with 1 mm step. The positioning device moved 10 steps of 1 mm on the X-direction and 10 steps of 1 mm with the Y-direction. With this technique a lesion of 22 x 14 mm was created. This experiment verified that the HIFU protocol was efficient in creating lesions in freshly excised tissue.

The robot was modified with the introduction of an extended table to support a small animal (dead in the experiment) on the positioning device. Figure 9.7 shows the setup used for this experiment to support the dead rabbit. Figure 9.8 shows a better view of the rabbit tissue demonstrate the coupling with the water.

The ablated region on the rabbit muscle is shown in figure 9.9. The size of the lesion is approximately the same with that created in the ONDA gel. Figure 9.10 shows a single lesion created to the rabbit liver demonstrating the depth of the lesion.
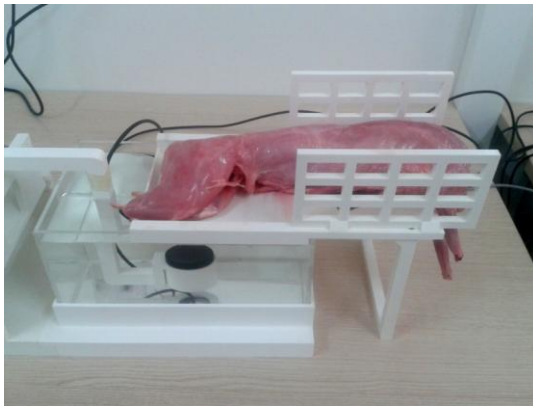
Figure 9.7: Photo of the extended table for small animals.
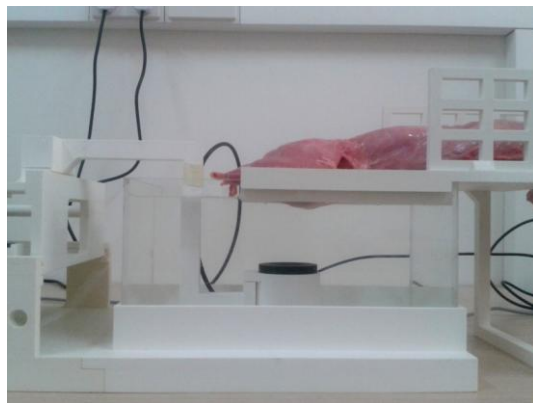
Figure 9.8: Side view of the table supporting a dead rabbit.
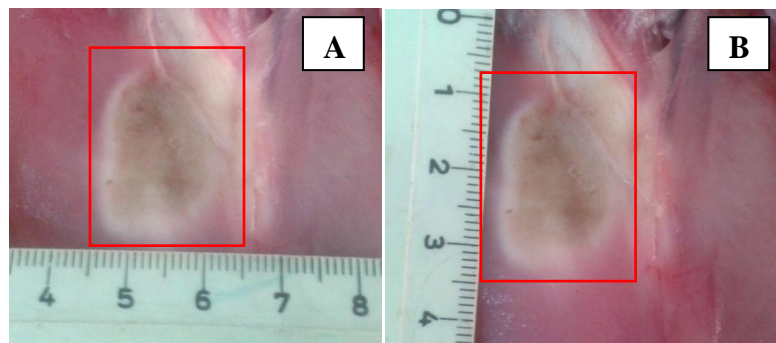
Figure 9.9: Dimension of the large lesion induced in the Rabbit muscle using a grid of 10 x 10 steps of 1 mm, 51 W of acoustic power, f=2 MHz, d=5 cm, R=10 cm, duration=8 s, Focal depth=0.5 cm.
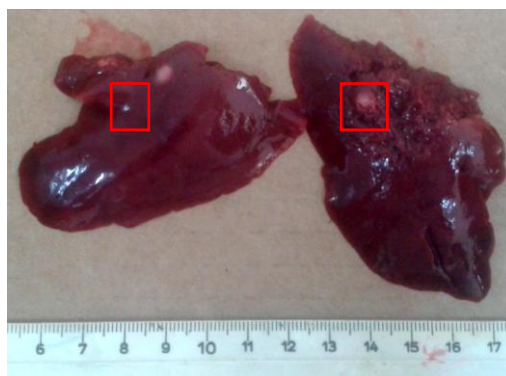
Figure 9.10: Single lesion in the liver of the rabbit using 51 W of acoustic power, f=2 MHz, d=5 cm, R=10 cm, duration=8 s, focal depth=0.5 cm.

9.4 Evaluation of the Z-axis using porcine muscle

The purpose for this experiment was to evaluate some improvements made to the positioning device. Z-axis was introduced in order to provide the ability to ablate at different depths. Also a revised pinion and rack system was installed on the positioning device. This system reduced the motion ratio between the plate and the pinion, thus reducing the speed of the stages. This improved the positioning accuracy and reliability of the system. The robot improvements are shown in figure 9.11. Like the previous tests the same protocol (51 W of acoustic power, f=2 MHz, d=5 cm, R=10 cm, duration=8 s, focal depth= 1 cm) was applied to create lesions in porcine muscle. Figure 9.12 shows the setup for this experiment. In order to prevent the reflection of ultrasound due to the air, an absorber was placed above the tissue.
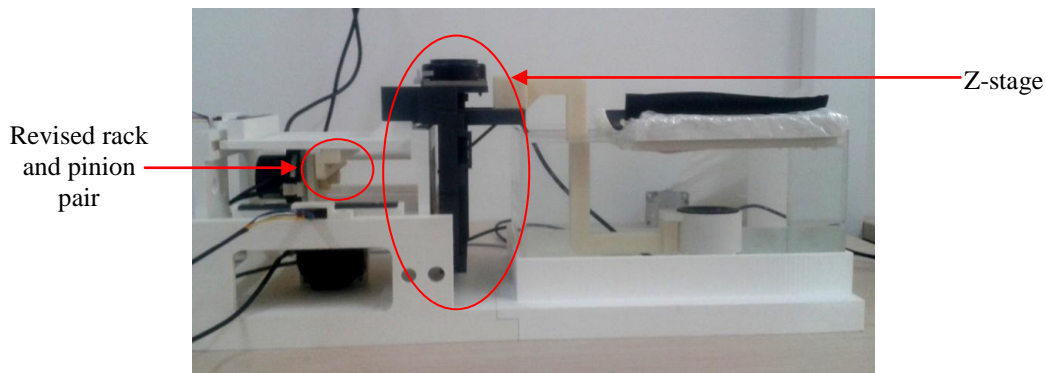
Figure 9.11: Photo of the Z-stage and revised pinion-rack pair installed on the robot.
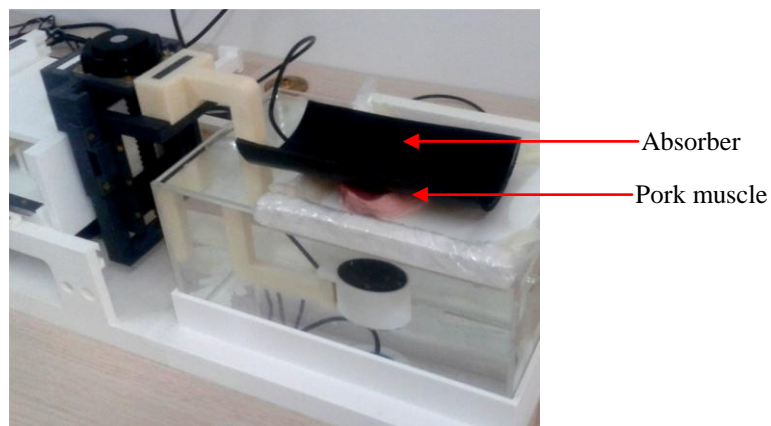
Figure 9.12: Photo of the experiment setup for the porcine tissue and the absorber (51 W of acoustic power, f=2 MHz, d=5 cm, R=10 cm, duration=8 s, focal depth=1 cm).

A slice of porcine muscle was ablated in order to test the positioning device accuracy and the ability to ablate larger areas with overlapping lesions. The result of the sonications is shown in figure 9.13. The lesion was created by moving the transducer on a grid of 5 x 5 steps. The step size was 2 mm for both, the X-stage and Y-stage. The size of the ablated region was approximately 14 mm x 14 mm.
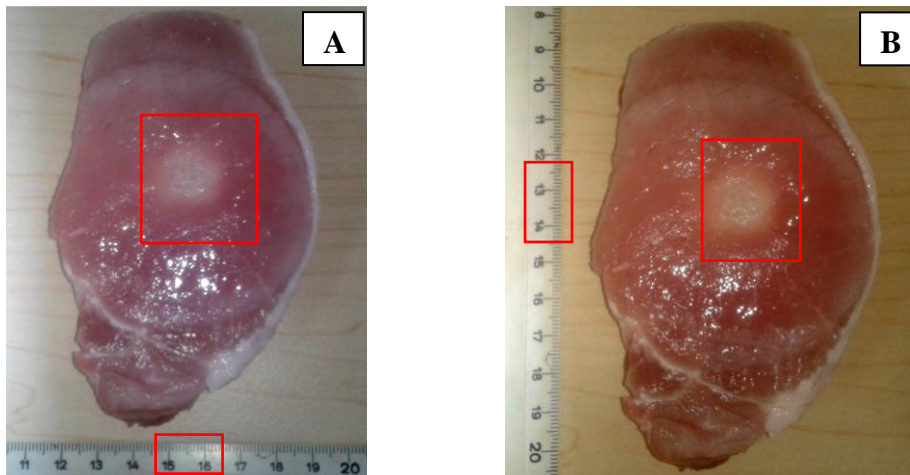
Figure 9.13: A) Size of the lesion on the X-axis, B) Size of the lesion on the Y-axis using a step of 2 mm, 51 W of acoustic power, f=2 MHz, d=5 cm, R=10 cm, duration= 8 s, focal depth=1 cm.

The depth of the lesion was large enough to ablate all the way throughout the slice (25 mm) as shown in figure 9.14. The acoustic power used to induce the lesions was 51 W for 8 s. The delay between the sonications was set to 20 s to allow the tissue to cool for inducing uniform lesions.

Figure 9.14: Depth of the ablation in porcine muscle with 51.4 W of acoustic power, f=2 MHz, d=5 cm, R=10 cm, duration= 8 s, focal depth=1 cm.

9.5 Evaluation of a different protocol with a different transducer

The purpose of this experiment was to test a protocol with a different transducer. A different amplifier (LA100H-CE, AR Kalmus, Bothell, WA, USA) was used shown in figure 9.15. This transducer operated at 2 MHz with a diameter of 4 cm and radius of curvature of 8 cm. In order to achieve the same levels of acoustic power with the previous HIFU setup it was necessary to increase the voltage. With this setup, the 90 W of electric power resulted to 50 W of acoustic power. Figure 9.16A shows lesions in the gel (side view) and figure 9.16B shows the top view of the lesions. The induced lesions were created with a step of 10 mm.
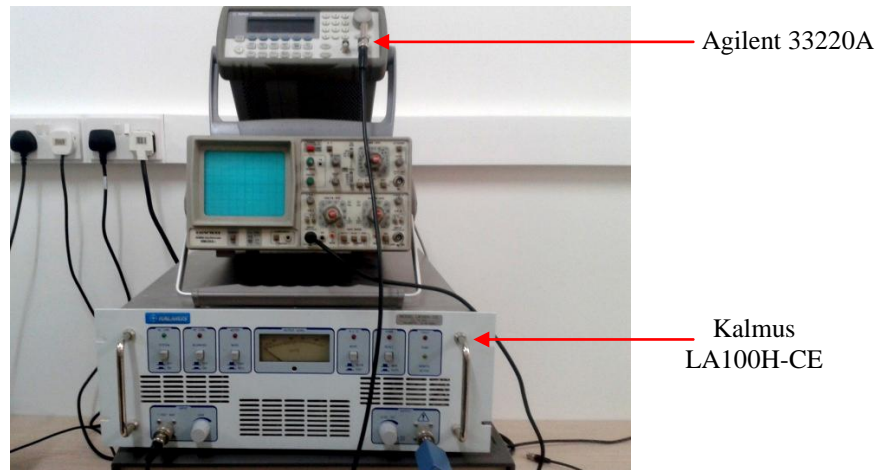
Figure 9.15: Photo of the signal generator with the amplifier used in the experiment.

To induce the lesions in the HIFU gel the duration of sonications was set at 20 s. The length of the lesions was approximately 40 mm which was larger compared to the previous experiments. Four discrete lesions were induced in the gel as shown in figure 9.16.
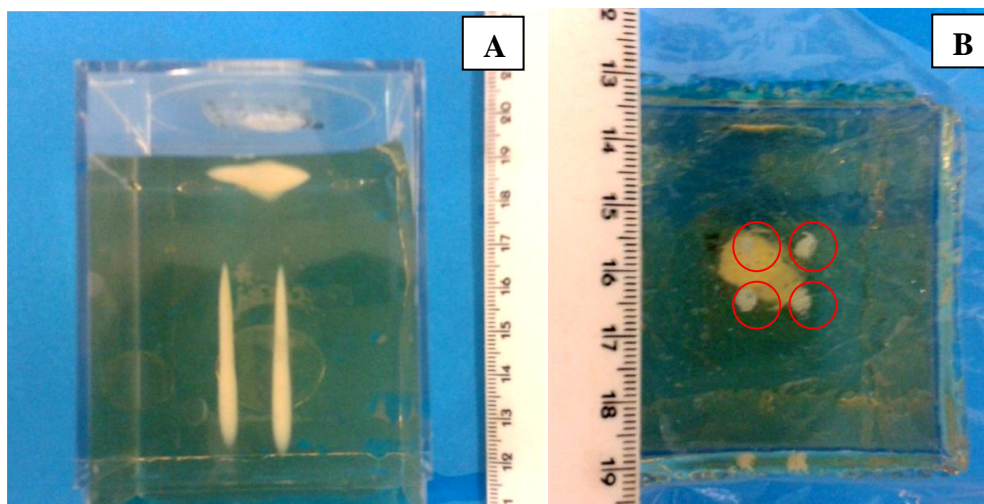
Figure 9.16: A) Side view of the lesions, B) Top view of the lesions (50 W of acoustic power, f=2 MHz, d=4 cm, R=8 cm, duration= 20 s, focal depth= 4 cm).

9.6 Accuracy test evaluation with the use of MRI

The purpose of this experiment was to evaluate the motion accuracy with the use of the MRI scanner. In this experiment discrete and overlapping lesions were produced to demonstrate the accuracy and repeatability of the device in MR environment. The experiment was conducted using a 1.5 T MR system (GE). Figure 9.17 shows the positioning device as placed on the MRI table. Figure 9.18 shows a closer view of the setup with the GPFLEX coil (USA instruments). Figure 9.19 demonstrates how the robot fits in the MRI table.

110
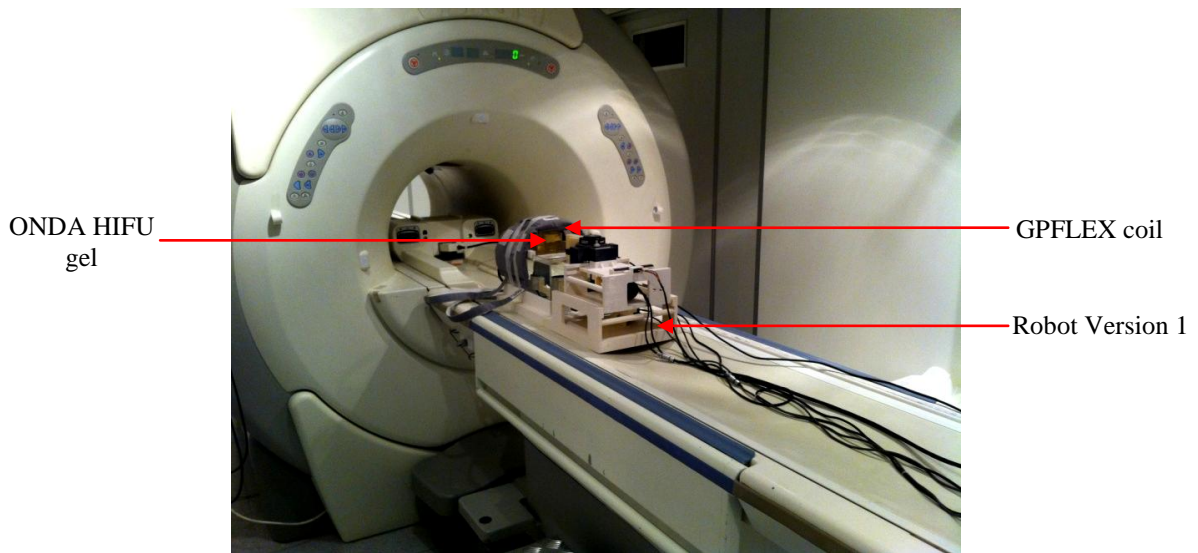
Figure 9.17: The experiment setup on the MRI table.
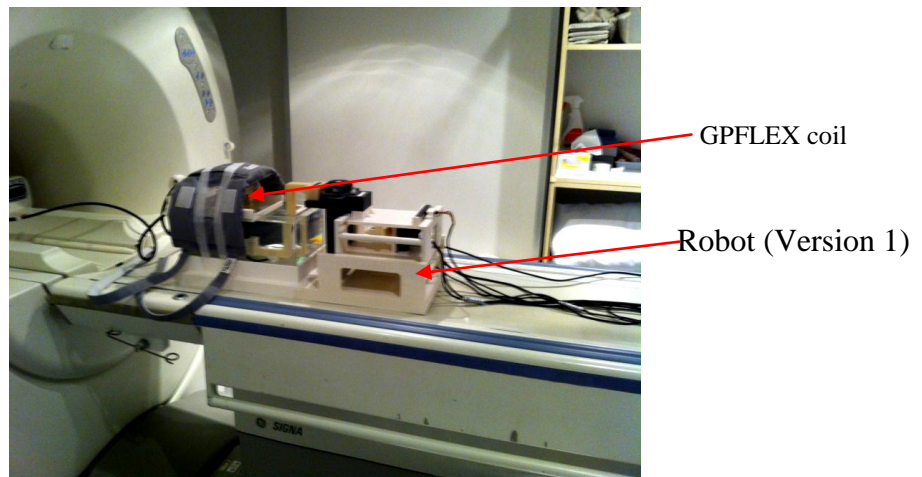
Figure 9.18: A closer view of the experiment setup with the GPFLEX coil.
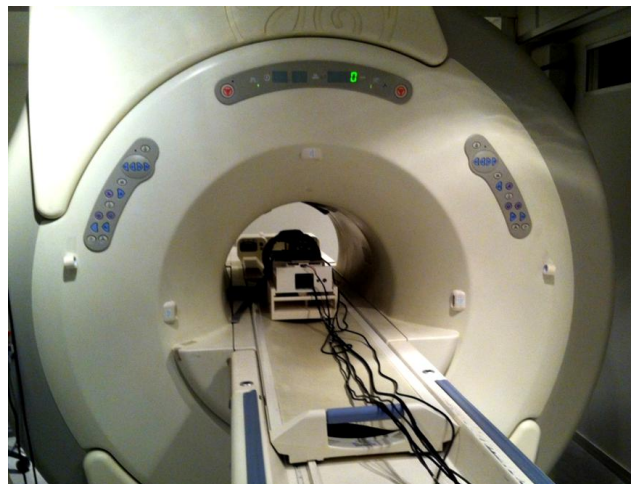
Figure 9.19: Photo demonstrating the size of the robot (version 1) in the MRI scanner.

9.6.1 Creation of discrete lesions using MRI guidance

In the initial test of the experiment, discrete lesions were created which demonstrated the repeatability and consistency of the robot. MR images of figure 9.20 show the lesions spaced by 10 mm. The sonications were executed with a 2 MHz ultrasonic

111

transducer with a diameter of 4 cm and a radius of curvature of 8 cm. A rectangular grid of 3 x 3 lesions was created. The acoustic power applied was 50 W for 20 s.

The progression of the lesions was monitored using MRI. The images were acquired with T2W FSE (Fast Spin Echo) pulse sequence. This sequence provided good contrast between the gel and the lesions. The lesion was monitored at the end of each sonication. The MR images were minimally affected by the positioning device. Also the positioning device performed safely and reliably in the strong magnetic field of the MRI. The parameters used for the MR images were TR=2500 ms, TE=60 ms, Slice thickness=3 mm, matrix=256 x 256, FOV=16 cm, NEX=3, ETL=8.

Figure 9.21 shows the photo of the lesions created. The lesions appeared to have uniform size and were equally spaced. The lesions were 30 mm long and their shape was aproximately the same demonstarting the consistency of the HIFU protocol.
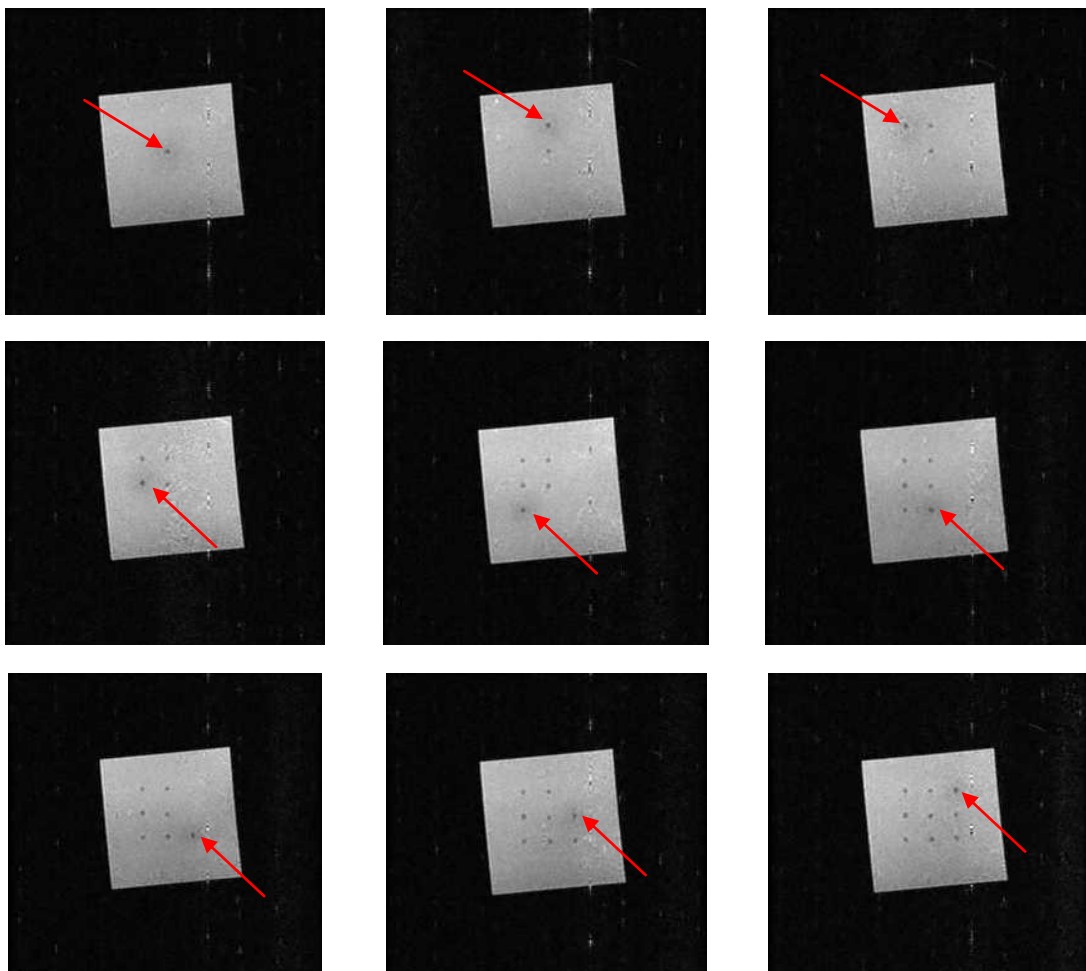
Figure 9.20: The series of MR images (T2-W FSE: TR=2500 ms, TE=60 ms, Slice thickness=3 mm, matrix=256 x 256, FOV=16 cm, NEX=3, ETL= 8) demonstrate the progression of the lesions (50 W of acoustic power, duration=20 s, f=2 MHz, d=4 cm, R=8 cm, focal depth= 2 cm).
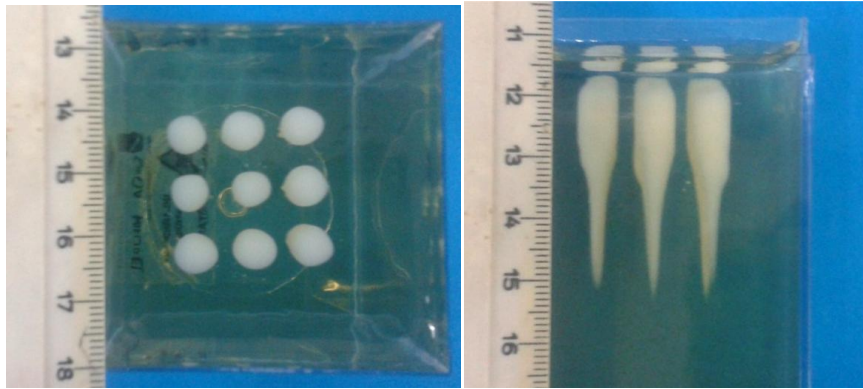
Figure 9.21: The photo of the induced lesions (50 W of acoustic power, duration=20 s, f=2 MHz, d=4 cm, R=8 cm, focal depth= 2 cm).

9.6.2 Creation of overlapping lesions using MRI guidance

Single lesions were created by using the same ultrasound protocol with the previous experiment. The transducer was maneuvered in a 4 x 4 grid thus, induced overlapping lesions with a 2 mm step. The motion sequence used is shown in figure 9.22. The images of figure 9.23 were acquired using the T2W FSE pulse sequence.

The acoustic power was set at 50 W and the transducer operated at 2 MHz for 30 s. The overlapping lesions ablated an area of approximately 15 x 15 mm. Imaging was acquired after each sonication. During imaging the gel was allowed to cool to avoid near field heating. This experiment demonstrated the ability to use the MRI scanner to guide this positioning device for the production of large lesion volumes.
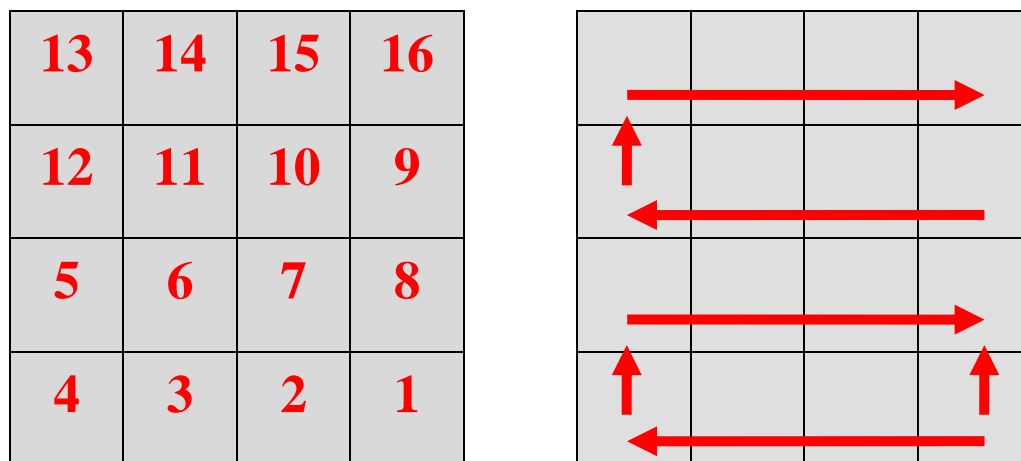
Figure 9.22: The diagram demonstrates the sonication sequence that was used to induce the 8 x 8 steps lesion shown in figure 9.23 and figure 9.24.
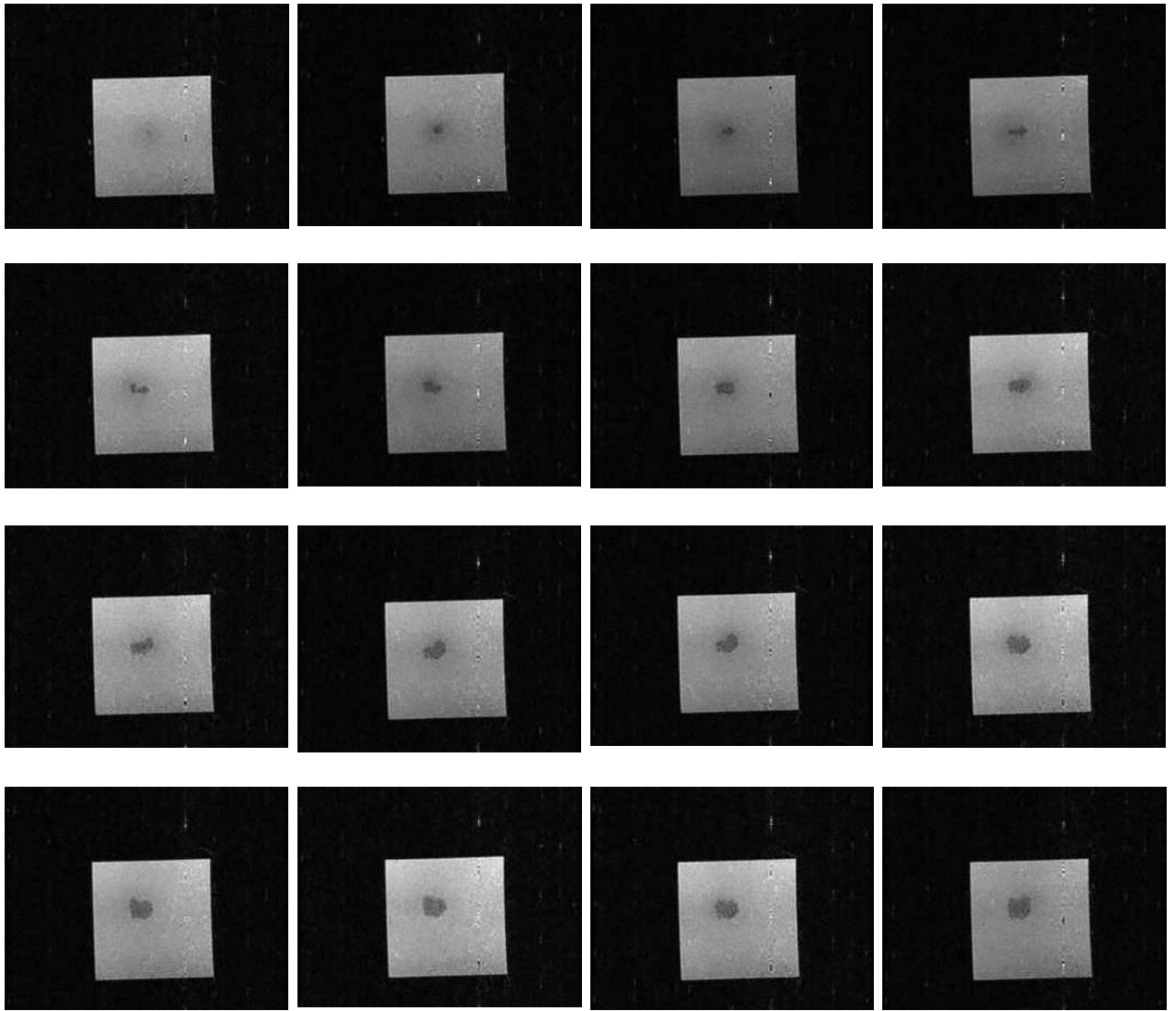
Figure 9.23: The MR images (T2-W FSE: TR=2500 ms, TE=60 ms, Slice thickness=3 mm, matrix=256 x 256, FOV=16 cm, NEX=3, ETL=8) demonstrate the progression of the lesion after each sonication (50 W of acoustic power, duration=20 s, f=2 MHz, d=4 cm, R=8 cm, focal depth= 2 cm).
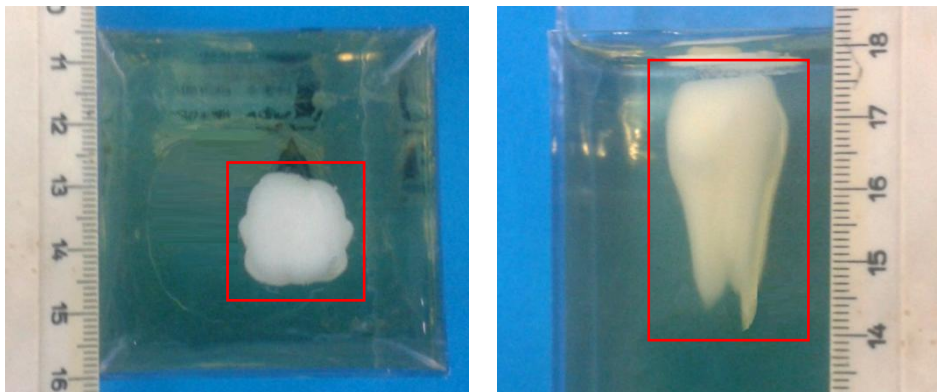
Figure 9.24: The photo of the lesion after the experiment (50 W of acoustic power, duration=20 s, f=2 MHz, d=4 cm, R=8 cm).

9.7 MRI evaluation of the MR compatiblity of the transducer

In this experiment the MR compatibility of the robot transducer shown in figure 9.25 was evaluated. The transducer operated at 1 MHz, had a focal distance of 95 mm, and a diameter of 40 mm. An RF amplifier (RFG 750 W, JJA, Seattle, WA, USA) was used. Figure 9.26 shows the complete electronic setup that includes the motor drivers with the two interface cards (NI-USB-6251). Figure 9.27 shows the setup of this experiment. The GPFLEX imaging coil (USA instruments) was used in this experiment.
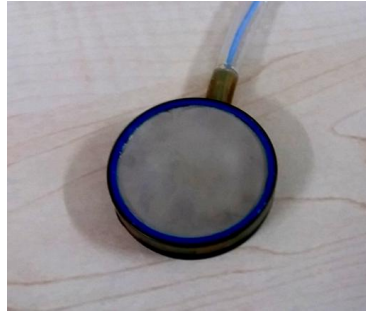
Figure 9.25: Photo of the transducer, f=1 MHz, R=95 mm, d=40 mm.

Figure 9.26: Electronics system of the positioning devices (first version).
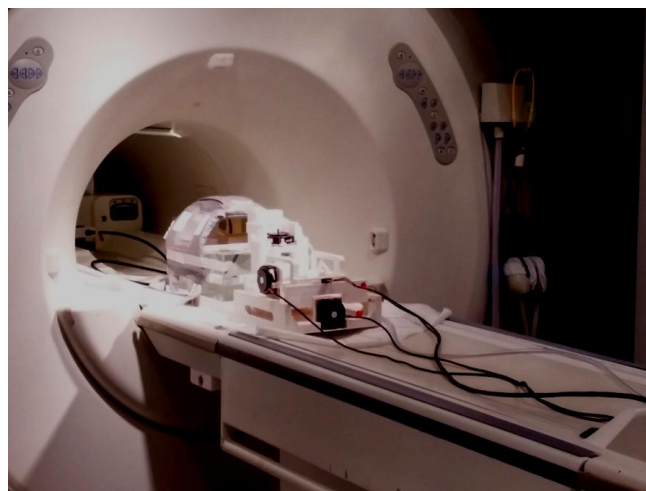
Figure 9.27: The experimental setup with the Robot (Version 3) as placed on the MRI table.

The first images showed the position of the robot transducer for targeting the desired location prior to the sonications. The images showed all the details and with no visible artifacts. These images acquired using Fast Gradient Recall Echo (FGRE) T2-weighted. The parameters used for this sequence were: TR= 4.87 ms, TE= 1.39 ms, slice thickness=5 mm, matrix=256 x 256, FOV=44 cm, NEX=1 and ETL=1.
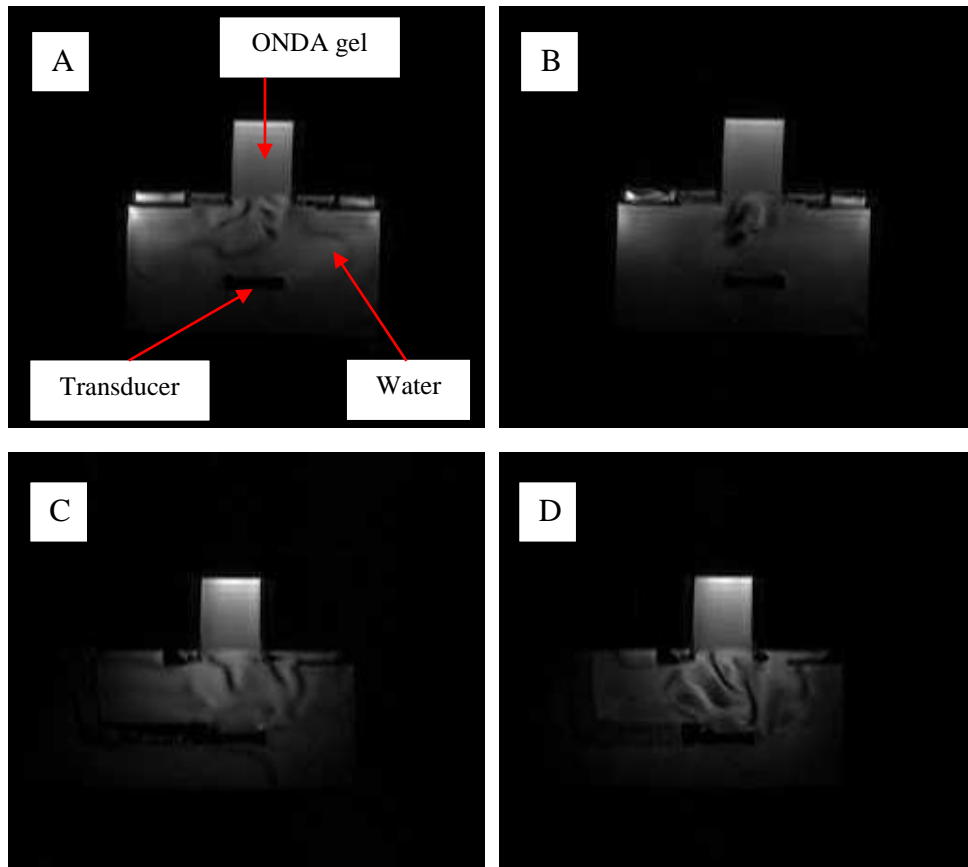
Figure 9.28: MR images showing the transducer acquired using FGRE T2-weighted (TR= 38.5 ms, TE= 20 ms, slice thickness=10 mm, matrix=256 x 256, FOV=20 cm, NEX=1).

9.7.1 Beam development

A sonication at lower power level was performed in order to observe the ultrasonic beam using the T1W SPGR pulse sequence. The parameters of the sequence were: TR= 38.5 ms, TE= 20 ms, slice thickness=10 mm, matrix=256 x 256, FOV=20 cm, NEX=1, and ETL=1. The image quality was minimally affected during the sonications. The MR images in figure 9.29 show the activation of the ultrasound. The beam of the transducer is clearly visible by the turbulence in the water during ultrasound activation. Also the dark area inside the ONDA gel was the result of heating. The thermal dose of the sonication was low enough so there was no thermal damage in the gel.
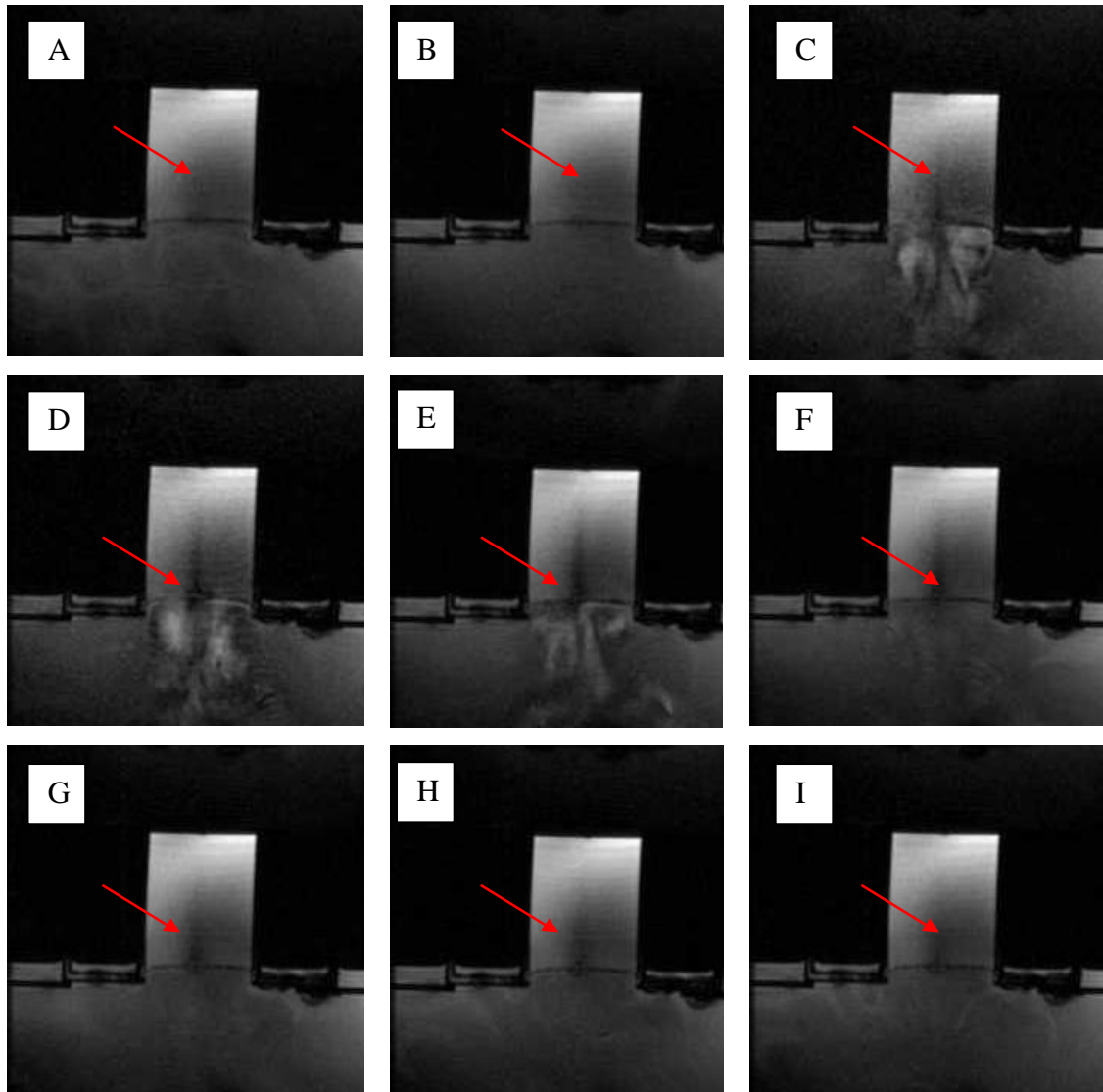
Figure 9.29: Low intensity sonication to observe the beam development using T1W SPGR pulse sequence (TR= 38.5 ms, TE= 20 ms, slice thickness=10 mm, matrix=256 x 256, FOV=20 cm, NEX=1, and ETL=1). Sonication parameters: f=1 MHz, R=95 mm, d=40 mm, 25 W of acoustical power for a duration of 30 s, focal depth= 3 cm.

9.8 Evaluation of the angular stage

To test the performance of the theta stage, lesions were induced in a polyaclylamide gel (ONDA). Initially two lesions were induced as shown in figure 9.30 to move the stage at an angle. The lesions were produced using a transducer which operated at 1.18 MHz. The sonications were performed at 45 W (acoustical power) for 60 s. A delay of 60 s was used to avoid near field heating. The length of the lesions was approximately 25 mm with a diameter of approximately 3 mm.

In another test overlapping lesions were created as shown in figure 9.31. The lesions were created in an angular arrangement demonstrating the consistency and repeatability of the theta stage.
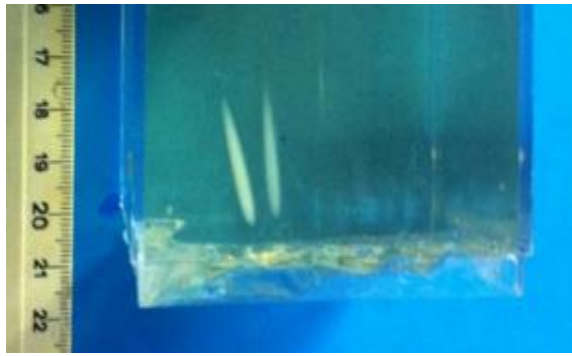
Figure 9.30: Lesions created at different angles. Sonication parameters: f=1.18 MHz, acoustic power=45 W, duration=60 s.

Figure 9.31: Overlapping lesions produced in gel phantom using the theta stage. Sonication parameters: Frequency at 1.18 MHz, acoustic power=45 W, duration=60 s.

9.9 Evaluation of the theta stage in a phantom with ribs

In order to evaluate the theta stage in a rib/gel phantom, sonications in two orientations were performed. Bottom to top and lateral approaches were investigated. The SPGR images were acquired in order to create temperature maps. To evaluate the effect under more realistic conditions the agar phantom used was molded around a rib cage. The rib cage was produced with ABS using a 3D manufacturing machine based on a female patient CT scans.

The phantom which consisted of agar, silica dioxide and evaporated milk was molded around the rib cage. The phantom was placed on the robot cover as shown in figure 9.32. The water container cover provided a good support for the rib/agar that was immersed in water. The water container was attached to the robot (version 3) and was placed on the table of the MRI scanner. To acquire the MR images, the GPFLEX coil was used around the phantom. The setup of this evaluation as placed on the MRI table is shown in figure 9.33.
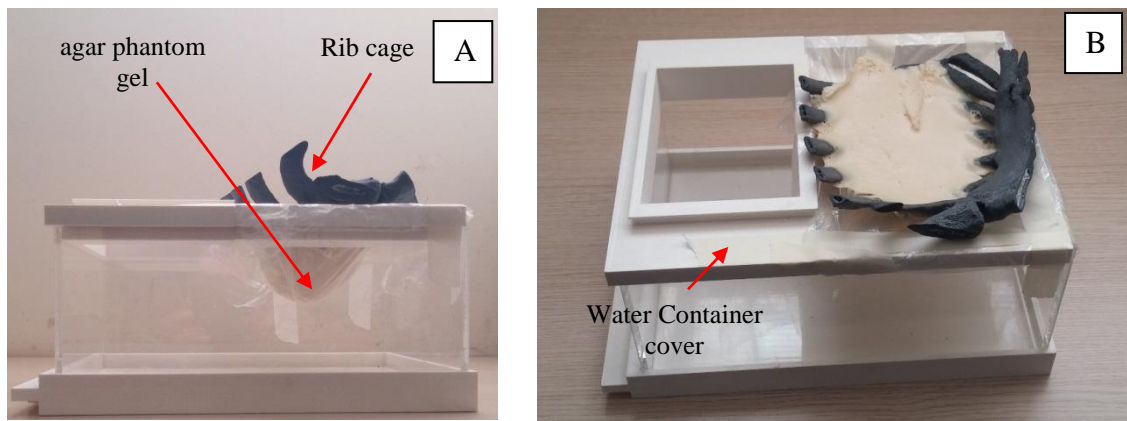
Figure 9.32: Placement of the rib/breast phantom on the water container of the robot.
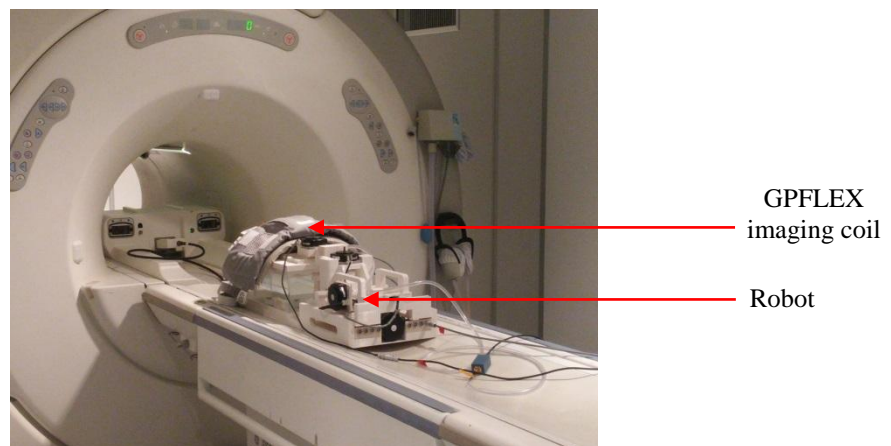
Figure 9.33: The setup of the test placed on the MRI table.

9.10 Bottom to top approach test

Theta stage was adjusted to target the phantom from bottom to top. Figure 9.34 show the axial view T1 weighted (T1W) SPGR magnitude image of the transducer and the phantom. With the bottom to top approach the far-field field targeted the rib model. The single element spherically focused transducer that was used had a focal length of 10 cm, diameter of 3 cm and operates at 1.18 MHz.
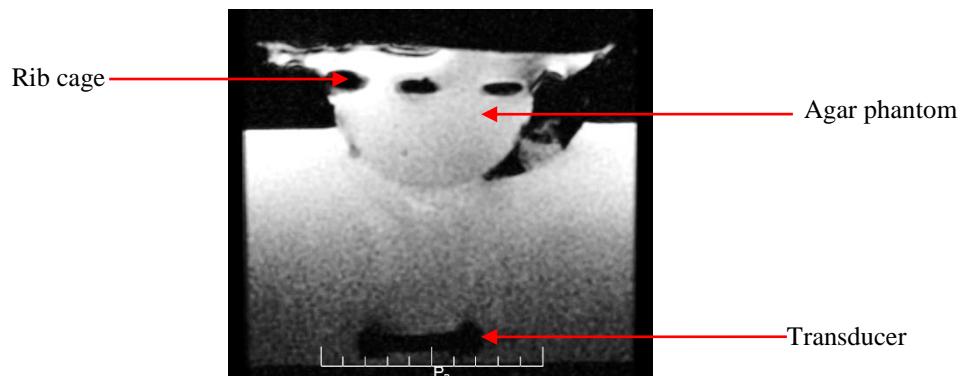
Figure 9.34: Bottom to top orientation. Axial view (T1W SPGR) image of the transducer and the phantom.

119

Figure 9.35 shows axial temperature maps for the coupling approach demonstrated in figure 9.34 (coupling to the breast phantom was bottom to top). The acoustical power of 30 W was applied for 60 s. During the first 5 images the FUS transducer was activated. Because of the reflection of the beam in the far-field, the temperature produced close to the ribs was high (close to 100 ℃).

9.10.1 MR thermometry

The development of temperature build-up during FUS sonications was assessed using appropriate MRI sequences which demonstrate the temperature dependent proton resonance frequency shift phenomenon (PRFS) [105]. This method relates the associated phase shift derived from the frequency shift of the MR signal due to the local temperature elevation (ΔT). This relationship is described as shown below:

$$\Delta T = \frac{\varphi(T) - \varphi(T_0)}{\gamma \alpha B_0 TE} \tag{1}$$

where φ(T) and φ(T$_0$) are the absolute phases of the MR signal at a starting and final temperature T and T$_0$ respectively, γ is the gyromagnetic ratio, α is the PRF change coefficient (0.01 ppm/°C), B$_0$ is the magnetic field strength and TE is the echo time.

The spoiled gradient echo sequence (SPGR) was used for thermometry: TR: 38.5 ms, TE: 20 ms, bandwidth (BW): 15 kHz, matrix: 128 X 128, slice thickness: 10 mm, NEX:1. The temporal resolution of thermometry was about 12 s. Thermometry slices were positioned along the short acoustic beam axis at a distance equal to the transducer's focal length (10 cm), to estimate the maximum temperature elevation. Thermometry was also assessed along the long axis of the beam. Phase maps were reconstructed by calculating the phase on a pixel-by-pixel basis after combining pixel data from real and imaginary channels. Although the scanner was capable of producing directly phase image reconstructions, the applied intra-scan gradient non-linearity corrections induce phase interpolation problems. All of the image processing was performed with custom-made software developed in MATLAB (MathWorks, Natick, United States). Temperature elevation was returned by the software as the maximum value in a prescribed region of interest (ROI) that was manually positioned. Temperature-color coded maps were produced by adjusting the color map (blue to red) for a range of minimum to maximum ROI temperature as shown in figure 9.35.
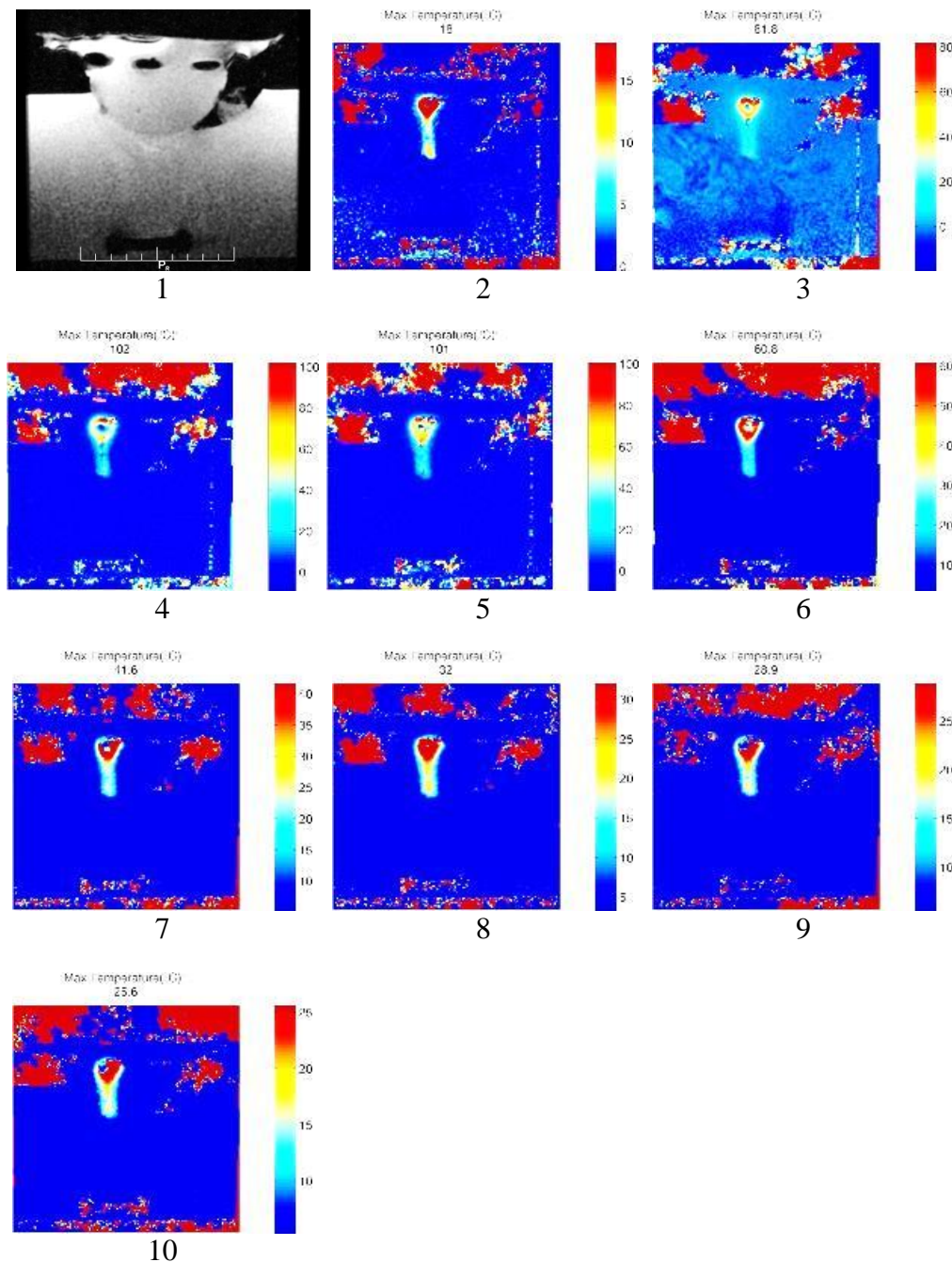
Figure 9.35: Thermometry maps for the bottom to top sonication of 30 W of acoustic power for 60 s, operating at 1.18 MHz.

9.10.2 Lateral orientation test

To avoid the ribs the theta stage was adjusted to deliver ultrasound laterally. This approach is shown in figure 9.36 (transducer is placed laterally). Figure 9.37 shows the MR temperature elevation in the phantom during sonication. The transducer was set at 30 W for 60 s. The MR thermometry maps showed the maximum temperature of approximately 30 ℃.

This phantom experiment demonstrated the theta axis benefits. The angular stage enabled targeting through a different path. Theta stage is a useful feature for the HIFU

system since it allows targeting in different anatomies by avoiding structures that may cause pain or other implications. During this test the angular axis demonstrated its functionality by moving successfully the transducer to lateral position for the sonication.
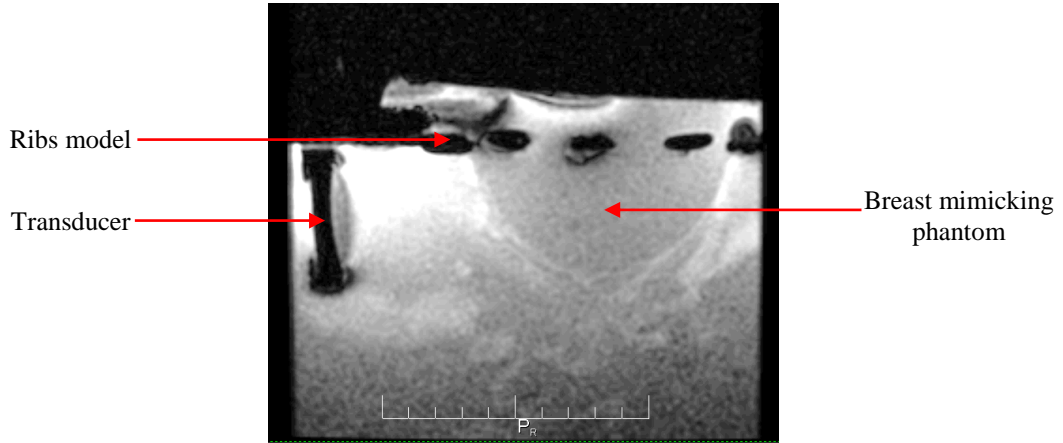
Figure 9.36: MRI image of the rib.
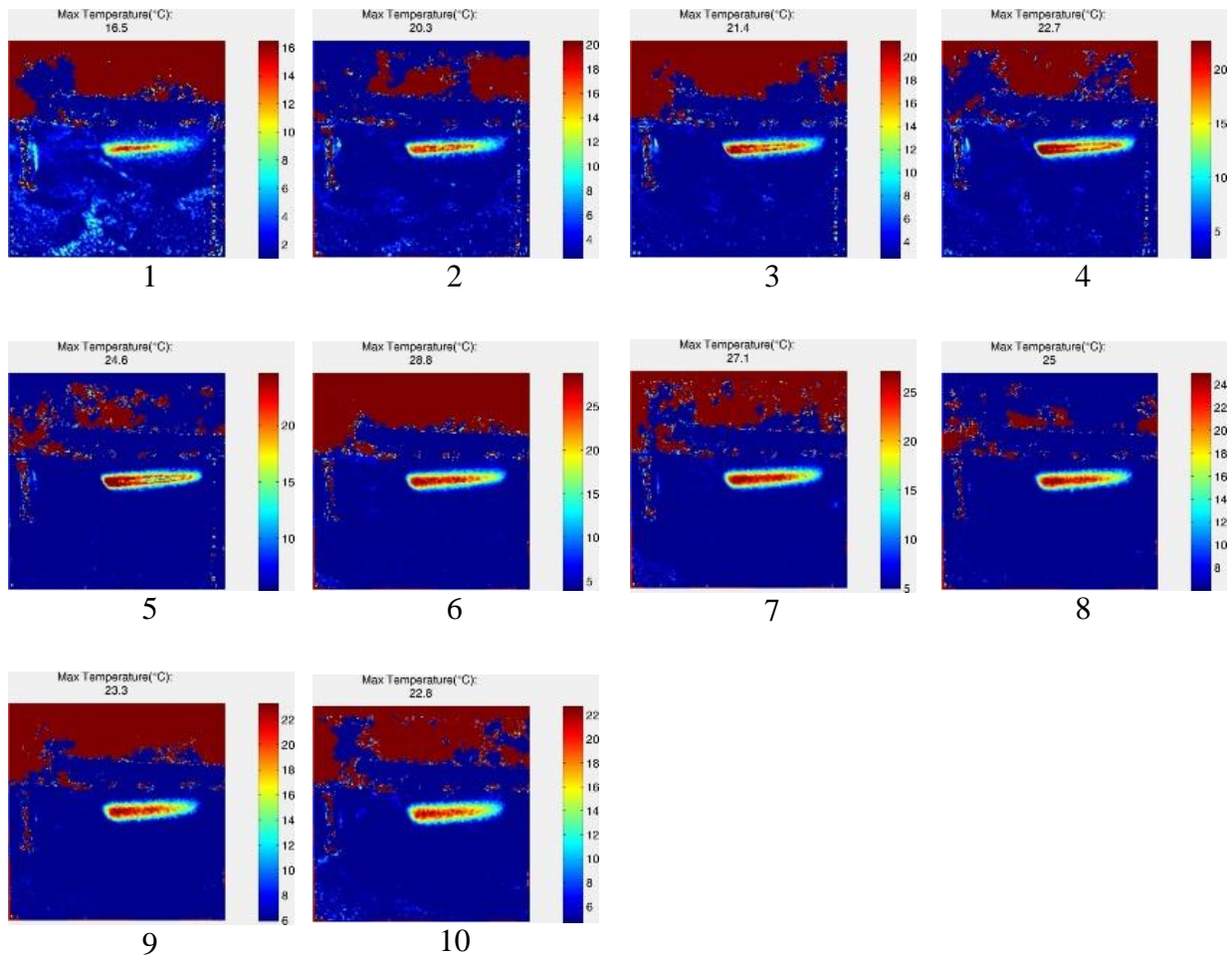
Figure 9.37: Thermometry maps for the lateral sonication of 30 W of acoustic power for 60 s, operating at 1.14 MHz.

9.11 Evaluation of the functionality of the immersed robotic system

To evaluate the repeatability and functionality of the robotic system a gel phantom was used. The gel phantom consisted of agar, silica and evaporated milk to mimic the realistic properties of tissue as described by Menikou et. al. [106]. Figure 9.38 shows the robot on the MRI with the gel phantom at the top. The transducer used to perform the sonications was operating at 0.4 MHz and has a focal distance of 7 cm and diameter of 3 cm.
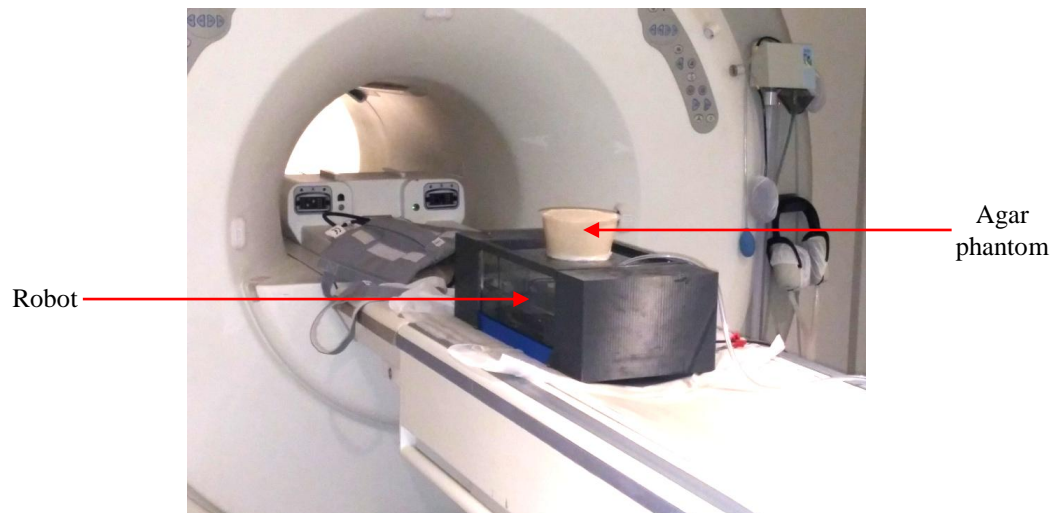
Figure 9.38: Photo of the Robot on the MRI table with the gel phantom on the top.

High-resolution MR imaging was performed in order to evaluate the motion of the transducer using a Fast Recovery Fast Spin Echo (FRFSE) T2-weighted fast spin echo sequence with the following parameters: TR= 2200 ms, TE= 61.2 ms, slice thickness=15 mm, matrix=192 x 192, FOV=17 cm, NEX=1, and echo train length (ETL)= 16.

The device moved the transducer four steps on X-axis and five steps on Y-axis to evaluate the motion accuracy. Figure 9.39 shows the MR images of the transducer movement of the X-axis immersed in water with a step size of 10 mm. With 20 such movements the average distance moved with the transducer was 9.96 mm (standard deviation was 0.66 mm). The standard deviation was in the order of the pixel size (1 pixel= 170 mm/256= 0.66 mm). The Y-axis movements shown in figure 9.40 are performed using 10 mm step. The average distance covered for 20 movements was 9.99 mm (standard deviation 0.78 mm). The standard deviation for the Y-axis was also in the order of the pixel size. The artifacts in the pulse sequence due to the transducer and positioning device were minimal.
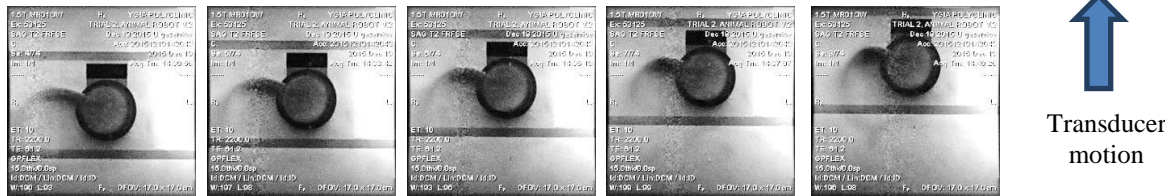
Figure 9.39: Motion accuracy test for X-stage. In each image the transducer was moved using a step size of 10 mm
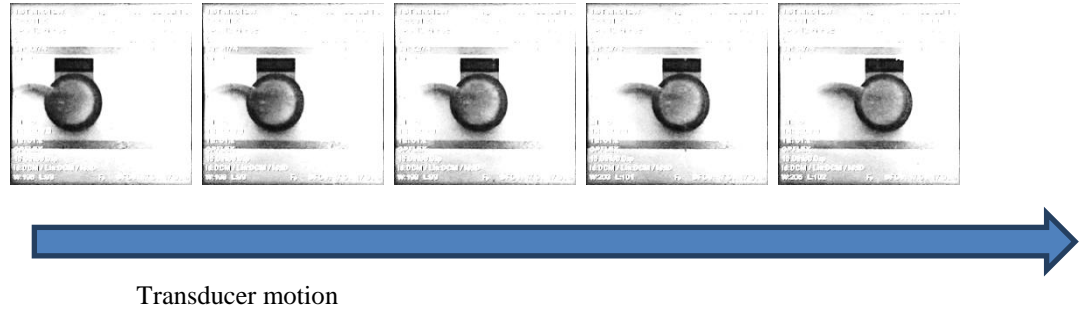
Transducer motion

Figure 9.40: Motion accuracy test for Y-stage. In each image the transducer moved using a step size of 10 mm.

9.11.1 Functionality test of the immersed robot

To evaluate the functionality of the positioning device, thermometry maps were used to locate the heat in the agar gel. The MR thermometry of a 120 s sonicaion operating at 0.4 MHz at an acoustical power of 40 W is shown in figure 9.41. This figure shows the corresponding MR thermometry at a plane perpenticular to the transducer face.

A grid of 3 X 3 steps of 5 mm is shown in figure 9.42. The exposure times was 120 s with an acoustical power of 40 W. The MR thermometry images demonstrated the functionality of the positioning device in creating thermal effects in large areas on the gel phantom.
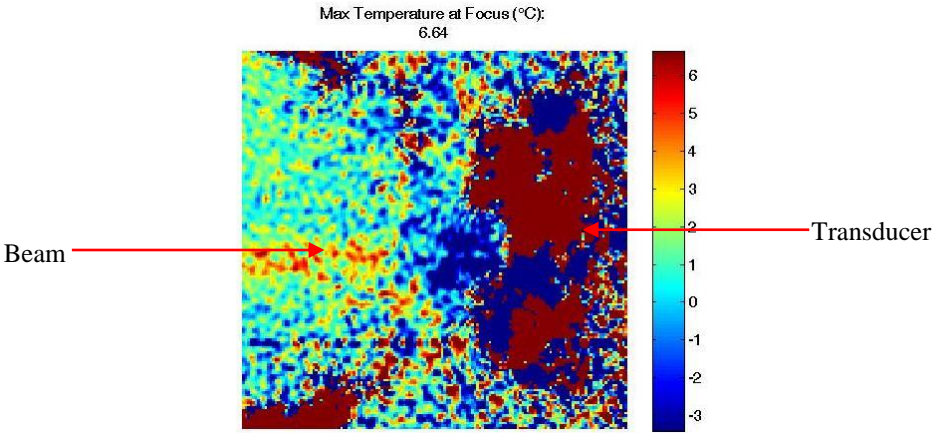
Figure 9.41: MR thermometry at a plane perpenticular to the transdcuer face with a 120 s sonicaion using the single element shericallly focused transducer operating at 0.4 MHz at an acoustical power of 40 W.
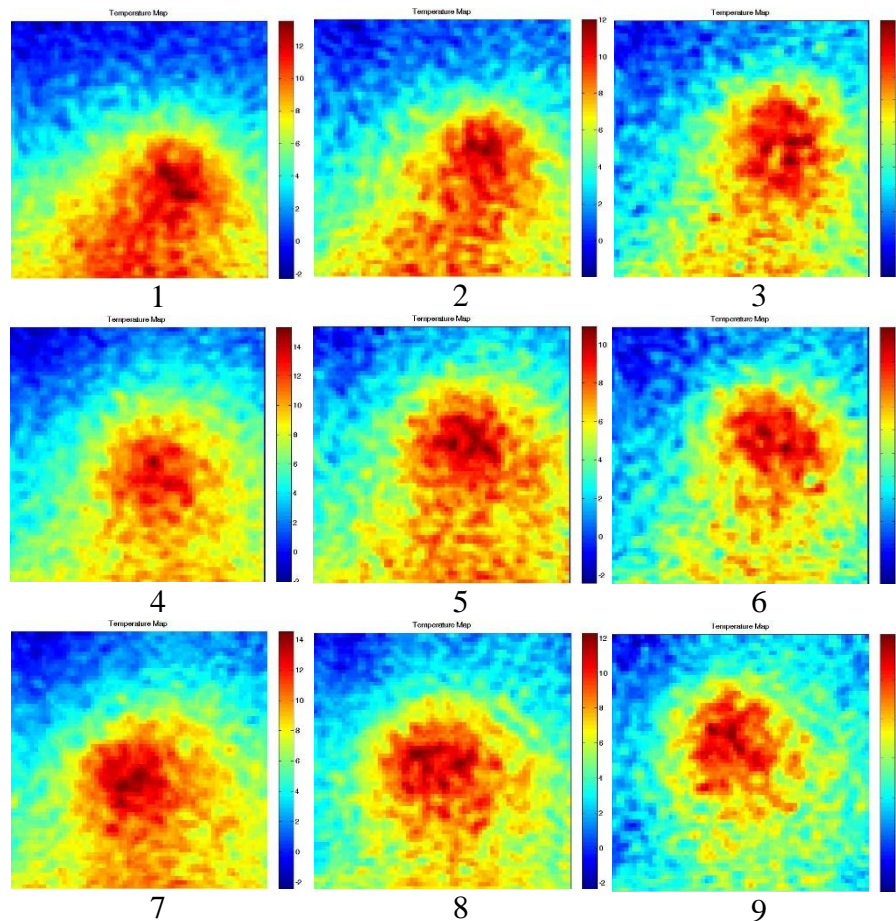
Figure 9.42: MR thermometry when the transducer moves in a 3 X 3 grid with a step of 5 mm using the single element shericallly focused transducer operating at 0.4 MHz. The exposure time was 120 s with an acoustical power of 40 W.

9.12 : Evaluation of the top to bottom coupling

The purpose of this experiment was to test the coupling of a top to bottom approach to deliver focused ultrasound. This concept could be used in the future for treatments. The test was conducted in an ONDA gel. To couple the ultrasound to the ONDA gel a nylon bag (filled with water) was used. Below the bag the ONDA gel was placed. The experimented setup is shown in figure 9.43.

The extended arm was coupled with the robot (version 3) and was placed on the MRI table. A 1.5T MRI scanner (GE) was used. The images were acquired using the lumbar spine imaging coil (USA instruments). To generate the ultrasonic waves a transducer operating at 1.18 MHz, with a diameter of 4 cm and a radius of curvature of 10 cm was used. The transducer was energized by the JJA 750 W RF generator.

Figure 9.43: The experiment setup that was used for the evaluation of the coupling for bottom to top ultrasound delivery.

The sonications were performed with 40 W of acoustic power for 30 s. This exposure was sufficient to produce lesions. MRI images were used in order to evaluate the positioning accuracy of the positioning device operated with the top to bottom coupling. Four discrete sonications were induced in the ONDA gel as shown in figure 9.44. Side view of the lesions is also illustrated. The lesions were created with 6 mm step between them.

The Coronal images were produced using a FRFSE T2-weighted fast spin echo sequence with the following parameters: TR= 2200 ms, TE= 55.5 ms, slice thickness=5 mm, matrix=364 x 320, FOV=15 cm, NEX=1 and ETL= 16. For the axial views the parameters of FRFSE T2W sequence were: TR= 2200 ms, TE= 61.8 ms, slice thickness=2 mm, FOV=15 cm, NEX=1 and ETL = 16

Figure 9.44 shows the creation of overlapping lesion. The lesions were produced 3 mm apart using the same HIFU protocol with discrete lesions. Figure 9.46 shows the lesion in the ONDA gel. The tests proved the effectiveness of the top to bottom setup and the coupling method. The membrane of the coupling did not showed signs of burn or deformation caused by high temperature which could compromise the integrity of

the coupling and cause reliability issues. The arm is ideal for applications that require this approach in order to access.
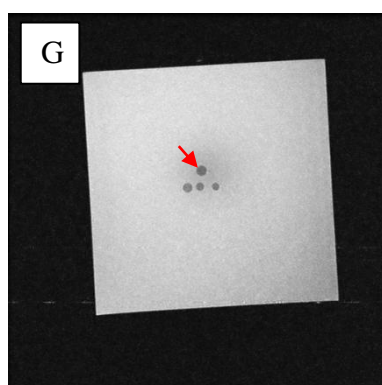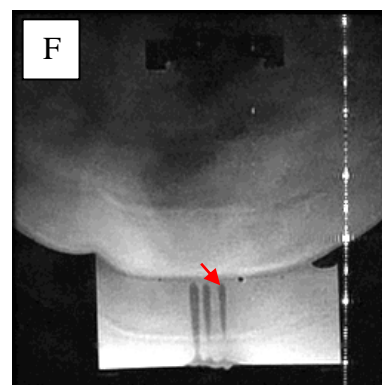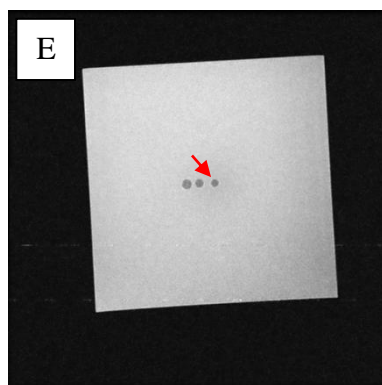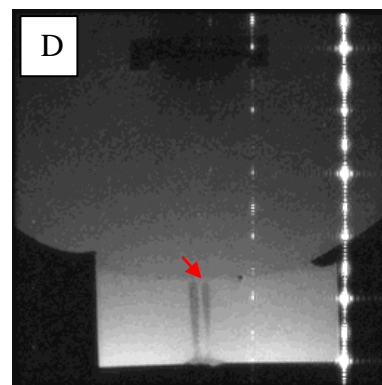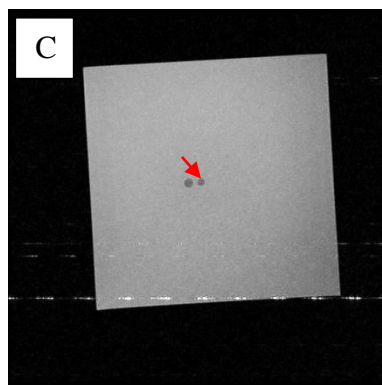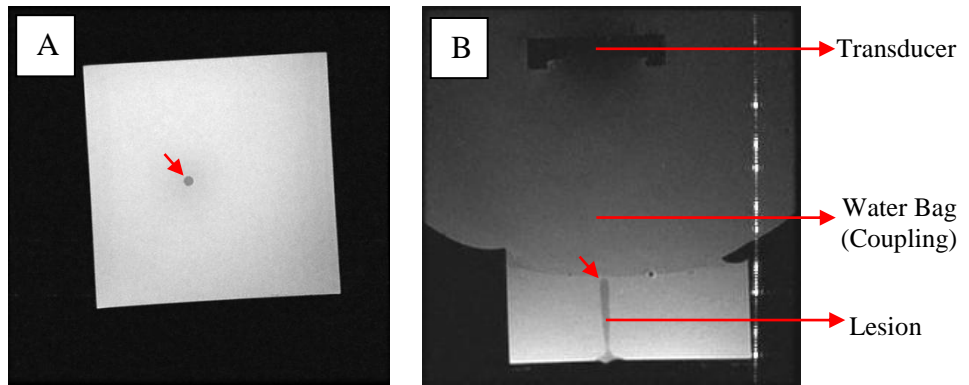
Figure 9.44: Discrete lesions progression using FRFSE pulse sequence. Left shows the upper view of the lesion and right shows the side view. Lesions were produced using a frequency of 1.18 MHz, at 40 W (acoustical) for 30 s.
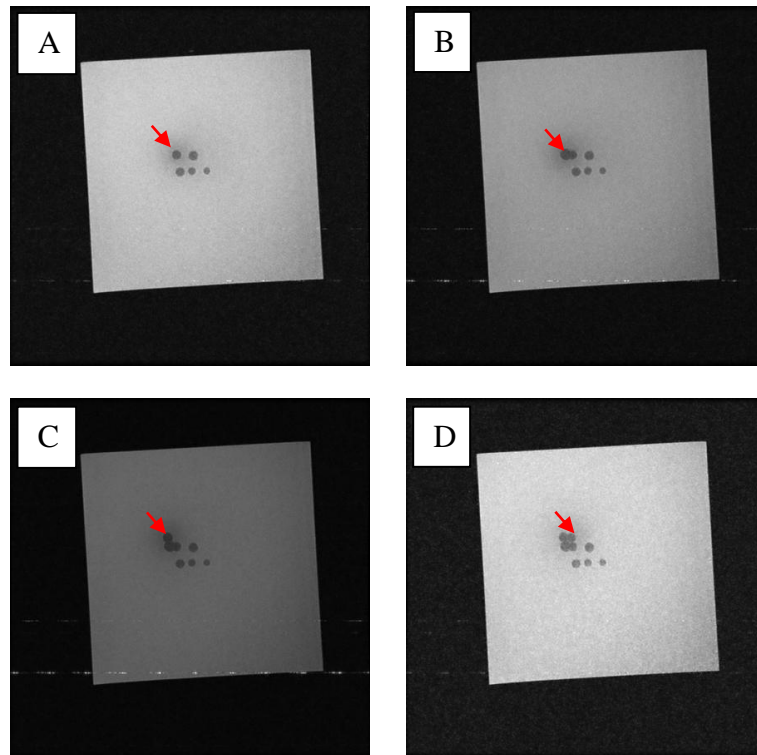
Figure 9.45: The upper view of the overlapping lesions. Lesions were produced using a frequency of 1.18 MHz, at 40 W (acoustic) for 30 s. The images acquired using the FRFSE pulse sequence.
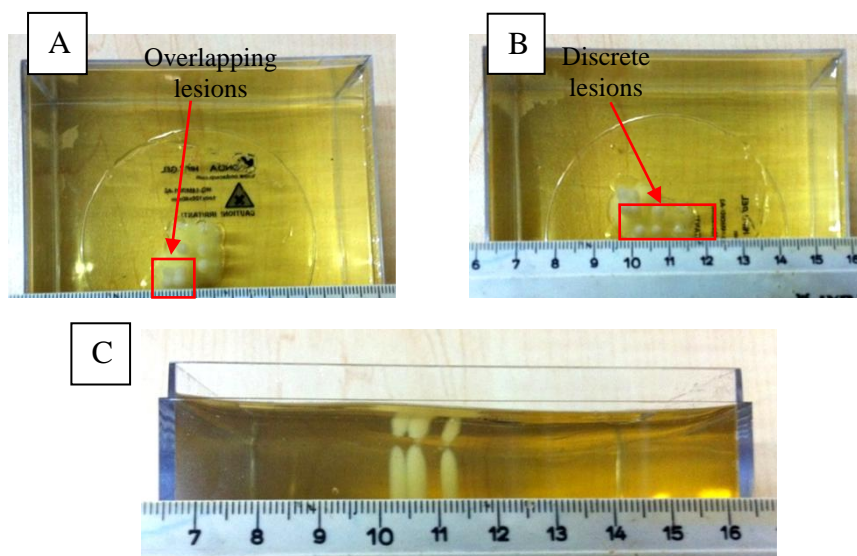
Figure 9.46: Lesions on ONDA gel. Photo (A) shows photo of the overlapping lesions, (B) shows photo of the discrete lesions, (C) shows photo of the side view of the lesions. (f=1 MHz, R=95 mm, d=40 mm, 45 W of acoustic power for a duration of 30 s).

Chapter 10 : Evaluation of focused ultrasound algorithms: issues for reducing near-field heating and treatment time.

10.1 Introduction

The robotic system of a HIFU system is responsible for the transducer motion in order to treat large tissue volume. In most of the cases these positioning devices move in a linear path treating tissue sequentially. The linear method does not give enough time to surrounding tissue in the near-field heating region to cool down, and thus near-field heating is produced [107]–[109].

The first study that proposed solutions for reducing the near-field heating by means of a simulation model was performed by Damianou and Hynynen [107]. In this study, it was proposed that by allowing 20 s delay between ultrasound firings greatly reduced the pre-focal heating. In another study by Fan and Hynynen [108], it has been shown that for 5 s pulse for single element transducers operating at 1.48 MHz, the delay needed varied from 30 s for a transducer with 8 cm diameter to 90 s for a transducer with 15 cm diameter. Three different scanning algorithms were used with each successive step close to each other (semisequential).

In another study by McDannold et al. [109] the optimum delay needed to eliminate pre-focal heating was investigated by using MRI, and it was found that delays around 60 s must be used in order to eliminate pre-focal heating.

Recently Mougenot et al. [110] reported that volumetric ablation resulted to enlarged ablate volume, with severe pre-focal heating close to the skin. In that study, multiplane MRI thermometry was proposed for monitoring the pre-focal temperature rise in order to prevent unintended thermal damage. Based on the chosen power, a linear relationship was established that estimated the temperature increase, thereby providing an a priori safety check for the existence of pre-focal heating. They proposed that their method could offer the clinician the possibility to abort the procedure if excessive pre-focal temperature was anticipated.

Several investigators have noted that such thermal buildup occurs also in the proximal tissues when executing a treatment with a phased array transducer [115], [117]- [118] needing even higher delay between successive sonications.

The previous studies provided solutions for reducing the near-field heating. However, using delays in the range of 20-60 s increased the treatment time drastically, especially for large ablating targets. Thus, there is a need for new algorithms for controlling the motion of the positioning devices. The goal of this study is to proposed non-linear transducer motion algorithms that completely avoid tissue damage in the pre-focal heating and thus, reducing the treatment time. Six algorithms (sequential, Euler, triangular, square, random and spiral) were proposed and evaluated. A simulation study was performed evaluating two main indicators: pre-focal heating and treatment time. The simulation model was then evaluated in an in vitro experimental model using a gel phantom.

10.2 Material and methods

10.2.1 Pre-focal heating concept

In a typical HIFU treatment, ultrasound is applied for few seconds in order to produce a thermal lesion in a biological tissue. A typical target volume is ablated by creating multiple lesions by successive sonications at a predetermined spacing. This spacing is normally defined by the elementary lesion diameter produced by the transducer (typically 1-2 mm) [107]. The successive sonications are produced based on a predetermined grid that covers the entire targeted area. The most frequently used grid is the sequential [53]- [113] and the spiral grid [114].

In the present paper a 10 x 10 sonication square grid was considered, meaning that the transducer was moved 100 times. We consider a 5 s sonication at each grid point with spatial average pulse average (SAPA) intensity of 1000 W/cm^2. This pulse duration was short enough to minimize the effect of blood cooling [115], and sufficiently high to cause thermal lesions [55]. The step of 2 mm between movements for this transducer, created overlapping lesions. The focus was assumed to be at a depth of 2 cm. With this transducer geometry and ultrasonic exposure (pulse duration, intensity) the length of the lesion was 20 mm (verified experimentally).The main goal was to ablate with zero delay between transducer movements in an effort to minimize the treatment time, provided that no pre-focal heating was produced. We have chosen to study the heating in a plane in the pre-focal which is 5 mm away from the lower side of the focal area. Figure 10.1 illustrates the ablation area (around the focus) and the near-field heating area in a plane perpendicular to the face of the transducer.
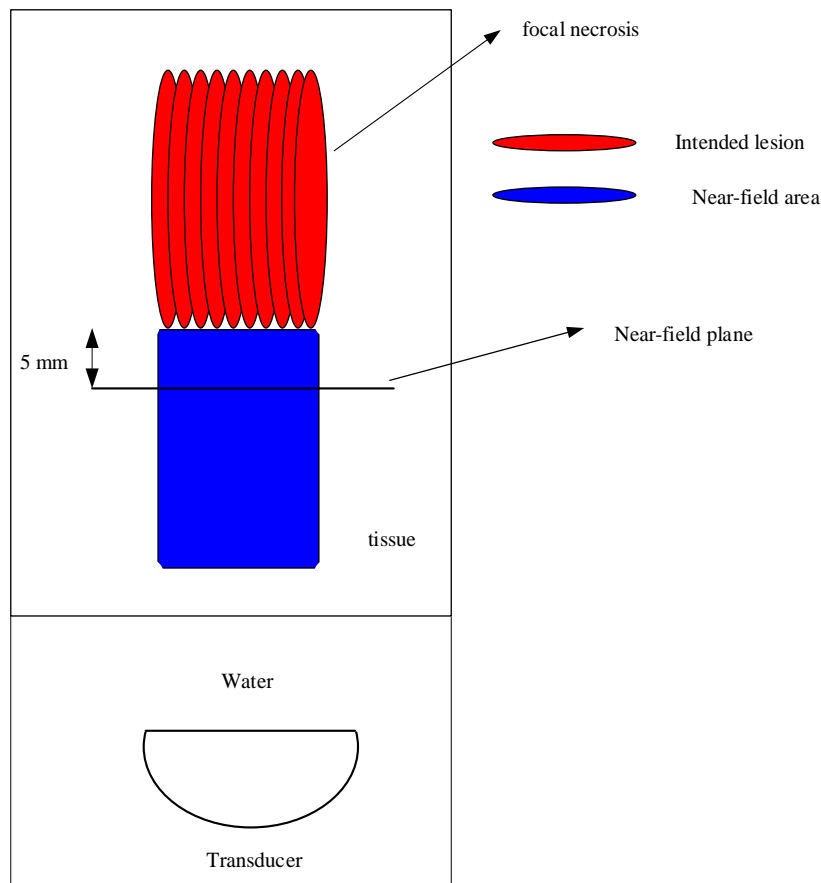
Figure 10.1: Illustration of the ablation area (around the focus) and the pre-focal heating area in a plane perpendicular to the face of the transducer.

10.2.2 Requirement of the algorithms

In order for an algorithm to be classified as successful it should be able to:

(a) Visit all cells of the target area.

(b) Avoid visiting adjacent cells as much as possible in consecutive movements.

(c). The algorithms should be picking the next cell to be treated according to a general rule stating that the shortest allowed distance to move the positioning device should be greater than one spatial step, in order to avoid visiting adjacent cells successively. Exception to this rule is the traditional sequential algorithm.

Many algorithmic solutions exist in finding the most prominent path within a grid. Every algorithm follows a different strategy based on the rules governing its logic. Algorithms like "Greedy algorithms", for instance, do not plan ahead when searching for a solution. Greedy algorithms rely on "Brute Force" and the improved abilities of computers today [116]. Dijikstra's algorithm [109] introduces a greedy approach aiming in finding the shortest path between a set of nodes as in graph theory of mathematics.

10.2.3Algorithms

10.2.3.1 Sequential algorithm

In this algorithm, the transducer moves from left to right in the x-axis and then at the end of the x-axis moves one step down in the y-axis (Figure 10.2). Then it starts moving from right to left and the process repeat itself. This is the algorithm used in many applications [53]- [113]. Since each grid point is close to each other, this algorithm although fast, produces severe near-field heating [107]- [108].

1	2	3	4	5	6	7	8	9	10
20	19	18	17	16	15	14	13	12	11
21	22	23	24	25	26	27	28	29	30
40	39	38	37	36	35	34	33	32	31
41	42	43	44	45	46	47	48	49	50
60	59	58	57	56	55	54	53	52	51
61	62	63	64	65	66	67	68	69	70
80	79	78	77	76	75	74	73	72	71
81	82	83	84	85	86	87	88	89	90
100	99	98	97	96	95	94	93	92	91

Figure 10.2: Motion plan for Sequential algorithm.

10.2.3.2 'Euler's Knight's Tour" algorithm

Euler's rule was first introduced on Chess board games imitating the movement of the "Knight" and it is called "Euler's Knight's Tour" algorithm [117]. If the "L" shape movement (figure 10.3) is implemented on the robotic system, then the cells adjacent to the "target zone" will be allowed time to cool down, until the next time they are visited, reducing any unwanted thermal effects. The aim of the algorithm was to visit all cells of the grid once. The algorithm executes by traversing through the grid in a "like" cyclic path until all cells have been visited. In this way the possibility of visiting two adjacent cells one after the other was forbidden. Euler's solution allowed the use of different sonications obtaining the same result even if a different starting point is selected and a different path was followed. This property of Euler's knight tour algorithm came as a contrast to the sequential approach when the same path was followed in every execution of the algorithm. If treatment follows Euler's approach,

because each successive movement was quite far from the previous movement, the cooling time needed (delay) could be lower than the time needed for the sequential.

1	4	31	24	51	6	65	10	53	8
32	23	2	5	64	25	52	7	68	11
3	30	33	50	27	66	69	84	9	54
22	49	28	63	46	85	26	67	12	83
29	34	47	78	61	70	95	82	55	72
48	21	62	45	90	81	86	71	96	13
35	44	79	60	77	94	91	100	73	56
20	41	38	89	80	87	76	93	14	97
39	36	43	18	59	92	99	16	57	74
42	19	40	37	88	17	58	75	98	15

Figure 10.3: Motion plan for Euler algorithm.

10.2.3.3 Triangular Algorithm Logic

This algorithm was inspired by mixing properties from the sequential movement algorithm and the Euler's knight tour algorithm (figure 10.4). This is a deterministic algorithm as its output stays the same every time. The movement follows a "V" shape, advancing always the positioning device one column to the right (x-axis) and either moving one row up on the y-axis or one row down on the y-axis. A nested double loop was implemented to control the row-column (x-y plane) movement.

1	12	3	14	5	1	2	18	9	20
11	2	13	4	15	20	19	8	19	10
21	32	23	34	25	21	22	38	29	40
31	22	33	27	35	40	39	28	39	30
41	52	43	54	45	41	42	58	49	60
51	42	53	44	55	60	59	48	59	50
61	72	63	74	65	61	62	78	69	80
71	62	73	64	75	80	79	68	79	70
81	92	83	94	85	81	82	98	89	100
91	82	93	84	95	100	99	88	99	90

Figure 10.4: Motion plan for Triangular algorithm.

133

10.2.3.4 Square tour algorithm

The spiral square motion algorithm has been derived by mixing the properties of sequential algorithm, Euler's knight tour algorithm and triangular algorithm. It introduces the concept of concentric "squares". Every square was inside another square with its dimensions reduced by one row and one column (figure 10.5). Every inner square was one row and one column smaller than the previous. The total number of columns and rows dictates how many squares are produced. The visiting cell sequence changed according to the number of rows and columns of the grid. The visiting sequence of this algorithm depended on the size of the grid. In order for the algorithm to perform its spiral tour and to avoid the pre-focal heating, the movement step of the positioning device was calculated dynamically. The step size was the number of concentric squares that could be produced in a given grid.

1	21	37	53	65	77	85	93	97	2
99	5	25	41	57	69	81	89	6	22
95	91	9	29	45	61	73	10	26	38
87	83	75	13	33	49	14	30	42	54
79	71	63	51	17	18	34	46	58	66
67	59	47	35	19	20	50	62	70	78
55	43	31	15	52	36	16	74	82	86
39	27	11	76	64	48	32	12	90	94
23	7	92	84	72	60	44	28	8	98
3	100	96	88	80	68	56	40	24	4

Figure 10.5: Motion plan for Square tour algorithm.

10.2.3.5 Random algorithm

Random movement depends on the value extracted from a random function provided by the algorithm (figure 10.6). This dependency on pure random motion produces several drawbacks to the overall performance of the positioning algorithm. There was a possibility for the algorithm to subsequently visit adjacent cells of the targeted area and as a result to deliver excessive heat to the cells close to that region momentarily. A second drawback was the possibility of the algorithm falling into an infinite loop if the same random numbers kept appearing continuously. Finally, a third drawback arose from the possibility of two consecutively generated random numbers to be so far apart, causing the positioning device to move from one side of the grid to the other. The

random algorithm approach falls into the non-deterministic category. In general the logic of the random algorithm was quite simple. A random number was generated, the number was checked if it was created before, if not, the positioning device was moved to that location, otherwise another number was generated.

1	89	2	36	84	46	44	26	10	76
87	12	99	98	11	22	86	41	64	27
65	52	35	85	55	25	26	38	7	67
5	50	47	19	51	90	97	17	15	8
24	33	70	9	82	75	4	73	68	92
6	88	72	69	37	81	39	80	96	78
58	18	71	94	59	54	100	62	20	91
31	56	95	66	60	57	21	30	3	61
42	13	53	16	49	40	48	34	14	32
77	45	83	23	74	79	93	28	43	63

Figure 10.6: Motion plan for Random algorithm.

10.2.3.6 The spiral square algorithm

This algorithm focuses its operational philosophy in the spreading of the visiting cells in a concentric grid in order to reduce the pre-focal heating effect (figure 10.7). The motion time was long because of the time spent in moving the robotic system between locations that were not close to each other.

1	21	41	61	81	2	22	42	62	82
8	28	48	68	88	9	29	49	69	3
87	73	93	14	34	54	74	94	89	23
67	53	77	97	18	38	58	15	10	43
47	33	57	20	40	60	78	35	30	63
27	13	37	99	100	80	98	55	50	83
7	92	17	79	59	39	19	75	70	4
86	72	96	76	56	36	16	95	90	24
66	52	32	12	91	71	51	31	11	44
46	26	6	85	65	45	25	5	84	64

Figure 10.7: Motion plan for Spiral algorithm.

In a square grid (rows equals the columns) the algorithm managed to cover all the cells. However, if the rows and columns were not equal (rectangle grid) some cells might remained unvisited, thus the algorithm performed a second tour to visit these cells.

10.2.4 Thermal Simulation model

10.2.4.1 Temperature simulations

The temperature vs. time history was obtained by solving numerically the bio-heat equation proposed by Pennes [118]. The explicit form of this equation is given by:

$$p_t c_t \frac{\partial T}{\partial t} = k\nabla^2 T + w_b c_b (T - T_a) + Q_p \tag{2}$$

where ρ_t is the density of the tissue, c_t is the specific heat of the tissue, T is the temperature of the tissue, t is the time, k is the thermal conductivity of the tissue, w_b is the blood perfusion rate, c_b is the specific heat of the blood, T_a is the arterial blood temperature, and Q_p is the ultrasonic power deposition rate. The numerical calculation of the power deposition rate was based on the solution of the Summerfield integral [119] using attenuation of 0.6 dB/cm-at 1MHz. The Rayleigh–Sommerfeld integral is the most common model for linear ultrasound propagation in simulations of thermal therapy. The disadvantages of the Rayleigh–Sommerfeld integral includes relatively long computation times, and significant errors in the pre-focal region. The numerical estimation of this integral was already described in great detail in the study by Damianou and Hynynen [107].

The first term in the above equation represent the temperature increase with respect to time, the second term represents the conduction effect which tends to decrease the temperature, the third term represents the convection effect due to blood which decreases the temperature. Since the experiments were conducted in a gel phantom, this term does not contribute at all in the temperature elevation. The fourth term represents the power absorbed due to the ultrasonic source which increases the temperature. The bioheat transfer equation was solved by using finite difference methods. The following parameters were used: ρ_t= 998 kg/m³, c_t=3770 J/kg°C, k=0.5 W/m°C, w_b=0 kg/m³s, c_b=3770 J/kg°C, T_a=37. More details of the method for estimating the temperature from Eq. (1) can be found in the article by Damianou and Hynynen [107].

Since the simulation model was elevated experimentally using a gel phantom, the blood perfusion c_b was set to zero. The simulations considered that there is water in front of the gel phantom, which provides coupling between the transducer and the gel phantom.

10.2.4.2 Thermal dose estimation

The estimation of the thermal dose for changing temperature exposures that cannot be described analytically was implemented by using the technique suggested by Separeto and Dewey [120]. The technique uses numerical integration to calculate the accumulated dose at a reference temperature under different temperature profiles. The reference temperature of 43 °C has been chosen. For small Δt the dose can be found by:

$$t_{43} = \sum_{t=0}^{t=final} R^{(43-T_t)}\Delta t \qquad (3)$$

where t_{43} is the equivalent time at 43 °C, and T_t is the average temperature during the time step Δt. The value of R of 0.25 was used for temperatures smaller than 43 °C and 0.5 for temperatures higher than 43 °C [120].

10.2.5 Motion navigation simulator

Based on the simulation model of Eq. (2), 65 temperature profiles were stored at 1 s time intervals (5 s on time, 60 s cooling time). These temperature profiles are based on the transducer geometry, intensity, pulse duration, tissue type and focal depth. For any different arrangement these parameters must be estimated again. Figure 10.8A shows a typical temperature change profile at a plane 5 mm from the focal area at the end of the 5 s pulse, and figure 10.8figure 10.7B shows the corresponding temperature change profile at 10 mm from the focal area. For simplicity, and faster calculations, the temperature change was rounded-off to the nearest integer. This rounding off was found not to affect the estimation of the thermal lesions. In other words if a pixel was not flagged as thermally damaged, the model of non-integer values did not showed the opposite. This was tested at different temperature profiles.

Then, these temperature profiles were inserted in the algorithm models. Therefore, during the simulation of motion, the simulator includes also the tissue temperature behaviour. Therefore, for each grid point in space and at any time interval, the temperature and thermal dose was measured (Eq. 2). When the thermal dose exceeded 240 mins at 43 °C [121], then that cell was marked with red colour indicating the

production of lesion. Figure 10.9 shows the flowchart of the simulator that evaluated the heating in the pre-focal heating for a specific navigation algorithm. The pre-focal heating simulator which was a fast and useful tool was inserted in the main software of the HIFU system. This simulator with short execution time is a very useful tool for the HIFU users in deciding which motion algorithm to use.
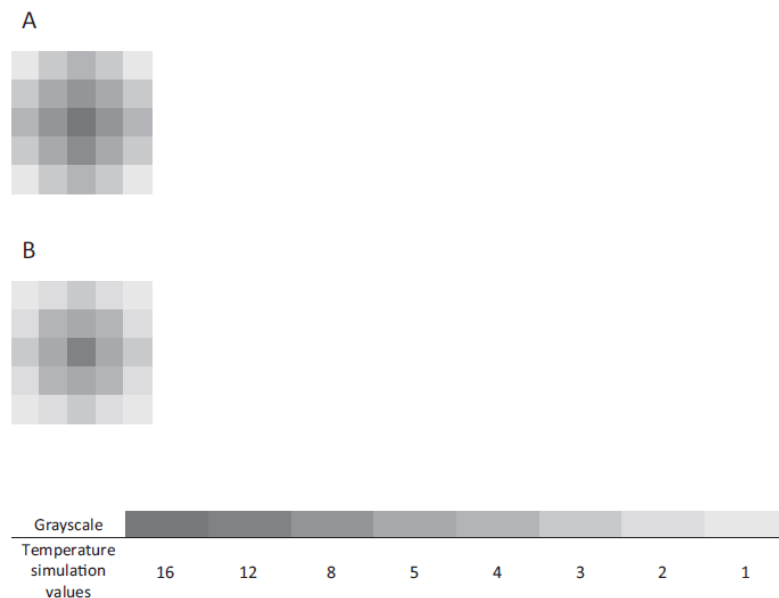
Figure 10.8: (A) Typical temperature profile at a plane 5 mm from the focal area at the end of the 5 s pulse which was used in the simulator, and (B) the corresponding temperature profile at 10 mm from the focal area. For simplicity, and speed, the temperatures were rounded-off to the nearest integer.

10.2.6 Experimental evaluation

10.2.6.1 HIFU system

The HIFU system consists of a signal generator (HP 33120A, Agilent technologies, Englewood, CO, USA), an RF amplifier (250 W, AR, Souderton, PA, USA), and a spherical transducer made from piezoelectric ceramic (Etalon, Lebanon, IN, USA). The spherically focused transducer operates at 1 MHz, has focal length of 10 cm and diameter of 4 cm.

10.2.6.2 Robotic system

The HIFU system was controlled by a system of stepping motors (VXM, VELMEX INC, Bloomfield, NY, USA). The VXM is a high performance stepping motor controller powered at 240 V able to use simultaneously up to 4 motor drives with communication provided by an RS232 interface. The controlling software was written in Visual Basic Dot Net (Microsoft, Redmond, Washington, USA). For the needs of this study only two axes (x-y) were used.
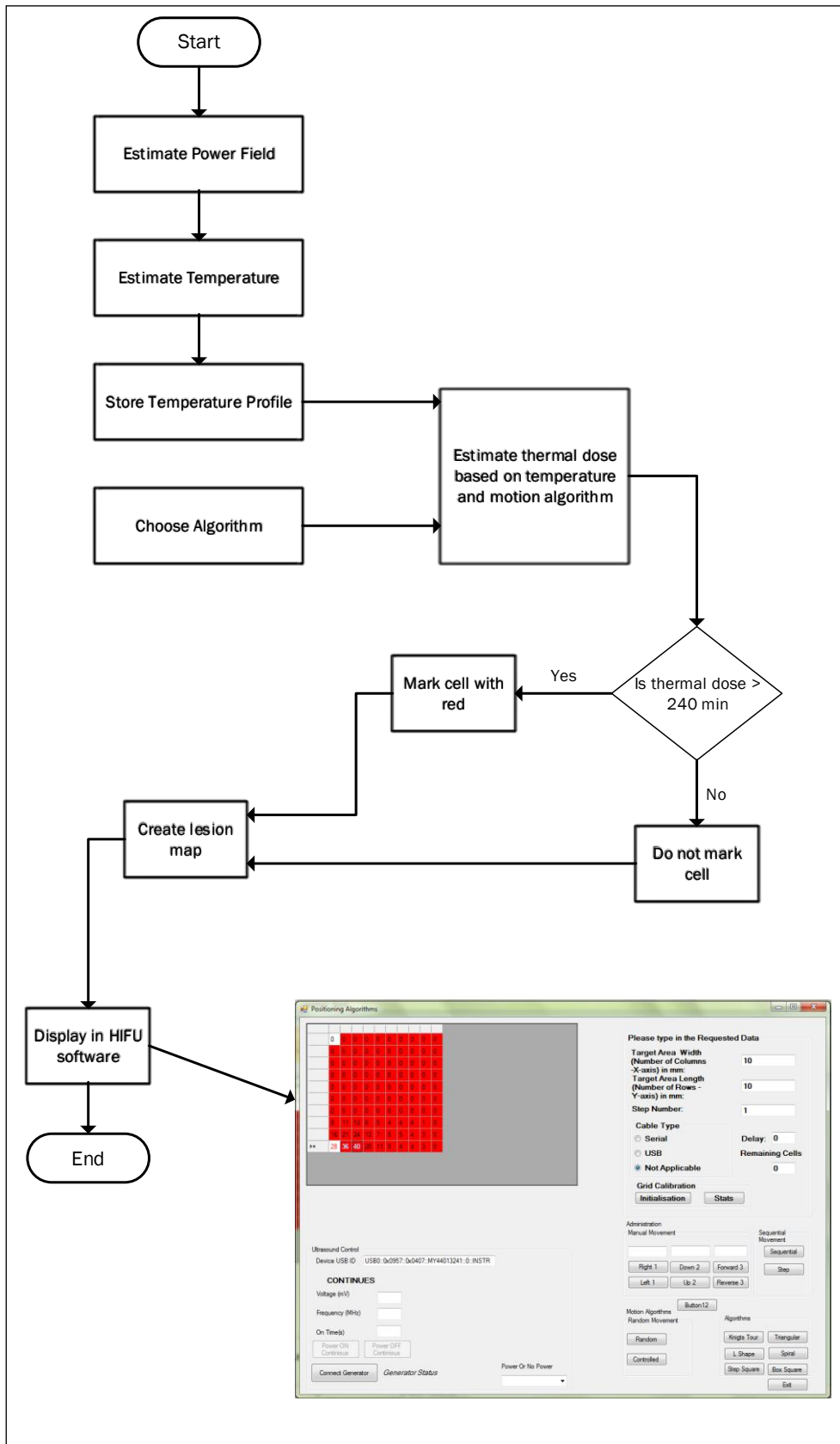
Figure 10.9: Flowchart of the lesion map simulator.

10.2.6.3 Gel phantom

The heating of the algorithms in the pre-focal region was evaluated in a commercial gel phantom (ONDA Corporation). The gel under evaluation was placed in a degassed water tank. The transducer was placed on the arm of the positioning device and was immersed in the water tank, thus providing good acoustical coupling between the gel and transducer. The attenuation of the gel as reported by the manufacturer was 0.6 dB-cm at 1 MHz [122].

10.3 Results

Figure 10.10A shows the 10 x 10 lesion map for the sequential algorithm at a near-field plane 5 mm from the focal region. Note that almost the entire area was covered with thermal damage. The Euler algorithm (Figure 10.10B) exhibited similar severe heating problems having almost 50 % of the area ablated. Problems with excessive heating especially in the central area of the pre-focal region were encountered also with the triangular algorithm (Figure 10.10C). The square algorithm produced minimal heating in the pre-focal (Figure 10.10D). The random algorithm (Figure 10.10E) produced unwanted heating in some locations depending on the navigation of the grid (which was random). Finally, the spiral square algorithm (Figure 10.10F) produced heating only in a small area in the center (3 x 3 grid) which was attributed to the navigation scheme of this algorithm. This algorithm created large steps in the exterior, and unavoidably small steps in the interior.
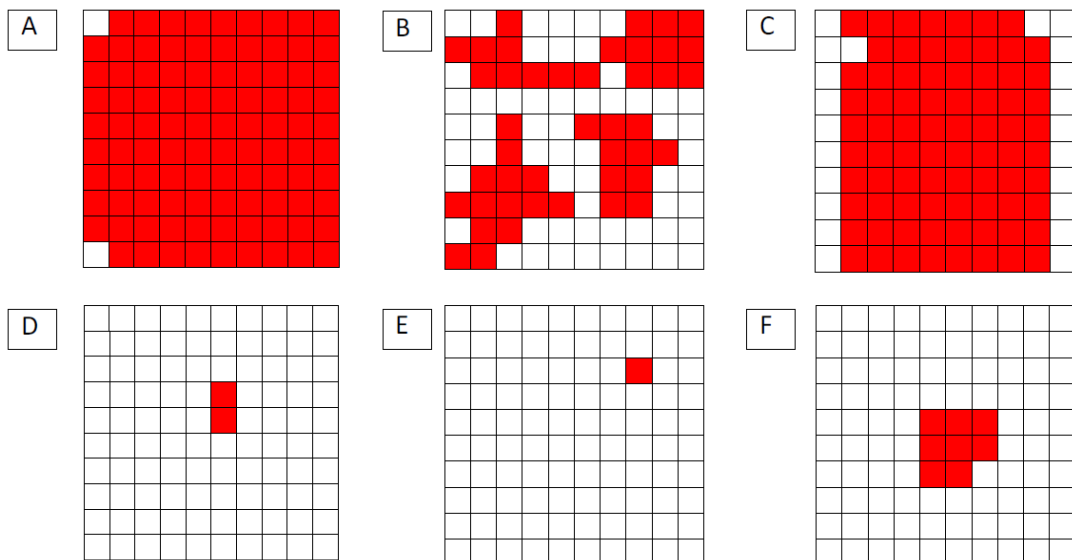
Figure 10.10: Simulated lesion map in the phantom gel for a 10 x 10 grid (step = 2 mm) at a pre-focal plane 5 mm from the focal region, with a 4 cm diameter single element transducer, focusing at 10 cm and operating at 1 MHz. Focal depth was 2 cm. (A) Sequential, (B) euler, (C) triangular, (D) square, (E) random, and (F) square spiral.

Figure 10.11A shows a photo of a gel cut 5 mm from the lowest part of the focal zone for the sequential algorithm demonstrating that all the area was covered with thermal damage. The Euler algorithm (figure 10.11B) demonstrated several areas of heating. Severe heating in most of the area was encountered also with the triangular algorithm (figure 10.11C). The square algorithm produced minimal heating in the pre-focal field (figure 10.11D). The random algorithm (figure 10.11E) produced unwanted heating in three random locations. Finally, the spiral square algorithm (figure 10.11F) produced heating only in a small area in the central part.
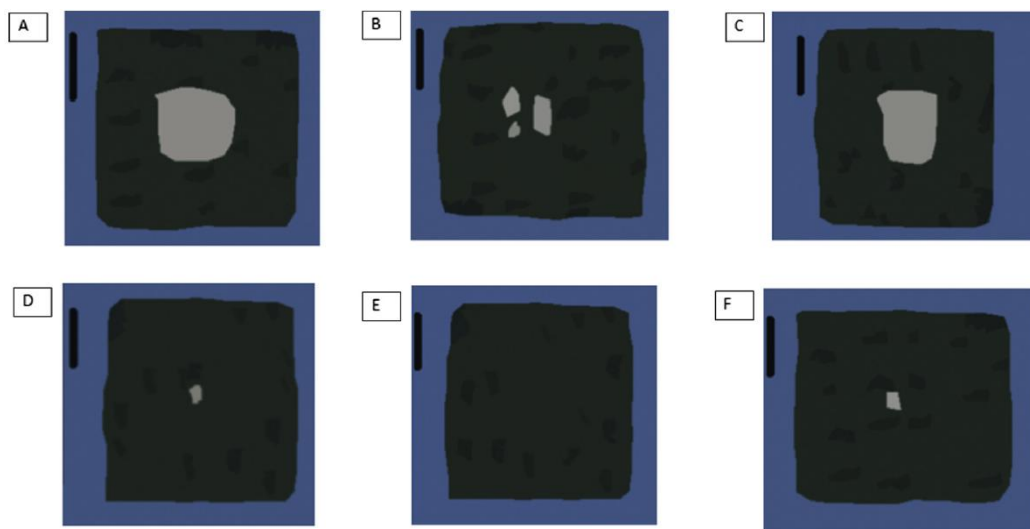
Figure 10.11: Photo of lesion in the phantom gel for a 10 x 10 grid (step = 2 mm) at a pre-focal plane 5 mm from the focal region, with a 4 cm diameter single element transducer, focusing at 10 cm and operating at 1 MHz. Focal depth was 2 cm. (A) Sequential, (B) euler, (C) triangular, (D) square, (E) random, and (F) square spiral. Bar = 10 mm.

The three promising algorithms (square, random, spiral square) were improved further. Since the square and spiral square algorithms exhibited heating only in the last 10 grid movements, a 10 s delay was used in these last 10 movements. For the random algorithm, a safety feature was added that does not allow spacing between movements that was smaller than 3 steps. Additionally, for the random algorithm if the spacing was 3 spatial steps, then a 10 s delay was used. Figure 10.12A shows the simulated lesion map cut 5 mm from the lowest part of the focal zone for the improved square algorithm demonstrating that no thermal damage was created in the pre-focal region. Same results were observed with the improved random algorithm (figure 10.12B) and improved spiral square algorithm (figure 10.12C). Figure 10.12D shows a photo of a gel cut 5 mm from the lowest part of the focal zone for the square algorithm demonstrating that no thermal damage was created in the pre-focal region. Same results were observed with the random (figure 10.12E) and spiral square (figure 10.12F).
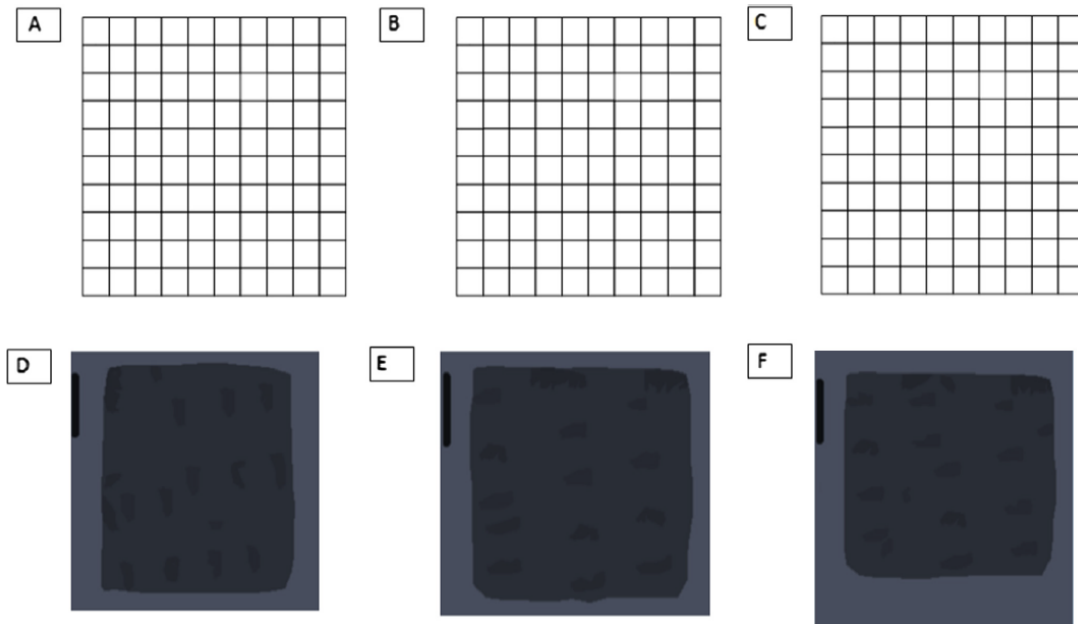
Figure 10.12: Simulated lesion map for a 10 x 10 grid (step = 2 mm) at a pre-focal plane, 5 mm from the focal region, with a 4 cm diameter single element transducer, focusing at 10 cm and operating at 1 MHz. (A) Improved square algorithm, (B) improved random algorithm, and (C) improved square spiral algorithm. Corresponding photos in the gel phantom, (D) improved square algorithm, (E) improved random algorithm and (F) improved square spiral algorithm. Bar = 10 mm.

Table 10.1 shows the time performance of each algorithm using the proposed robotic system. The robot time with no delay is shown in the second column. Obviously the fastest algorithm was the sequential (102 s), since each new grid point was one spatial step away from the previous. The second fastest was the triangular (207 s) since each grid point was very close to the previous point. Similarly, the Euler algorithm was the third fastest (219 s). The spiral square was fourth (306 s) and the random algorithm was fifth. The random algorithm's speed varied between 370 s and 417 s (20 trials tested) because as the name implies, the selection of the next step was randomly selected. Finally, the square algorithm was the slowest (472 s) since the steps between successive grid points were large at the beginning, and decreased at the end.

Table 10.1:Time performance of each algorithm using the proposed robotic system for the 6 different algorithms.

Algorithm	R robot time (with no delay) (s)	Delay needed to eliminate completely near field heating (s)	Number of points that delay was used	S scanning time (s)	T=R+ Total time = Robot time+ Scanning time (s)	Total time (min)	Reduction in time compared to maximum (%)
Sequential	102	60	100	6000	6102	102	-
Euler	219	30	100	3000	3219	54	49
Triangular	207	45	100	4500	4707	78	23.5
Square	472	10	10	100	572	9.5	90.7
Random	370-413	10	5-10	50-100	420-513	7-8.55	93.13-91.66
Square spiral	306	10	10	100	406	6.76	93.4

Since the simulation model was proven quite successful in predicting the thermal maps as confirmed by the experimental data, we proceeded with further simulations in order to find the delay needed for each algorithm to eliminate completely the pre-focal heating. These results which are very important are presented in table 10.1. Column 3 shows the delay needed to eliminate pre-focal heating completely, and column 4 shows the number of grid points that required such delay. The sequential, Euler and triangular needed a delay to be applied in all 100 grids points. The spiral and square algorithms require a 10 s delay in the last 10 grid points (interior of the algorithms) as demonstrated in figure 10.12. In the random algorithm a 10 s delay was needed when a successive grid point was within 3 spatial steps (usually varies between 5-10 grid points).

Table 10.2 shows the execution time using the simulator for the 6 different algorithms ranging from 16.25 s to 19.89 s. This table proved that the proposed simulator, which can be used in the software of HIFU systems, was quite fast. This simulator must guide the users in selecting the right algorithm that eliminates the pre-focal heating.

Table 10.2: Execution time using the simulator for the 6 different algorithms.

Algorithm	Time (s)
Sequential	16.25
Euler	19.92
Triangular	20.01
Square	20.49
Random	19.89
Square spiral with step	20.62

Chapter 11 Conclusion

The different robots developed in this study can provide a tool for focused ultrasound guidance in MR environment. MRI is the only method which enables detection of temperature changes completely non-invasively. Each robot was tested in MRI to evaluate the compatibility, positioning accuracy and functionality. The small dimensions of the focus (diameter of a few millimeters) require multiple overlapping lesions hence, automation can reduce treatment time. To produce overlapping lesions to ablate large regions, the transducer must be maneuvered with small steps. The use of MR thermometry enables focus localization to safely guide the ultrasound with accuracy to the target.

To develop the robots, non magnetic materials were used to avoid imaging distortion or potential safety hazards. ABS plastic was used for the structure of the robots, and the mounting hardware such as screws and shafts was made out of copper and brass. The water container was made from clear acrylic plastic for visual inspection. The motors moving the stages operate with piezoelectric principles.

After extensive testing of each robot some of its features were revised to improve reliability and accuracy. In the latest version (see Chapter 4) more complex mechanisms were introduced which significantly improved the motion. The size of latest versions became more compact as a result of the evolution and the performance (motion range, and accuracy) was improved. The proposed positioning devices can be used with all the commercial MRI scanners, since they can be placed on the MRI table.

A primary purpose of these robots is to deliver ultrasound into the various organs for the treatment using HIFU. By utilizing continuous ultrasound cell destruction can be achieved. Experiments were conducted to ONDA gel and agar phantoms due to similar acoustic properties, with tissue. Thermal protocols for various ultrasonic transducers were conducted in ONDA gel. The lesions produced in ONDA gel, have the same position, size and shape as those produced in real tissue. The lesions appear as white solids inside the gel enabling the accurate calculation of the lesions. The agar phantoms were used to investigate the temperature profile of the ultrasonic protocols. The protocols were also tested in dead rabbit and porcine tissue. All these experiments demonstrated the functionality of the robotic system and of the HIFU transducers.

To ensure various organs are accessible in future clinical trials using these robots, various coupling mechanisms were tested. The positioning device with the use of different coupling devices was capable of targeting using bottom to top, top to bottom and lateral approaches. Additionally two angular stages (see Chapter 5 and Chapter 6) were designed to allow focusing through different angles to avoid delicate nerves and vital portions inside the brain. The two different angular stages improved the targeting ability for two different configurations (bottom to top and lateral) by enabling ultrasound propagation through alternative trajectories. The use of angular axis in robotic systems of MRgFUS is mandatory because structures (for examples nerves and blood vessel) can be avoided.

The 2 DOF immersed MRI-compatible focused ultrasound system (Chapter 7) designed for use with small animals. The accuracy of the proposed robotic system was evaluated with MRI by performing motion paths and comparing measured with desired positions. The spatial accuracy of the focused ultrasound heating was evaluated using MR thermometry in experiments in custom made agar/silica/milk gel phantom. This robot can be adjusted in the future to be used for brain ablation with the patient lying in supine position.

Testing showed that the robots didnot significantly affect MR images (Chapter 9). Three categories that describe the MR compatibility properties of a device were defined by the American Society of Testing and Materials (ASTM) [96]. MR Safe "refers to an item that poses no known physical risks in all MR environments, not taking into account image artifacts". MR Conditional is "an item that has been demonstrated to pose no known hazards in a specified MR environment with specified conditions of use", and MR unsafe "an item that is known to pose hazards in MR environments" [96]-[75]. The proposed devices are categorized as MR conditional, because during activation of the motors the SNR drops down to 2,11. However, during a sonication the positioning device has to be idle, to allow the temperature to increase. Therefore, the operation of the positioning device does not restricted in any way. Moreover, the MR compatibility test demonstrated that it is possible to activate the transducer during imaging for MR thermometry with no significant impact to the image quality.

The immersed robotic system was capable of positioning the ultrasound focus in two dimensions, with good spatial accuracy and can be used to deliver multiple heating

spots along a desired grid. The MRI compatibility of the system enables simultaneous imaging and motion with the system without severe mutual interference. These features were obtained through the use of custom-made non-magnetic linear stages driven by piezoceramic motors and MR compatible optical encoders.

Both the motors and encoders are driven by sinusoidal signals at frequencies (few KHz) which are much lower than the bandwidth of the MR scanner (64 MHz) enabling good isolation between the robot and MRI system.

The range of motion of the system is sufficient for small animal studies, but could easily be extended to cover applications in humans. It can be extended to over 30 cm in the x-axis and close to 30 cm in the y –axis (there is limitation due to the bore diameter in this direction) with the current design if desired.

The robotic system is 14 cm in height. In the MRI table there is 5 cm space, therefore if MRI table modifications are done; this system can be inserted in the MRI table, leaving 9 cm of structure above the table. With design modifications, this can be lowered to 6 cm. Therefore, this system can be easily converted into a commercial product for use in humans. Potential applications in humans could be liver, kidney, brain, fibroids, bones and breast.

The heating experiments demonstrated the feasibility of accurate temperature imaging using the PRF technique during rectangular scanning, enabling this system to continuously heat volumes greater than the focal volume of an individual shot. The proposed grid was easily selected and modified, allowing greater functionality and reduced complexity than phased array systems for customized studies during small animal research. This system is envisioned as being suitable for investigating novel therapeutic strategies with the intent to be used in conjunction with phased array systems for clinical use.

A simple and fast simulation model was implemented, which produced lesion maps for different algorithms of the robotic HIFU system (Chapter 10). These lesion maps were based on simulated temperatures, and thermal dose. This simulation model although simple, seems to correctly predict the lesion map as confirmed by the experiments performed in the gel phantom.

Six algorithms were evaluated in the proposed study. The sequential and triangular algorithm produced severe heating in a plane 5 mm away from the focal zone with

zero delay. This was due to the proximity between successive movements of the robotic system. Due to the proximity between successive movements of the robotic system, the Euler algorithm decreased the pre-focal heating, but yet there was severe heating in the plane under evaluation. The spatial step with the Euler algorithm was larger than the spatial step of the sequential algorithm. The remaining three algorithms (square, random, and spiral square) reduced the pre-focal heating substantially even with zero delay between sonications. Both spiral square and square algorithms moved at large spatial steps in the exterior of the grid and moved at smaller steps in the interior. In the interior the movement steps were inevitably small, and this produced near-field heating in the interior (3 x 3 square grid). Finally, the random algorithm although slow due to the random selection of movements, produced minimal heating at random locations (usually in 2-4). Although minimal, this heating had to be avoided.

The sequential, Euler and triangular algorithms needed long delay between sonications in order to eliminate pre-focal heating completely. The delay needed for the sequential algorithms as derived from our model was 60 s, which is in very good agreement with the values reported by Fan and Hynynen [108]. The delay needed for the Euler and triangular algorithms were 30 and 45 s respectively. In order to eliminate completely the pre-focal heating for the square, and spiral square algorithms, a delay of 10 s was used in the last 10 movements. This 10 s delay that increased treatment time, eliminated completely the pre-focal heating. An improved version of the random algorithm forbids any successive movement to be smaller than 3 spatial steps. Additionally by using a 10 s delay for these proximal movements (up to 3 spatial steps) as an additional safety, eliminated completely the pre-focal heating at the expense of additional treatment time.

Usually for HIFU treatment, the sequential algorithm was used which required long delays in the order of 60 s [108]. With a 5 s HIFU pulse and assuming 100 movements as chosen in this paper, the treatment time was 100 x 60 (6000 s) + 102 s (robot time), which totals 6102 s or 102 min. It was shown that with the square spiral algorithm the treatment time was reduced to 10 x 10 s (delay in the last 10 movements) + 306 s (robot time) which totals 406 s or 6.76 min. Therefore, a reduction of approximately 93 % was achieved in the treatment time. Improved treatment time relative to the sequential was achieved also with the square algorithm (9.5 min) and with the random algorithm (7-8.55 min). Thus, either the square spiral, or square, or random algorithms

eliminated pre-focal heating with reduced treatment time (90-93 % reduction). This simulation model, which can be executed roughly in 20 s, could be used by the operators of the dedicated HIFU software.

The ablated gel volume that we evaluated was 2 cm x 2 cm (plane perpendicular to transducer) x 2 cm (lesion length) or 8 cm^3. With the square spiral algorithm this was ablated in 6.76 min or 0.1126 h. This rate of ablated tissue which is approximately 71 cm3/hour compares much better than what was proposed in a previous study [109] for a similar transducer and pulse duration (5 s) with a rate of 1.7 cm^3/h. For phased arrays [109] the rates of ablated volume were higher (7.2-11.6 cm^3/h) for a similar pulse duration (5 s). Therefore we have shown that by using non-linear algorithms we can decrease the treatment time with complete elimination of pre-focal heating, thus improving drastically the rate of ablated volume.

The phased array study by Payne et al. [123] showed that both simulation and experimental results with electronically steering of the ultrasound beam using a 256-element phased array, significantly increases the thermal dose deposited in the pre-focal field when compared with the same beam trajectory executed through mechanical steering only. In that study a sequential electronic steering trajectory was used with 60 s cooling time and spacing of 1 cm between sonications. This large spacing underestimated the thermal build up in the pre-focal area. Phased arrays produced more pre-focal heating due to a combination of beam overlap and increased grating lobe clutter. Recently, Ellens and Hynynen [124] presented a simulation study with a flat ultrasonic transducer arrays, and with 6500 small elements operating at 500 kHz. In this study targets with geometry of fibroids were successfully ablated without causing damage in the near of far-field.

Nonlinear effects are known to be involved in lesion production by HIFU [125]. The relative role of these nonlinear phenomena is not yet well understood because models that represent heating due to HIFU exposure do not exist. Nonlinear effects appear at high acoustic pressure and are responsible for the acceleration of heating, and the distortion of the thermal field. The effect of acoustic nonlinearities results in generation of higher harmonics during the propagation of ultrasound. The proposed model does not include nonlinear effects which are expected to affect the pre-focal region.

The proposed model is simplistic in the sense that assumes a homogenous tissue. It ignores tissue heterogeneities that normally exist, and obstacles such as bone or ribs. Moreover, it ignores interfaces between two layers that definitely affect the thermal response [126]. Because of the simplicity of the proposed model, it is most likely to be more accurate for the application of thermal ablation of fibroids [127]; a target with minimal ultrasonic obstacles. The delay used between successive ablations in a typical fibroid treatment [127] is between 90 and 120 s, which often results to treatment times of 3 h. Therefore, the selection of the optimum algorithm could result to significant reduction of treatment time and thus, reducing patient discomfort.

In the future, this simulator will be tested with other ultrasonic parameters, such as the frequency, degree of focusing, pulse duration, and focal depth. The invention of this pilot study was to demonstrate that the navigation algorithms play the most important role in reducing pre-focal heating. By evaluating in the future more commercially available protocols for oncological targets, it will be possible to reduce the treatment time. This algorithms need to be tested also for the phased array technology, since this technology is dominating the clinical trials [128]- [95].

11.1 Future work

The positioning devices in the future can be used with a phased array ultrasonic transducer. This will establish positioning using electronic steering. In addition the functionality of the immersed robot for animals will be improved since it will allow targeting in various depths for clinical test. The combination of mechanical and electronically steering of the beam will allow better positioning and it will be possible to reduce the treatment time. Steering for small movements can be performed electronically. For larger regions a combination of both will be used. Also since the mechanical motion can cover larger area, smaller phased arrays are required with fewer elements thus, reducing the complexity of the system. In addition each element can be adjusted to compensate for phase shift caused by inhomogeneities of the tissue and ultrasonic obstacles such as skull bone to retain sharp focus to the target.

This positioning device will be expanded for biopsy interventions and treatment of multiple organs accessible to HIFU. With the use of different coupling mechanisms designed for use in conjunction with the same positioning device (Chapter 4) will be able to reach different organs. The coupling described in section 9.12 potentially will be possible to be used for treatment of fibroids or organs accessible in the abdominals,

such as kidney and liver. The patient will be placed on the table in the supine position as shown in Figure 11.1. In this position the patient will be more comfortable during the treatment. With the devices that are currently available, the patient must be placed in the prone positioned which may be uncomfortable during long HIFU sessions.
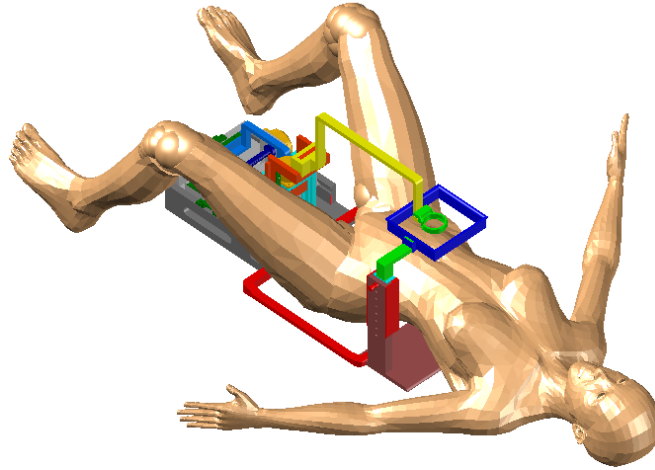
Figure 11.1: Drawing that demonstrated the placement of the patient using the coupling for fibroid treatment.

To customize this positioning device for biopsy interventions an end effector will be introduced as shown in Figure 11.2. The end effector will be attached to the Z-stage via a coupling for easy swap between the angular stages (Chapter 5 and Chapter 6). The biopsy device will be used to guide a biopsy needle with MR guidance. After the installation of the end effector to the positioning device, it will be converted to a 6 DOF. The extra 3 DOF of the biopsy arm will move the needle around in two angular axes and a third for moving the needle. Similar principles will be adopted with the phi-stage for the two angular motions to ensure accurate and reliable motion.
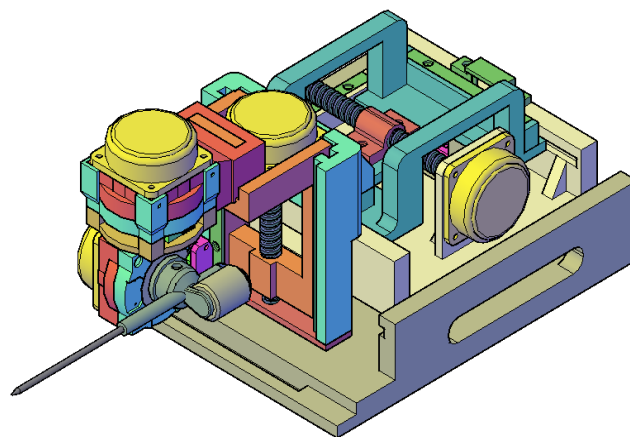
Figure 11.2: Drawing of the positioning device (Version 3) with the use of the end effector for biopsy interventions

As a continuation of the prostate robotic system introduced by Yiallouras et al. [76] a transrectal probe was introduced. The probe is made of ABS plastic and includes an ultrasonic transducer (f=2.5 MHz, R=6 cm, d=30 mm) merged with the shaft which was attached onto the angular stage of the device. The probe includes two nozzles for the water circulation in order to fill the probe with degassed water. To secure the water inside the probe it was covered with a latex bag and sealed against the probe. MRI images (Figure 11.3) showed well defined images of the transducer with minimal effect to the image quality. This probe could potentially be used also with the current positioning device in order to access prostate.
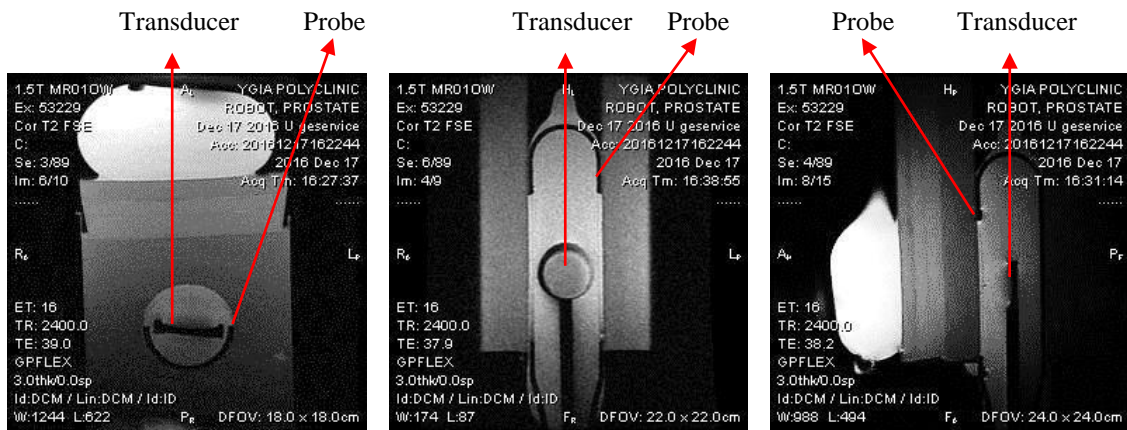
Figure 11.3: MRI images of the transrectal probe in a rectum phantom. The imaging parameters were: T2 TFE pulse sequence, ETL=16, TR=2400 ms, TE=37.9 ms, FOV=24 x 24 cm.

The probe functionality was tested in agar phantom which mimics the rectum. After continious sonications of 60 s, the temperature was raised approximately 15℃. MR thermometry maps shown in Figure 11.4, demonstrated the efficicacy of this coupling method.
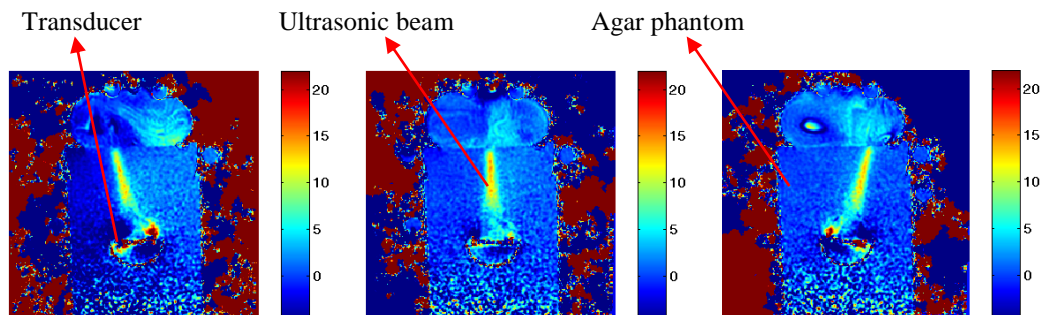
Figure 11.4: MR thermometry maps demonstrating the efficacy of the coupling method. The images acquired with T1-SPGR pulse sequence with TR=38.5 ms, TE=20 ms, FOV=21 x21 cm, matrix=128 x 128, NEX=1.

151

Also a more complex simulation model can be developed that will include calculation for different tissue properties and phase corrections for the phased array systems. The simulations can be used to predict any complications of the treatment and compare possible trajectories for choosing the optimal path. These improvements can be used to improve treatments time and significantly reduce the risks for clinical trials.

References

[1] J. G. Lynn, R. L. Zwemer, A. J. Chick, and A. E. Miller, "A NEW METHOD FOR THE GENERATION AND USE OF FOCUSED ULTRASOUND IN EXPERIMENTAL BIOLOGY.," *J. Gen. Physiol.*, vol. 26, no. 2, pp. 179–193, 1942.

[2] W. J. Fry and F. J. Fry, "Fundamental Neurological Research and Human Neurosurgery Using Intense Ultrasound," *IRE Trans. Med. Electron.*, vol. ME-7, no. 3, pp. 166–181, Jul. 1960.

[3] R. MEYERS, W. J. FRY, F. J. FRY, L. L. DREYER, D. F. SCHULTZ, and R. F. NOYES, "Early experiences with ultrasonic irradiation of the pallidofugal and nigral complexes in hyperkinetic and hypertonic disorders.," *J. Neurosurg.*, vol. 16, no. 1, pp. 32–54, Jan. 1959.

[4] K. Hynynen and F. A. Jolesz, "Demonstration of Potential Noninvasive Ultrasound Brain Therapy Through an Intact Skull," *Ultrasound Med. Biol.*, vol. 24, no. 2, pp. 275–283, Feb. 1998.

[5] N. Vykhodtseva, V. Sorrentino, F. A. Jolesz, R. T. Bronson, and K. Hynynen, "MRI detection of the thermal effects of focused ultrasound on the brain," *Ultrasound Med. Biol.*, vol. 26, no. 5, pp. 871–880, 2000.

[6] C. M. C. Tempany, E. a Stewart, N. McDannold, B. J. Quade, F. a Jolesz, and K. Hynynen, "MR imaging-guided focused ultrasound surgery of uterine leiomyomas: a feasibility study.," *Radiology*, vol. 226, pp. 897–905, 2003.

[7] E. a. Stewart, J. Rabinovici, C. M. C. Tempany, Y. Inbar, L. Regan, B. Gastout, G. Hesley, H. S. Kim, S. Hengst, and W. M. Gedroye, "Clinical outcomes of focused ultrasound surgery for the treatment of uterine fibroids," *Fertil. Steril.*, vol. 85, no. 1, pp. 22–29, 2006.

[8] H. S. Kim, J.-H. Baik, L. D. Pham, and M. a Jacobs, "MR-guided high-intensity focused ultrasound treatment for symptomatic uterine leiomyomata: long-term outcomes.," *Acad. Radiol.*, vol. 18, no. 8, pp. 970–976, 2011.

[9] M. a. Behera, M. Leong, L. Johnson, and H. Brown, "Eligibility and accessibility of magnetic resonance-guided focused ultrasound (MRgFUS) for the treatment of uterine leiomyomas," *Fertil. Steril.*, vol. 94, no. 5, pp. 1864–1868, 2010.

[10] K. Funaki, H. Fukunishi, T. Funaki, and C. Kawakami, "Mid-term outcome of magnetic resonance-guided focused ultrasound surgery for uterine myomas: From six to twelve months after volume reduction," *J. Minim. Invasive Gynecol.*, vol. 14, no. 5, pp. 616–621, 2007.

[11] C. Zini, "Ultrasound- and MR-guided focused ultrasound surgery for prostate cancer," *World J. Radiol.*, vol. 4, no. 6, p. 247, 2012.

[12] A. Napoli, M. Anzidei, C. De Nunzio, G. Cartocci, V. Panebianco, C. De Dominicis, C. Catalano, F. Petrucci, and C. Leonardo, "Real-time magnetic resonance-guided high-intensity focused ultrasound focal therapy for localised prostate cancer: Preliminary experience," *Eur. Urol.*, vol. 63, pp. 395–398, 2013.

[13] E. C. Gombos, D. F. Kacher, H. Furusawa, and K. Namba, "Breast focused ultrasound surgery with magnetic resonance guidance.," *Top. Magn. Reson. Imaging*, vol. 17, pp. 181–188, 2006.

[14] H. Furusawa, K. Namba, S. Thomsen, F. Akiyama, A. Bendet, C. Tanaka, Y. Yasuda, and H. Nakahara, "Magnetic Resonance-Guided Focused Ultrasound Surgery of Breast Cancer: Reliability and Effectiveness," *J. Am. Coll. Surg.*, vol. 203, pp. 54–63, 2006.

[15] A. Khiat, D. Gianfelice, M. Amara, and Y. Boulanger, "Influence of post-treatment delay on the evaluation of the response to focused ultrasound surgery of breast cancer by dynamic contrast enhanced MRI," *Br. J. Radiol.*, vol. 79, pp. 308–314, 2006.

[16] D. Gianfelice, A. Khiat, M. Amara, A. Belblidia, and Y. Boulanger, "MR imaging-guided focused ultrasound surgery of breast cancer: Correlation of dynamic contrast-enhanced MRI with histopathologic findings," *Breast Cancer Res. Treat.*, vol. 82, pp. 93–101, 2003.

[17] D. Gianfelice, A. Khiat, Y. Boulanger, M. Amara, and A. Belblidia, "Feasibility of magnetic resonance imaging-guided focused ultrasound surgery as an adjunct to tamoxifen therapy in high-risk surgical patients with breast carcinoma.," *J. Vasc. Interv. Radiol.*, vol. 14, pp. 1275–1282, 2003.

[18] K. Hynynen, O. Pomeroy, D. N. Smith, P. E. Huber, N. J. McDannold, J. Kettenbach, J. Baum, S. Singer, and F. a Jolesz, "MR imaging-guided focused ultrasound surgery of fibroadenomas in the breast: a feasibility study.," *Radiology*, vol. 219, no. 11, pp. 176–185, 2001.

[19] A. Okada, T. Murakami, K. Mikami, H. Onishi, N. Tanigawa, T. Marukawa, and H. Nakamura, "A case of hepatocellular carcinoma treated by MR-guided focused ultrasound ablation with respiratory gating.," *Magn. Reson. Med. Sci.*, vol. 5, no. 3, pp. 167–171, 2006.

[20] D. Kopelman, Y. Inbar, A. Hanannel, G. Dank, D. Freundlich, A. Perel, D. Castel, A. Greenfeld, T. Salomon, M. Sareli, A. Valeanu, and M. Papa, "Magnetic resonance-guided focused ultrasound surgery (MRgFUS). Four ablation treatments of a single canine hepatocellular adenoma.," *HPB (Oxford).*, vol. 8, pp. 292–298, 2006.

[21] A. Napoli, M. Anzidei, B. C. Marincola, G. Brachetti, F. Ciolina, G. Cartocci, C. Marsecano, F. Zaccagna, L. Marchetti, E. Cortesi, and C. Catalano, "Primary pain palliation and local tumor control in bone metastases treated with magnetic resonance-guided focused ultrasound.," *Invest. Radiol.*, vol. 48, pp. 351–8, 2013.

[22] J. E. Lee, S. Yoon, K. A. Kim, J. T. Lee, L. Shay, and K. S. Lee, "Successful Use of Magnetic Resonance-Guided Focused Ultrasound Surgery for Long-Term Pain Palliation in a Patient Suffering from Metastatic Bone Tumor" Journal of the Korean Society of radiology, vol. 65, no. 2, pp. 133–138, 2011.

[23] D. Kopelman, Y. Inbar, a. Hanannel, R. M. Pfeffer, O. Dogadkin, D. Freundlich, B. Liberman, and R. Catane, "Magnetic resonance guided focused ultrasound surgery. Ablation of soft tissue at bone-muscle interface in a porcine model," *Eur. J. Clin. Invest.*, vol. 38, pp. 268–275, 2008.

[24] R. Catane, a. Beck, Y. Inbar, T. Rabin, N. Shabshin, S. Hengst, R. M. Pfeffer, a. Hanannel, O. Dogadkin, B. Liberman, and D. Kopelman, "MR-guided focused ultrasound surgery (MRgFUS) for the palliation of pain in patients with bone metastases - Preliminary clinical experience," *Ann. Oncol.*, vol. 18, no. October 2006, pp. 163–167, 2007.

[25] R. Bihrle, R. S. Foster, N. T. Sanghvi, F. J. Fry, and J. P. Donohue, "High-

intensity focused ultrasound in the treatment of prostatic tissue," *Urology*, vol. 43. pp. 21–26, 1994.

[26] A. Gelet, J. Y. Chapelon, J. Margonari, Y. Theillère, F. Gorry, R. Souchon, and R. Bouvier, "High-intensity focused ultrasound experimentation on human benign prostatic hypertrophy.," *Eur. Urol.*, vol. 23 Suppl 1, pp. 44–47, 1993.

[27] A. Pulkkinen, B. Werner, E. Martin, and K. Hynynen, "Numerical simulations of clinical focused ultrasound functional neurosurgery.," *Phys. Med. Biol.*, vol. 59, no. 7, pp. 1679–700, Apr. 2014.

[28] J. L. Thomas, "Ultrasonic beam focusing through tissue inhomogeneities with a time reversal mirror: application to transskull therapy," *IEEE Trans. Ultrason. Ferroelectr. Freq. Control*, vol. 43, pp. 1122–1129, 1996.

[29] W. J. FRY, J. W. BARNARD, E. J. FRY, R. F. KRUMINS, and J. F. BRENNAN, "Ultrasonic lesions in the mammalian central nervous system.," *Science*, vol. 122, pp. 517–518, 1955.

[30] A. N. Guthkelch, L. P. Carter, J. R. Cassady, K. H. Hynynen, R. P. Iacono, P. C. Johnson, E. A. M. T. Obbens, R. B. Roemer, J. F. Seeger, D. S. Shimm, and B. Steal, "Treatment of malignant brain tumors with focused ultrasound hyperthermia and radiation: results of a phase I trial," *J. Neurooncol.*, vol. 10, pp. 271–284, 1991.

[31] K. M. Quan, D. J. Watmough, and J. R. Mallard, "Theoretical considerations in relation to the treatment of brain tumours by means of local hyperthermia generated by ultrasound fields.," *Eur. J. Surg. Oncol.*, vol. 17, pp. 454–465, 1991.

[32] M. Pernot, J.-F. Aubry, M. Tanter, J.-L. Thomas, and M. Fink, "High power transcranial beam steering for ultrasonic brain therapy," *Phys. Med. Biol.*, vol. 48, no. 16, pp. 2577–2589, Aug. 2003.

[33] K. Hynynen, G. T. Clement, N. McDannold, N. Vykhodtseva, R. King, P. J. White, S. Vitek, and F. a Jolesz, "500-Element Ultrasound Phased Array System for Noninvasive Focal Surgery of the Brain: a Preliminary Rabbit Study With Ex Vivo Human Skulls.," *Magn. Reson. Med.*, vol. 52, no. 1, pp. 100–7, Jul. 2004.

[34] X. Yin and K. Hynynen, "A numerical study of transcranial focused ultrasound beam propagation at low frequency.," *Phys. Med. Biol.*, vol. 50, no. 8, pp. 1821–36, Apr. 2005.

[35] P. J. White, G. T. Clement, and K. Hynynen, "Local frequency dependence in transcranial ultrasound transmission.," *Phys. Med. Biol.*, vol. 51, no. 9, pp. 2293–305, May 2006.

[36] A. Y. Ammi, T. D. Mast, I. H. Huang, T. A. Abruzzo, C. C. Coussios, G. J. Shaw, and C. K. Holland, "Characterization of Ultrasound Propagation Through Ex-vivo Human Temporal Bone," *Ultrasound Med. Biol.*, vol. 34, pp. 1578–1589, 2008.

[37] F. Marquet, M. Pernot, J.-F. Aubry, G. Montaldo, L. Marsac, M. Tanter, and M. Fink, "Non-invasive transcranial ultrasound therapy based on a 3D CT scan: protocol validation and in vitro results.," *Phys. Med. Biol.*, vol. 54, no. 9, pp. 2597–613, May 2009.

[38] S. J. Monteith, R. Medel, N. F. Kassell, M. Wintermark, M. Eames, J. Snell, E. Zadicario, J. Grinfeld, J. P. Sheehan, and W. J. Elias, "Transcranial magnetic

resonance-guided focused ultrasound surgery for trigeminal neuralgia: a cadaveric and laboratory feasibility study.," *J. Neurosurg.*, vol. 118, no. February, pp. 319–328, 2013.

[39] E. A. Kaye, Y. Hertzberg, M. Marx, B. Werner, G. Navon, M. Levoy, and K. B. Pauly, "Application of Zernike polynomials towards accelerated adaptive focusing of transcranial high intensity focused ultrasound," *Medical Physics*, vol. 39, no. October. p. 6254, 2012.

[40] B. Larrat, M. Pernot, J.-F. Aubry, E. Dervishi, R. Sinkus, D. Seilhean, Y. Marie, a-L. Boch, M. Fink, and M. Tanter, "MR-guided transcranial brain HIFU in small animal models.," *Phys. Med. Biol.*, vol. 55, no. 2, pp. 365–88, Jan. 2010.

[41] J. Song, A. Pulkkinen, Y. Huang, and K. Hynynen, "Investigation of standing-wave formation in a human skull for a clinical prototype of a large-aperture, transcranial mr-guided focused ultrasound (MRgFUS) phased array: An experimental and simulation study," *IEEE Trans. Biomed. Eng.*, vol. 59, no. 2, pp. 435–444, 2012.

[42] N. Vykhodtseva, N. Mcdannold, H. Martin, R. T. Bronson, and K. Hynynen, "Apoptosis in ultrasound-produced threshold lesions in the rabbit brain," *Ultrasound Med. Biol.*, vol. 27, no. 1, pp. 111–117, 2001.

[43] K. Hynynen, N. McDannold, H. Martin, F. a Jolesz, and N. Vykhodtseva, "The threshold for brain damage in rabbits induced by bursts of ultrasound in the presence of an ultrasound contrast agent (Optison®)," *Ultrasound Med. Biol.*, vol. 29, no. 3, pp. 473–481, Mar. 2003.

[44] N. McDannold, M. Moss, R. Killiany, D. L. Rosene, R. L. King, F. a Jolesz, and K. Hynynen, "MRI-guided focused ultrasound surgery in the brain: tests in a primate model.," *Magn. Reson. Med.*, vol. 49, no. 6, pp. 1188–91, Jun. 2003.

[45] K. Hynynen, N. McDannold, G. Clement, F. a Jolesz, E. Zadicario, R. Killiany, T. Moore, and D. Rosen, "Pre-clinical testing of a phased array ultrasound system for MRI-guided noninvasive surgery of the brain--a primate study.," *Eur. J. Radiol.*, vol. 59, no. 2, pp. 149–56, Aug. 2006.

[46] M. a O'Reilly, A. Muller, and K. Hynynen, "Ultrasound insertion loss of rat parietal bone appears to be proportional to animal mass at submegahertz frequencies.," *Ultrasound Med. Biol.*, vol. 37, no. 11, pp. 1930–7, Nov. 2011.

[47] H.-L. Liu, C.-H. Fan, C.-Y. Ting, and C.-K. Yeh, "Combining microbubbles and ultrasound for drug delivery to brain tumors: current progress and overview.," *Theranostics*, vol. 4, no. 4, pp. 432–44, Jan. 2014.

[48] N. J. McDannold, N. I. Vykhodtseva, and K. Hynynen, "Microbubble contrast agent with focused ultrasound to create brain lesions at low power levels: MR imaging and histologic study in rabbits.," *Radiology*, vol. 241, no. 1, pp. 95–106, 2006.

[49] N. Vykhodtseva, N. McDannold, and K. Hynynen, "Induction of apoptosis in vivo in the rabbit brain with focused ultrasound and Optison.," *Ultrasound Med. Biol.*, vol. 32, no. 12, pp. 1923–9, Dec. 2006.

[50] C. D. Arvanitis, M. S. Livingstone, and N. McDannold, "Combined ultrasound and MR imaging to guide focused ultrasound therapies in the brain.," *Phys. Med. Biol.*, vol. 58, no. 14, pp. 4749–61, Jul. 2013.

[51] P. J. White, G. T. Clement, and K. Hynynen, "Longitudinal and shear mode ultrasound propagation in human skull bone.," *Ultrasound Med. Biol.*, vol. 32,

no. 7, pp. 1085–96, Jul. 2006.

[52] F. a Jolesz, I.-F. Talos, R. B. Schwartz, H. Mamata, D. F. Kacher, K. Hynynen, N. McDannold, P. Saivironporn, and L. Zao, "Intraoperative magnetic resonance imaging and magnetic resonance imaging–guided therapy for brain tumors," *Neuroimaging Clin. N. Am.*, vol. 12, no. 4, pp. 665–683, Nov. 2002.

[53] C. Damianou, K. Ioannides, and N. Milonas, "Positioning device for MRI-guided high intensity focused ultrasound system," *Int. J. Comput. Assist. Radiol. Surg.*, vol. 2, no. 6, pp. 335–345, Apr. 2008.

[54] K. Hynynen, A. Darkazanli, C. A. Damianou, E. Unger, and J. F. Schenck, "The usefulness of a contrast agent and gradient-recalled acquisition in a steady-state imaging sequence for magnetic resonance imaging-guided noninvasive ultrasound surgery.," *Invest. Radiol.*, vol. 29, pp. 897–903, 1994.

[55] N. Mylonas and C. Damianou, "MR compatible positioning device for guiding a focused ultrasound system for the treatment of brain deseases," *Int. J. Med. Robot. Comput. Assist. Surg.*, vol. 10, no. 1, pp. 1–10, Mar. 2014.

[56] F. A. Jolesz, "Magnetic Resonance Image-Guided Neurosurgery," *Hungarian Studies*, vol. 19. pp. 233–242, 2006.

[57] N. McDannold, R. L. King, F. a. Jolesz, and K. Hynynen, "The use of quantitative temperature images to predict the optimal power for focused ultrasound surgery: In vivo verification in rabbit muscle and brain," *Med. Phys.*, vol. 29, no. 3, p. 356, 2002.

[58] J. L. Foley, S. Vaezy, and L. a. Crum, "Applications of high-intensity focused ultrasound in medicine: Spotlight on neurological applications," *Appl. Acoust.*, vol. 68, no. 3, pp. 245–259, Mar. 2007.

[59] T. Scarcelli, J. F. Jordão, M. a O'Reilly, N. Ellens, K. Hynynen, and I. Aubert, "Stimulation of hippocampal neurogenesis by transcranial focused ultrasound and microbubbles in adult mice.," *Brain Stimul.*, vol. 7, no. 2, pp. 304–7, 2014.

[60] S.-K. Wu, M.-T. Yang, K.-H. Kang, H.-C. Liou, D.-H. Lu, W.-M. Fu, and W.-L. Lin, "Targeted delivery of erythropoietin by transcranial focused ultrasound for neuroprotection against ischemia/reperfusion-induced neuronal injury: a long-term and short-term study.," *PLoS One*, vol. 9, no. 2, p. e90107, Jan. 2014.

[61] Y. Anzai, R. Lufkin, A. DeSalles, D. R. Hamilton, K. Farahani, and K. L. Black, "Preliminary experience with MR-guided thermal ablation of brain tumors.," *AJNR. Am. J. Neuroradiol.*, vol. 16, no. 1, pp. 39-48-52, Jan. 1995.

[62] N. McDannold, G. T. Clement, P. Black, F. Jolesz, and K. Hynynen, "Transcranial magnetic resonance imaging- guided focused ultrasound surgery of brain tumors: Initial findings in 3 patients," *Neurosurgery*, vol. 66, no. 2, pp. 323–332, 2010.

[63] F. Y. Yang, M. C. Teng, M. Lu, H. F. Liang, Y. R. Lee, C. C. Yen, M. L. Liang, and T. T. Wong, "Treating glioblastoma multiforme with selective high-dose liposomal doxorubicin chemotherapy induced by repeated focused ultrasound," *Int. J. Nanomedicine*, vol. 7, pp. 965–974, 2012.

[64] F.-Y. Yang, T.-T. Wong, M.-C. Teng, R.-S. Liu, M. Lu, H.-F. Liang, and M.-C. Wei, "Focused ultrasound and interleukin-4 receptor-targeted liposomal doxorubicin for enhanced targeted drug delivery and antitumor effect in glioblastoma multiforme.," *J. Control. Release*, vol. 160, no. 3, pp. 652–8, Jun. 2012.

[65]   S. D. Leblang, K. Hoctor, and F. L. Steinberg, "Leiomyoma shrinkage after MRI-guided focused ultrasound treatment: Report of 80 patients," *Am. J. Roentgenol.*, vol. 194, no. 1, pp. 274–280, 2010.

[66]   O. Al-Bataineh, J. Jenne, and P. Huber, "Clinical and future applications of high intensity focused ultrasound in cancer," *Cancer Treat. Rev.*, vol. 38, no. 5, pp. 346–353, 2012.

[67]   K. Funaki, H. Fukunishi, T. Funaki, and C. Kawakami, "Mid-term outcome of magnetic resonance-guided focused ultrasound surgery for uterine myomas: From six to twelve months after volume reduction," *J. Minim. Invasive Gynecol.*, vol. 14, pp. 616–621, 2007.

[68]   K. Funaki, H. Fukunishi, and K. Sawada, "Clinical outcomes of magnetic resonance-guided focused ultrasound surgery for uterine myomas: 24-Month follow-up," *Ultrasound Obstet. Gynecol.*, vol. 34, no. July, pp. 584–589, 2009.

[69]   a. Okada, Y. Morita, H. Fukunishi, K. Takeichi, and T. Murakami, "Non-invasive magnetic resonance-guided focused ultrasound treatment of uterine fibroids in a large Japanese population: Impact of the learning curve on patient outcome," *Ultrasound Obstet. Gynecol.*, vol. 34, no. July, pp. 579–583, 2009.

[70]   S. H. Landis, T. Murray, S. Bolden, and P. A. Wingo, "Cancer statistics, 1999," *CA. Cancer J. Clin.*, vol. 49, no. 1, pp. 8–31, Jan. 1999.

[71]   D. Gianfelice, A. Khiat, M. Amara, A. Belblidia, and Y. Boulanger, "MR imaging-guided focused US ablation of breast cancer: histopathologic assessment of effectiveness-- initial experience," *Radiology*, vol. 227, no. 3, pp. 849–855, 2003.

[72]   D. B. Zippel and M. Z. P. Frcs, "The Use of MR Imaging Guided Focused Ultrasound in Breast Cancer Patients; a Preliminary Phase One Study and Review," *Breast Cancer*, vol. 12, no. 1, pp. 32–38, 2005.

[73]   R. Kovatcheva, J.-N. Guglielmina, M. Abehsera, L. Boulanger, N. Laurent, and E. Poncelet, "Ultrasound-guided high-intensity focused ultrasound treatment of breast fibroadenoma—a multicenter experience," *J. Ther. Ultrasound*, vol. 3, no. 1, p. 1, 2015.

[74]   U. Lindner, S. Ghai, P. Spensieri, E. Hlasny, T. H. Van Der Kwast, S. a McCluskey, M. a Haider, W. Kucharczyk, and J. Trachtenberg, "Focal magnetic resonance guided focused ultrasound for prostate cancer: Initial North American experience.," *Can. Urol. Assoc. J.*, vol. 6, no. 6, pp. E283-6, 2012.

[75]   C. Yiallouras, C; Damianou, "Review of MRI positioning devices for guiding focused ultrasound systems," 2014.

[76]   C. Yiallouras, N. Mylonas, and C. Damianou, "MRI-compatible positioning device for guiding a focused ultrasound system for transrectal treatment of prostate cancer.," *Int. J. Comput. Assist. Radiol. Surg.*, vol. 9, no. 4, pp. 745–53, Jul. 2014.

[77]   T. Ripert, M.-D. Azémar, J. Ménard, Y. Bayoud, R. Messaoudi, F. Duval, and F. Staerman, "Transrectal high-intensity focused ultrasound (HIFU) treatment of localized prostate cancer: review of technical incidents and morbidity after 5 years of use," *Prostate Cancer Prostatic Dis.*, vol. 13, no. 2, pp. 132–137, Jun. 2010.

[78]   H. U. Ahmed, E. Zacharakis, T. Dudderidge, J. N. Armitage, R. Scott, J. Calleary, R. Illing, A. Kirkham, A. Freeman, C. Ogden, C. Allen, and M.

Emberton, "High-intensity-focused ultrasound in the treatment of primary prostate cancer: the first UK series," *Br. J. Cancer*, vol. 101, no. 1, pp. 19–26, Jul. 2009.

[79] K. U. KÖHRMANN, M. S. MICHEL, J. GAA, E. MARLINGHAUS, and P. ALKEN, "High Intensity Focused Ultrasound as Noninvasive Therapy for Multilocal Renal Cell Carcinoma: Case Study and Review of The Literature," *J. Urol.*, vol. 167, no. 6, pp. 2397–2403, Jun. 2002.

[80] F. WU, Z.-B. WANG, W.-Z. CHEN, J. BAI, H. ZHU, and T.-Y. QIAO, "Preliminary Experience Using High Intensity Focused Ultrasound for the Treatment of Patients With Advanced Stage Renal Malignancy," *J. Urol.*, vol. 170, no. 6, pp. 2237–2240, Dec. 2003.

[81] H. C. Klingler, M. Susani, R. Seip, J. Mauermann, N. Sanghvi, and M. J. Marberger, "A Novel Approach to Energy Ablative Therapy of Small Renal Tumours: Laparoscopic High-Intensity Focused Ultrasound," *Eur. Urol.*, vol. 53, no. 4, pp. 810–818, Apr. 2008.

[82] R. O. Illing, J. E. Kennedy, F. Wu, G. R. ter Haar, A. S. Protheroe, P. J. Friend, F. V Gleeson, D. W. Cranston, R. R. Phillips, and M. R. Middleton, "The safety and feasibility of extracorporeal high-intensity focused ultrasound (HIFU) for the treatment of liver and kidney tumours in a Western population," *Br. J. Cancer*, vol. 93, no. 8, pp. 890–895, Oct. 2005.

[83] H. Zhu, K. Zhou, L. Zhang, C. Jin, S. Peng, W. Yang, K. Li, H. Su, W. Chen, J. Bai, F. Wu, and Z. Wang, "High intensity focused ultrasound (HIFU) therapy for local treatment of hepatocellular carcinoma: Role of partial rib resection," *Eur. J. Radiol.*, vol. 72, pp. 160–166, 2009.

[84] G. Xu, G. Luo, L. He, J. Li, H. Shan, R. Zhang, Y. Li, X. Gao, S. Lin, and G. Wang, "Follow-Up of High-Intensity Focused Ultrasound Treatment for Patients with Hepatocellular Carcinoma," *Ultrasound Med. Biol.*, vol. 37, pp. 1993–1999, 2011.

[85] G. R. Mundy, "Mechanisms of bone metastasis," *Cancer*, vol. 80, no. S8, pp. 1546–1556, 1997.

[86] L. J. Suva, R. J. Griffin, and I. Makhoul, "Mechanisms of bone metastases of breast cancer," *Endocr. Relat. Cancer*, vol. 16, no. 3, pp. 703–713, Sep. 2009.

[87] R. E. Coleman, "Metastatic bone disease: clinical features, pathophysiology and treatment strategies," *Cancer Treat. Rev.*, vol. 27, no. 3, pp. 165–176, Jun. 2001.

[88] G. D. Roodman, "Mechanisms of bone metastasis.," *N. Engl. J. Med.*, vol. 360, no. 16, pp. 1655–1664, 2004.

[89] J. Berenson, L. Rajdev, and M. Broder, "Pathophysiology of bone metastases," *Cancer Biol. Ther.*, vol. 5, no. 9, pp. 1078–1081, Sep. 2006.

[90] A. Delaney, S. M. Fleetwood-Walker, L. A. Colvin, and M. Fallon, "Translational medicine: cancer pain mechanisms and management," *Br. J. Anaesth.*, vol. 101, no. 1, pp. 87–94, Apr. 2008.

[91] B. J. A. Laird, J. Walley, G. D. Murray, E. Clausen, L. A. Colvin, and M. T. Fallon, "Characterization of cancer-induced bone pain: an exploratory study," *Support. Care Cancer*, vol. 19, no. 9, pp. 1393–1401, Sep. 2011.

[92] D. B. Rodrigues, P. R. Stauffer, D. Vrba, and M. D. Hurwitz, "Focused ultrasound for treatment of bone tumours," *Int. J. Hyperth.*, vol. 31, no. 3, pp.

260–271, Apr. 2015.

[93] R. Catane, a. Beck, Y. Inbar, T. Rabin, N. Shabshin, S. Hengst, R. M. Pfeffer, a. Hanannel, O. Dogadkin, B. Liberman, and D. Kopelman, "MR-guided focused ultrasound surgery (MRgFUS) for the palliation of pain in patients with bone metastases - Preliminary clinical experience," *Ann. Oncol.*, vol. 18, no. October 2006, pp. 163–167, 2007.

[94] D. Gianfelice, C. Gupta, W. Kucharczyk, P. Bret, D. Havill, and M. Clemons, "Palliative treatment of painful bone metastases with MR imaging--guided focused ultrasound.," *Radiology*, vol. 249, no. 1, pp. 355–363, 2008.

[95] A. Napoli, M. Anzidei, B. C. Marincola, G. Brachetti, F. Ciolina, G. Cartocci, C. Marsecano, F. Zaccagna, L. Marchetti, E. Cortesi, and C. Catalano, "Primary Pain Palliation and Local Tumor Control in Bone Metastases Treated With Magnetic Resonance-Guided Focused Ultrasound," *Invest. Radiol.*, vol. 48, no. 6, pp. 351–358, Jun. 2013.

[96] R. Gassert, E. Burdet, and K. Chinzei, "MRI-compatible robotics," *IEEE Eng. Med. Biol. Mag.*, vol. 27, no. June, pp. 12–14, 2008.

[97] J. F. Schenck, "The role of magnetic susceptibility in magnetic resonance imaging: MRI magnetic compatibility of the first and second kinds.," *Medical physics*, vol. 23. pp. 815–850, 1996.

[98] "Ettinger R, Watkins R, Rohling K. General Electric Company, assignee. Magnetic resonance guided focused ultrasound therapy system with inclined track to move transducers in a small vertical space. US Patent US 5275165, 1994." .

[99] "Cline H, Rohling K, Abeliing W. General Electric Company, assignee. Mechanical positioner for magnetic resonance guided ultrasound therapy. US Patent US5443068, 1995." .

[100] et al. Yehezkeli O, Freundlich D, Magen N, "INSIGHTECTXSONICSLTD, assignee. Mechanical positioner for MRI guided ultrasound therapy system WO0209812," 2002.

[101] G. S. Fischer, A. Krieger, I. Iordachita, C. Csoma, L. L. Whitcomb, and G. Fichtinger, "MRI compatibility of robot actuation techniques - A comparative study," *Lect. Notes Comput. Sci. (including Subser. Lect. Notes Artif. Intell. Lect. Notes Bioinformatics)*, vol. 11, pp. 509–517, 2008.

[102] R. Chopra, L. Curiel, R. Staruch, L. Morrison, and K. Hynynen, "An MRI-compatible system for focused ultrasound experiments in small animal models," *Med. Phys.*, vol. 36, no. 5, p. 1867, 2009.

[103] C. Damianou, K. Ioannides, V. Hadjisavvas, N. Mylonas, A. Couppis, and D. Iosif, "In vitro and in vivo brain ablation created by high-intensity focused ultrasound and monitored by MRI.," *IEEE Trans. Ultrason. Ferroelectr. Freq. Control*, vol. 56, no. 6, pp. 1189–98, Jun. 2009.

[104] N. Mylonas, "MR compatible positioning device for guiding a focused ultrasound system for the treatment of brain deseases," no. February 2013, pp. 1–10, 2014.

[105] V. Rieke and K. Butts Pauly, "MR thermometry," *J. Magn. Reson. Imaging*, vol. 27, no. 2, pp. 376–390, Feb. 2008.

[106] G. Menikou, T. Dadakova, M. Pavlina, M. Bock, and C. Damianou, "MRI compatible head phantom for ultrasound surgery," *Ultrasonics*, vol. 57, pp.

144–152, Mar. 2015.

[107] C. Damianou and K. Hynynen, "Focal spacing and near-field heating during pulsed high temperature ultrasound therapy," *Ultrasound Med. Biol.*, vol. 19, no. 9, pp. 777–787, Jan. 1993.

[108] X. Fan and K. Hynynen, "Ultrasound surgery using multiple sonications—Treatment time considerations," *Ultrasound Med. Biol.*, vol. 22, no. 4, pp. 471–482, Jan. 1996.

[109] N. J. McDannold, F. A. Jolesz, and K. H. Hynynen, "Determination of the Optimal Delay between Sonications during Focused Ultrasound Surgery in Rabbits by Using MR Imaging to Monitor Thermal Buildup in Vivo," *Radiology*, vol. 211, no. 2, pp. 419–426, May 1999.

[110] C. Mougenot, M. O. Köhler, J. Enholm, B. Quesson, and C. Moonen, "Quantification of near-field heating during volumetric MR-HIFU ablation," *Med. Phys.*, vol. 38, no. 1, p. 272, 2011.

[111] M. O. Köhler, C. Mougenot, B. Quesson, J. Enholm, B. Le Bail, C. Laurent, C. T. W. Moonen, and G. J. Ehnholm, "Volumetric HIFU ablation under 3D guidance of rapid MRI thermometry," *Med. Phys.*, vol. 36, no. 8, p. 3521, 2009.

[112] Hong Wan, P. VanBaren, E. S. Ebbini, and C. A. Cain, "Ultrasound surgery: comparison of strategies using phased array systems," *IEEE Trans. Ultrason. Ferroelectr. Freq. Control*, vol. 43, no. 6, pp. 1085–1098, Nov. 1996.

[113] K. Hynynen, O. Pomeroy, D. N. Smith, P. E. Huber, N. J. McDannold, J. Kettenbach, J. Baum, S. Singer, and F. A. Jolesz, "MR Imaging-guided Focused Ultrasound Surgery of Fibroadenomas in the Breast: A Feasibility Study," *Radiology*, vol. 219, no. 1, pp. 176–185, Apr. 2001.

[114] R. Salomir, J. Palussire, F. C. Vimeux, J. A. De Zwart, B. Quesson, M. Gauchet, P. Lelong, J. Pergrale, N. Grenier, and C. T. W. Moonen, "Local hyperthermia with MR-guided focused ultrasound: Spiral trajectory of the focal point optimized for temperature uniformity in the target region," *J. Magn. Reson. Imaging*, vol. 12, no. 4, pp. 571–583, Oct. 2000.

[115] B. E. Billard, K. Hynynen, and R. B. Roemer, "Effects of physical parameters on high temperature ultrasound hyperthermia," *Ultrasound Med. Biol.*, vol. 16, no. 4, pp. 409–420, Jan. 1990.

[116] P. B. Paar Christof, Pelzl Jan, "Understanding Cryptography: A Textbook for Students and Practitioners," Springer, 2010, p. 7.

[117] I. Parberry, "An efficient algorithm for the Knight's tour problem," *Discret. Appl. Math.*, vol. 73, no. 3, pp. 251–260, Mar. 1997.

[118] H. H. Pennes, "Analysis of tissue and arterial blood temperatures in the resting human forearm," *J. Appl. Physiol.*, vol. 1, no. 2, pp. 93–122, 1948.

[119] H. T. O'Neil, "Theory of Focusing Radiators," *J. Acoust. Soc. Am.*, vol. 21, no. 5, p. 516, 1949.

[120] S. A. Sapareto and W. C. Dewey, "Thermal dose determination in cancer therapy," *Int. J. Radiat. Oncol.*, vol. 10, no. 6, pp. 787–800, Apr. 1984.

[121] C. Damianou, K. Hynynen, and X. Fan, "Application of the thermal dose concept for predicting the necrosed tissue volume during ultrasound surgery," in *Proceedings of IEEE Ultrasonics Symposium*, pp. 1199–1202.

[122]

"http://www.ondacorp.com/images/brochures/Onda_GelPhantom_DataSheet.pdf." .

[123] A. Payne, U. Vyas, N. Todd, J. de Bever, D. A. Christensen, and D. L. Parker, "The effect of electronically steering a phased array ultrasound transducer on near-field tissue heating," *Med. Phys.*, vol. 38, no. 9, p. 4971, 2011.

[124] N. Ellens and K. Hynynen, "Simulation study of the effects of near-and far-field heating during focused ultrasound uterine fibroid ablation using an electronically focused phased array: A theoretical analysis of patient safety," *Med. Phys.*, vol. 41, no. 7, p. 72902, 2014.

[125] K. Hynynen, "Demonstration of enhanced temperature elevation due to nonlinear propagation of focussed ultrasound in dog's thigh in vivo," *Ultrasound Med. Biol.*, vol. 13, no. 2, pp. 85–91, 1987.

[126] C. Damianou, "MRI monitoring of the effect of tissue interfaces in the penetration of high intensity focused ultrasound in kidney in vivo," *Ultrasound Med. Biol.*, vol. 30, no. 9, pp. 1209–1215, Sep. 2004.

[127] F. M. Fennessy, C. M. Tempany, N. J. McDannold, M. J. So, G. Hesley, B. Gostout, H. S. Kim, G. A. Holland, D. A. Sarti, K. Hynynen, F. A. Jolesz, and E. A. Stewart, "Uterine leiomyomas: MR imaging-guided focused ultrasound surgery--results of different treatment protocols.," *Radiology*, vol. 243, no. 3, pp. 885–93, Jun. 2007.

[128] W. J. Elias, D. Huss, T. Voss, J. Loomba, M. Khaled, E. Zadicario, R. C. Frysinger, S. A. Sperling, S. Wylie, S. J. Monteith, J. Druzgal, B. B. Shah, M. Harrison, and M. Wintermark, "A Pilot Study of Focused Ultrasound Thalamotomy for Essential Tremor," *N. Engl. J. Med.*, vol. 369, no. 7, pp. 640–648, Aug. 2013.

APPENDIX 1

Journal publications

[1] Yiannakou M., Trimikliniotis M., Yiallouras C. and Damianou C. "Evaluation of focused ultrasound algorithms: Issues for reducing pre-focal heating and treatment time" Ultrasonics (2015). DOI: 10.1016/j.ultras.2015.10.007

[2] Menikou G., Yiannakou M., Yiallouras C., Ioannides C. and Damianou C. "MRI-compatible bone phantom for evaluating ultrasonic thermal exposures" (2016), DOI: 10.1016/j.ultras.2016.05.020

[3] Menikou G., Yiallouras C., Yiannakou M. and Damianou C. "MRI-guided focused ultrasound robotic system for the treatment of bone cancer" The International Journal of Medical Robotics and Computer Assisted Surgery, (2016), DOI: 10.1002/rcs.1753

[4] M. Yiannakou, G. Menikou C. Yiallouras, K. Ioannides, C. Damianou, MRI guided focused ultrasound robotic system for animal experiments, accepted in the International Journal of Medical Robotics and Computer Assisted Surgery, Dec 2016.

[5] C. Damianou, M. Yiannakou, G. Menikou, C. Yiallouras, 'MRI guided coupling for a Focused Ultrasound system using a top to bottom propagation', Journal of Therapeutic Ultrasound, accepted Oct 2016.

[6] N. Papadopoulos, G. Menikou, M. Yiannakou, C. Yiallouras, K. Ioannides, C. Damianou, 'Evaluation of a small flat rectangular therapeutic ultrasonic transducer intended for intravascular use', Ultrasonics 2017

Submitted patent

Damianou C., Yiannakou M., 'Multi-purposed robotic system for MRI guided focused ultrasound treatment' submitted patent.

Submitted journal publications

[1] G. Menikou, M. Yiannakou, C. Yiallouras, C. Ioannides, C. Damianou, 'MRI-compatible breast/rib phantom for evaluating ultrasonic thermal exposures', The International Journal of Medical Robotics and Computer Assisted Surgery.

[2] C. Yiallouras, M. Yiannakou, G. Menikou, C. Kouzoupos, K. Ioannides, C. Damianou, 'A three axis modular robotic system for MRI guided focused ultrasound applications', Ultrasonics 2016.

Conference papers

[1] Yiannakou M., Yiallouras C., Mylonas N.,Damianou N., MR-guided focused ultrasound robot for animal experiments', ISTU 14, Las Vegas, USA, April 2-5, 2014.

[2] C. Damianou, M. Yiannakou, 'Rabbit model for Alzheimer amyloid beta plaques for mri guided focused ultrasound in synergy with antibody drugs', 3 rd European symposium on focused ultrasound therapy, London October 14-17, 2015.

[3] C. Damianou, M. Yiannakou, Amyloid Aβ plaque reduction with antibodies crossing the blood brain barrier opened in 3 sessions with focused ultrasound in a rabbit model', oral presentation, International Society of therapeutic Ultrasound (ISTU 2016), ISTU, Tel Avis, Israel, March 14-16, 2016.

[4] G. Menikou, M. Yiannakou, C. Yiallouras, K. Ioannides, C. Damianou, 'MRI-compatible bone phantom for evaluating ultrasonic thermal exposures', poster presentation, International Society of therapeutic Ultrasound (ISTU 2016), ISTU, Tel Avis, Israel, March 14-16, 2016.

[5] M. Yiannakou, C. Yiallouras, C. Damianou, 'MRI guided focused ultrasound robotic system for animal experiments', poster presentation, International Society of therapeutic Ultrasound (ISTU 2016), ISTU, Tel Avis, Israel, March 14-16, 2016.